INFORMATION TO USERS

This material was produced from a microfilm copy of the original document. While the most advanced technological means to photograph and reproduce this document have been used, the quality is heavily dependent upon the quality of the original submitted.

The following explanation of techniques is provided to help you understand markings or patterns which may appear on this reproduction.

1. The sign or "target" for pages apparently lacking from the document photographed is "Missing Page(s)". If it was possible to obtain the missing page(s) or section, they are spliced into the film along with adjacent pages. This may have necessitated cutting thru an image and duplicating adjacent pages to insure you complete continuity.

2. When an image on the film is obliterated with a large round black mark, it is an indication that the photographer suspected that the copy may have moved during exposure and thus cause a blurred image. You will find a good image of the page in the adjacent frame.

3. When a map, drawing or chart, etc., was part of the material being photographed the photographer followed a definite method in "sectioning" the material. It is customary to begin photoing at the upper left hand corner of a large sheet and to continue photoing from left to right in equal sections with a small overlap. If necessary, sectioning is continued again — beginning below the first row and continuing on until complete.

4. The majority of users indicate that the textual content is of greatest value, however, a somewhat higher quality reproduction could be made from "photographs" if essential to the understanding of the dissertation. Silver prints of "photographs" may be ordered at additional charge by writing the Order Department, giving the catalog number, title, author and specific pages you wish reproduced.

5. PLEASE NOTE: Some pages may have indistinct print. Filmed as received.

Xerox University Microfilms

300 North Zeeb Road
Ann Arbor, Michigan 48106

7815369

LINDSTED, ROBERT DEAN
  A PHOTOGRAPHIC TECHNIQUE TO OBTAIN DROPLET
  AND FLOW PATTERN DATA IN TWO-PHASE FLOW FOR
  USE IN MODELING.

  THE UNIVERSITY OF OKLAHOMA, PH.D., 1977

THE UNIVERSITY OF OKLAHOMA

GRADUATE COLLEGE

A PHOTOGRAPHIC TECHNIQUE

TO OBTAIN

DROPLET AND FLOW PATTERN DATA

IN

TWO-PHASE FLOW FOR USE IN MODELING

A DISSERTATION

SUBMITTED TO THE GRADUATE FACULTY

in partial fulfillment of the requirements for the

degree of

DOCTOR OF PHILOSOPHY

BY

ROBERT DEAN LINDSTED

Norman, Oklahoma

1977

A PHOTOGRAPHIC TECHINQUE

TO OBTAIN

DROFLET AND FLOW PATTERN DATA

IN

TWO-PHASE FLOW FOR USE IN MODELING

APPROVED BY

DISSERTATION COMMITTEE

ACKNOWLEDGMENTS

The author wishes to express his gratitude to his major advisor, Dr. John Francis, for his guidance and suggestions during the course of this study. Likewise, the suggestions, encouragement and cooperation of Dr. Ray Smith has been much appreciated. In addition, the cooperation and suggestions of the rest of the Doctoral Committee consisting of Dr. Tom Love, Dr. Ed Blick, and Dr. Cedomir Sliepcevich is gratefully acknowledged.

Special thanks is also expressed to Dr. Lester Cheng and Dr. Glen Zumwalt for their interest and technical advice on this project. In addition, the help of a number of students who were involved with both the data taking and reduction is acknowledged as follows: Toby Harrison (photography), Allen Abrahams (photography and droplet data reduction), David Evans (computer data reduction), Marty Todd (droplet data reduction), Mike Paddock (data presentation) and Denée Thomas (droplet data reduction, editing and encouragement).

Finally, the author expresses his thanks to his wife, Sharon, and children, Pam, Byron and Kyle, for their patience and understanding during the entire course of this study.

TABLE OF CONTENTS

LIST OF TABLES

LIST OF ILLUSTRATIONS

A PHOTOGRAPHIC TECHNIQUE

TO OBTAIN

DROPLET AND FLOW PATTERN DATA

IN

TWO-PHASE FLOW FOR USE IN MODELING

CHAPTER I

INTRODUCTION

The general topic of two-phase flow is very broad,
covering gas-solid, gas-liquid, liquid-liquid and liquid-
solid flows. The equations describing two-phase flow are
both more numerous than for describing single-phase flow and
more complex due to the interaction between phases. Since
the general nature of two-phase flow is involved and complex,
it is difficult to describe adequately in any universal sense.
Normally the flow conditions are classified according to
flow regimes and then the behavior for each particular flow
regime is analyzed.

This study will be concerned with two-phase, two-com-
ponent flow. More specifically, it will concentrate on gas-
liquid flow using an air-water system at approximately

atmospheric conditions. As a result, the assumption of two-component flow as well as no phase change is appropriate.

There are still many possible flow patterns that have been identified in two-phase, gas-liquid systems. However, due to gravitational effects on flows with large density differences the flow regimes can be further classified as either vertical or horizontal flow. This study will be restricted to vertical flow only.

Figure 1 shows several possible flow regimes for vertical two-phase flow in the order of decreasing liquid flow, or increasing gas flow, going from left to right. It should be noted that on each end of the two-phase spectrum there is an extreme case where one phase is dispersed within the other. Between these extremes exists a number of possible flow patterns, depending on the flow conditions. The dividing line between the adjacent flow regimes cannot be well defined, however, since the transition from one to another occurs gradually and the identification of each regime is usually made by visual inspection.

Again, this study will be restricted primarily to dispersed-annular flow. This is the type of flow in which a liquid layer film forms a continuous interface on the wall of the flow tube for the stream of gas which flows in the center of the channel. The gas core region may contain any number of droplets of various sizes, depending on the quality and

|Bubble Flow | Slug Flow | Churning-Slug Flow | Wispy-Annular Flow | Dispersed-Annular Flow | Dispersed or Mist Flow |
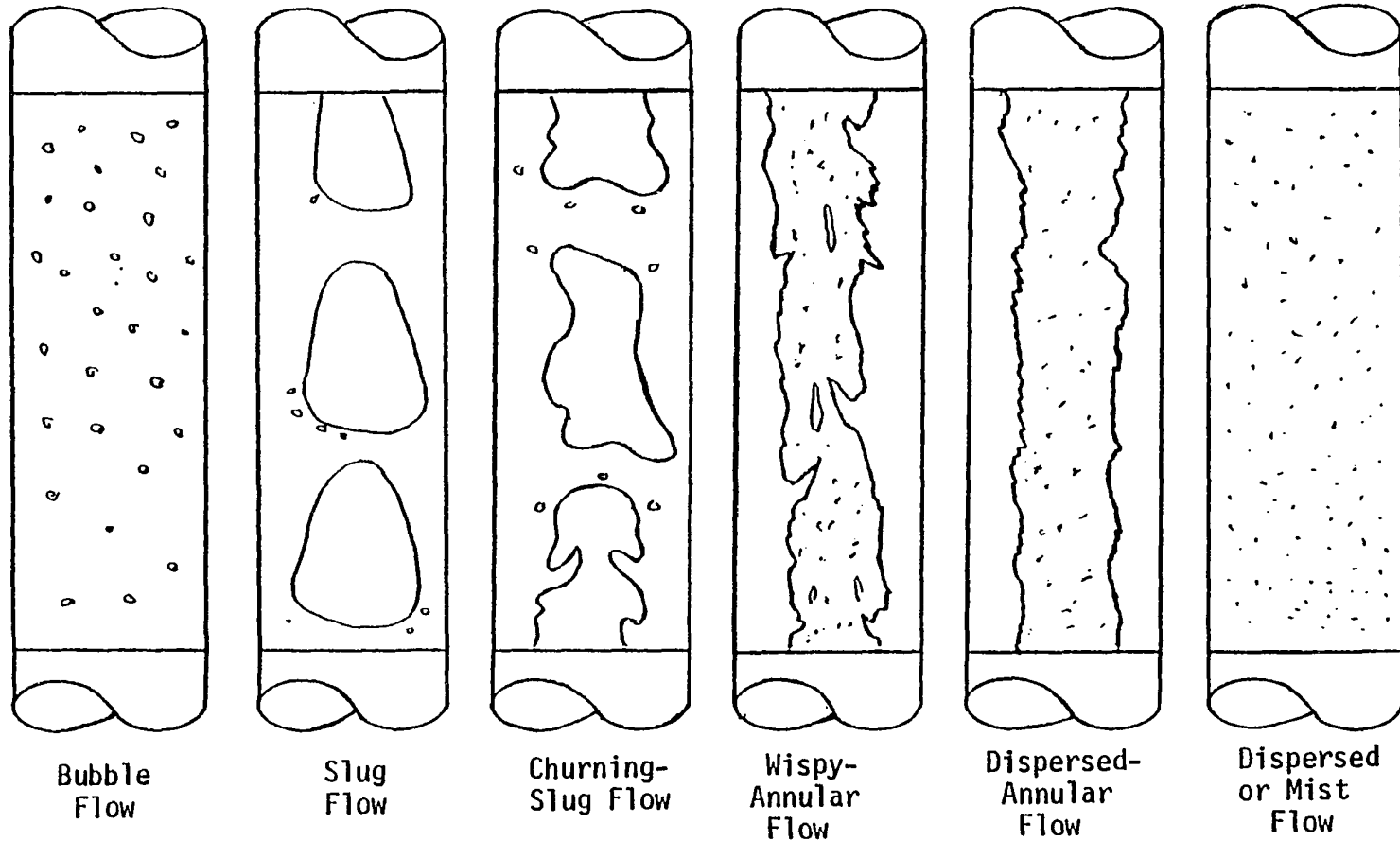
Figure 1. Different Flow Regimes Observed for Vertical Two-Phase Flows in the Order of Decreasing Liquid Flow (Left to Right).

the flow conditions. In addition, the gas-liquid interface is not smooth, but "wavy". The gas-liquid interface is further complicated by an exchange of the liquid's mass between waves on the wall and entrainment of droplets in the gas core. The interchange process at the gas-liquid interface can be attributed to the shearing forces on the tips of the waves.

In order to assess the place of this present study with respect to existing literature, a brief review will be made concerning analytical models and measurement techniques for droplets and liquid film thickness using photographic techniques in two-phase flow. Finally, the goals of this study will be stated with respect to the current direction as indicated by two phase flow literature.

Literature Review of Analytical Models

The earliest and simplest models for describing two-phase flow are referred to as "mixture" models or "homogeneous" models. The phases in these models are assumed to be thoroughly mixed and by using "effective" or "average" values of the properties of the component phases, especially density, the overall flow is treated as a single homogeneous fluid. In addition, some mixture models, such as the work of Tangren et al.[1] assume the phases to be in thermal equilibrium at all times. This model has become a standard for mixture models because of its prediction of sonic and essentially

critical or choking velocity for two-phase air-water mix-
tures.* Calculations by Smith[2], however, indicated that in-
sufficient time to achieve thermal equilibrium actually
exists, especially when there is mass transfer required. Im-
provements were made on the homogeneous thermal equilibrium
models by Fauske,[3] who used a slip ratio defined as the ratio
of gas to liquid velocities, to modify the density variation
assumptions as they appeared in the homogeneous thermal equi-
librium model. Fauske's value for slip ratio was inversely
proportional to the square root of the ratio of the gas and
liquid densities. Other investigators have also modified the
mixture models to account for changes in the flow behavior,
especially near critical flow conditions. Moody[4] and Cruver
and Moulton[5] account for such changes by using a slip ratio
that is inversely proportional to the cube root of the ratio
between gas and liquid densities.

These later references mark a transition from the pure
mixture models to "mixture with separated phase" models.
These models use a mixture density, but the phases are con-
sidered separately for a balance of the mass, momentum and
energy transport rates in order to maintain thermal equilib-
rium through the flow. Henry[6] and Henry and Fauske[7] further

---

*Most of the analytical work with mixture models has
been done in conjunction with critical flow and sonic velocity
in two-phase flow. As a result, the comparison and discussion
of the mixture models will be presented primarily in terms of
these parameters.

developed these models by considering the phases separately but using a critical slip ratio with a maximum value of one. It should be noted that the experimental results of Vogrin,[8] Klingbiel[9] and Fauske[10] could not confirm the higher slip ratio defined in terms of the ratio of the gas and liquid densities, that was derived by early investigators[11].

Results of these various mixture models have generally been good in the very low quality region but very poor and misleading when used to describe flow conditions at higher qualities, or when the phases are not distributed in accordance with mixture model assumptions. Smith, et al.,[12] have shown that large discrepancies exist between experimental sonic velocity data and values of sonic velocity using the mixture model.

To summarize, the characteristics of the homogeneous or mixture model will be listed. First, the model does not represent the actual physical flow conditions very well. Next, the results from such models for parameters such as pressure drop, critical flow through nozzles, sonic velocity, etc., have been found to be in considerable error, especially over a wide range of quality values. In addition, the mixture models, except for those models that employ a separated-phase model to assist in obtaining the value of the effective density, do not offer an opportunity for further development or improvement. More importantly, the mixture models do not

have any mechanism to account for two-phase flow parameters such as entrainment, interfacial waves, interfacial shear stress, velocity distribution, etc. The advantage of the mixture models is mainly their simplicity and the reasonable results obtained when compared to experimental results at low qualities. A more detailed discussion of the various mixtures as well as a comparison of their results can be found in the work by Smith, et al.[13]

The separated flow models take into account that the two phases may have different properties and velocities. Although separated flow models have been developed with various degrees of sophistication and complexity, the universal application of the model is often difficult since local averaged properties and velocities are functions of both the flow conditions as well as the distribution of each phase over the cross-sectional area. In the simplest separated flow models only one variable, such as velocity, is allowed to differ for the two phase. Often, more advanced models introduce correlations and experimental data to simplify the equations or reduce the number of unknowns. In order to avoid excessive use of correlations, however, it is necessary to write separate equations for the continuity, momentum and energy balance of each phase. This increase in sophistication and precision results in a corresponding increase in complexity.[14] In general, the assumption of a continuous gas phase, as in the case of

dispersed-annular flow shown in Figure 1, is well suited to separated flow analysis. Thus, the separated models are most descriptive, from a physical point of view, for flow conditions having high quality.

Hewitt and Hall-Taylor[15] presented separate equations for each phase but assumed velocity, mass flux and shear stress on the wall to be constant. The flow equations for this model are based on just two flow areas; one describes all gas flow, and one all liquid flow. In addition, the density value used in the separated energy equation was obtained from the mixture model concept; thus the model was not a separated model in the strictest sense. An improvement in the Hewitt and Hall-Taylor model was made by assuming three flow regions; one each to describe the liquid film on the wall, the gas core and the liquid entrainment.

Smith[16,17] also used separated flow equations but included effects of the interface between the gas and liquid phases. This was done by considering the gas and liquid to be in annular flow and describable by separated single-phase equations. Empirical relationships for the momentum and energy transport rates were used to relate the interfacial effects of one phase on the other. Specifically, this model allowed for momentum effects of the liquid on the air by considering drag on spherical droplets with wakes. The model also allowed for energy transport between phases at both the

the liquid film and droplet interface. Finally, a correction factor was introduced to modify the flow area for each phase in order to compensate for the assumptions of smooth interface area and uniform droplet distribution.

Wallis [18,19] who was later joined by Sullivan,[20] also developed a separated model for describing two-phase flow. This model considered a simple force balance on the gas core region making use of an interfacial shear stress that can be empirically determined in terms of a superficial gas friction factor, which was based on gas flowing alone in the flow tube. Wallis suggested an improvement in this model which takes into account the droplet entrainment in the gas core region by modifying certain two-phase flow parameters by the ratio of the gas mass flow rate to the total mass flow rate in the core region.

In general, there are two major advantages of the separated models used in describing two-phase flow. First, results at the high quality flow conditions are very good. Second, the separated model has a great potential for further development despite its complicated nature. This potential can be realized only when additional experimental data, specifically relating to the flow pattern and liquid-gas distribution, can be obtained.

The goal of the separated flow models is to address the interfacial parameters. This can only be done when the

flow pattern has been thoroughly established for a whole range of two-phase flow conditions. The characteristics of both the liquid entrainment (droplets) and the liquid film, including waves, are the needed flow pattern data for model building. Additional discussion of these and other separated two-phase flow models can be found in the work of Martindale[21] and Sullivan.[22]

Literature Review of Measurement Techniques Using Photography

As mentioned in the literature review of the analytical models describing two-phase flow, considerable interest exists for making accurate and complete measurements of droplet data and liquid film thickness. To date, many methods for determining droplet size, number and distribution have been employed. One method, called the "Impingement Coating Technique", consists of coating a plate with soft magnesium oxide to be held in droplet flow and allowing holes to be made in the magnesium oxide film by the impinging droplets. Ryley and Fallon[23] and Farmer, et al.;[24] have used this technique to record the number and size of droplets. Another technique, which has met with only moderate success, is referred to as the "Electrical Contacts Method" where droplets are allowed to strike an electrically-charged wire. The decrease in charge can be related to droplet size so the number of droplets as well as the droplet size can be determined.

Erroneous signals from other flow in the tube as well as in-
accuracies in the droplet count have been reported by MacVean
and Wallis [25] while using this technique.

Growing emphasis has been placed on photographic tech-
niques as a means of analyzing two-phase flow. Normally
flash photographs are taken through transparent walls which
allow a study to be made of droplet size. In annular flow,
however, the liquid film on the wall prevents a good view of
the droplets in the core region through the wall of the tube.
Cooper, et al.,[26] and Arnold and Hewitt[27] have taken photo-
graphs of the gas core and droplet entrainment by removing
the liquid film on the wall. The removal of this liquid film,
however, will interfere with the exchange of liquid between
the film on the wall and the entrainment in the gas core.
Cousins and Hewitt,[28] Hewitt and Hall-Taylor,[29] and Cumo,
et al.,[30] have all presented photographic data after first
removing the liquid film from the wall. In addition, Hewitt
and Hall-Taylor also show examples of axial photograph[31] but
no usable data has been reported until the work of Gass [32],
which is an immediate predecessor of this current work.

As a result of information reported in literature,
droplet data to date, could be described as preliminary and
insufficient. This is confirmed by investigators such as
Crowe, et al.,[33] who must assume values for typical droplet
size for use in their model at the present time.

In addition to entrainment data, liquid film thickness is a needed flow parameter in two-phase flow. To date, most data has been taken using probes of one type or another. A review of most of the probe techniques used in two-phase flow can be found in the work of Bergles.[34] The EPRI report on Experiment Methods in Two-Phase Flow Studies[35] discusses in detail the conductance probe technique. This technique consists of measuring the conductance between two electrodes which pass through a non-conducting wall of the channel and are positioned flush with the inner surface of the flow tube. In general, the accuracy of many film measuring techniques are still in question. As well, reliable values of film thickness are still needed for flow conditions at low qualities.

Goals for this Study

In view of the current needs and interests indicated in two-phase flow literature, this study will first address itself to establishing a technique for obtaining comprehensive and complete droplet data using axial photography. The data will include parameters relating to size, number, shape and distribution of the droplets over a wide range of flow rates and qualities. An important aspect of this data is felt to lie in the method of photographic analysis as well as the technique for data presentation. Thus, in addition to average values of droplet data, curves which relate the

probability of finding droplets having parameters within a given range will also be presented.

Besides droplet data, liquid film thickness and flow pattern parameters such as the blockage due to waves and droplets in the gas core region will also be evaluated using the axial photographic technique. The measurement of these parameters, along with comprehensive droplet data, will lead to velocity profiles as well as geometric and mass blockage factors which can be evaluated and presented as functions of the flow conditions and the liquid-gas distribution in the flow tube.

This study addressed itself to establishing the flow pattern for two-phase flow. It is recognized that interfacial data is needed and very valuable. While this work does not deal directly with the interface processes, it does provide a well established description of the flow pattern which is considered a prerequisite for obtaining usable interfacial process parameters.

CHAPTER II

EXPERIMENTAL EQUIPMENT AND PROCEDURE

The experimental system, shown in Figure 2, consisted of a vertical 1.258 inch ID Plexiglas tube with upward flow. The air was supplied by two compressors, 10 hp and 25 hp, connected in parallel. At low flow rates, continuous runs as long as four hours in duration could be made. At the higher flow rates occasional shut down was required, mainly to keep the air temperatures below an 85°F to 90°F range. The air stream was monitored by a one inch ID sharp-edge orifice which was made to ASME standards with a diameter ratio, β, of 0.75.

Two-phase flow was generated by injecting water into the air stream through two equally spaced, .25 inch OD copper tubes. These water injection tubes were located 38 inches below the test section and the air stream began its vertical path 57 inches from the test section.

The water injected into the flow loop was supplied by the water from a reservoir and was pumped with sufficient pressure to allow it to enter the air stream. The water reservoir also served as a heat exchanger since the air was
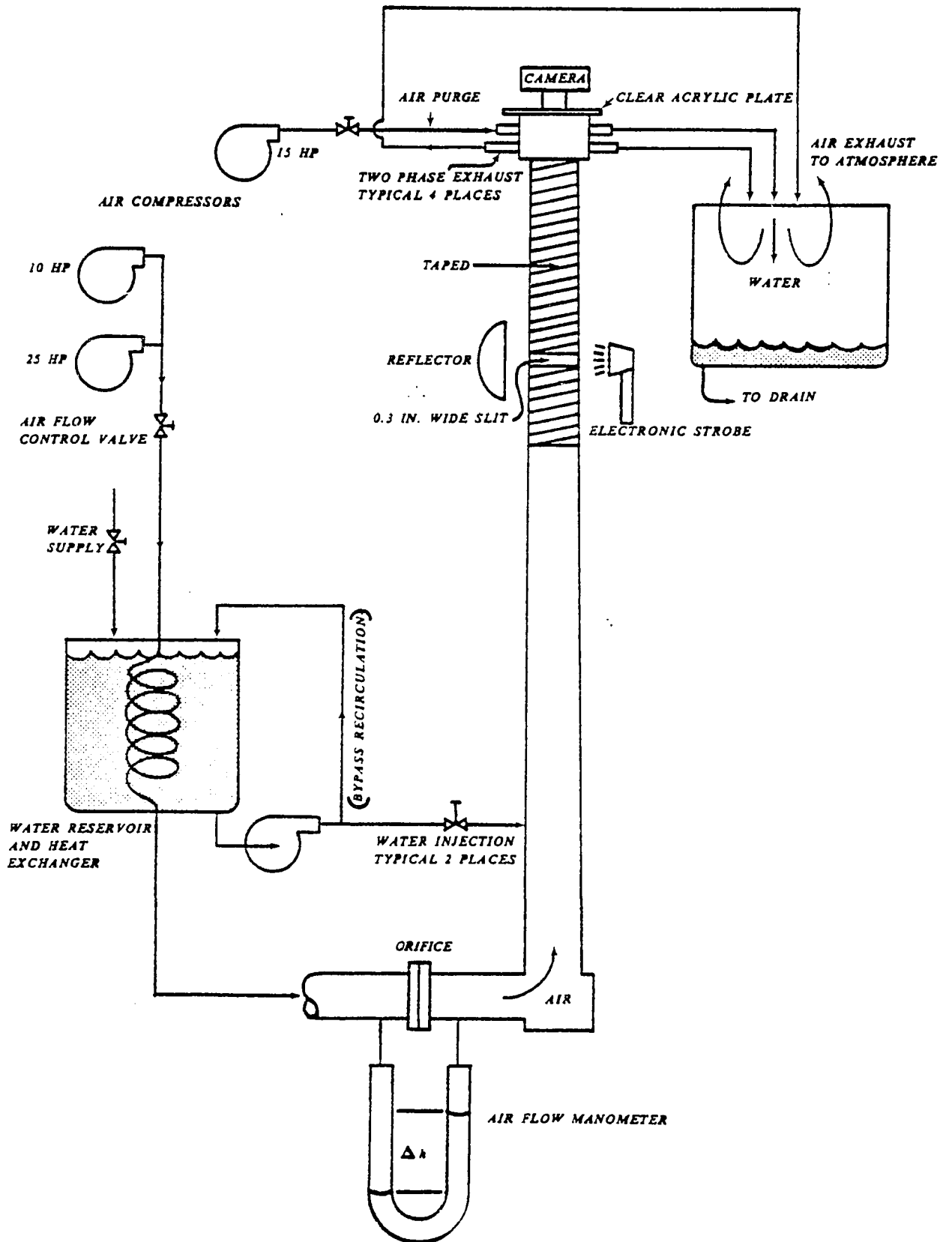
FIGURE 2. TWO PHASE FLOW LOOP.

passed through the reservoir in an attempt to keep the temperature of the air and water approximately the same in order to minimize the heat transfer effects between the two phases. However, when the temperature difference between the water and air exceeded approximately 10°F, the compressors supplying the air were shut down and allowed to cool.

The lens of the camera was located 66 inches directly above the point where the air began its upward flow. Care was taken to align the tube and camera such that axial photographs could be taken. The flow tube was rendered opaque by taping from the top of the tube just below the camera lens for a distance of 18 inches down the tube, leaving only a 0.3 inch slit at the focus distance, which was 8.7 inches for the particular lens that was used in this study.

A clear, acrylic plate was mounted on top of the flow tube in order to protect the lens of the camera from the air and water mixture in the tube.

In order to exhaust the two-phase mixture at the top of the flow tube, four plastic tubes, 3/4 inch ID located 2 inches down from the lens and equally spaced around the perimeter were installed. Thus, the two phase-flow was exhausted to atmospheric pressure. In addition, just below the acrylic plate but higher than the four exhaust tubes, a higher pressure air purge system was used in order to keep any water which did not go out the exhaust tubes from collecting on the plate. It was found that purge flow rates of

2.5 to 3.5 lbm/min, depending on the two-phase flow conditions, were sufficient to keep the axial view of the camera clear.

The photographic system used for this work was similar to the system developed in earlier work done at Wichita State University by Gass.[36] Slides showing axial two-phase flow were taken using a 35 mm, Nikon F camera with a Nikkor-H 50 mm, 1:2 lens and an f-11 aperture setting, and having a shutter speed of approximately 1/60 second. The focial plane was lit through a 0.3 inch slit by a Honeywell Strobonar 710 photographic strobe with a flash duration of approximately 0.0002 seconds. A parabolic reflector was mounted directly opposite the strobe light to achieve more uniform lighting. Kodachrome 64 film was used for the color slides.

Although the main thrust of this work was to use photographic techniques to study two-phase flow, data in the form of pressure drop and velocity readings were made to check the velocity values reported in the analysis section of this thesis. A Vishay/Ellis-20 digital strain indicator and a pressure transducer were used to obtain pressure measurements which allowed 896 counts for a pressure difference of only one psia. Static pressure readings were taken using holes tapped in the wall of the flow tube and velocity measurements were made at the focus plane using a pitot static tube. Extra care was prerequisite in order to prevent the entrance of moisture into the strain indicator.

To avoid this, a "trap" system was developed to collect the water that was present in the pressure reading tubes and still allow pressure readings to be obtained.

Considerable trouble was experienced in taking velocity readings for flow conditions with qualities less than 75%. Even at qualities of 90%, droplets and moisture in the pitot static tube required frequent shut downs of the flow loop.

The quality of the two-phase mixture, defined by the mass flow of gas divided by the total mass flow of the mixture, was determined for each run by calculating the gas flow rate from the pressure drop across the sharp-edged orifice, and then collecting and weighing the water out the exhaust tubes over a given period of time. Approximately ten minutes were allowed after each change in the water or gas flow rates to insure steady conditions in the flow tube.

CHAPTER III

EXPERIMENTAL DATA AND RESULTS

Range of Flow Conditions

Using the flow loop shown in Figure 2, photographs were taken of axial two-phase flow. Wallis[37] has pointed out that some distinction should be made between droplet data taken using photographic techniques and other sampling methods, such as probes.[38,39] Photographs show the number of droplets that are instantaneously contained in a control volume, whereas probe sampling would give the number of droplets which pass a given point during a specified time. For this study a lighted slit of 0.3 inch was defined as the control volume. In general, as gas velocities and droplet velocities increase, the size of the control volume should also be increased.

Figure 3 shows the range of flows for this study. Earlier work[40] has shown that a marked transition in the flow pattern occurs around 15% quality, and that flow below this quality can no longer be treated as separated flow. As a result, a range of qualities from 15 to 90% was selected for this study. The lowest gas flow rate was selected as approximately the minimum rate which could sustain
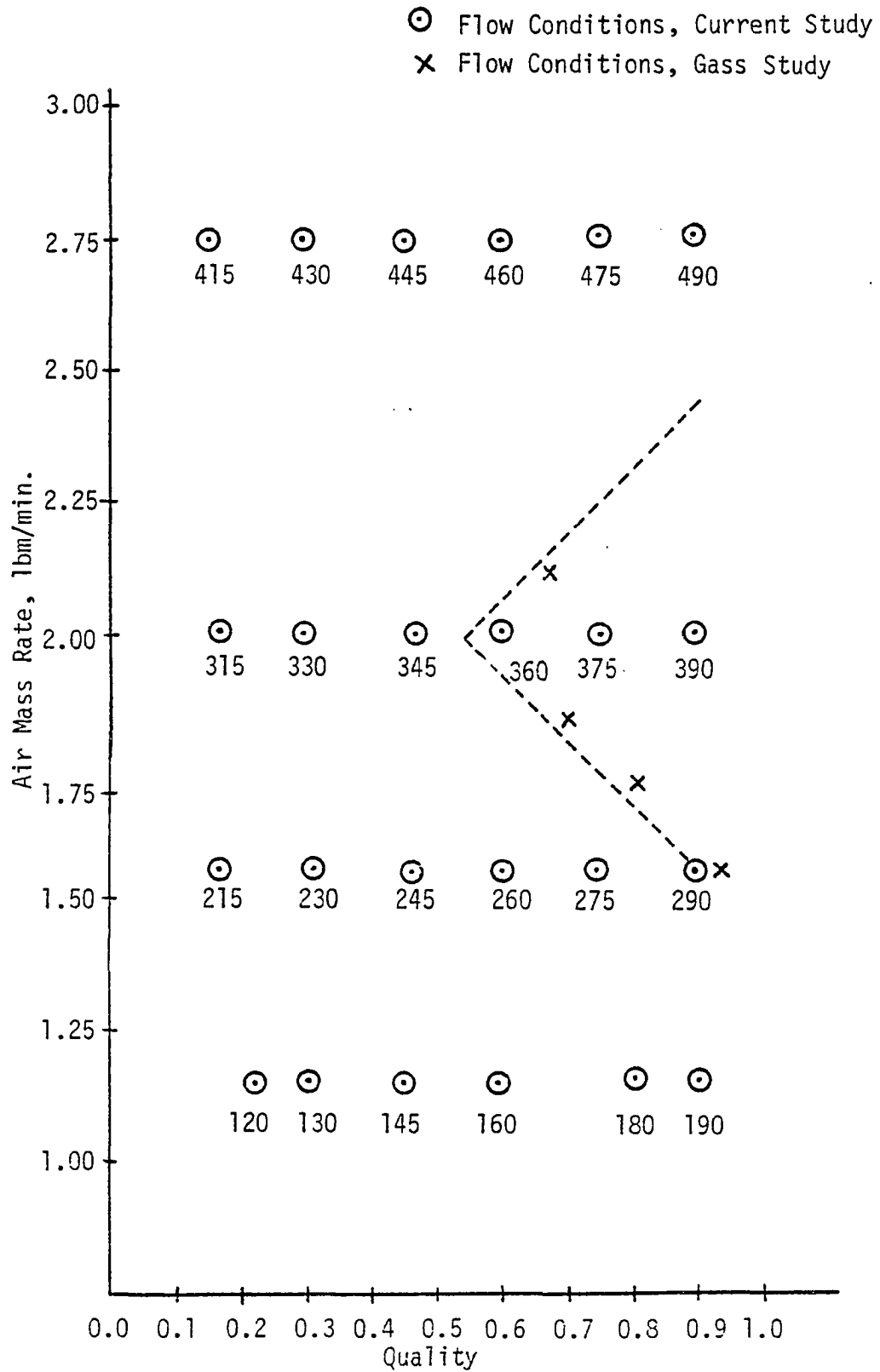
Figure 3. Range of Flow Conditions Covered in This Study.

upward flow of the liquid film on the walls of the flow tube. Higher gas flow rates were set as increments of this flow rate and still within the capabilities of the flow loop. Figure 3 also shows the limited range of gas flow rates and qualities studied by Gass[41] in previous work. Although a number of system modifications were made to increase the range of flow conditions, perhaps the most significant was an increase in the volume of air in the purge system, which kept the droplets swept off the acrylic plate in front of the lens at the increased gas flow rates and at the lower qualities.

Table 1 gives the gas flow rate and quality for each flow condition. (Note: The first number in the flow condition run number corresponds to the gas flow rate level, i.e., 1 corresponds to 1.14 lbm/min, 2 corresponds to 1.55 lbm/min, etc., and the last two numbers correspond to the desired quality value.)

Fifteen to eighteen slides were taken for each flow condition, but due to water blockage, focus and interference of the droplets and waves upstream and downstream of the focal plane, not all slides produced usable data. Table 1, column 4, shows the number of usable slides for each flow condition. Data was also taken at flow condition 115 and 215; however, it should be noted that at these flow conditions most of the pictures showed the tube to be blocked by water, thus confirming a transition point around 15% quality.

Table I.   Flow Condition Numbers Correlated to
Gas Flow Rate and Quality

Flow Condition Number	Gas Flow Rate (lbm/min)	Quality	Number of Slides	Total Number of Droplets	Average No. of Droplets Per Slide
120	1.14	.21	8	277	35
130	1.14	.30	8	190	24
145	1.14	.45	9	101	11
160	1.14	.59	9	74	8
180*	1.14	.80	15	221	15
190	1.14	.90	14	220	16
230	1.55	.31	9	122	14
245	1.55	.46	15	150	10
260	1.55	.61	18	181	10
275	1.55	.75	13	70	5
290	1.55	.90	17	51	3
315	1.98	.16	8	283	35
330	1.98	.29	13	666	51
345	1.98	.44	15	568	38
360	1.98	.60	11	138	13
375	1.98	.75	10	38	4
390	1.98	.87	19	18	1
415	2.71	.24	5	108	22
430	2.71	.32	13	510	39
445	2.71	.45	15	740	49
460	2.71	.60	18	503	28
475	2.71	.75	17	123	7
490	2.71	.89	17	19	1

Note: Due to water blocking the flow tube for most of the pictures at flow conditions 115 and 215, sufficient data was not obtained to be considered as a valid sample of the flow and droplet distributions at these conditions.

*The tube for flow conditions at 180 was found to be out of alignment: Its flow values will not be plotted for most functions.

It was felt that the data sample of readable slides was so small that these flow conditions could not be included in this study. In addition, for flow condition 180 the tube was found to be out of alignment and flow values corresponding to this condition will not be plotted for most of the calculated flow parameters.

Data Taking Procedure

Once a series of slides had been taken at a given flow condition, the slides were projected and traced at approximately 4 to 5 times the actual flow tube size. Figure 4 shows a series of these slides and allows one to see the difference in the thickness of the liquid film on the wall as well as the distribution and number of droplets for each of the four gas flow rates over a range of qualities.

Slides A, B and C of Figure 4 correspond to flow conditions 130, 160 and 190 respectively. Comparison can be made with photographs at these same qualities for flow rate 2 (slides D, E and F), flow rate 3 (G, H and I) and flow rate 4 (J, K and L). Slide M, taken at flow condition 115, shows how the flow tube looks at the transition point for separated flow. Slide N shows an example of a photograph that was considered unreadable due to the action of the waves and droplets in the flow tube. Slide O was taken at the same flow condition as Slide A and indicates the difference that could exist between two samples from the same flow condition.
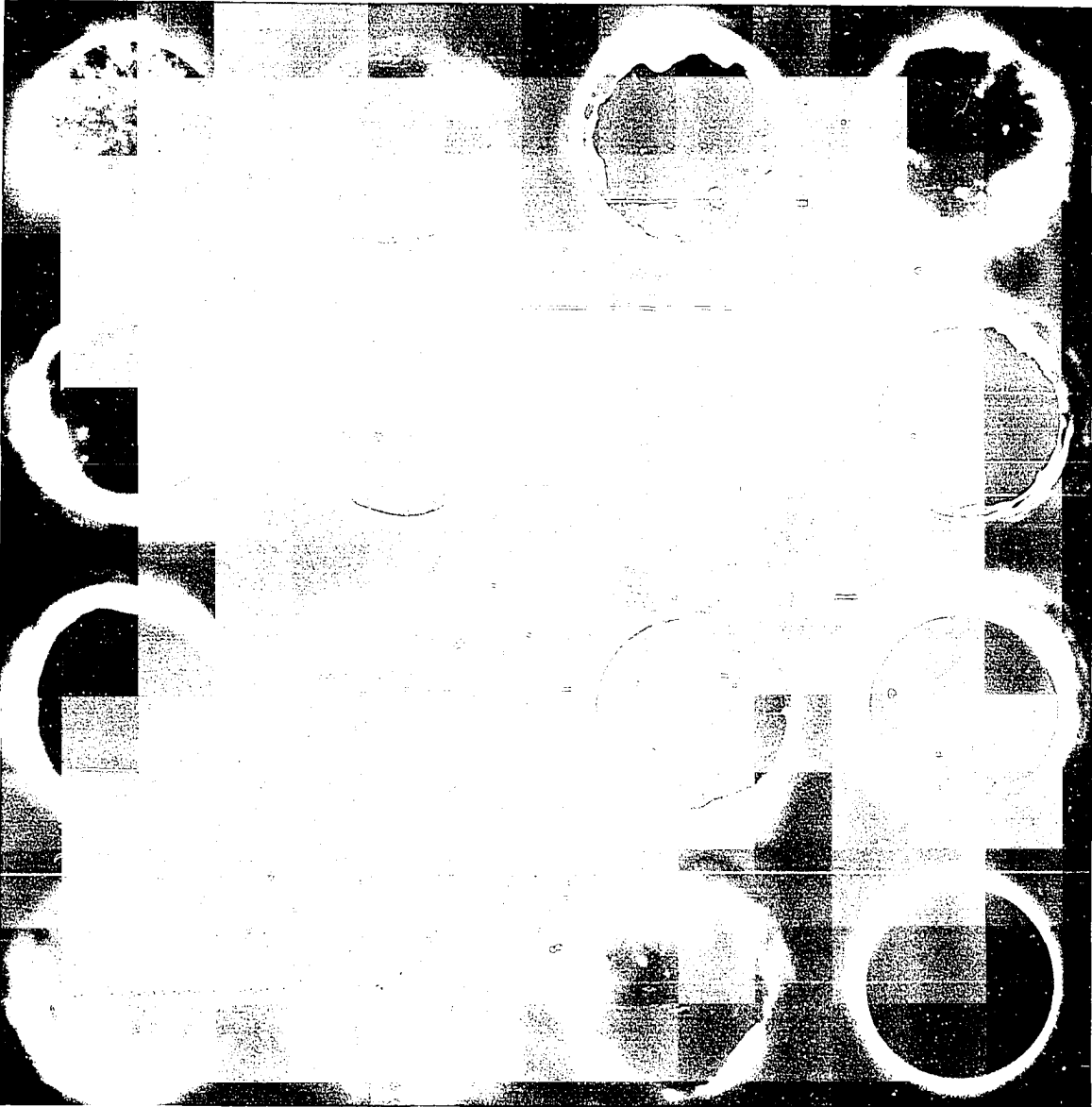
(Note: The flow condition and slide number for photographs A
through P are as follows: A-130/15, B-160/14, C-190/7, D-230/18,
E-260/19, F-290/3, G-330/25, H-360/12, I-390/26, J-430/33, K-460/
19, L-490/8, M-115/29, N-120/21, O-130/16, P-blank.)

Figure 4. Axial Photographs Showing Difference in the Thickness
of the Liquid Film and the Distribution and Number of
Droplets.

Slide P of Figure 4 shows walls of the flow tube with no air or water flow. By projecting this slide on a sheet of paper, the center and radius of the tube can be geometrically determined. Keeping the position of the slide projector constant, each slide for a given flow condition was then traced, taking care that only the waves and the droplets that were in the lighted control volume region were traced. Figure 5 shows an example of a typical tracing. Once the details of the slide had been traced, the edge of the blank tube tracing was matched as close as possible to the edge of the flow tube with two-phase flow present. Then by using the radius of the blank tube, both the center point and the wall of the tube were drawn into the tracing. As seen from Figure 4, Slide P, the blank tube projects as a ring, corresponding to the top and the bottom of the control volume, with the midpoint of this ring being defined as the diameter of the flow tube for the calculation of liquid film thickness as well as other parameters.

In determining whether a wave or droplet should be included in the control volume or not, the focus, color, and brightness of each wave and droplet were considered. Even small droplets were included in the tracing as long as some area could be enclosed by tracing around the perimeter of the droplet.

The droplets were all assumed to be elliptical. A major axis, defined as the longest straight line that could
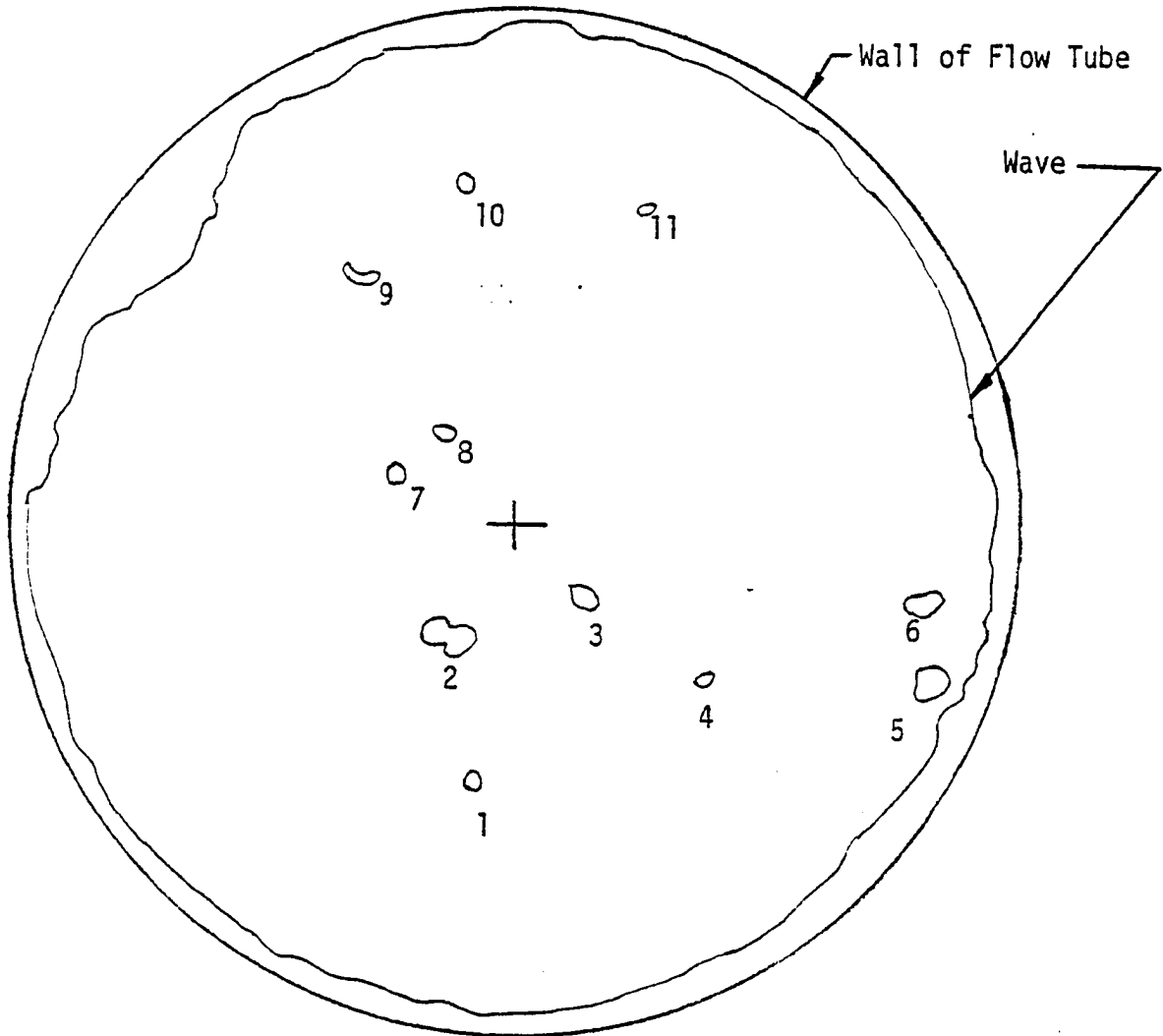
(Note: Tracing corresponds to Flow Condition 475, Slide No. 10.)

Figure 5. Typical Tracing Showing the Wall of the Flow Tube, Waves, and Droplets.

be drawn across the droplet, was constructed. A minor axis, defined as the length of the perpendicular bisector of the major axis, was then determined. Finally the radial position of each droplet was measured from the center of the flow tube to the center of each droplet. Table II shows a typical data sheet which was completed for each slide. It should be noted that the slide tracing and droplet sizing steps were time consuming and tedious jobs. In some flow conditions this process took up to 15 hours per slide, particularly when the number of droplets was large. This was compensated for somewhat by the relative ease in which slides at the higher qualities could be traced and sized.

The area of the gas core for each slide was measured using a planimeter to trace around the inside of the water film thickness. This gas core area was then converted into an equivalent radius by the expression

$$r_g = \sqrt{\frac{A_{gc}}{\pi}}$$

where A_{gc} is the area of the gas core as measured by the planimeter and r_g is the equivalent gas core radius. The average thickness of the liquid film on the wall of the tube was determined by

$$\delta_{ave} = R - r_g$$

where δ_{ave} is the average liquid film thickness on the flow tube wall and R is the radius of the flow tube.

Table II. Typical Droplet Data Sheet

Droplet Number	Major Axis	Minor Axis	Radial Position
1	.10	.07	1.32
2	.27	.09	.65
3	.17	.09	.52
4	.08	.05	1.28
5	.23	.15	2.31
6	.19	.13	2.16
7	.11	.08	.66
8	.12	.08	.60
9	.20	.05	1.50
10	.09	.06	1.74
11	.08	.05	1.76

Note: All dimensions are in inches and refer to distances measured on the tracing. This data refers to Flow Condition 475, Slide No. 10.

Once r_g was calculated, it was also drawn on the tracing as shown in Figure 6. This gas core radius shows that there was blockage in the gas core due to both the droplets and to the wave tips on the liquid film which extended inside the gas core radius. The area of waves causing blockage was then determined by measuring the gas core area again, only this time the equivalent gas core radius or the tip of the wave, whichever was nearest to the center of the tube, was traced by the planimeter. The difference between this area core measurement and A_{gc} was the area of the waves causing blockage in the core area.

This entire process was programmed on a computer so the data from a large number of slides and flow conditions could be analyzed. In addition, the computer program calculated the droplet area based on the assumption that each droplet was an ellipse. Using the radius of the blank tube from the tracing and comparing to the actual radius of the tube, a scaling factor was calculated so all the parameters could be scaled down from the enlarged tracings to their actual size and areas corresponding to a 1.258 inch diameter tube. Appendix A shows a sample output of the computer program for a single slide at one flow condition. Due to the large quantity of data, only curves summarizing the data will be included in this work, but a complete profile of the droplet data is available.[42]
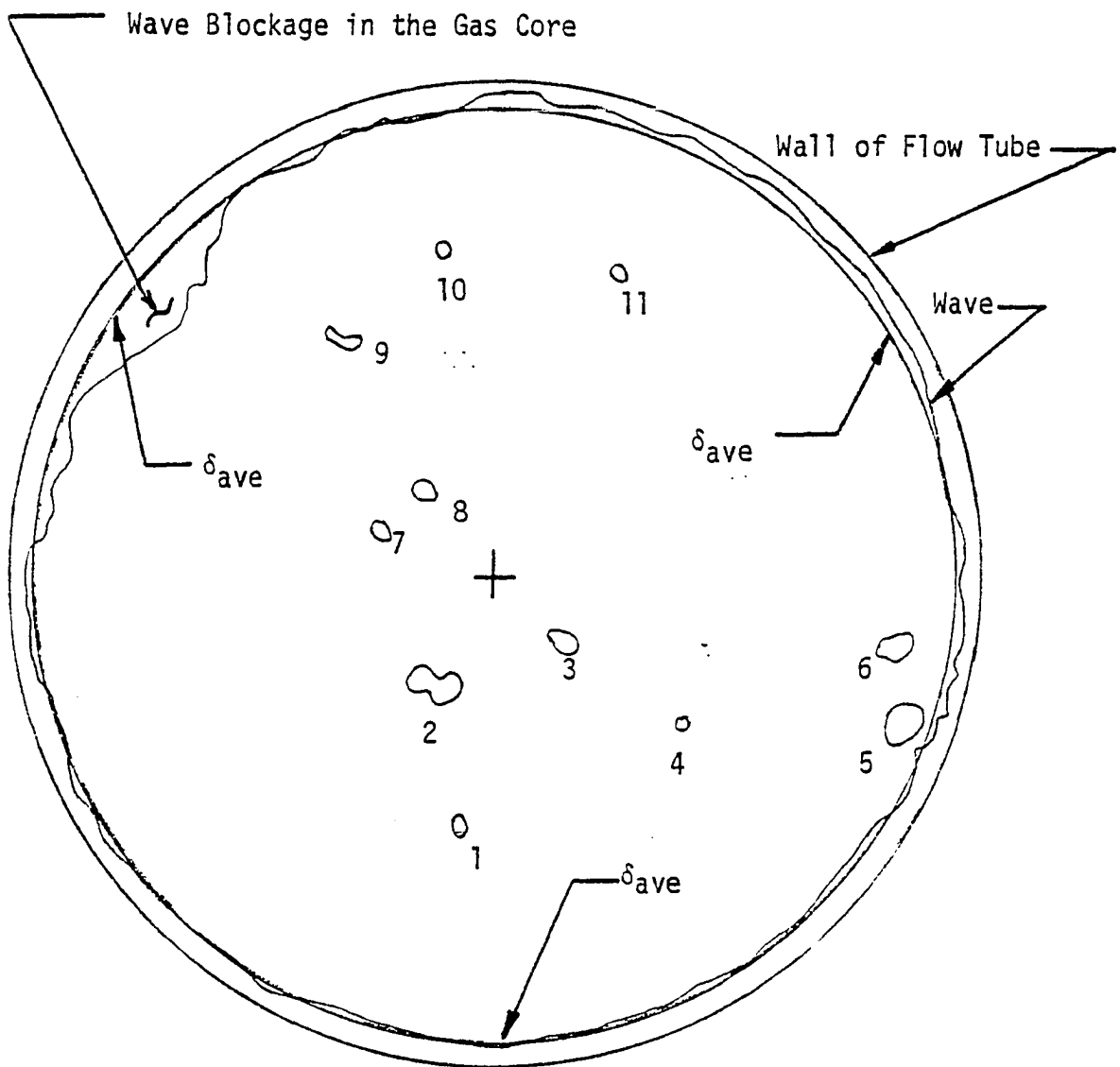
(Note: Tracing corresponds to Flow Condition 475, Slide No. 10.)

Figure 6. Typical Tracing Showing δ_{ave}.

Distribution Function Curves for Liquid Droplets Description

As seen from Figure 4, axial photography has the po-
tential to supply the needed droplet data for two-phase flow
analysis. However, a technique must be devised that will
supply quantitative data in a concise but complete format
from these photographs. Thus, the droplet data for the vari-
ous flow rates and qualities can be summarized using three
types of distribution function curves. The first, referred
to hereafter as Function Value, is the fraction of droplets
at a given flow condition that fell within a specified incre-
ment of the base variable. For example, Figure 8a shows the
Function Value, or the fraction of droplets, that have their
major axis within a given increment. In this case the range
of major axis dimensions is allowed to vary from 0.01 inches
to 0.1 inches in 100 increments of 0.001 each. A separate
curve has been drawn for each quality. For example, approxi-
mately 15% of the total droplets in Flow Condition 120 (i.e.,
a flow rate of 1.14 lbm/min and 21% quality) have a major
axis dimension of .03. The Function Value curves also give
the total number of droplets used to determine the three dis-
tribution function curves for each flow condition.

A second distribution curve will be referred to as
Cumulative Function Value and is the summation of all Function
Values for the given base variable, up to and including the
increment under consideration. For example, from Figure 8b
approximately 55% of the droplets in Flow Condition 120 have

major axis dimensions less than or equal to .038 inches,
while at Flow Condition 145 only 40% of the droplets had
major axis dimensions of .040 inches or less. In addition,
using the total number of droplets for each flow and also
the number of samples for each flow condition as given in
Table 1, the actual number of droplets as well as the aver-
age number of droplets per sample can be determined.

The third distribution curve will be referred to as
the Average Function Value and is shown in Figure 8c. This
averaging technique was developed by Evans[43] in an attempt
to smooth out the data as presented by the Function Value
Curves. The technique consisted of (1) adding together the
Function Values for nine consecutive increments; (2) divid-
ing the total number of droplets in the nine increment in-
terval by the total number of droplets for the whole range;
and (3) plotting this fraction as the Average Function Value
at the midpoint of the center increment. To get the Average
Function Value for the next increment, the first increment
and its fraction of droplets were subtracted while the tenth
increment and its fraction of droplets were included in the
count. Figure 7 shows a schematic diagram for this averag-
ing scheme. From Figure 8c one sees the range of major
axis dimensions between .02 and .03 inch to have the great-
est probability of occurring at flow rate 1.

Table III relates the "a", "b" and "c" coding on Fig-
ures 8 through 43 to the three distribution curve functions,

INCREMENTS

1 2 3 4 5 6 7 8 9 10

9 Increments Summed for First Function Value

9 Increments Summed for Second Function Value

Increment Midpoint for
Plot of First Average
Function Value

Increment Midpoint for
Plot of Second Average
Function Value

Line Representing the Range of the Base
Variable for the Distribution Function
Curves.
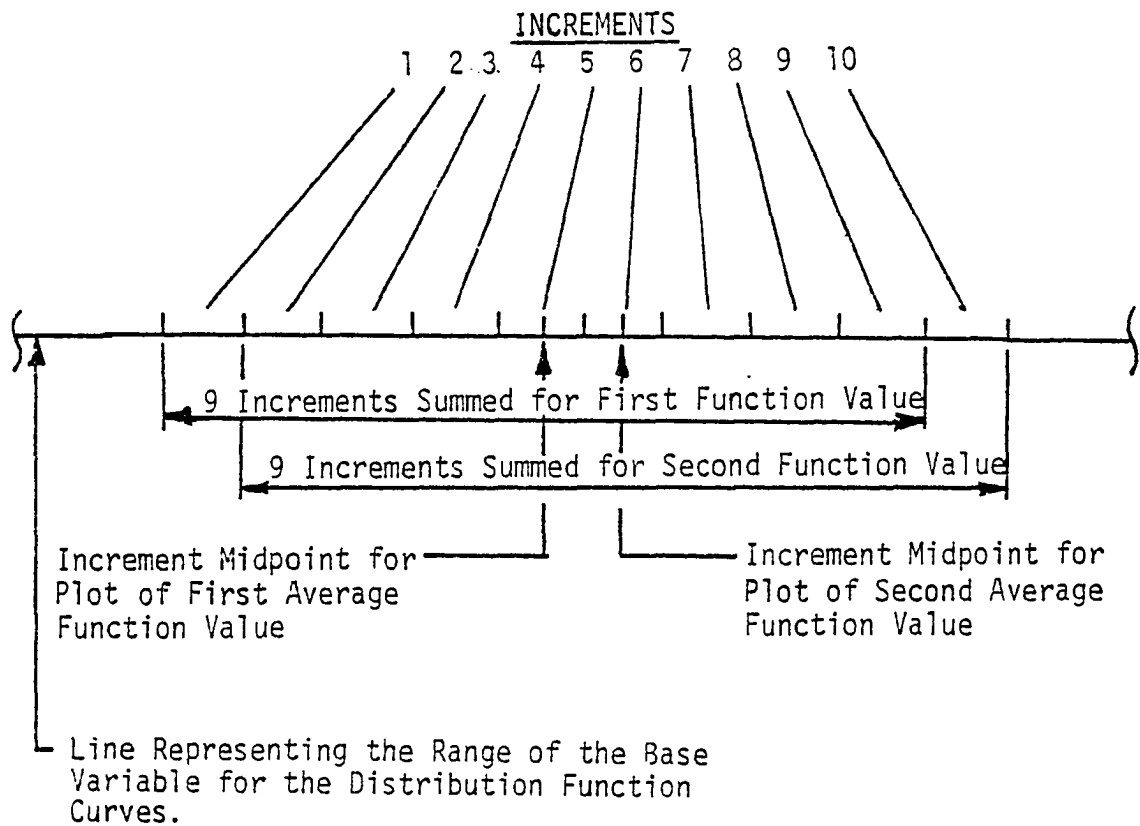
Figure 7. Diagram Showing the Technique for Calculating
the Average Function Value Curves.

Table III. Coding For The "a", "b" and "c" in
the Figure Numbers With the Three
Distribution Curve Functions.

Figure Number	Distribution Curve
Figure xa Figure xb Figure xc	Function Value Curves Cumulative Function Value Curves Average Function Value Curves

Table IV. Coding for the Various Base Variables
for Each of the Flow Rate Values.

Base Variables	Gas Flow Rate Values			
	100	200	300	400
	Figure Numbers			
1. Major Axis Dimension	8	17	26	35
2. Equivalent Diameter Dimension	9	18	27	36
3. Axis Ratio - All Droplets	10	19	28	37
4. Axis Ratio - Small Droplets	11	20	29	38
5. Axis Ratio - Large Droplets	12	21	30	39
6. Relative Radial Position, Constant Radius Increment - All Droplets	13	22	31	40
7. Relative Radial Position, Constant Radius Increment - Small Droplets	14	23	32	41
8. Relative Radial Position Constant Radius Increment - Large Droplets	15	24	33	42
9. Relative Radial Position, Constant Area Increment	16	25	34	43

Symbol	Flow	# of Drops
+	120	261
x	130	174
▷	145	88
▽	160	62
◁	180	212
△	190	212

Major Axis Dimension, inches
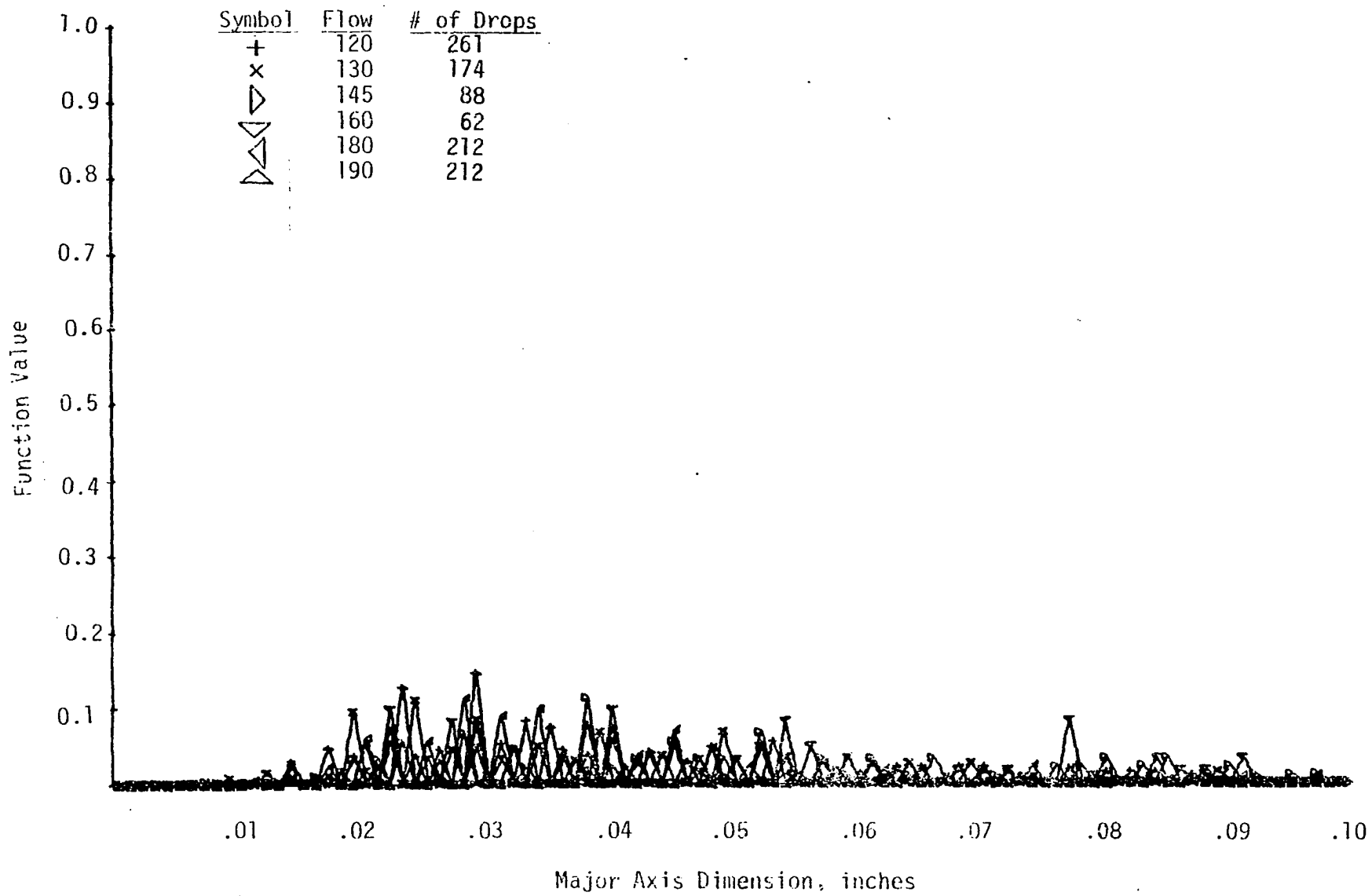
Figure 8a.   The Function Value of the Major Axis Distribution for Flow Rate 1.
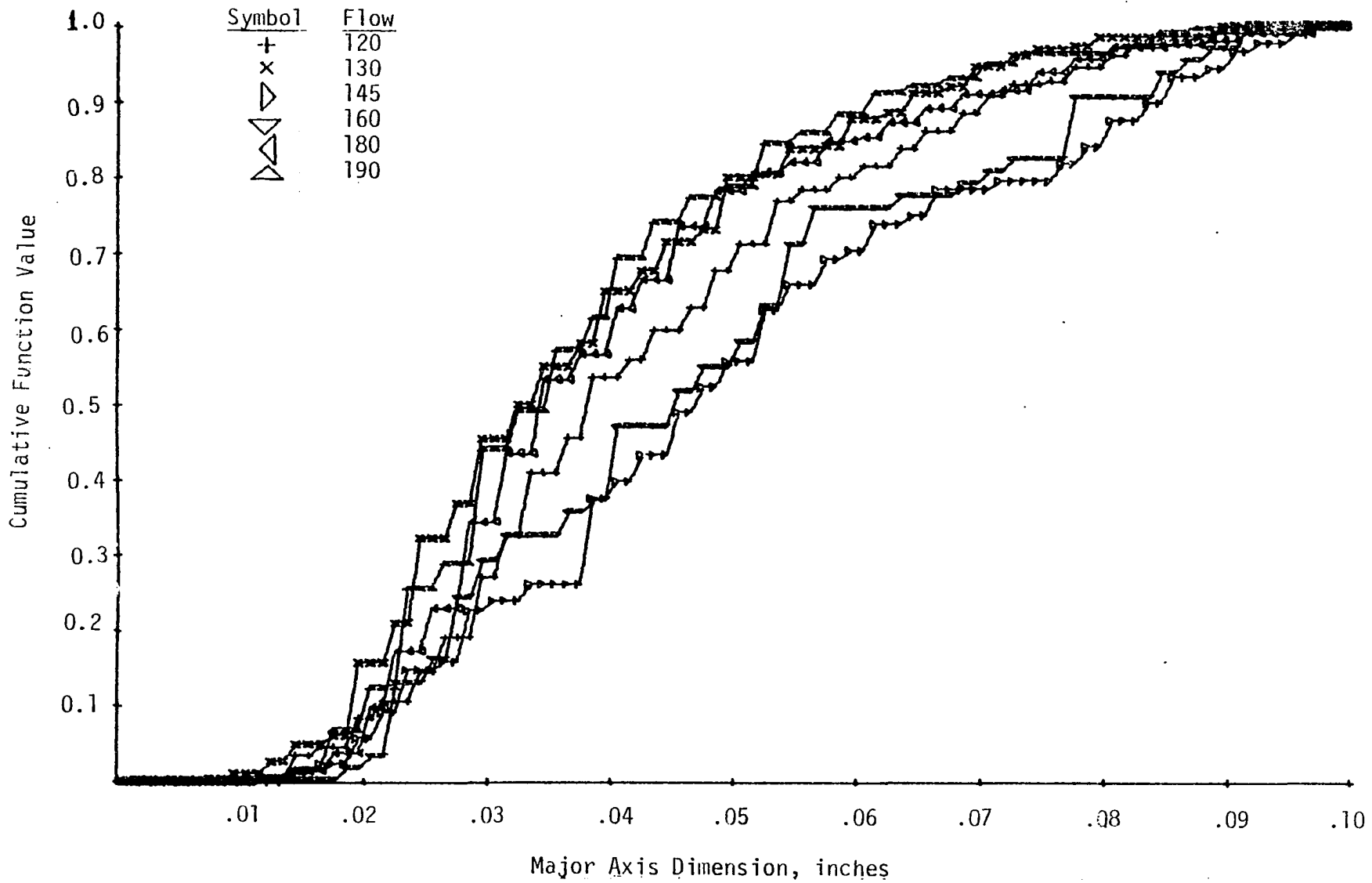
Figure 8b. The Cumulative Function Value of the Major Axis Distribution of Flow Rate 1.
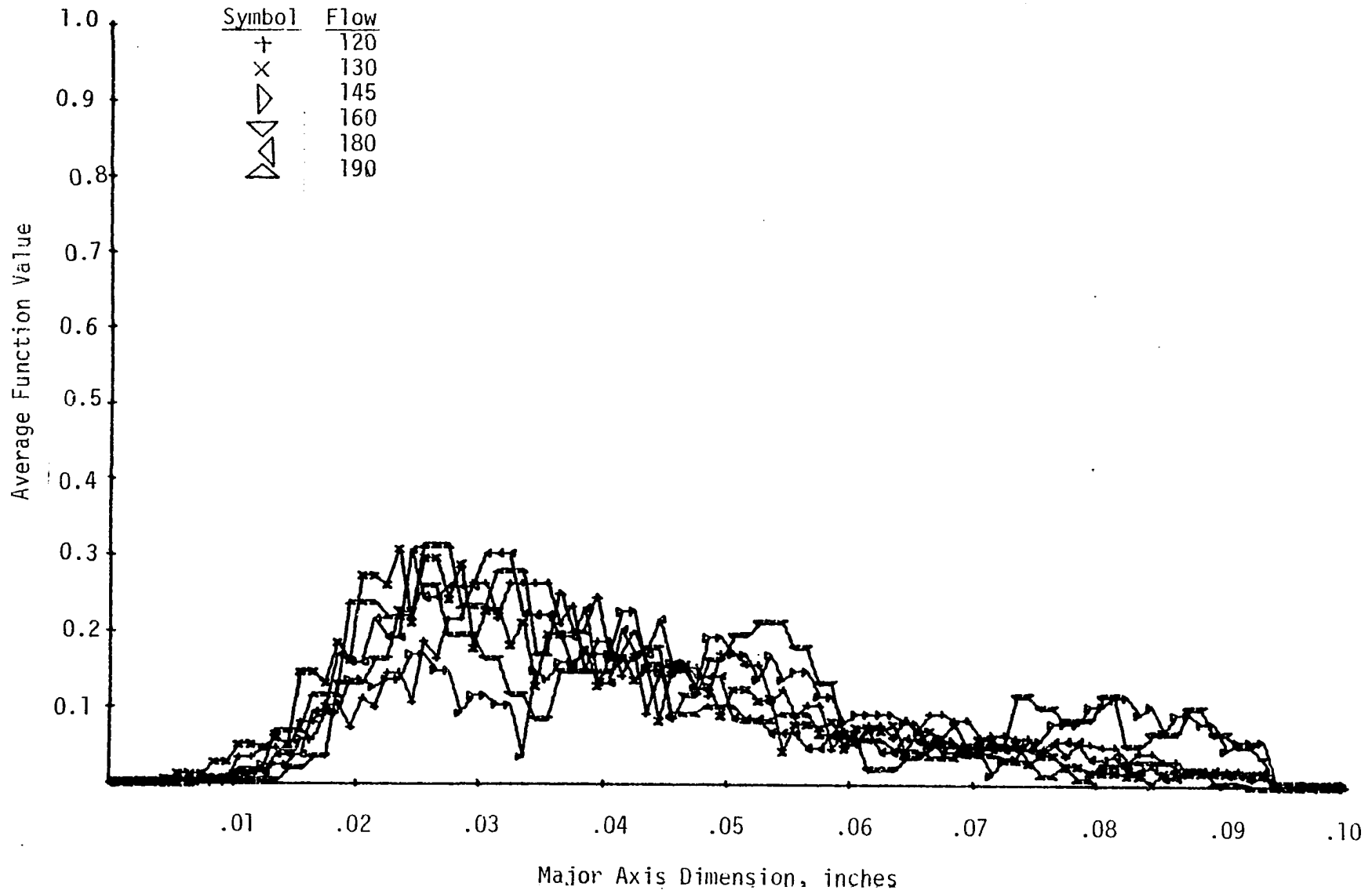
Figure 8c. The Average Function Value of the Major Axis Distribution of Flow Rate 1.

37
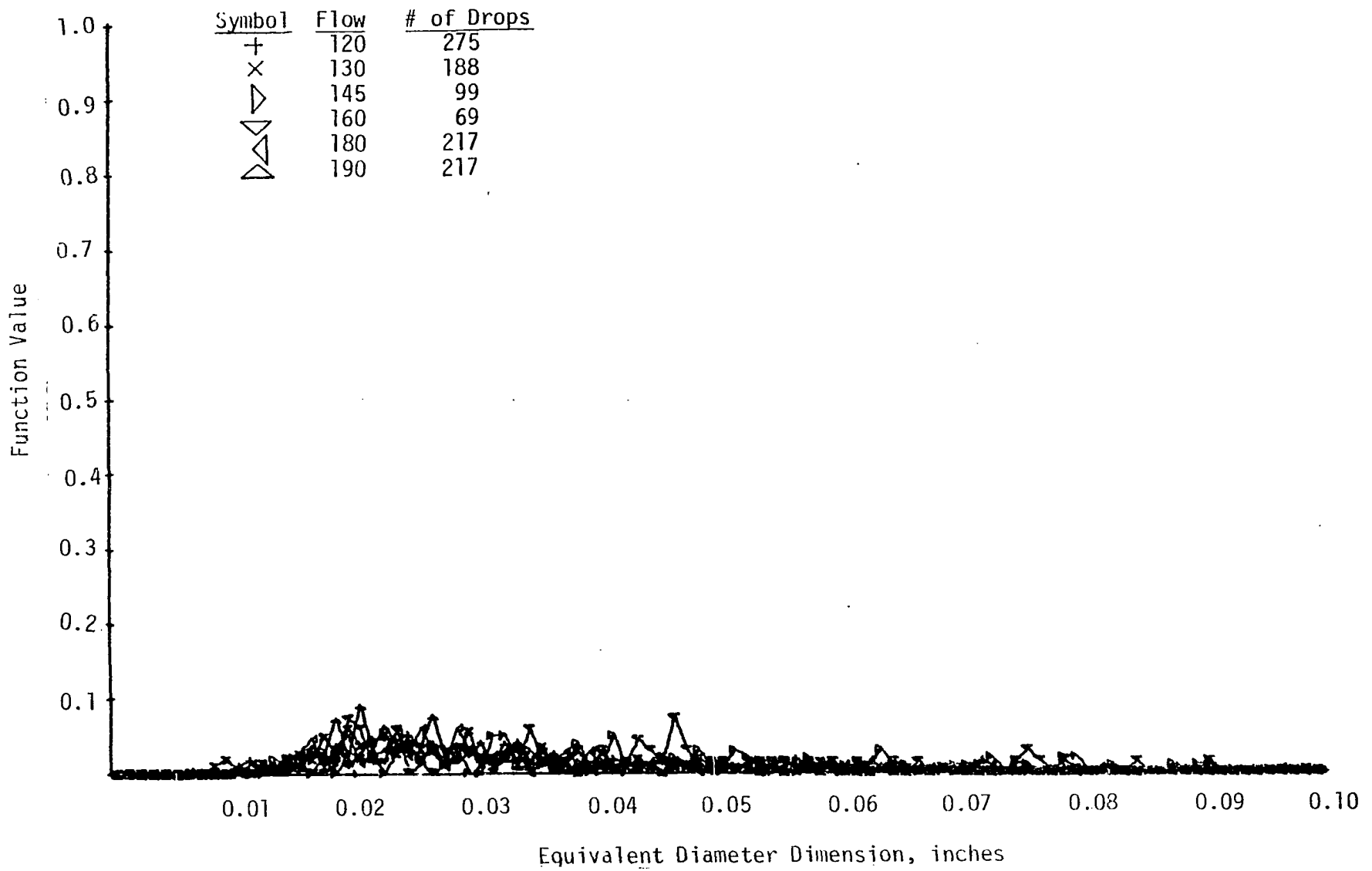
Figure 9a. The Function Value of the Equivalent Diameter Distribution of Flow Rate 1.
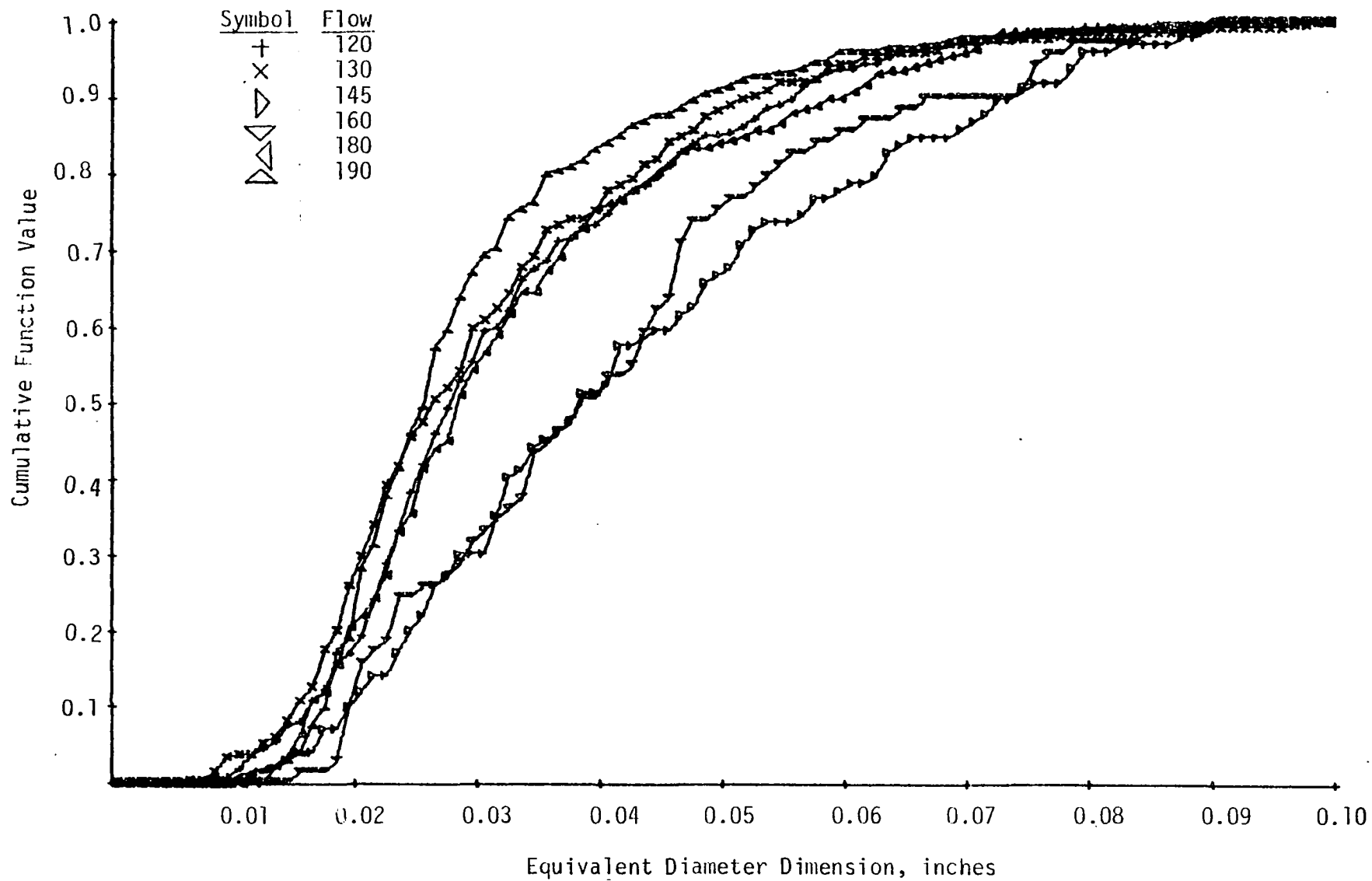
Figure 9b. The Cumulative Function Value of the Equivalent Diameter of Flow Rate 1.
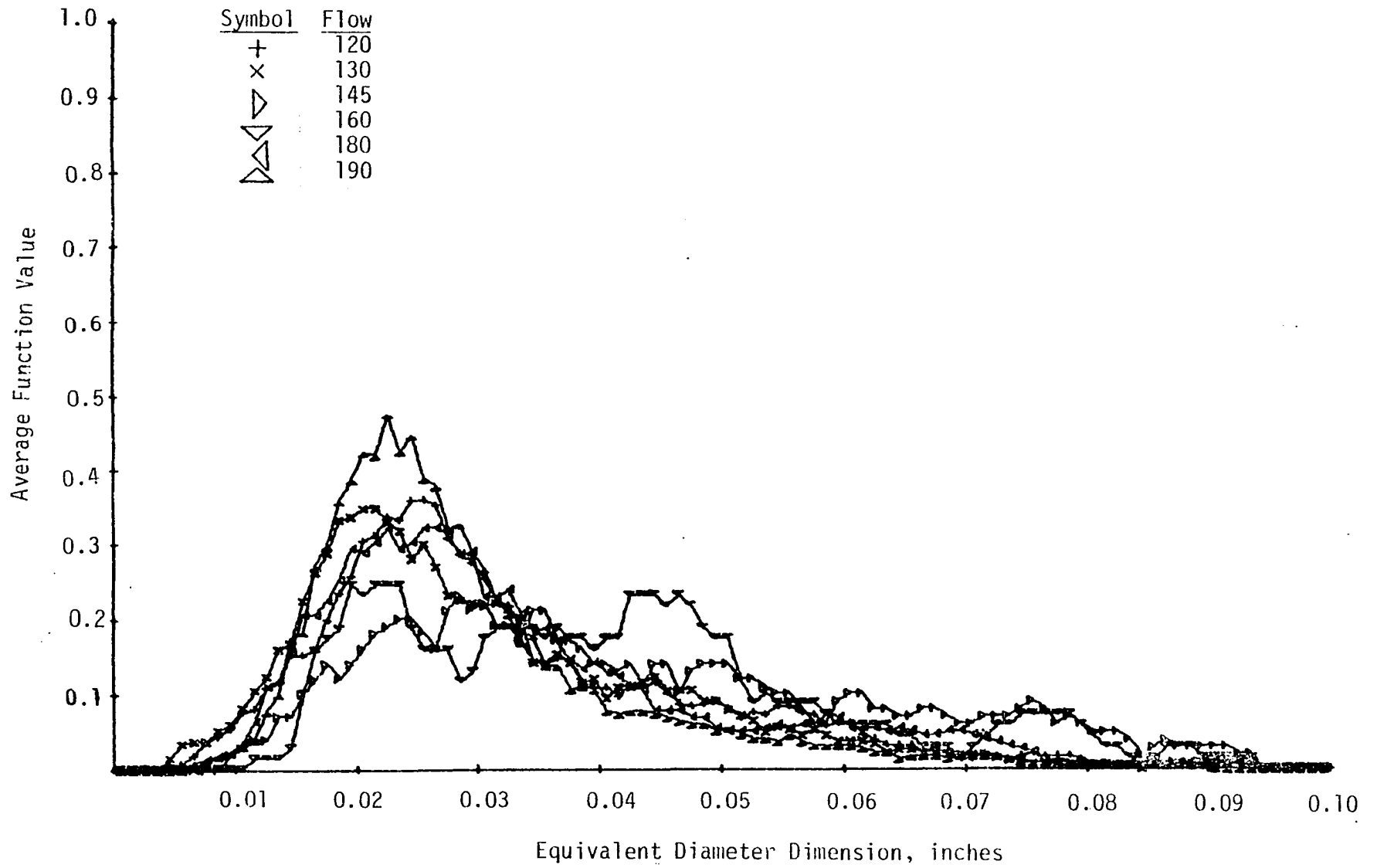
Figure 9c. The Average Function Value of the Equivalent Diameter Distribution of Flow Rate 1.
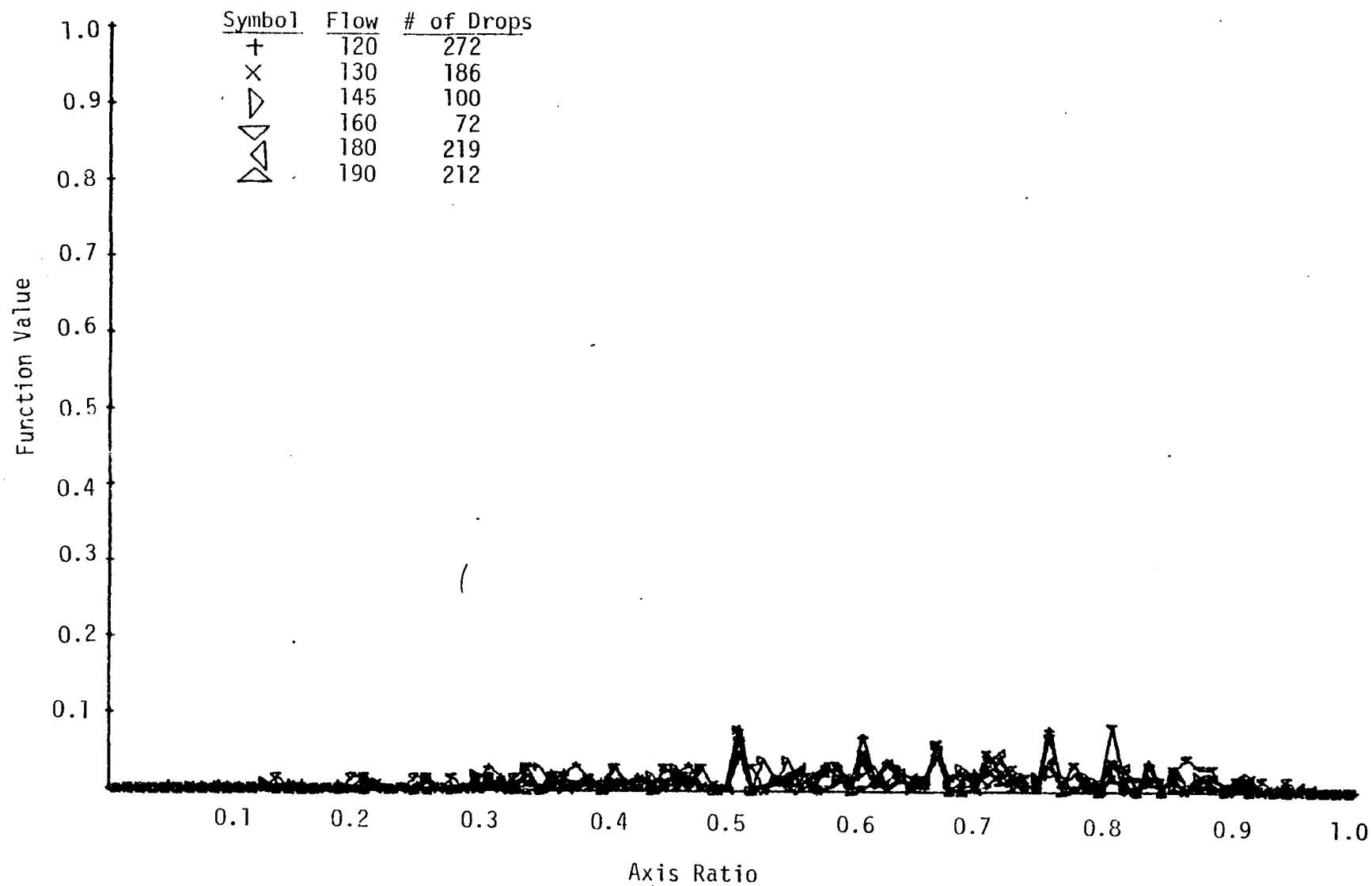
Figure 10a. The Function Value of the Axis Ratio Distribution of Flow Rate 1.
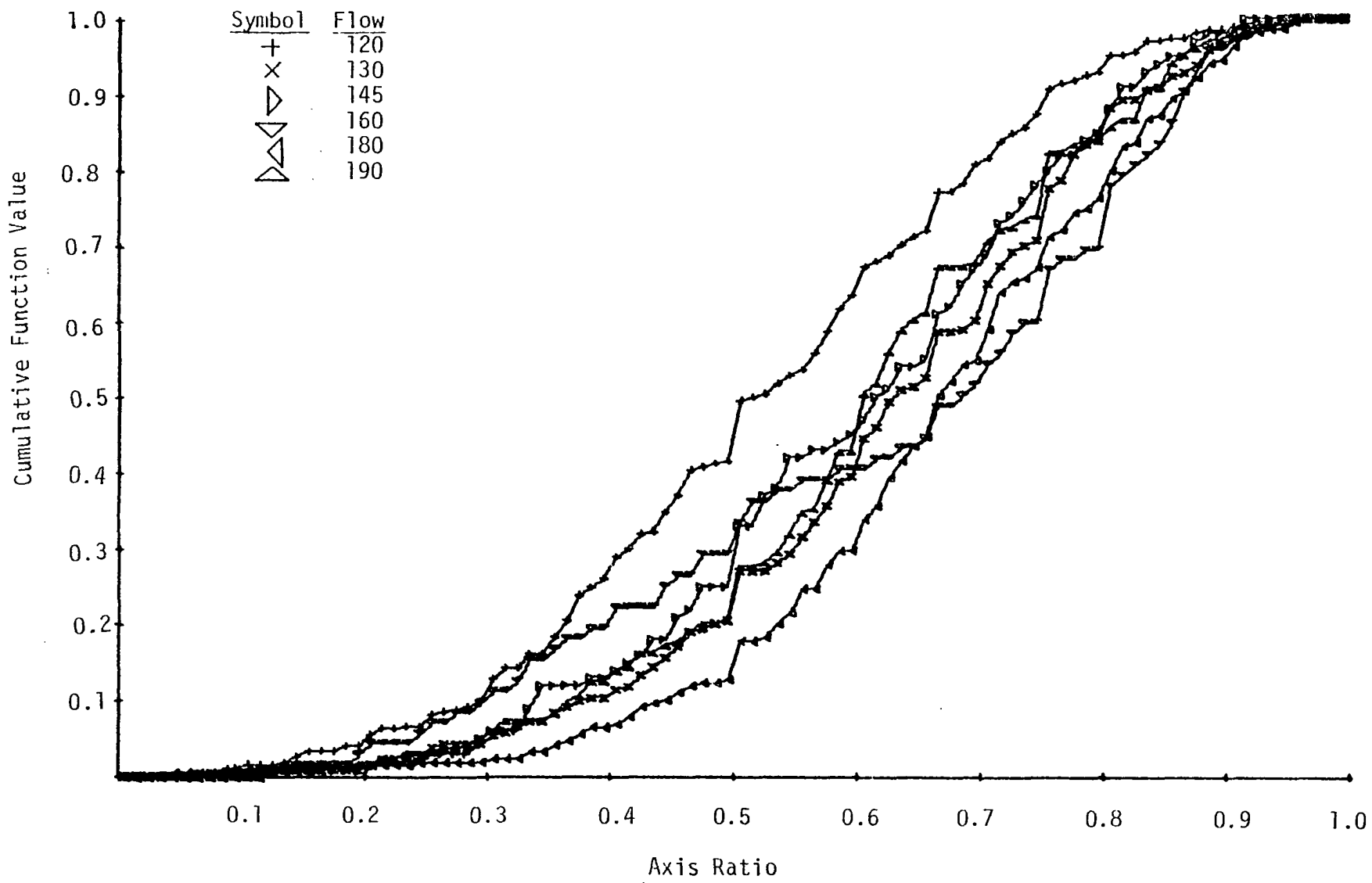
Figure 10b. The Cumulative Function Value of the Axis Ratio Distribution of Flow Rate 1.
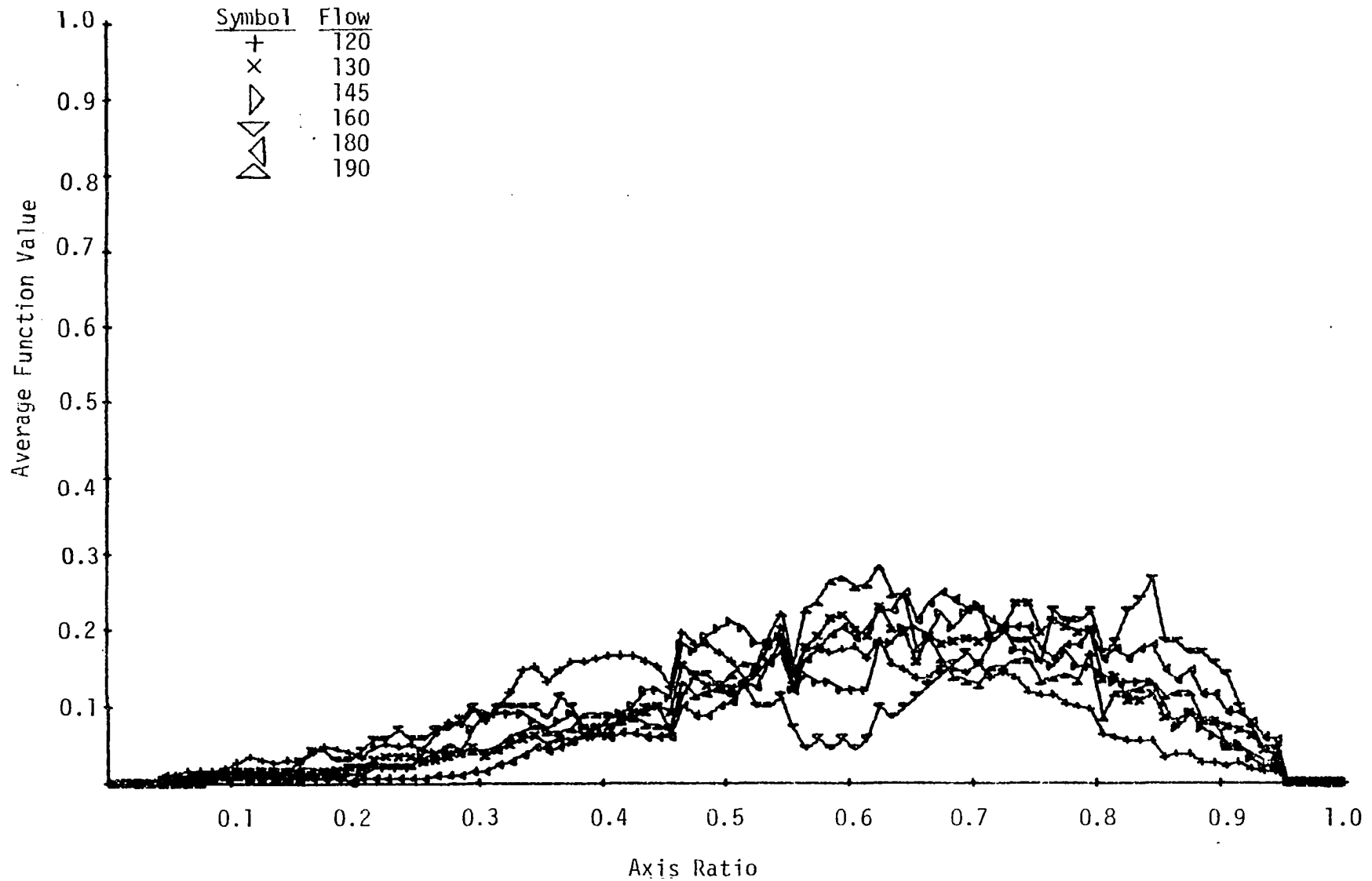
Figure 10c. The Average Function Value of the Axis Ratio Distribution of Flow Rate 1.
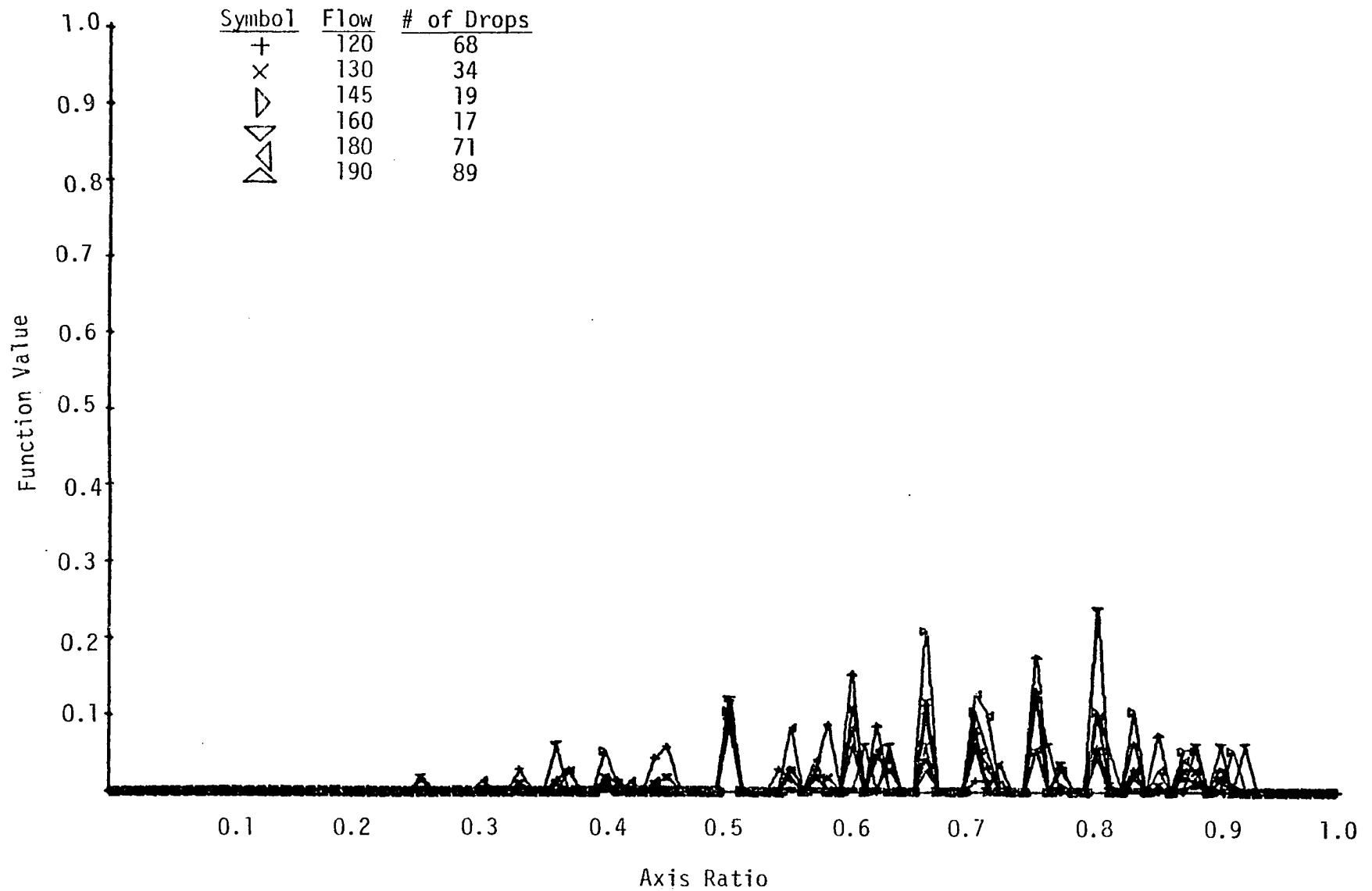
Figure 11a. The Function Value of the Axis Ratio Distribution (small droplets) of Flow Rate 1.
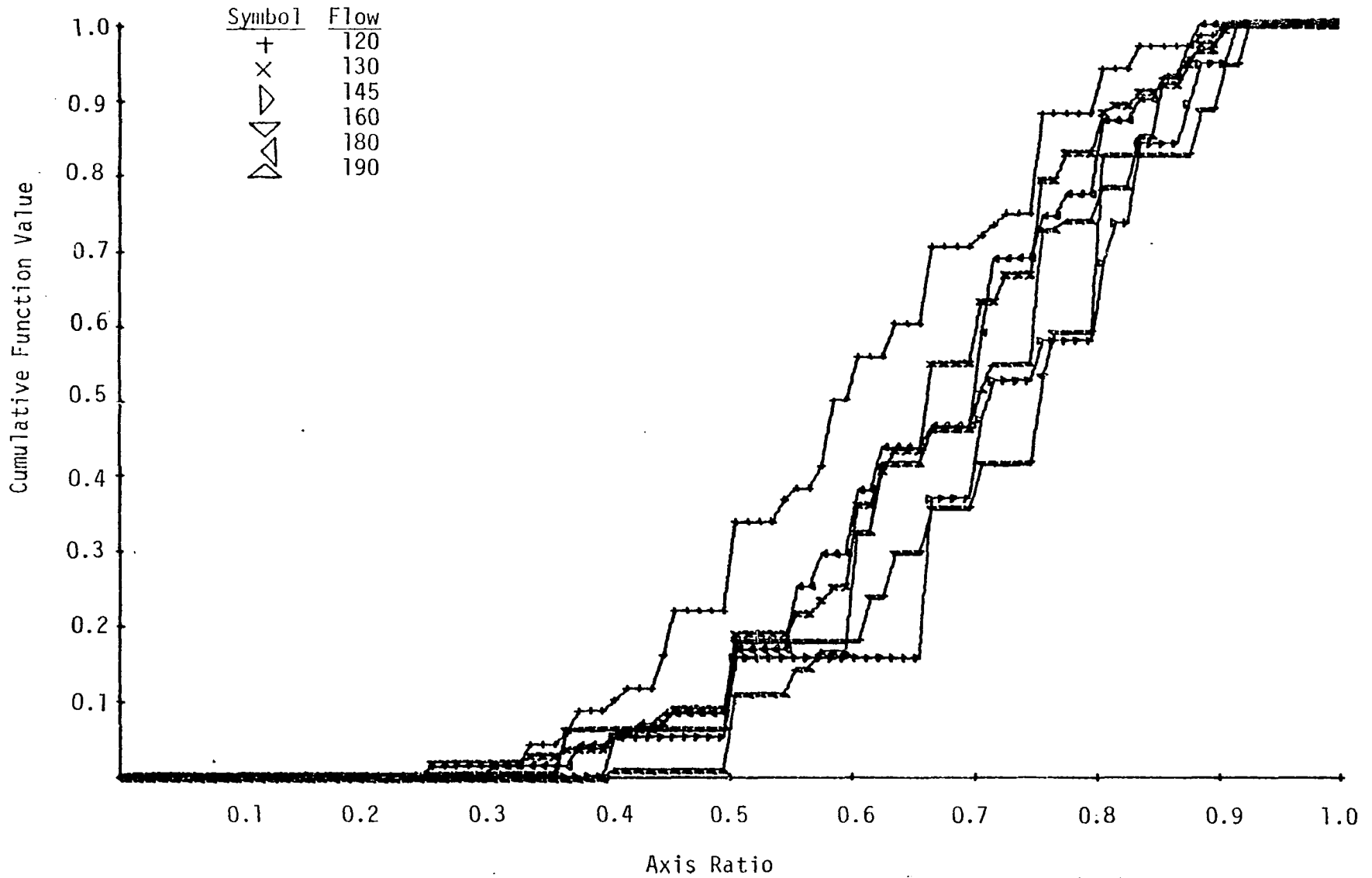
Figure 11b. The Cumulative Function Value of the Axis Ratio Distribution (small droplets) of Flow Rate 1.
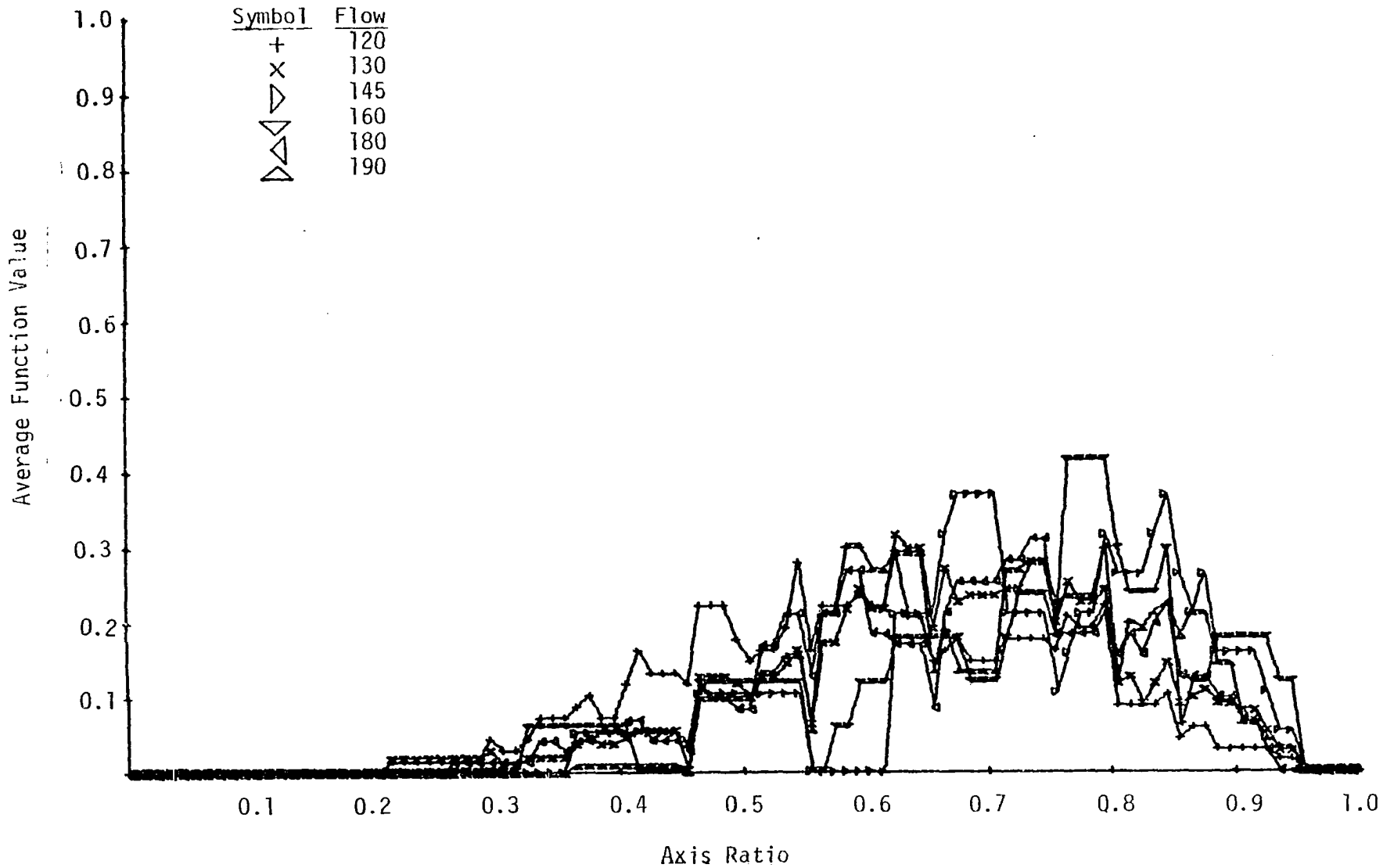
Figure 11c.   The Average Function Value of the Axis Ratio Distribution of (small droplets) of Flow Rate 1.
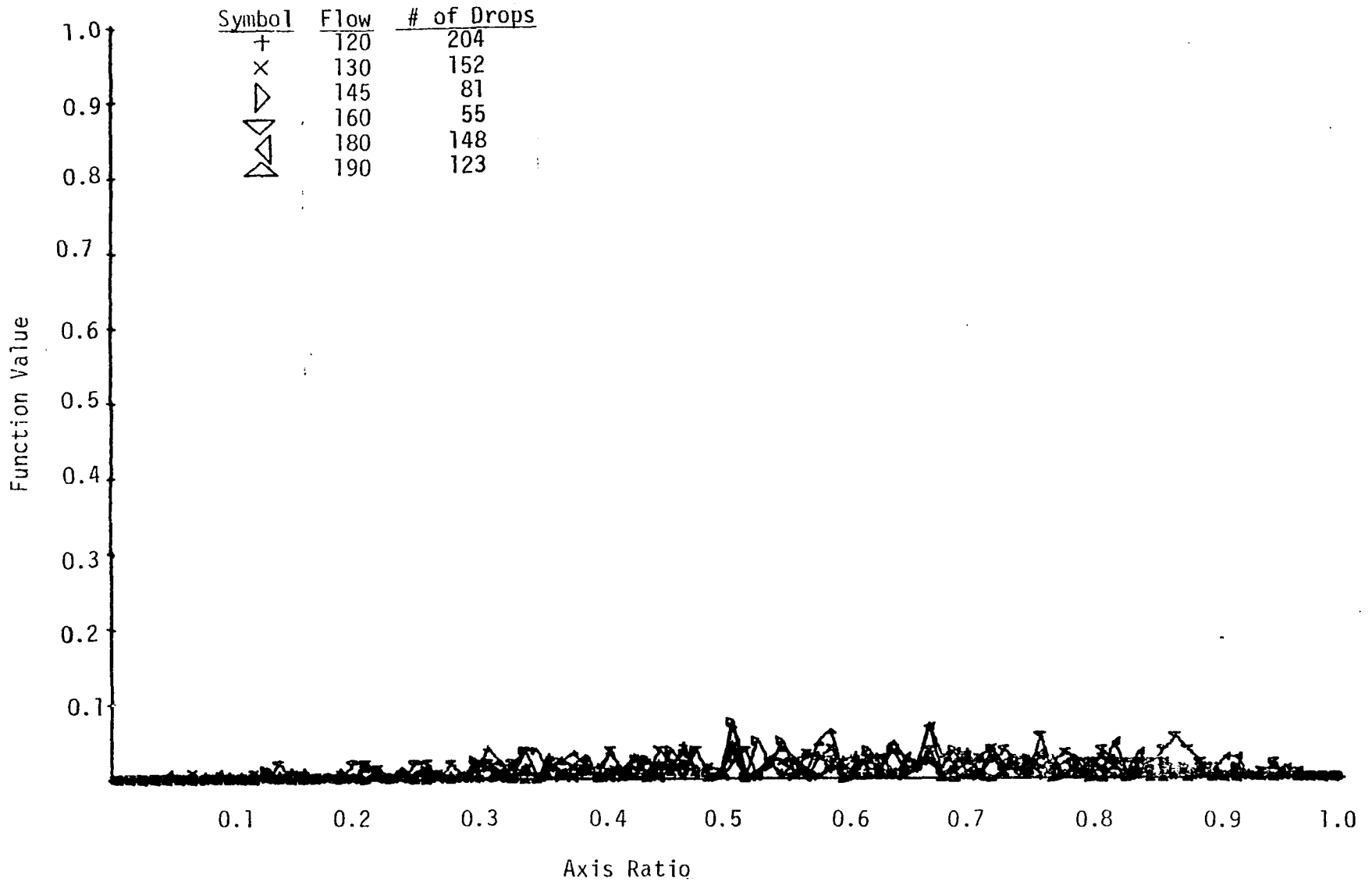
Figure 12a. The Function Value of the Axis Ratio Distribution (large droplets) of Flow Rate 1.
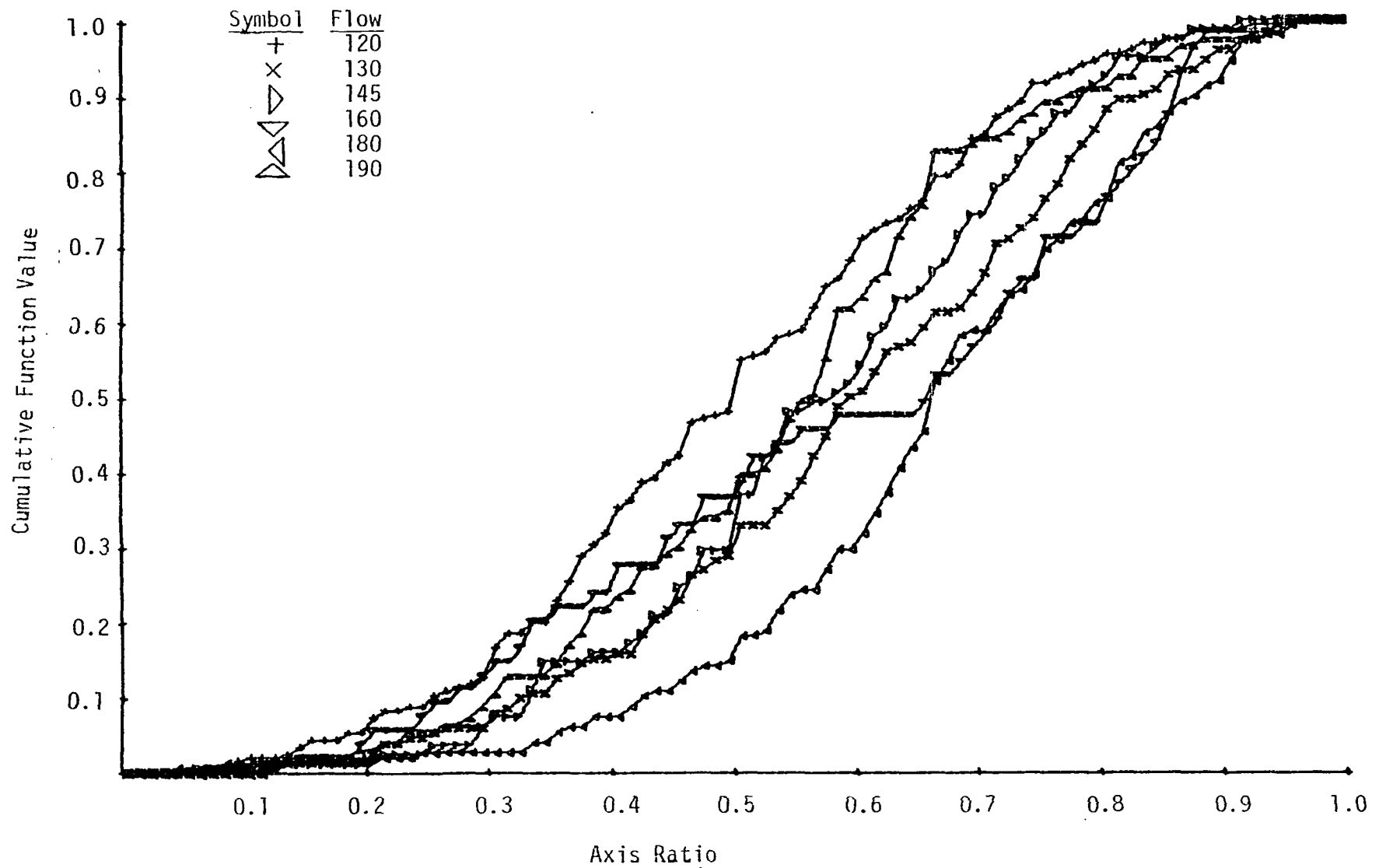
Figure 12b. The Cumulative Function Value of the Axis Ratio Distribution of (large droplets) of Flow Rate 1.
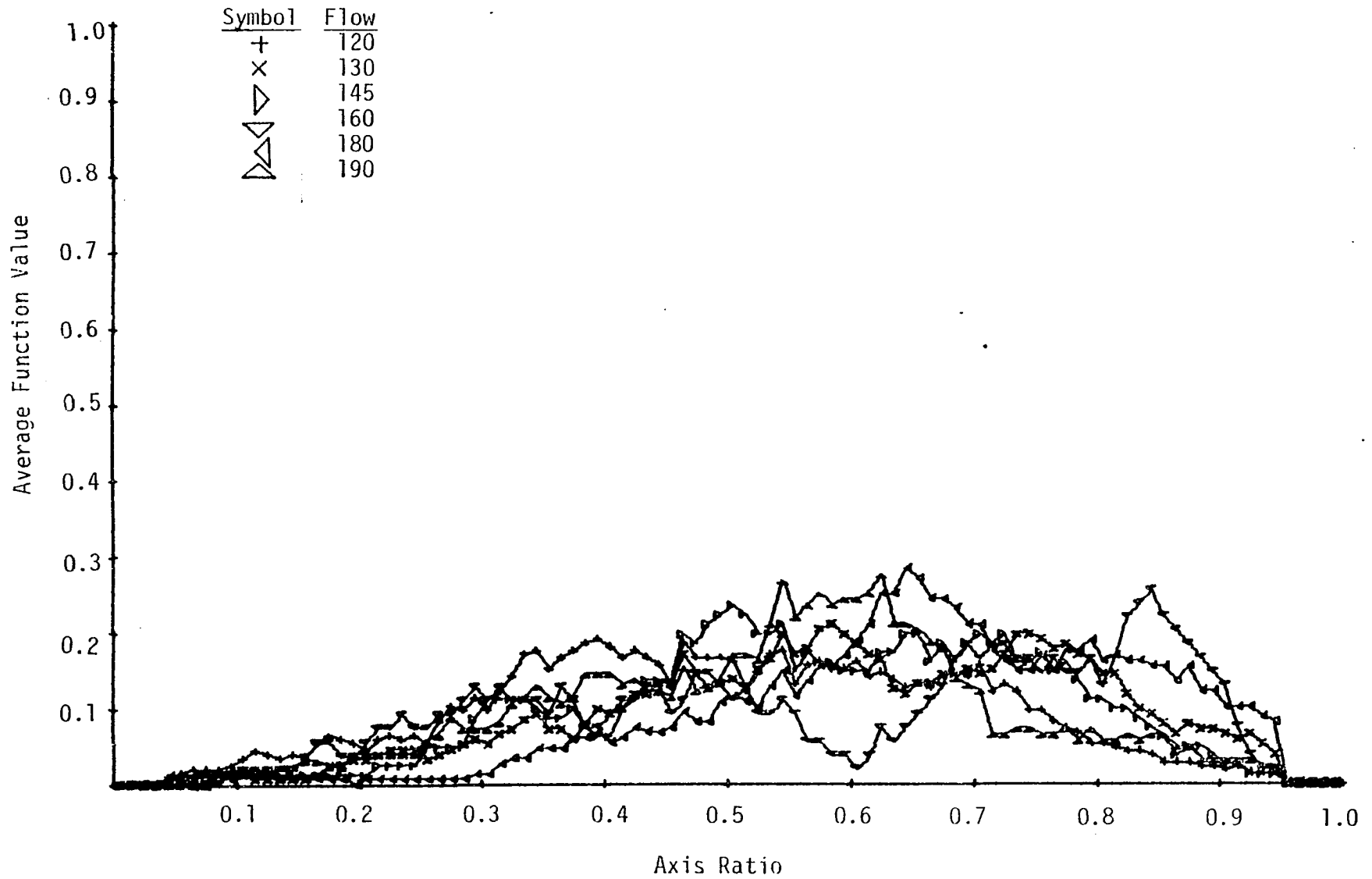
Figure 12c. The Average Function Value of the Axis Ratio Distribution (large droplets) of Flow Rate 1.

Symbol	Flow	# of Drops
+	120	276
×	130	190
▷	145	101
▽	160	74
◁	180	221
△	190	220
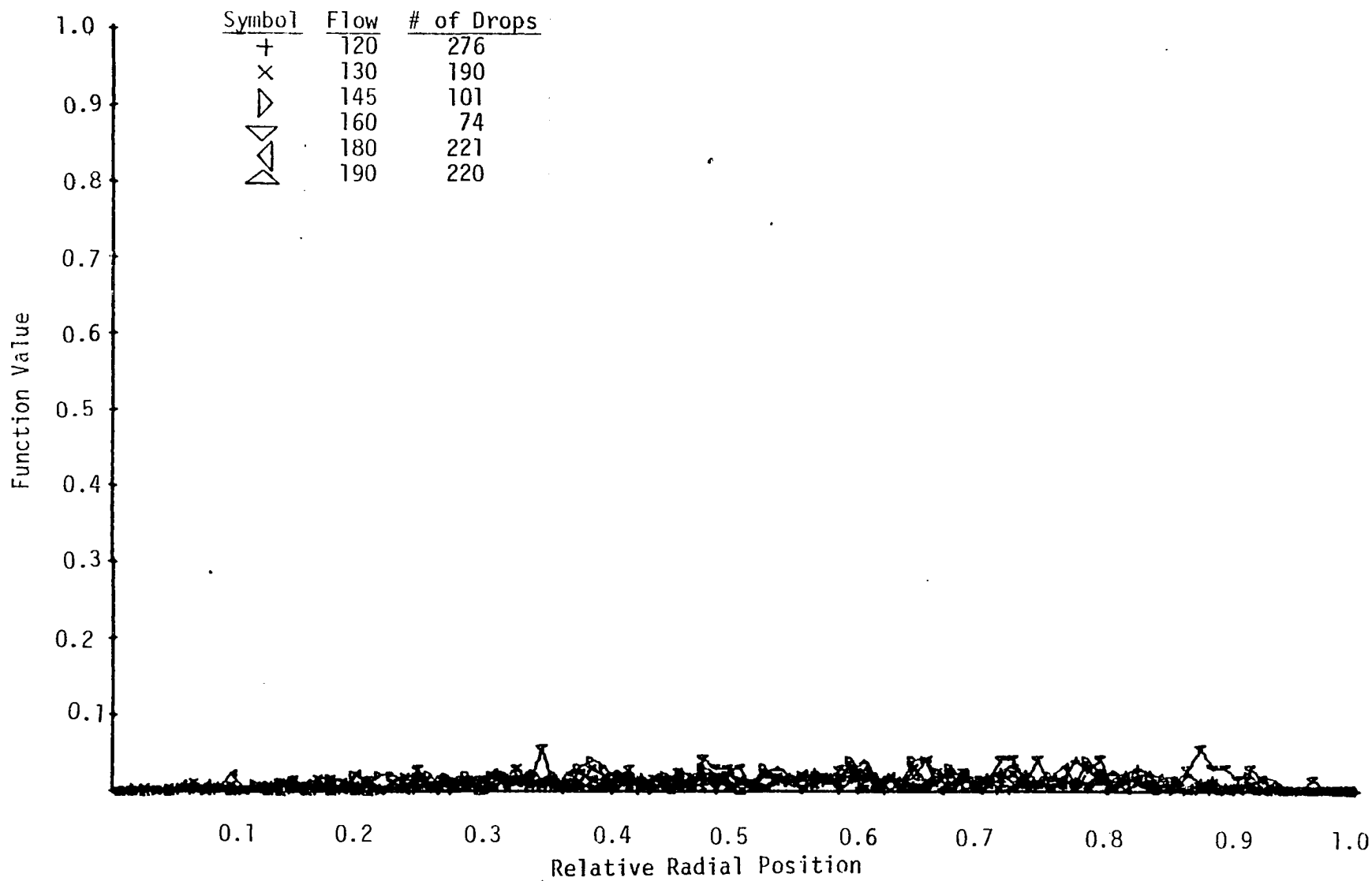
Figure 13a. The Function Value of The Relative Radial Position Distribution (constant radius increments) of FlowRate 1.
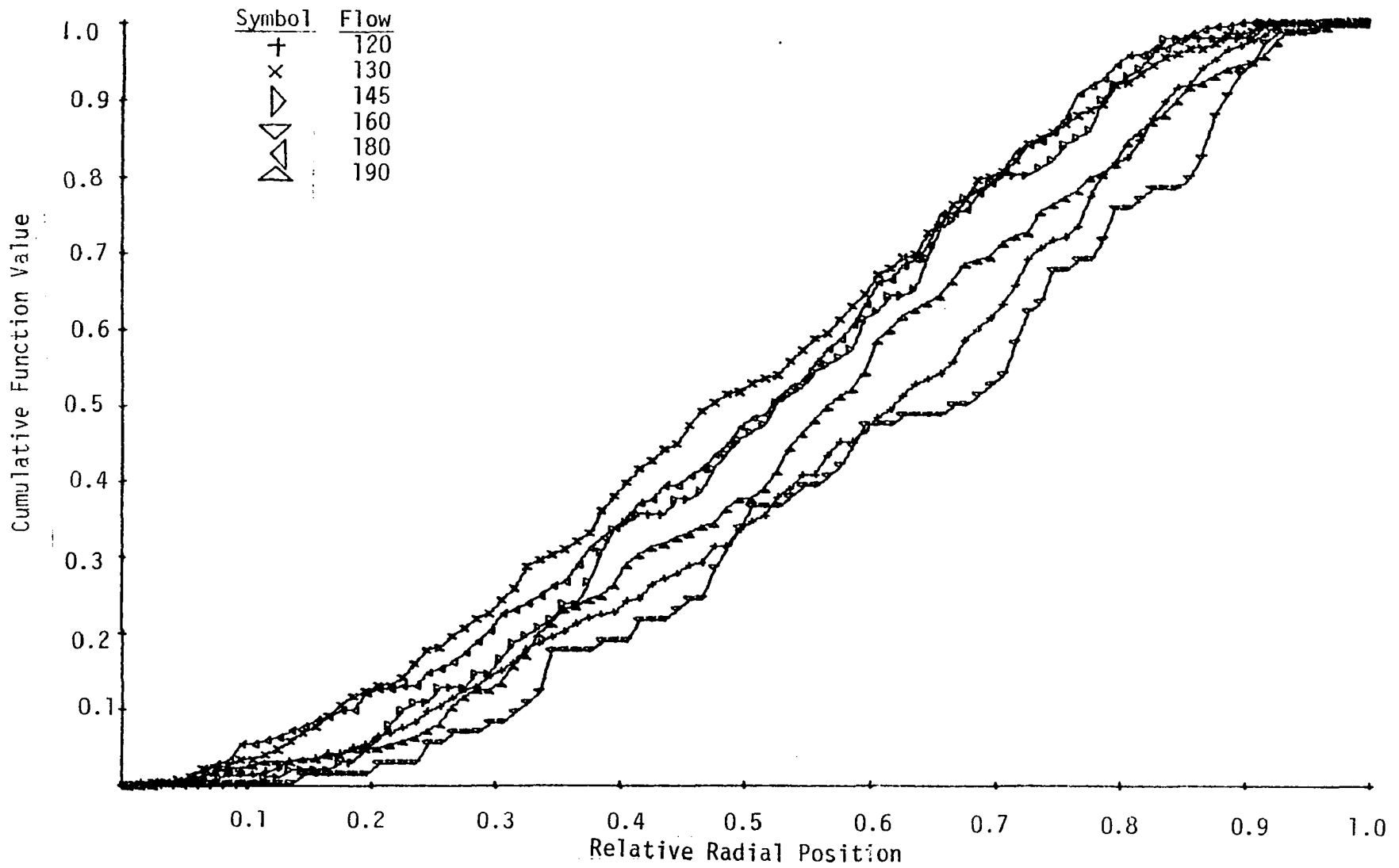
Figure 13b. The Cumulative Function Value of the Relative Radius Position Distribution (constant radius increments) of Flow Rate 1.
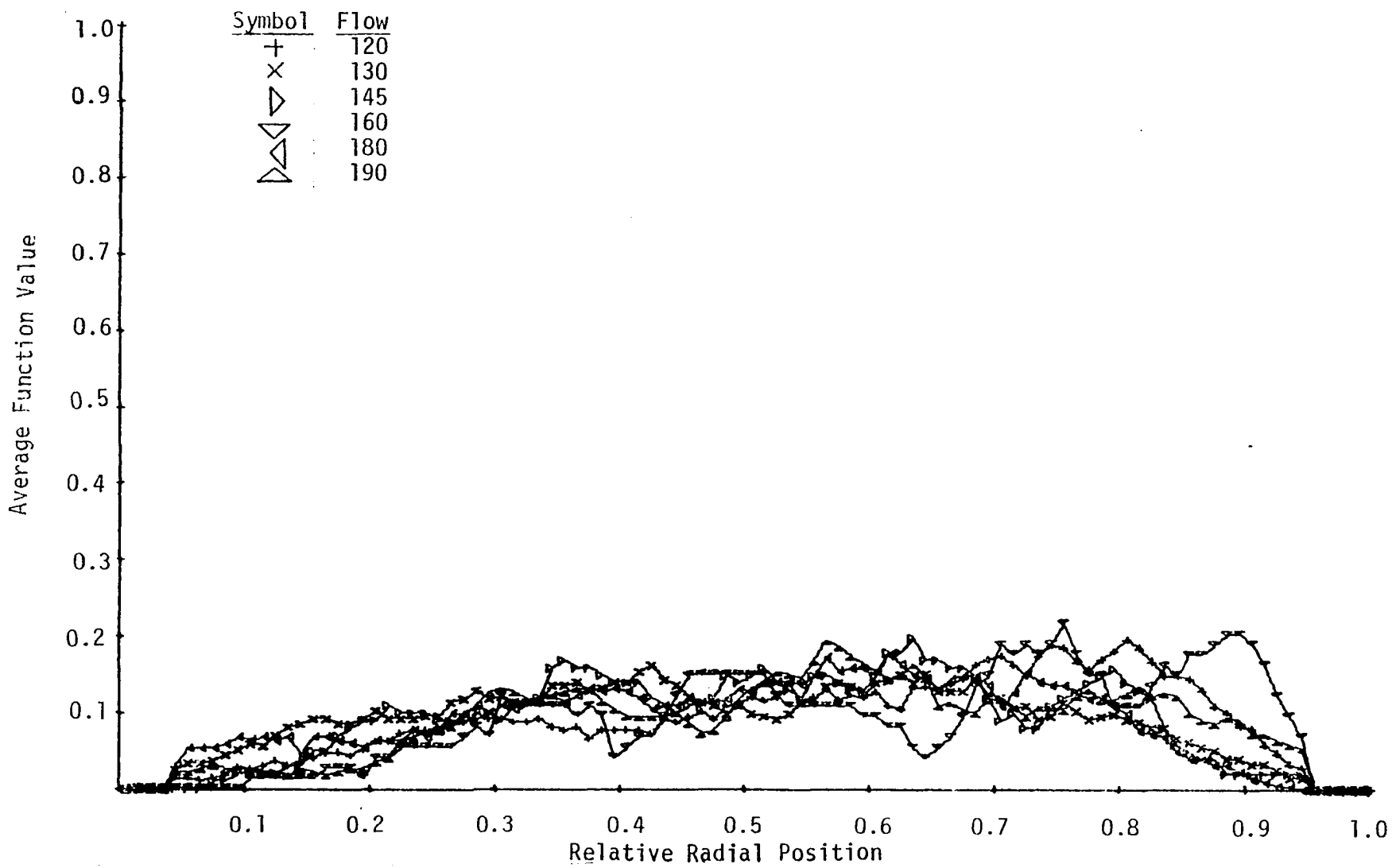
Figure 13c.   The Average Function Value of the Relative Radial Position Distribution (constant radius increments) of Flow Rate 1

Symbol	Flow	# of Drops
+	120	37
×	130	16
▷	145	13
▽	160	8
◁	180	37
△	190	55
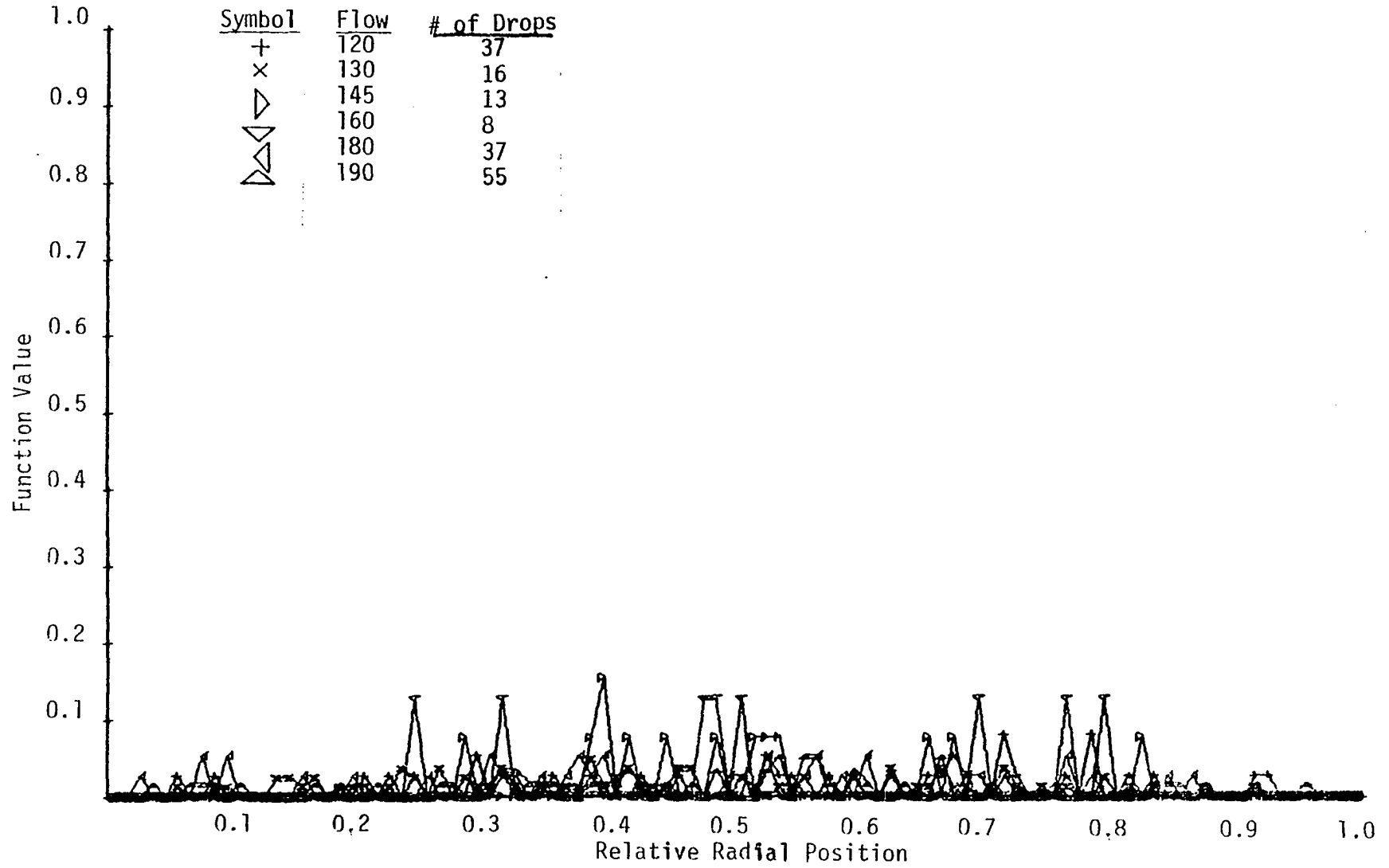
Figure 14a. The Function Value of the Relative Radial Position Distribution (small droplets) (constant radius increments) of Flow Rate 1.
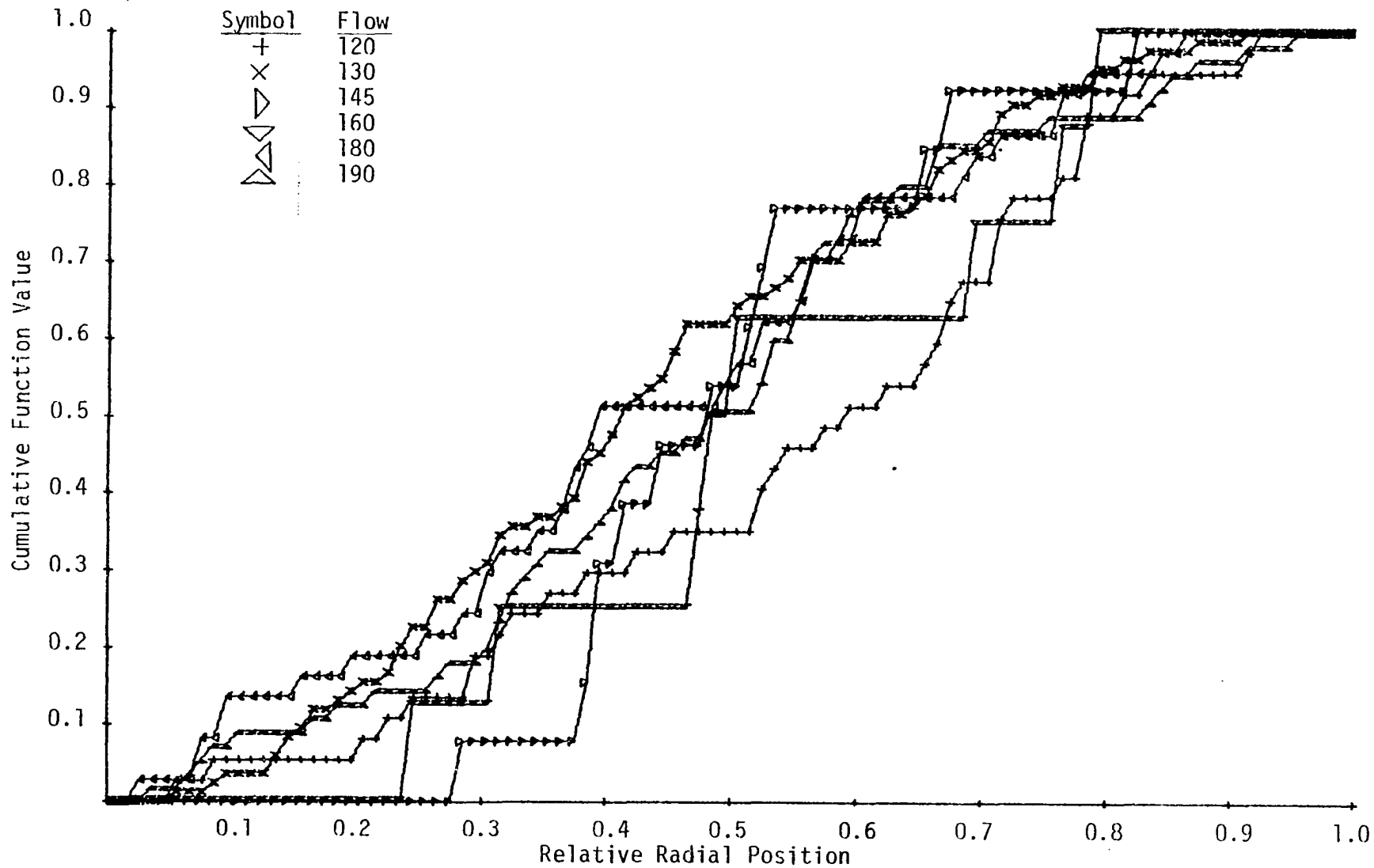
Figure 14b. The Cumulative Function Value of the Relative Radial Position Distribution (small droplets) (constant radius increments) of Flow Rate 1.
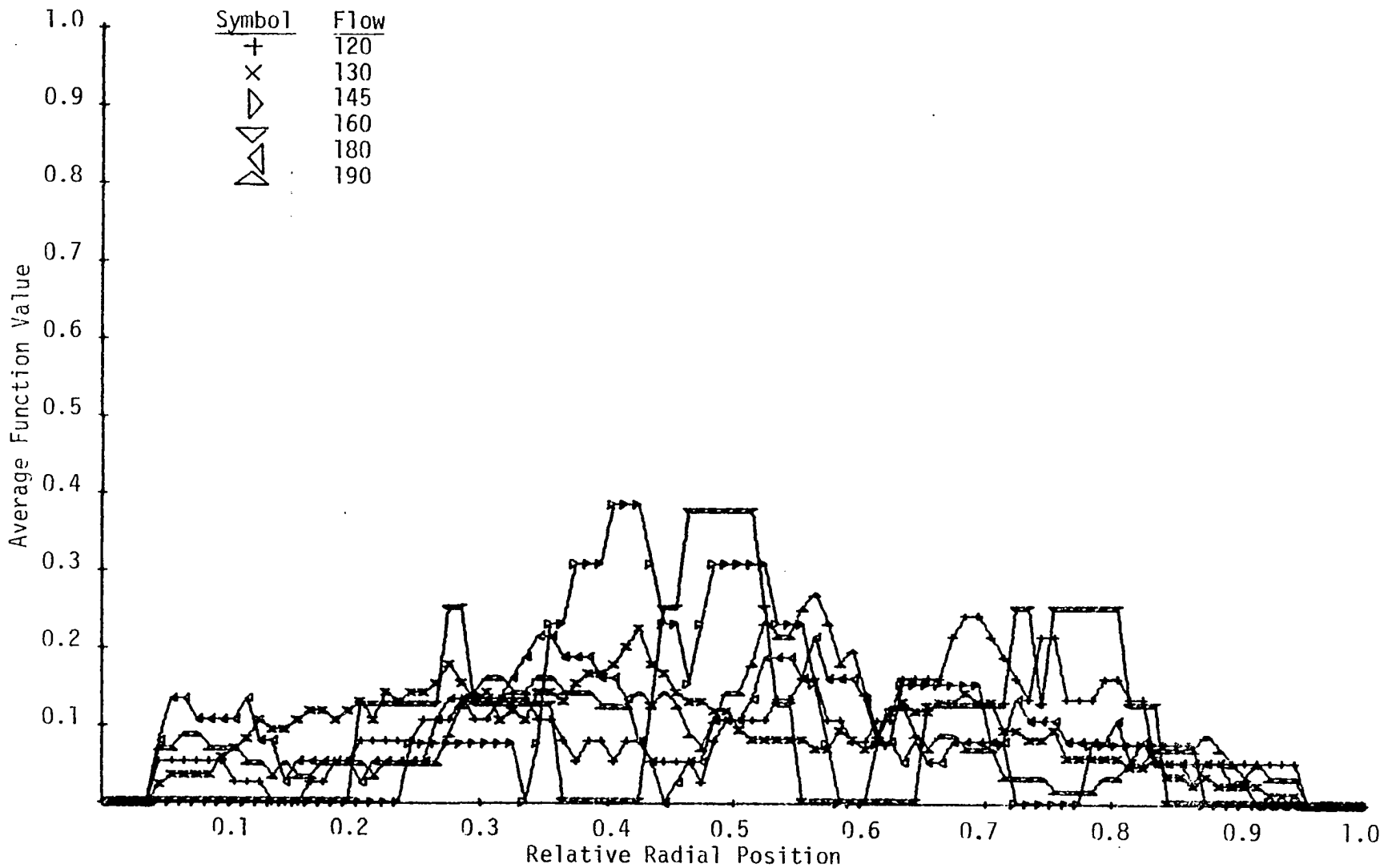
Figure 14c. The Average Function Value of the Relative Radial Position Distribution (small droplets) (constant radius increments) of Flow Rate 1.

Symbol	Flow	# of Drops
+	120	239
×	130	174
▷	145	88
▽	160	66
◁	180	184
△	190	165

Function Value

Relative Radial Position
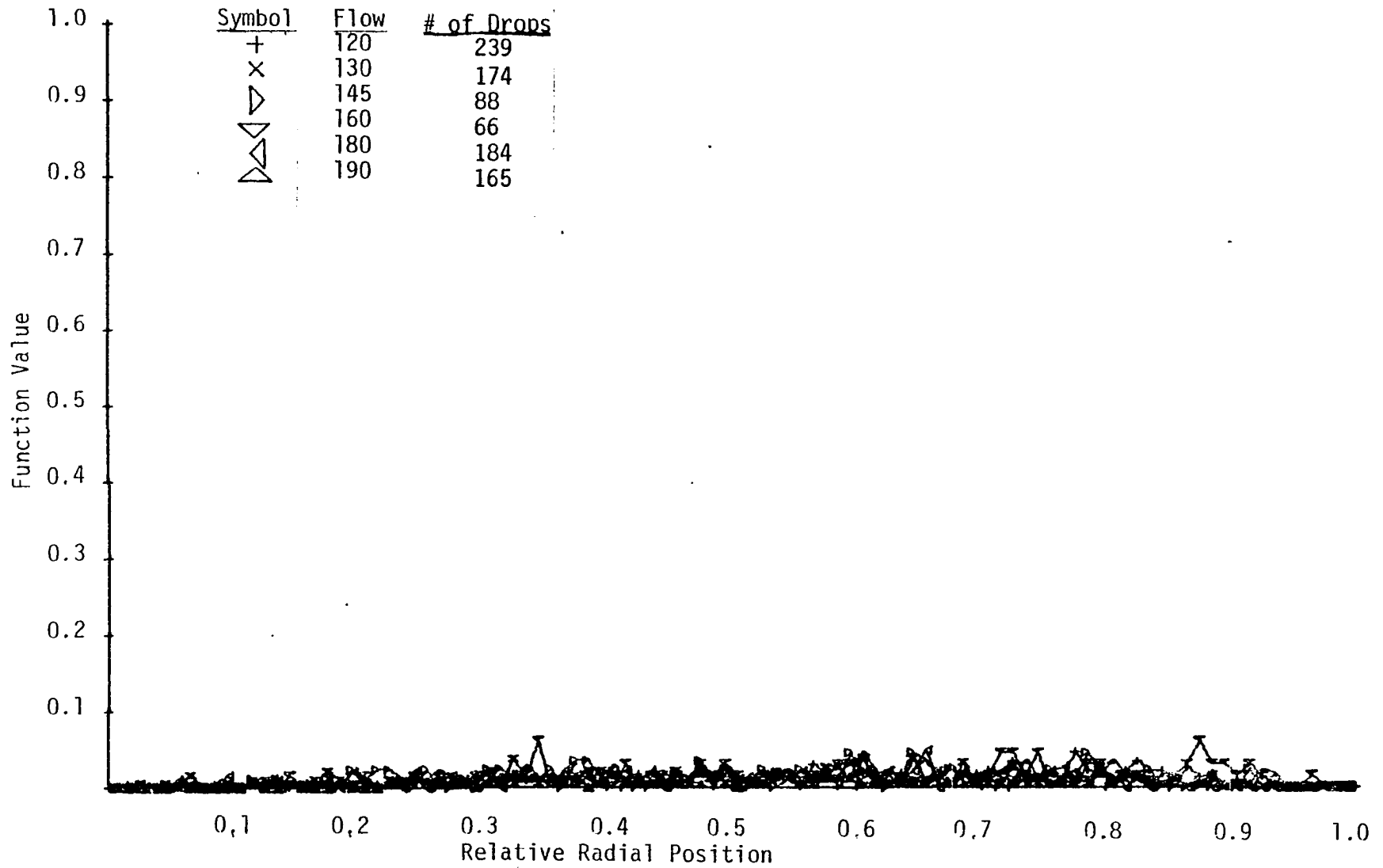
Figure 15a.   The Function Value of the Relative Radial Position Distribution (large droplets) (constant radius increments) of Flow Rate 1.

56
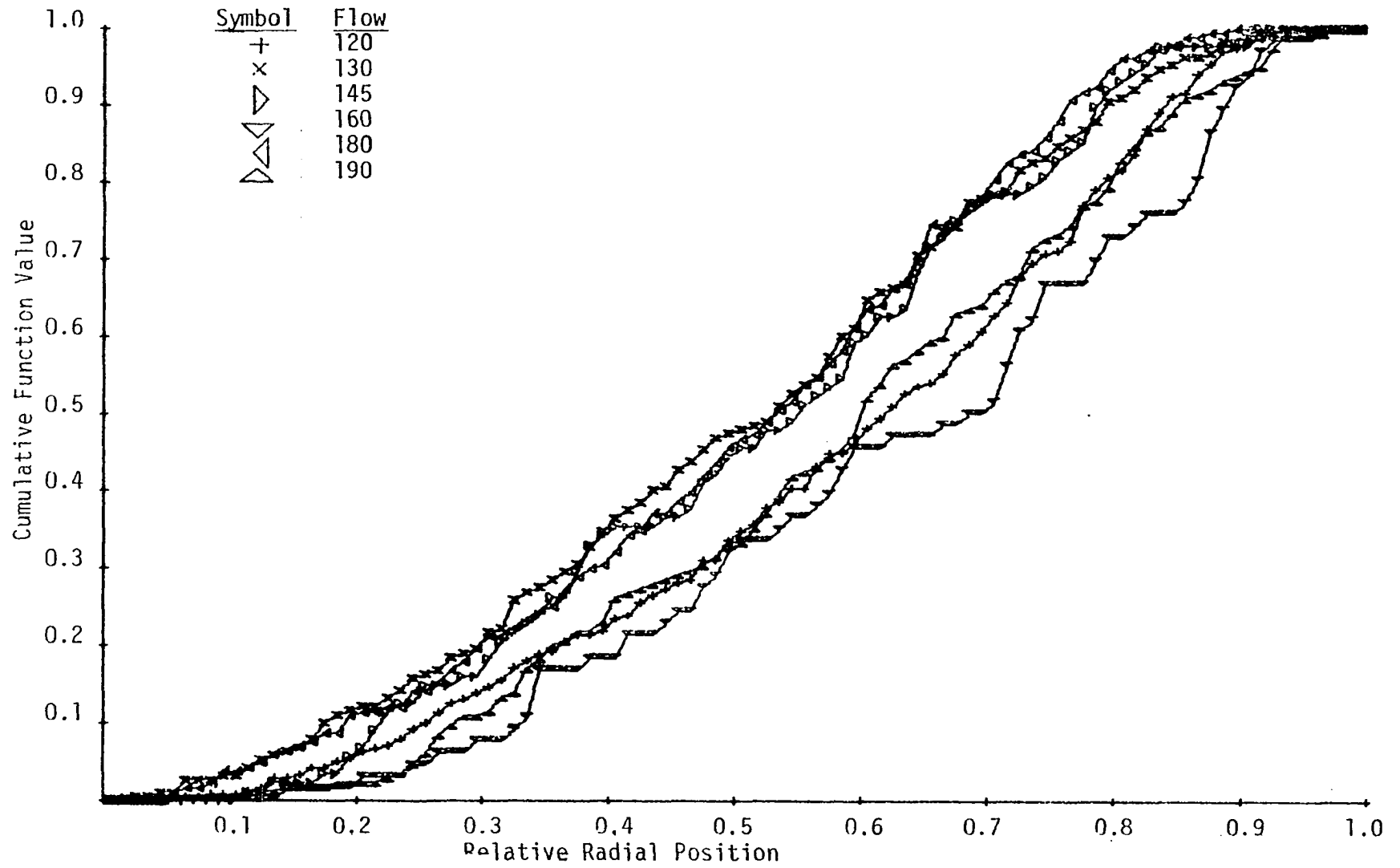
Figure 15b. The Cumulative Function Value of the Relative Radial Position Distribution (large droplets) (constant radius increments) of Flow Rate 1.
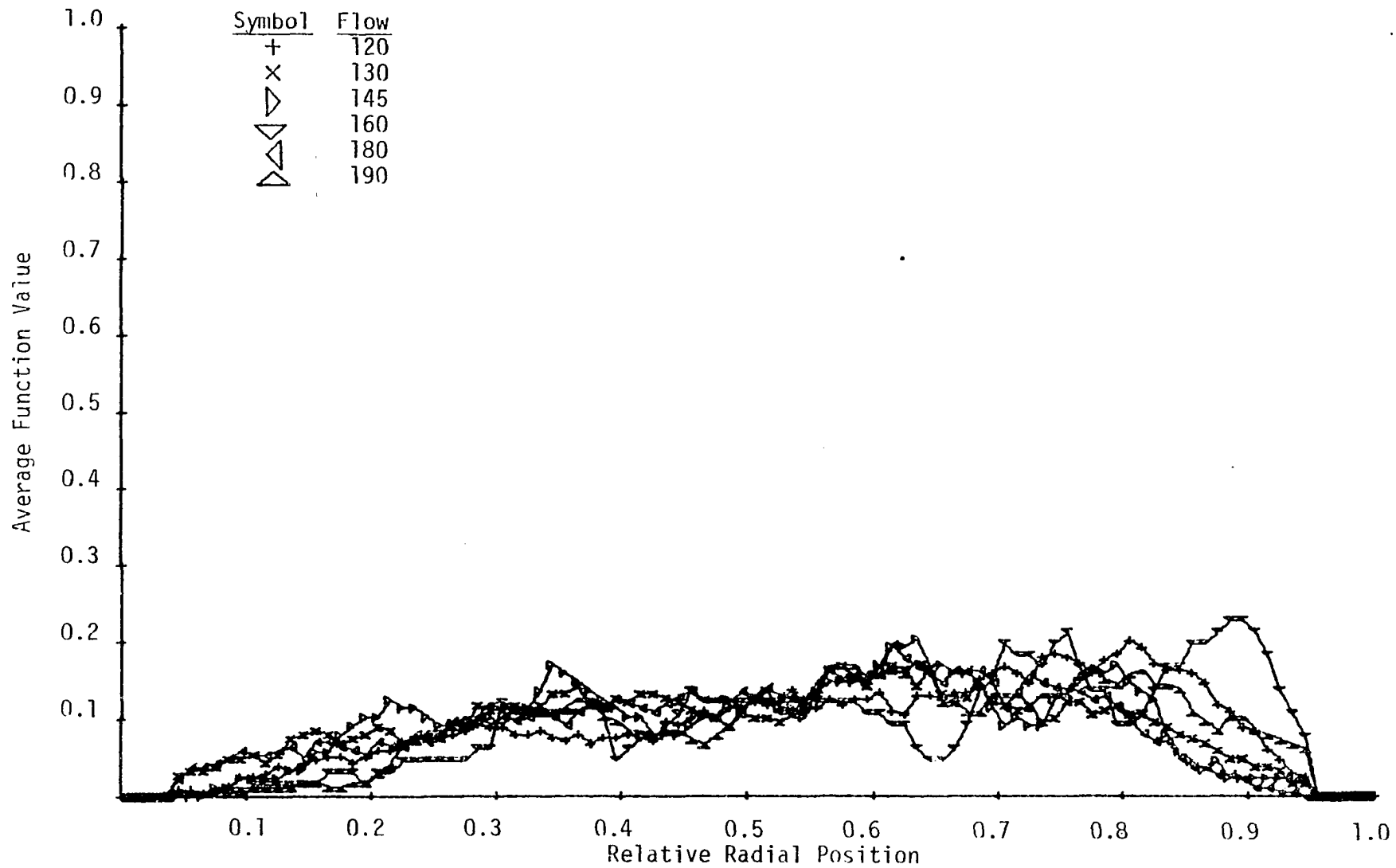
Figure 15c. The Average Function Value of the Relative Radial Position Distribution (large droplets) (constant radius increments) of Flow Rate 1.

58

Symbol	Flow	# of Drops
+	120	276
×	130	190
▷	145	101
▽	160	74
◁	180	221
△	190	220
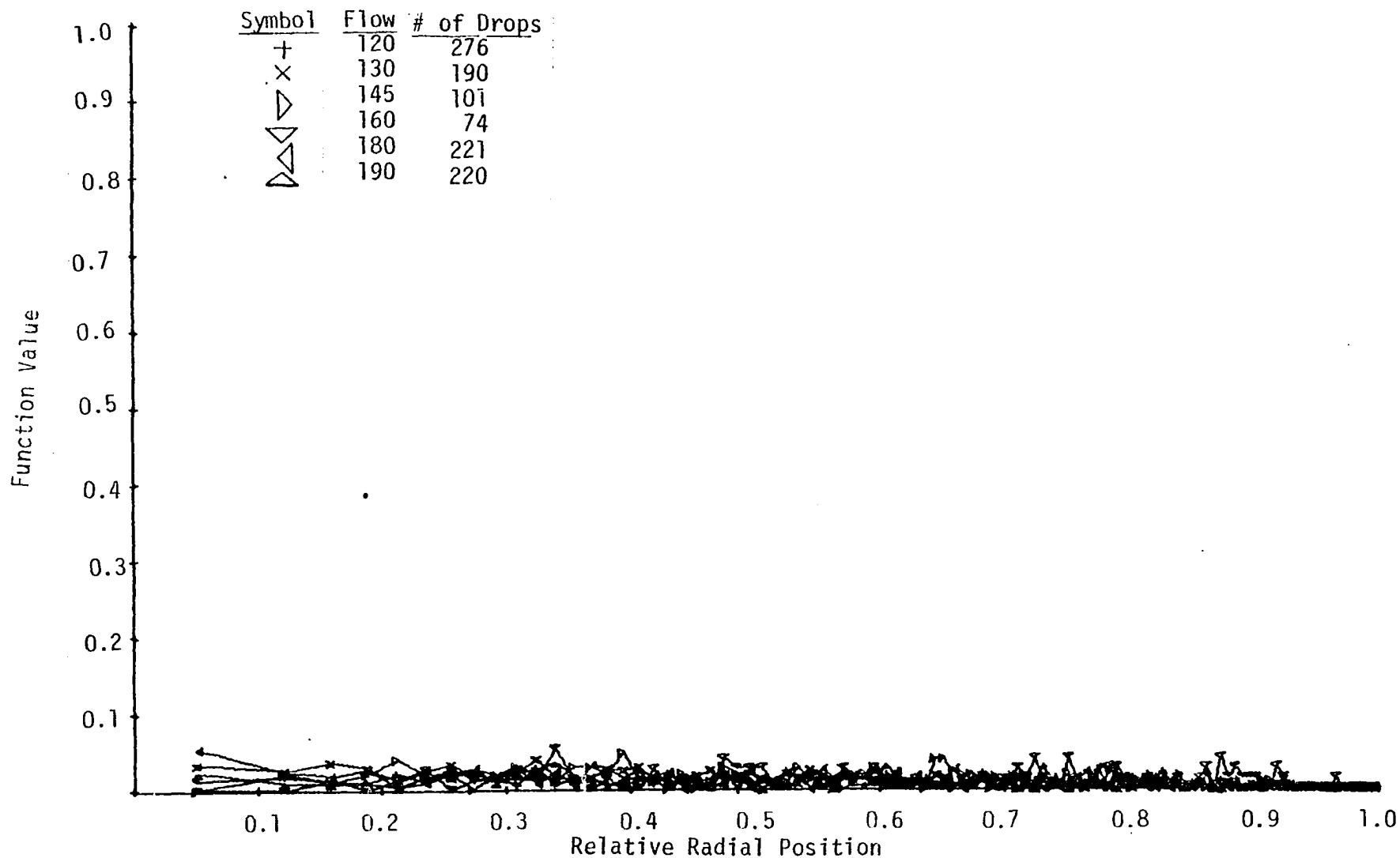
Figure 16a.   The Function Value of the Relative Radial Position Distribution (constant area increments) of Flow Rate 1.
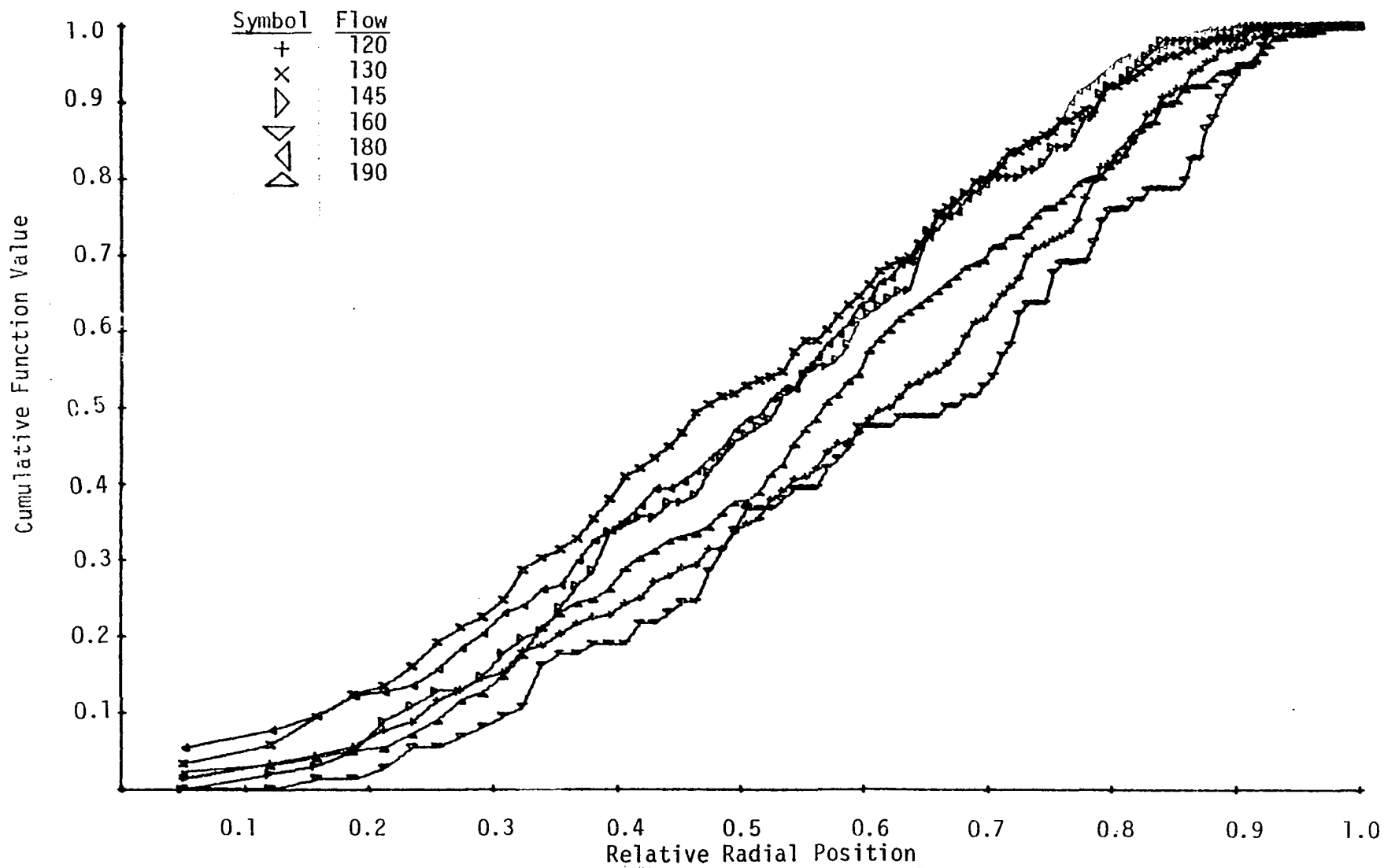
Figure 16b. The Cumulative Function Value of The Relative Radial Position Distribution (constant area increments) of Flow Rate 1.
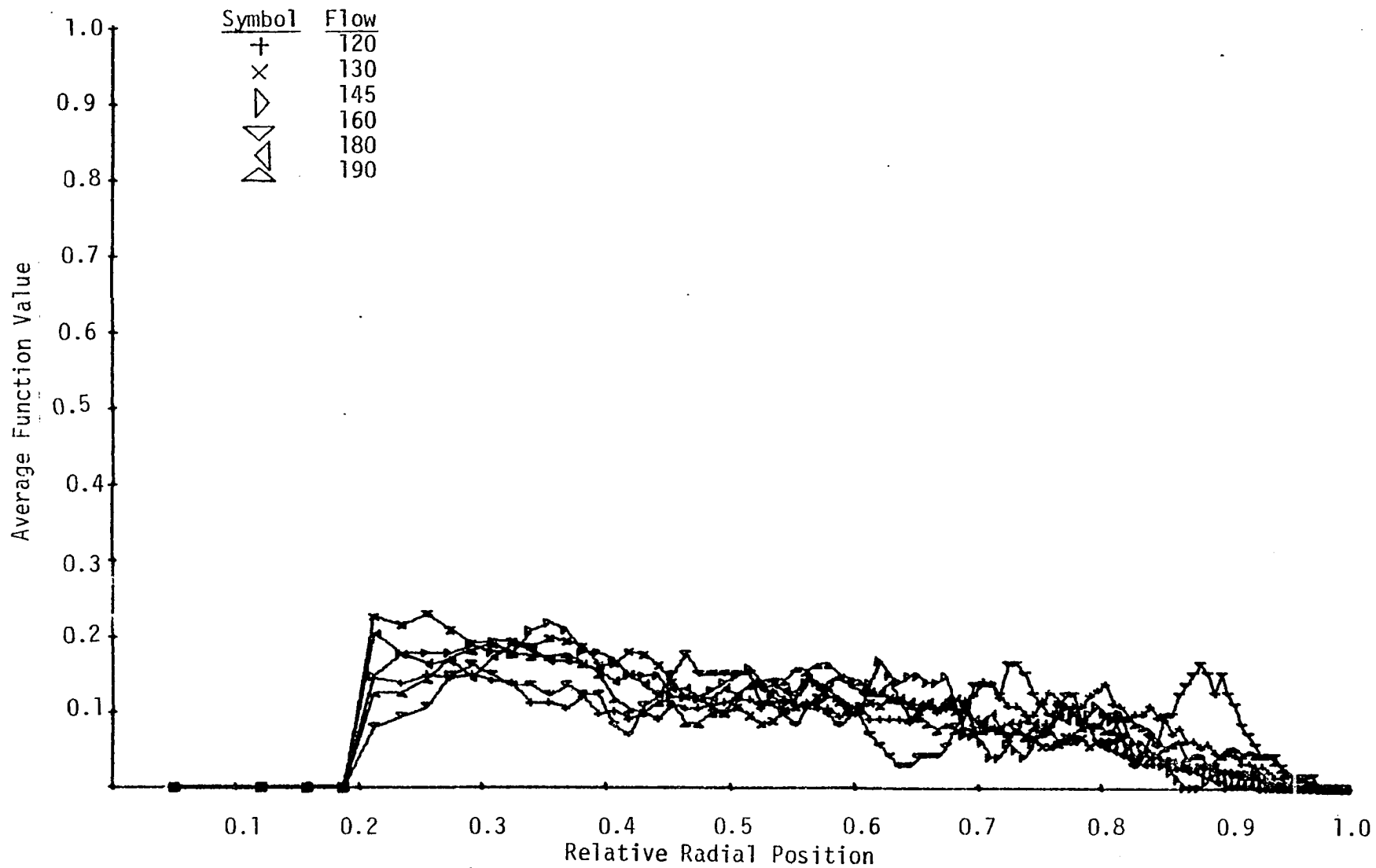
Figure 16c. The Average Function Value of the Relative Radial Position Distribution (constant area increments) of Flow Rate 1.
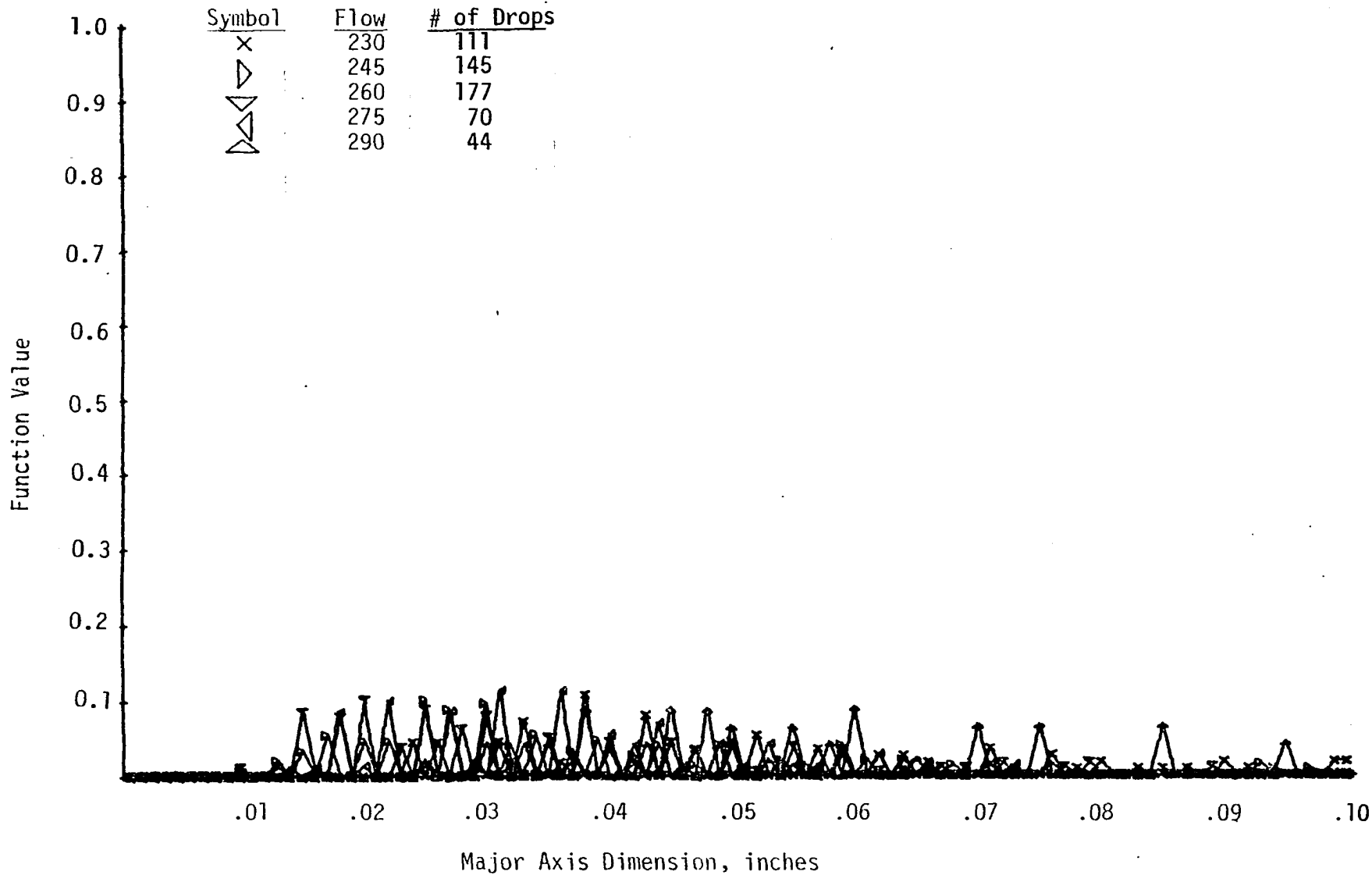
Figure 17a. The Function Value of the Major Axis Distribution of Flow Rate 2.
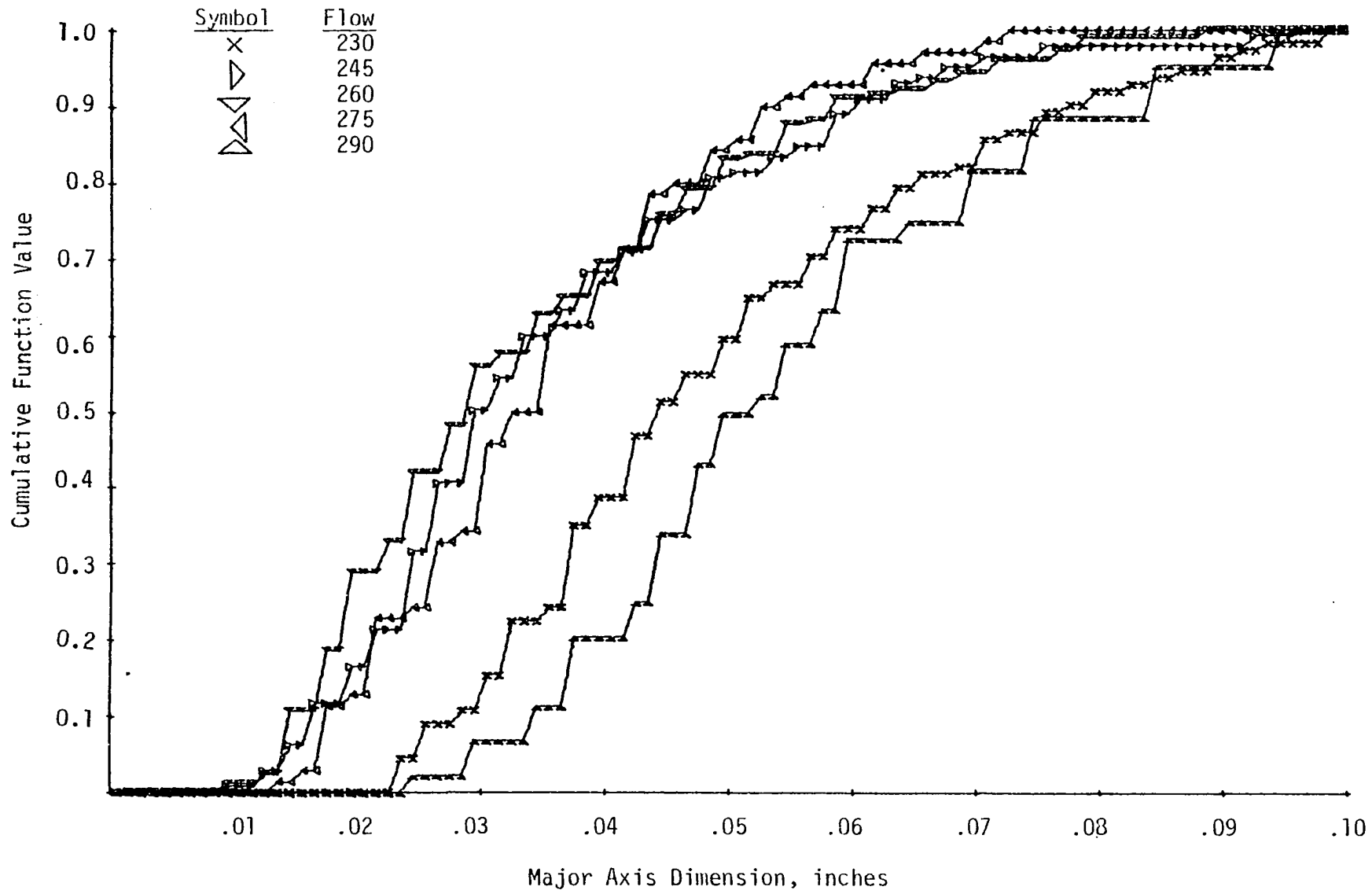
Figure 17b.   The Cumulative Function Value of the Major Axis Distribution of Flow Rate 2.
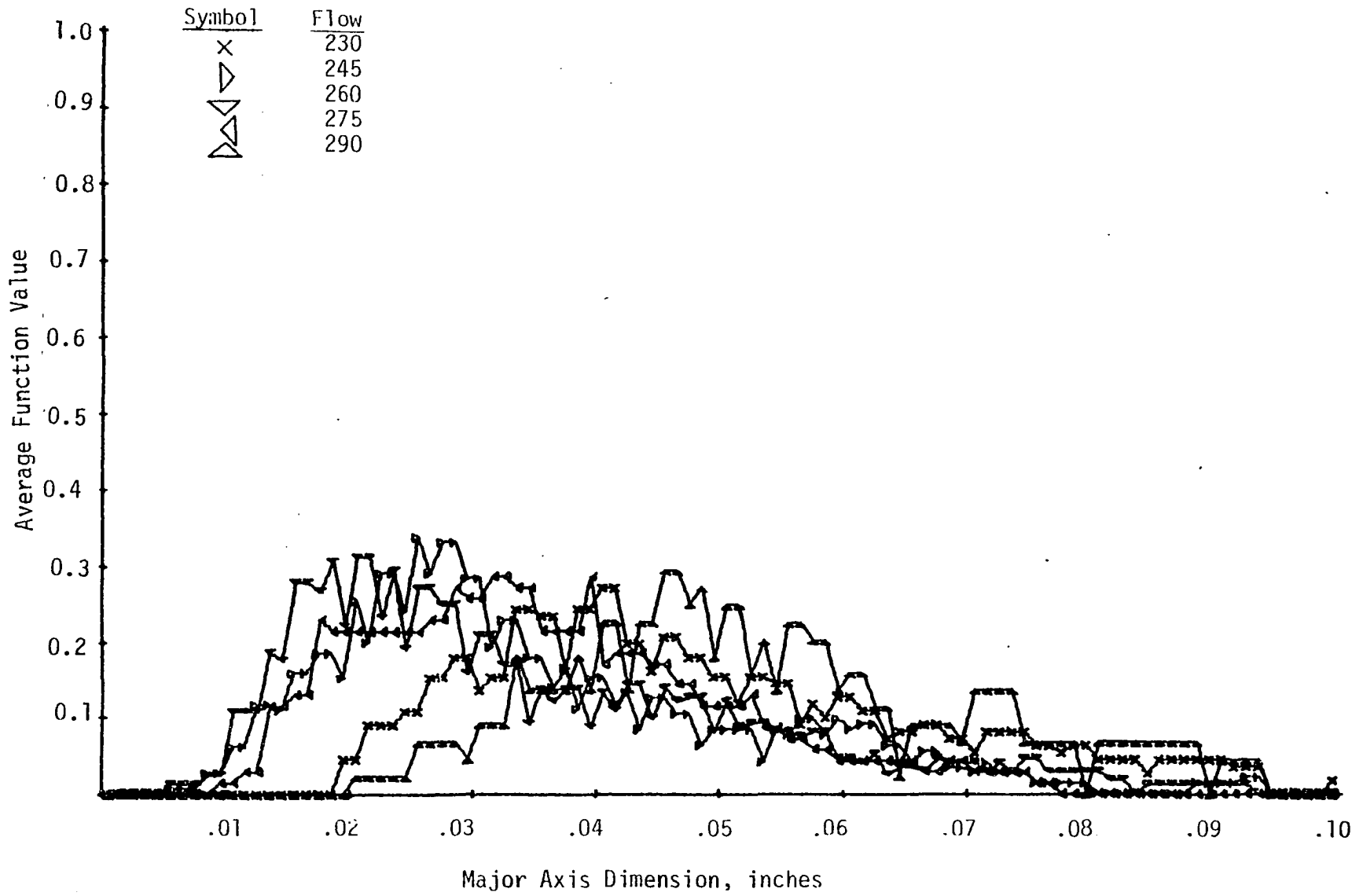
Figure 17c.   The Average Function Value of the Major Axis Distribution of Flow Rate 2.

64
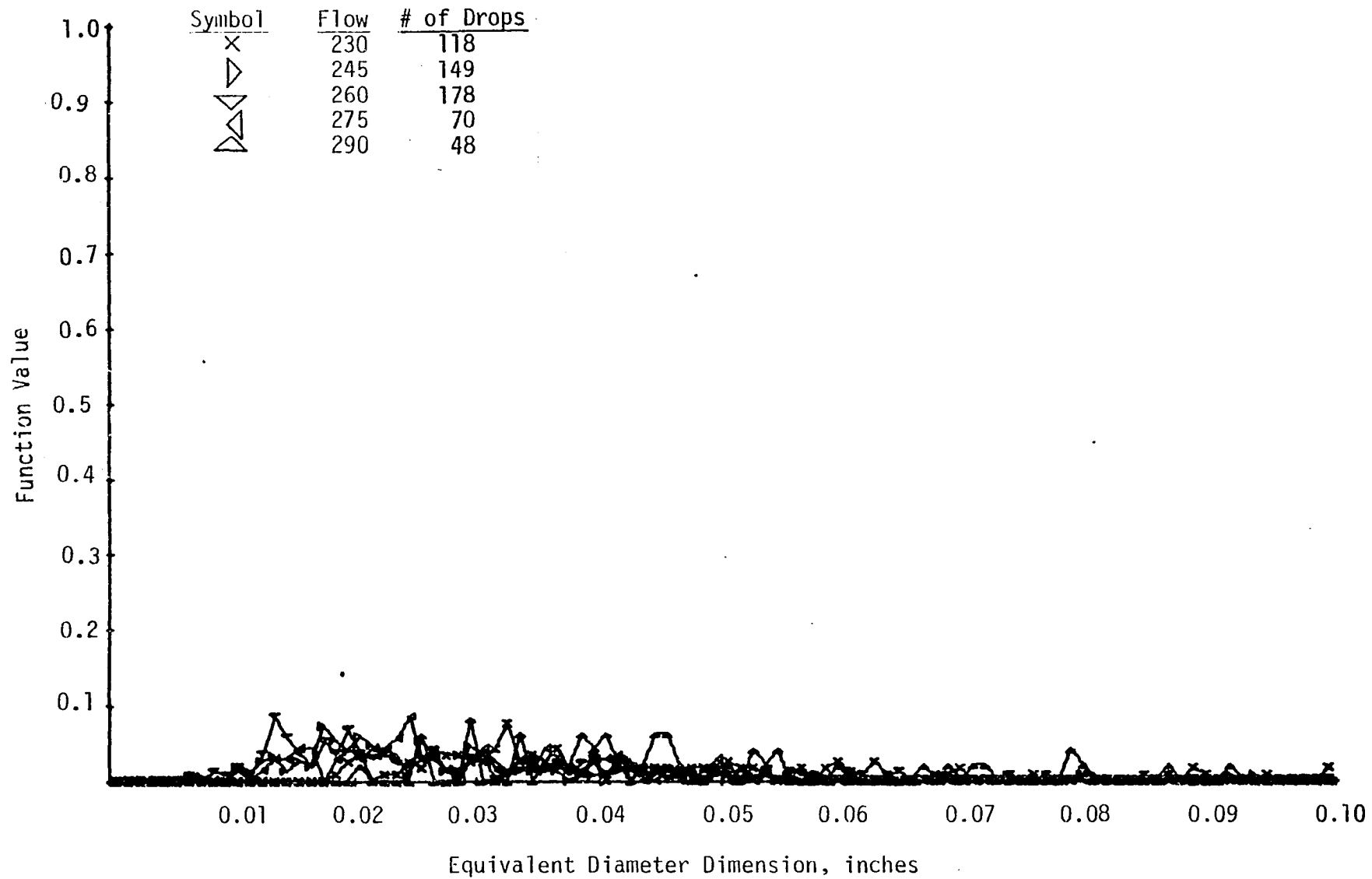
Figure 18a. The Function Value of the Equivalent Diameter Distribution of Flow Rate 2.
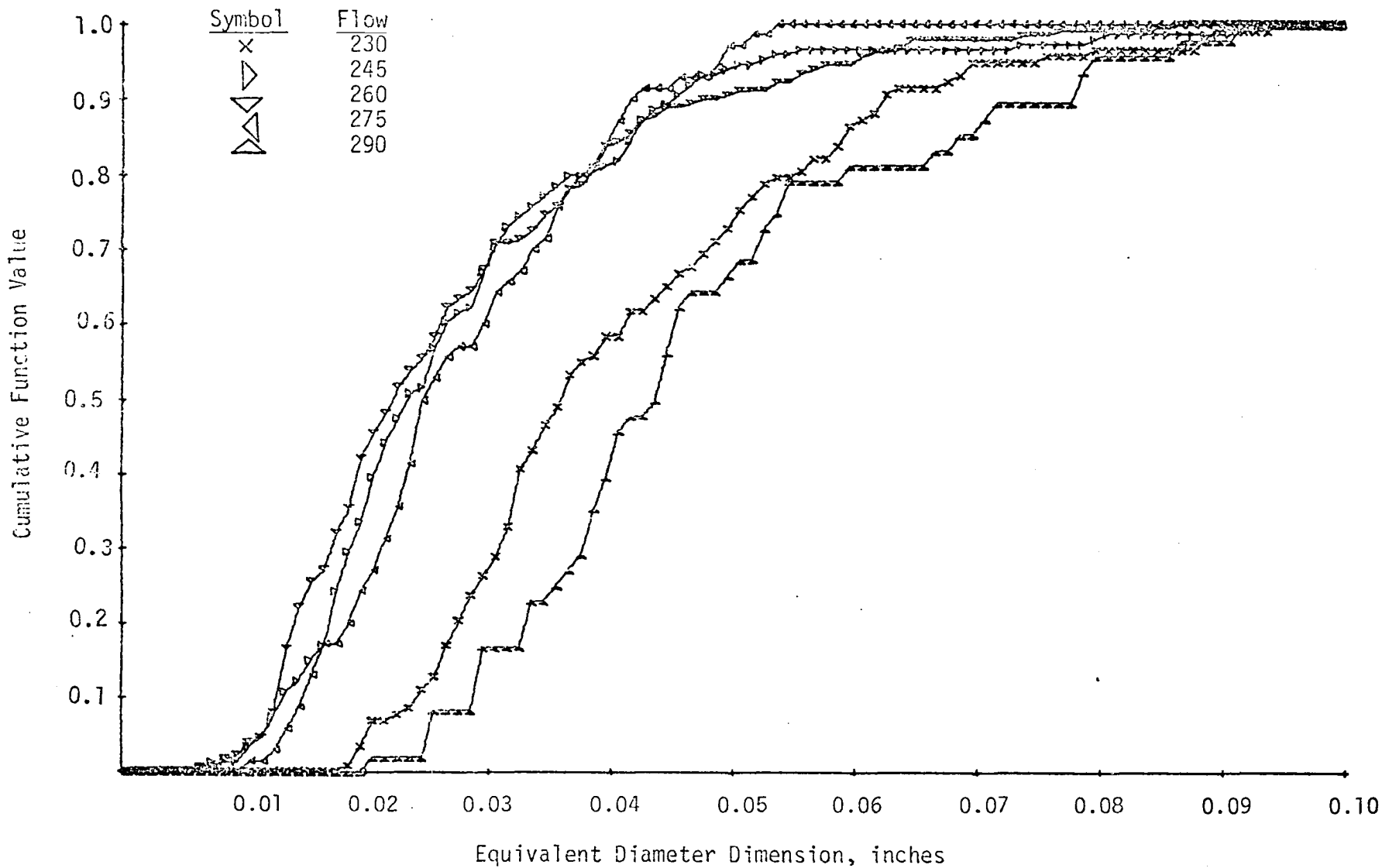
Figure 18b. The Cumulative Function Value of the Equivalent Diameter Distribution of Flow Rate 2.
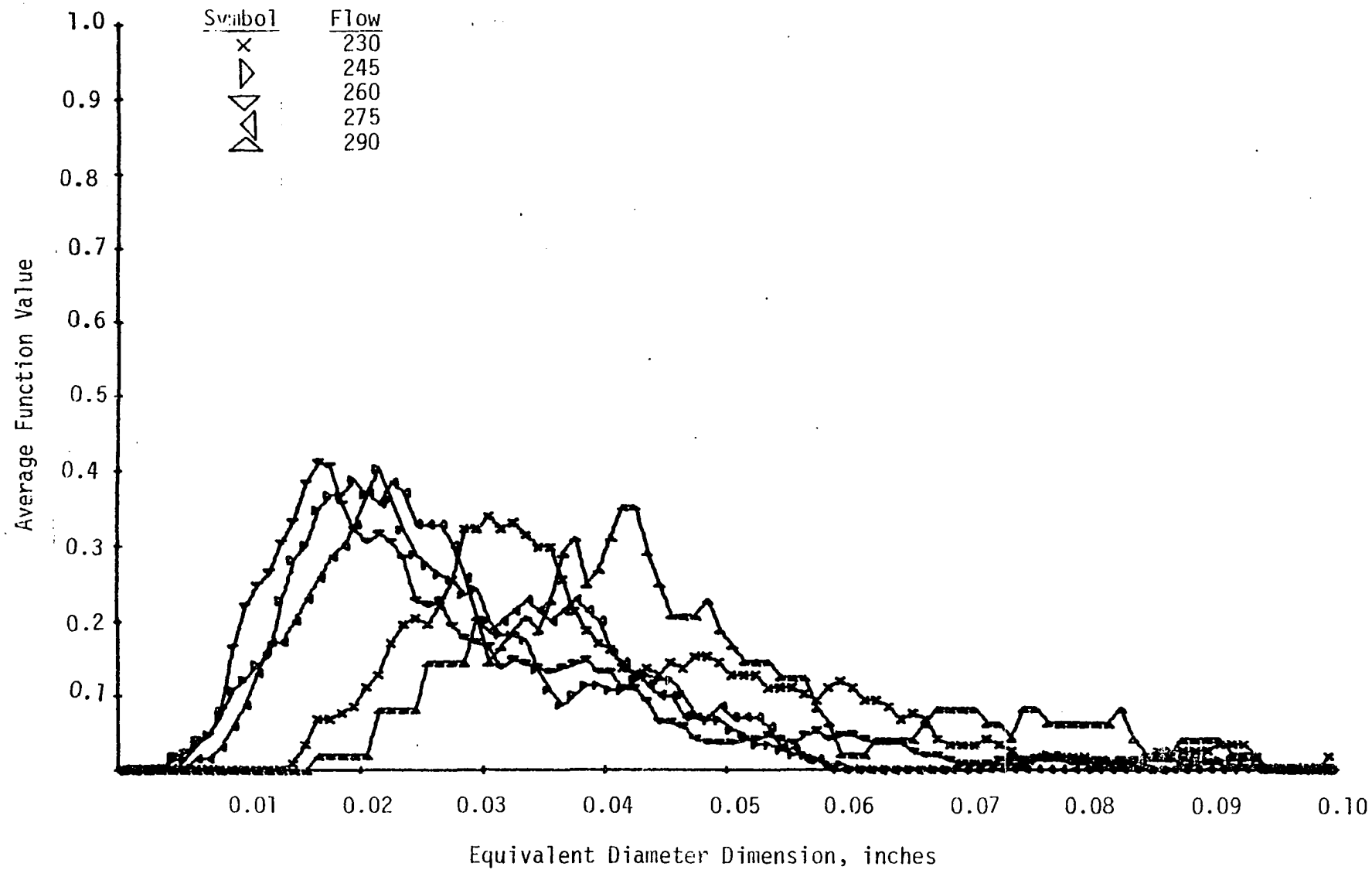
Figure 18c. The Average Function Value of the Equivalent Diameter Distribution of Flow Rate 2.
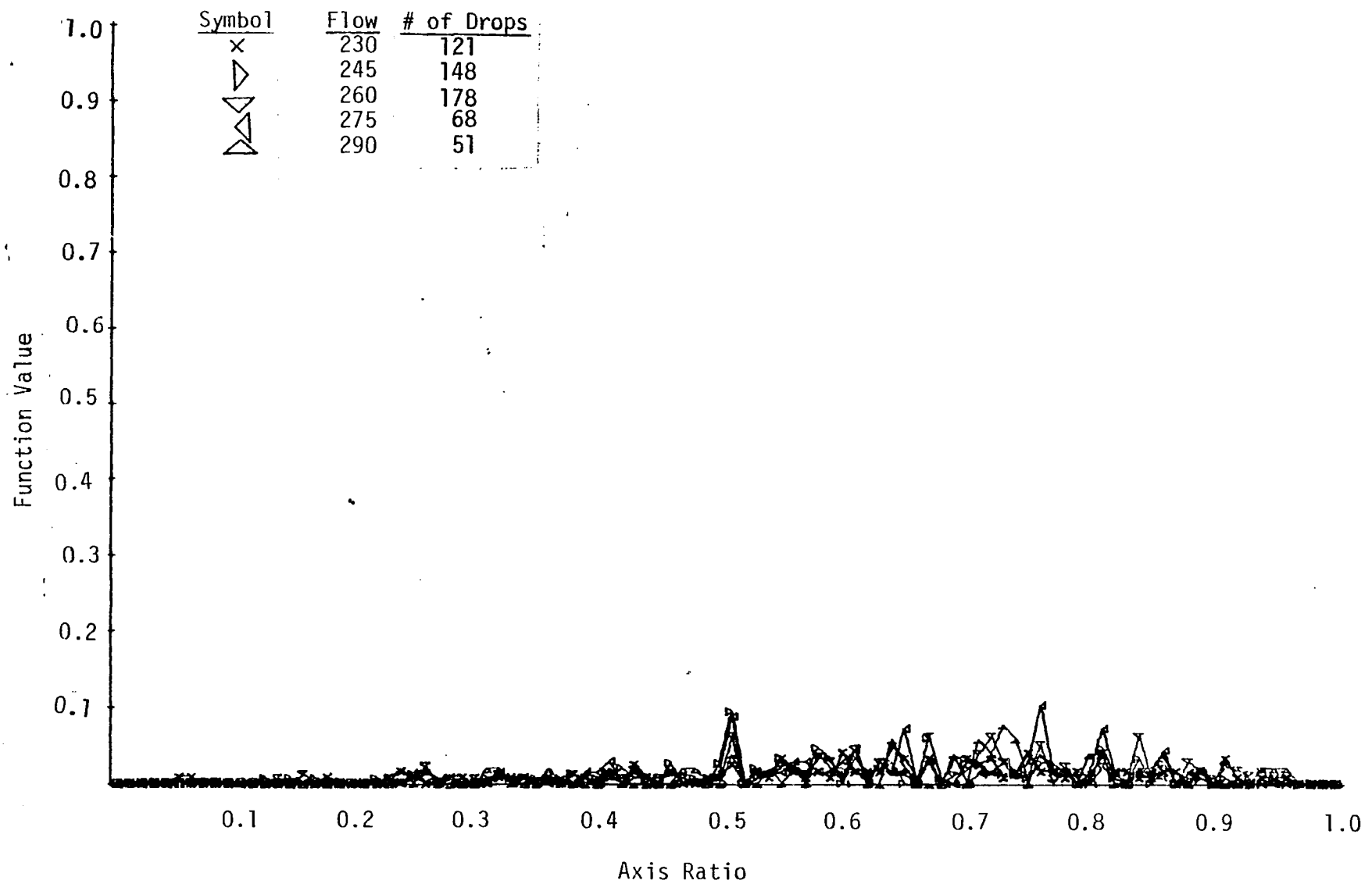
Figure 19a.   The Function Value of the Axis Ratio Distribution of Flow Rate 2.
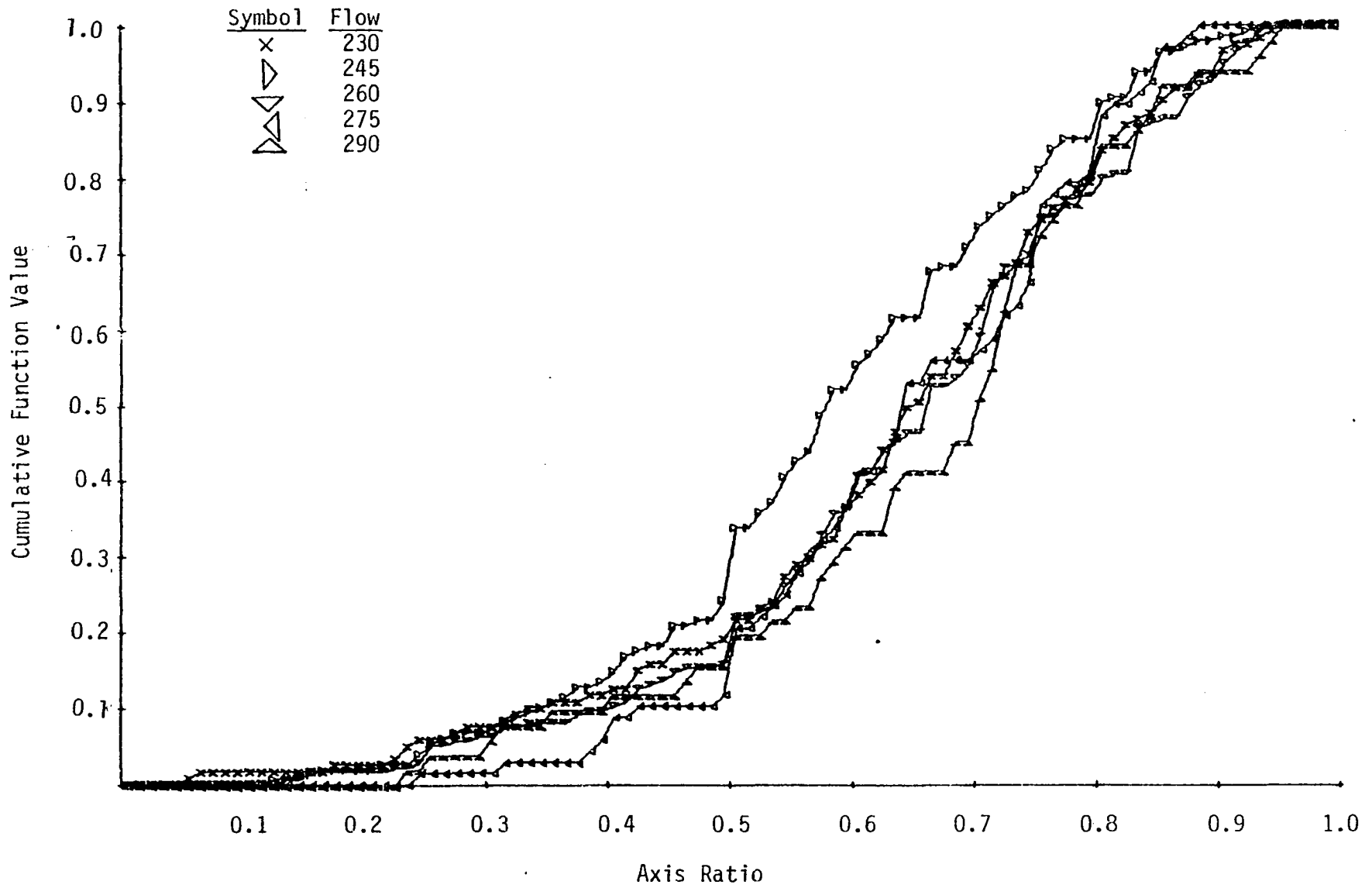
Figure 19b. The Cumulative Function Value of the Axis Ratio Distribution of Flow Rate 2.
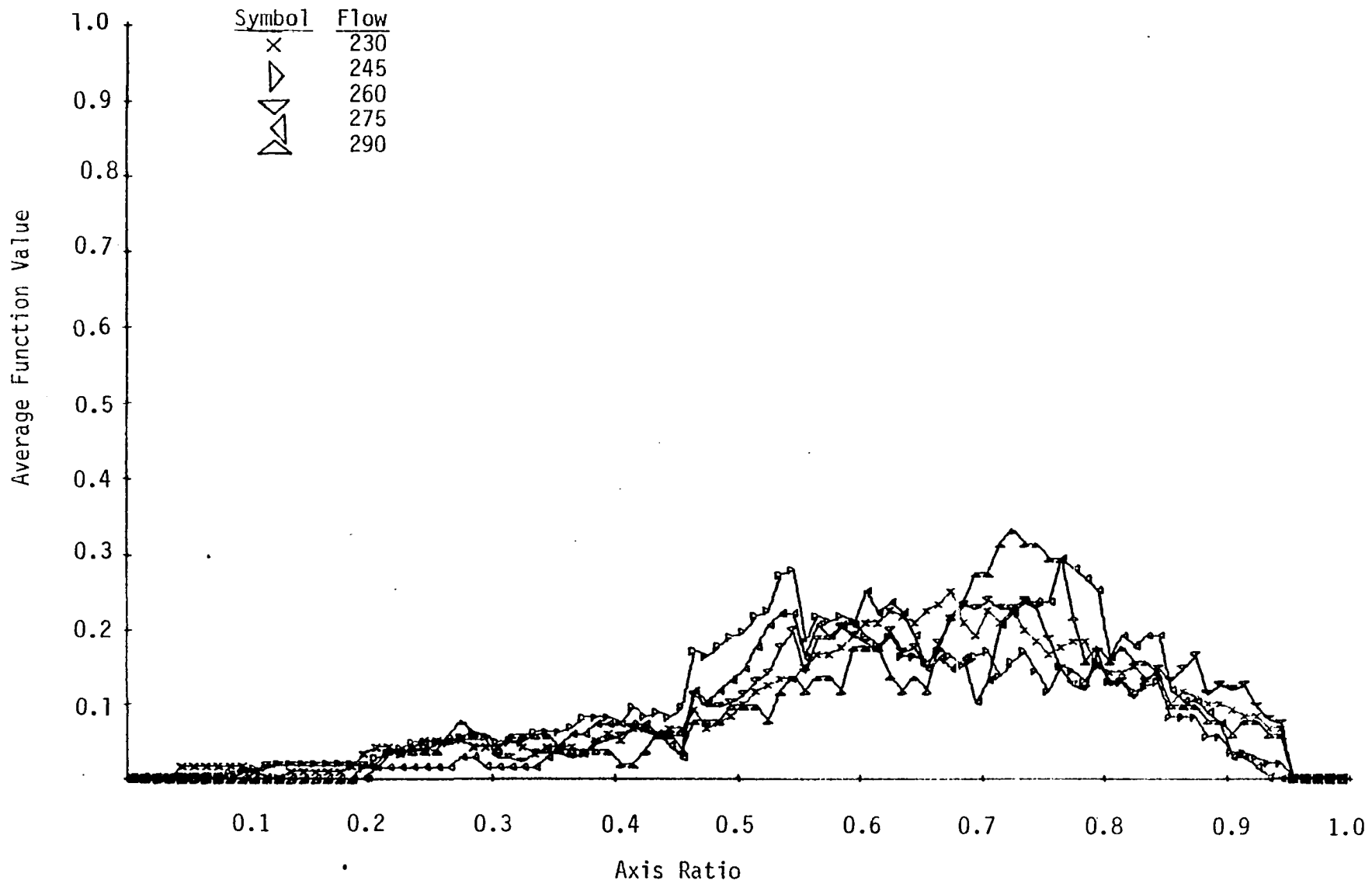
Figure 19c. The Average Function Value of the Axis Ratio Distribution of Flow Rate 2.
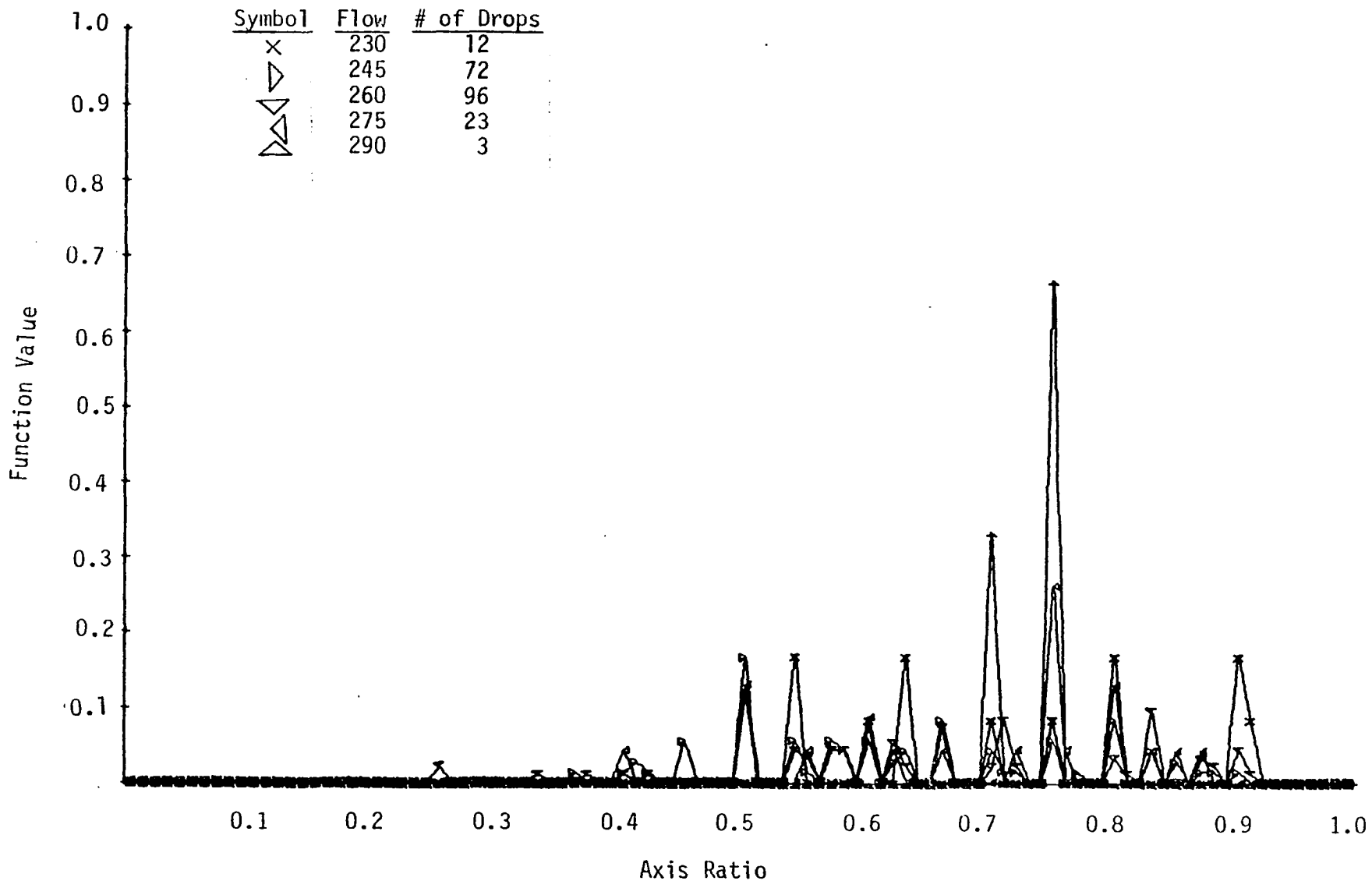
Figure 20a.   The Function Value of the Axis Ratio Distribution (small droplets)
of Flow Rate 2.
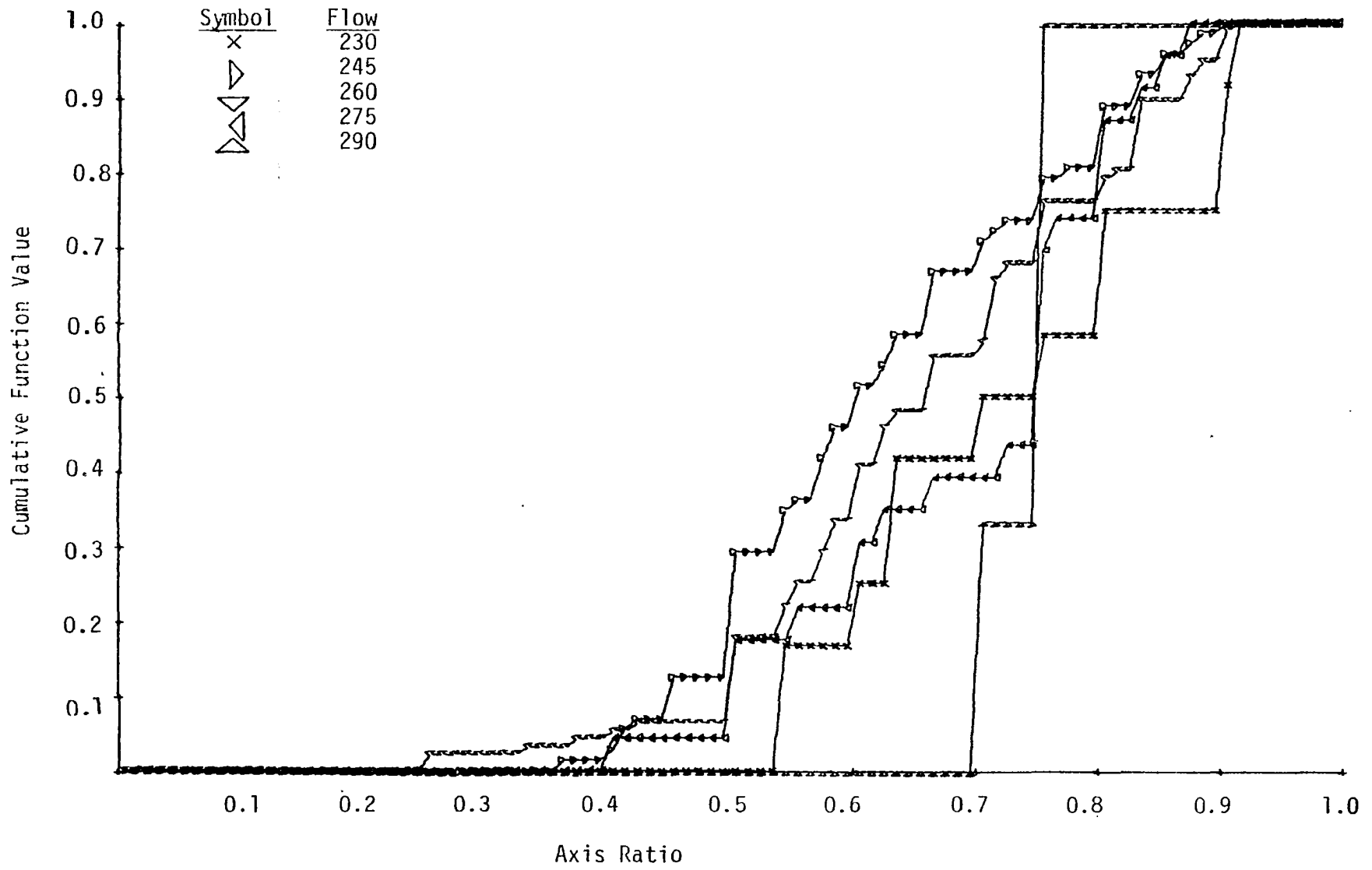
Figure 20b. The Cumulative Function Value of the Axis Ratio Distribution (small droplets) of Flow Rate 2.
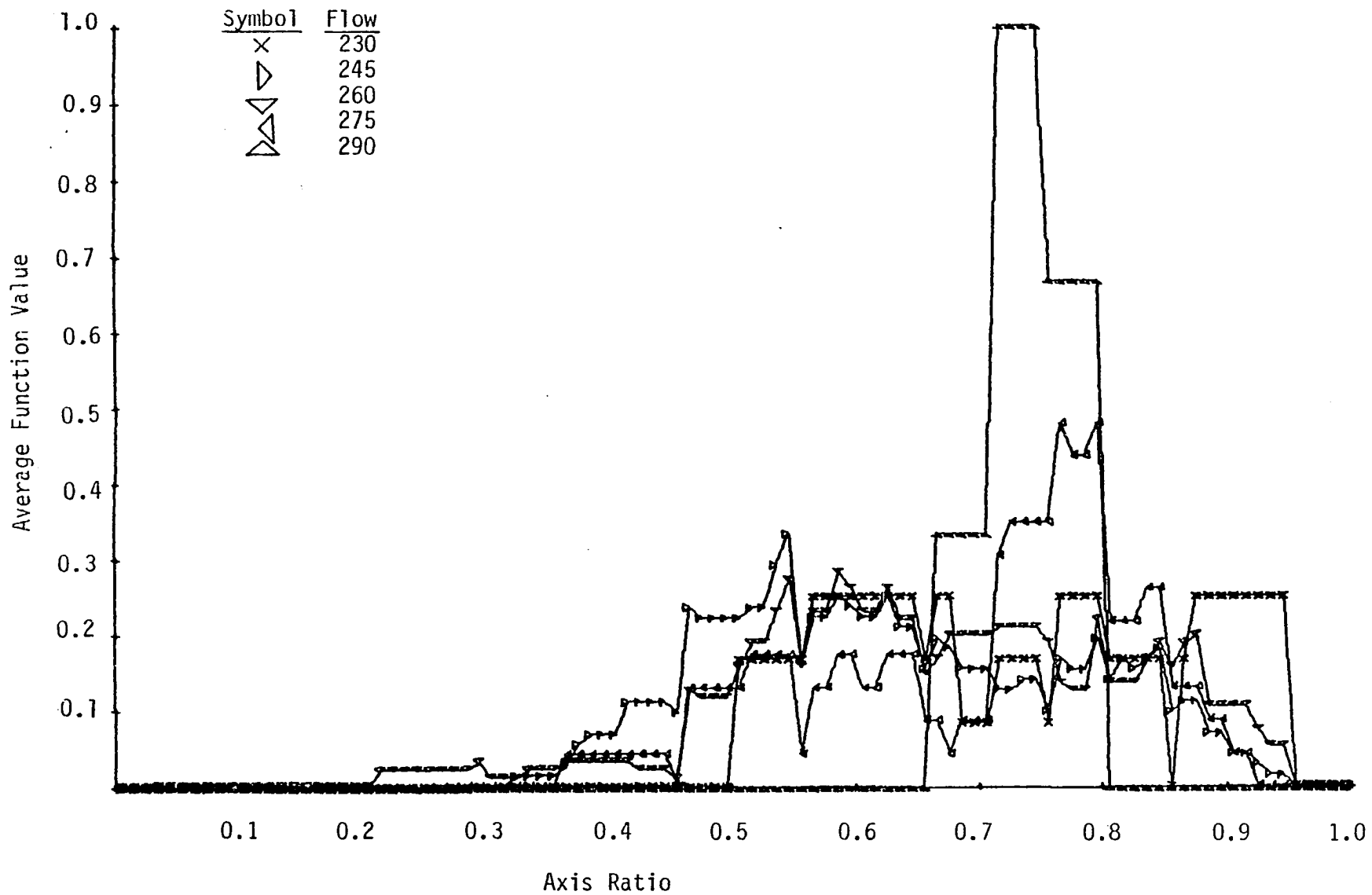
Figure 20c. The Average Function Value of the Axis Ratio Distribution (small droplets) of Flow Rate 2.
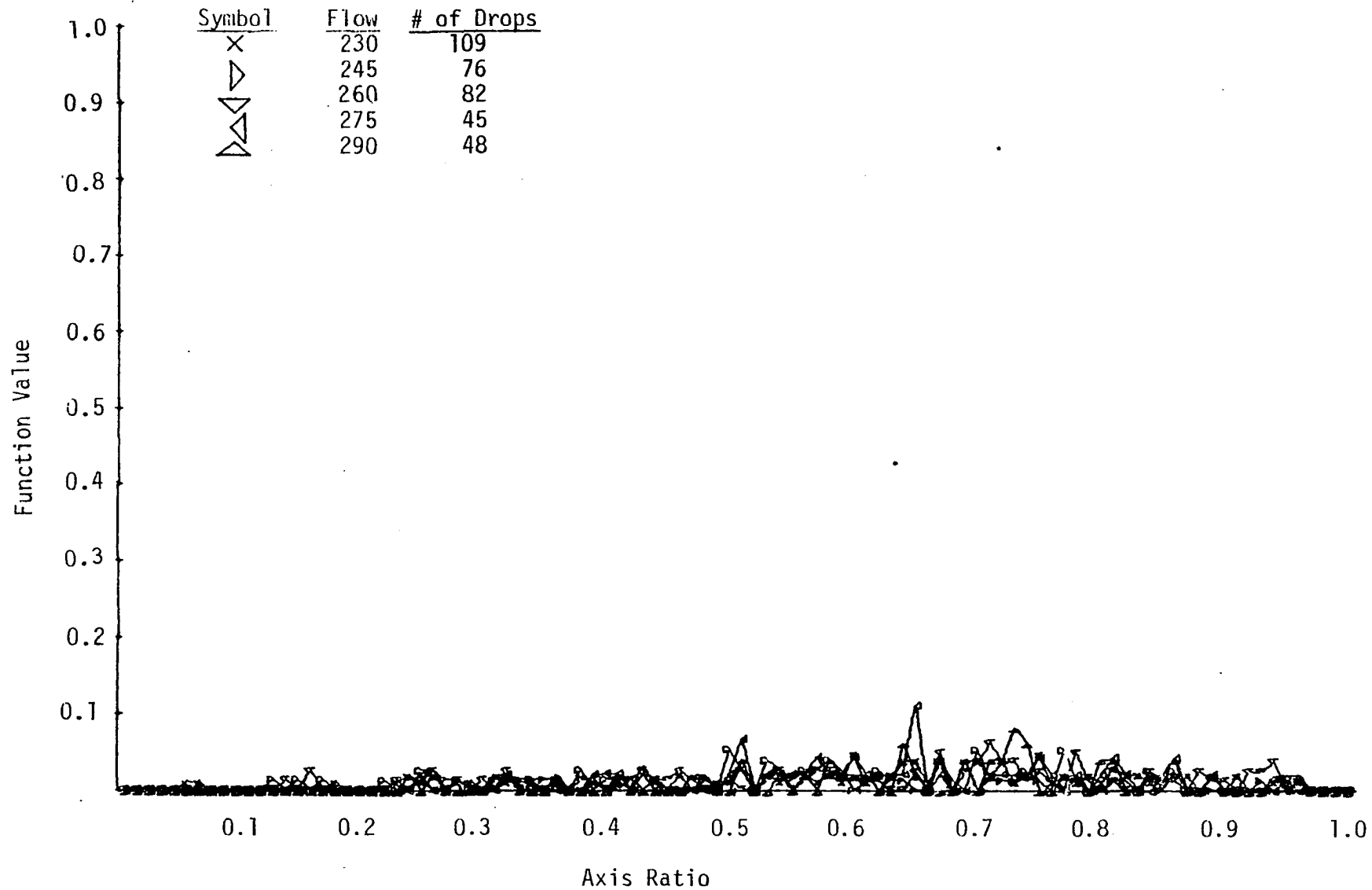
Figure 21a. The Function Value of the Axis Ratio Distribution (large droplets) of Flow Rate 2.
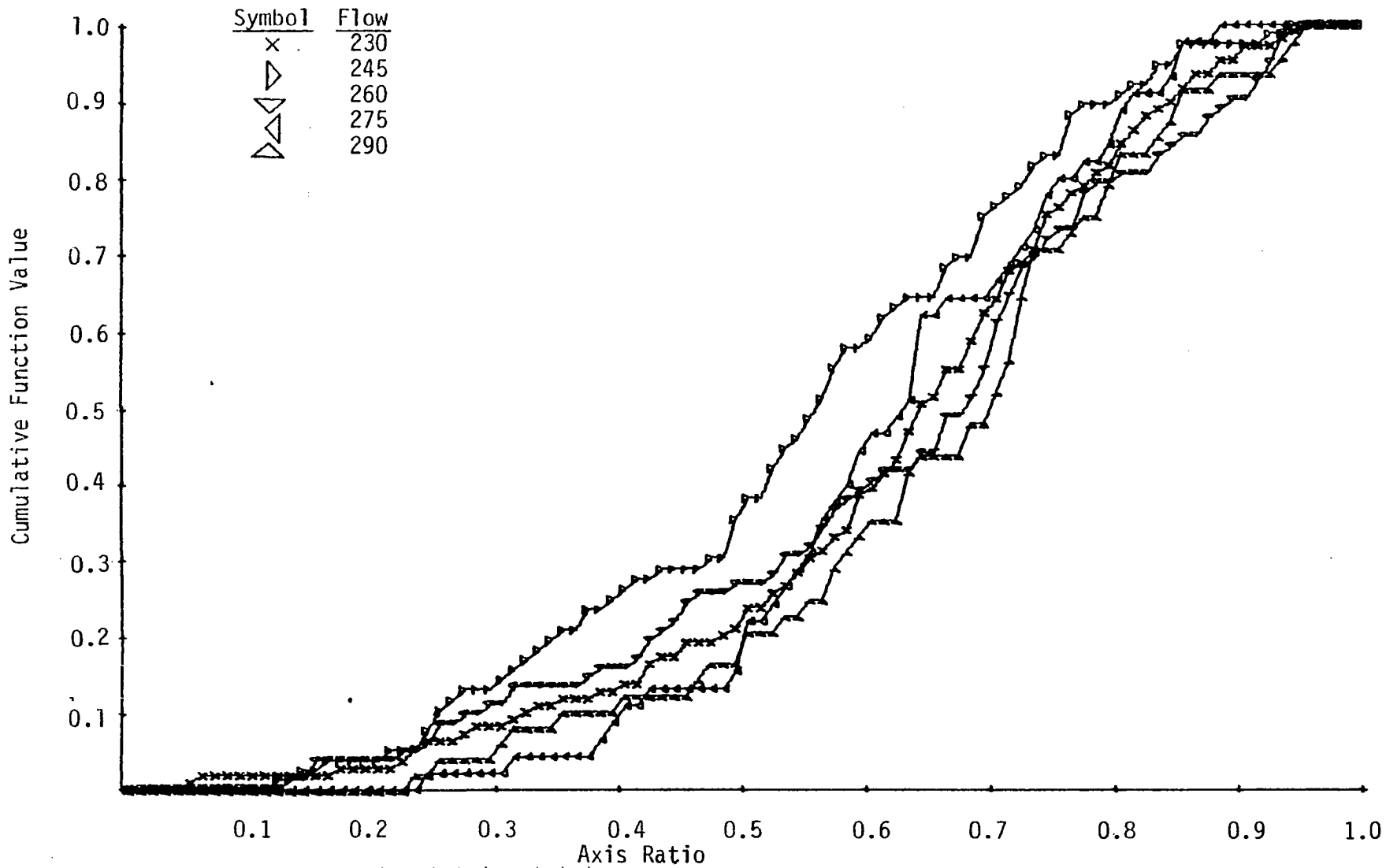
Figure 21b. The Cumulative Function of the Axis Ratio Distribution (large droplets) of Flow Rate 2.
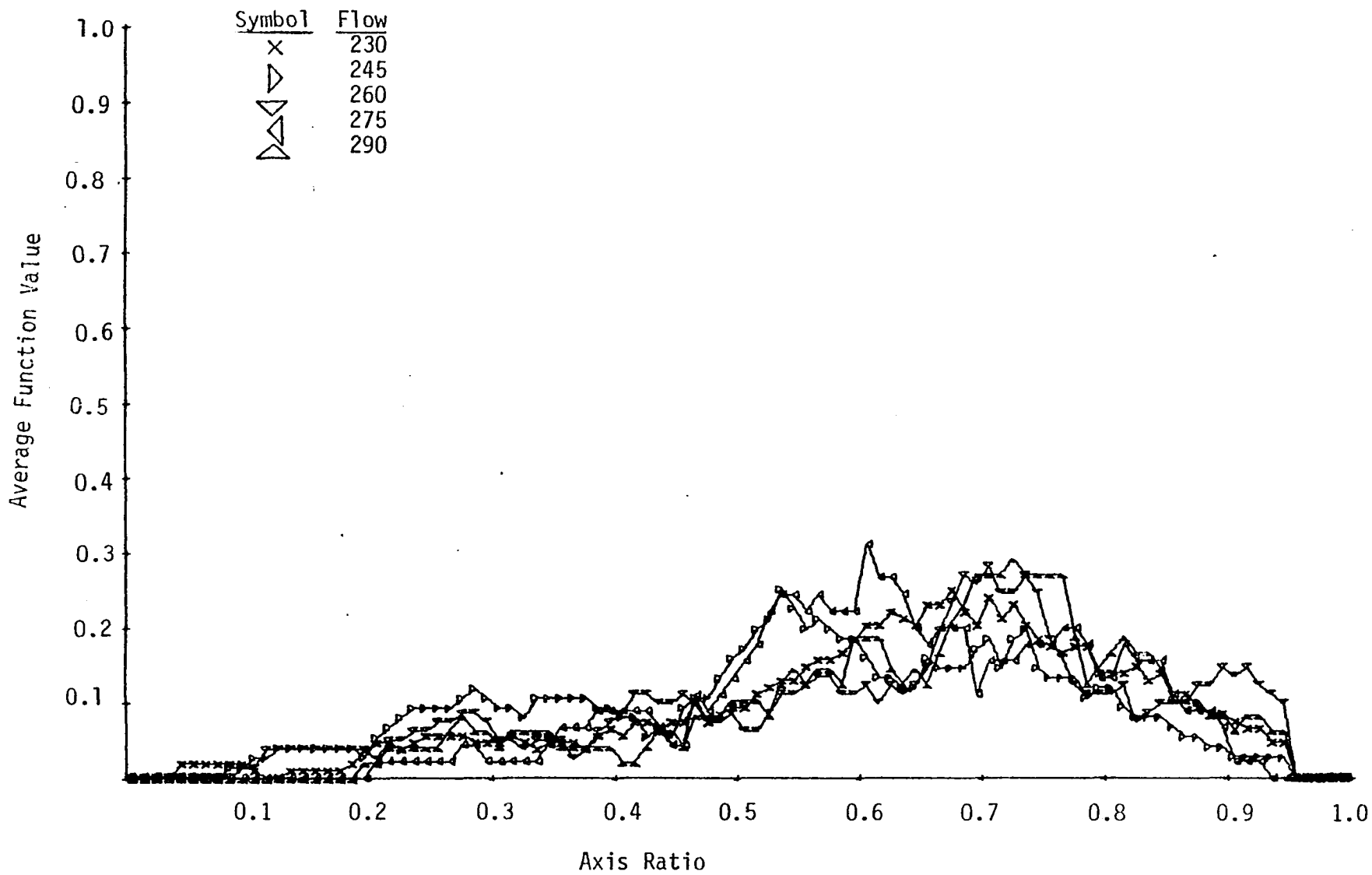
Figure 21c. The Average Function Value of the Axis Ratio Distribution (large droplets) of Flow Rate 2.
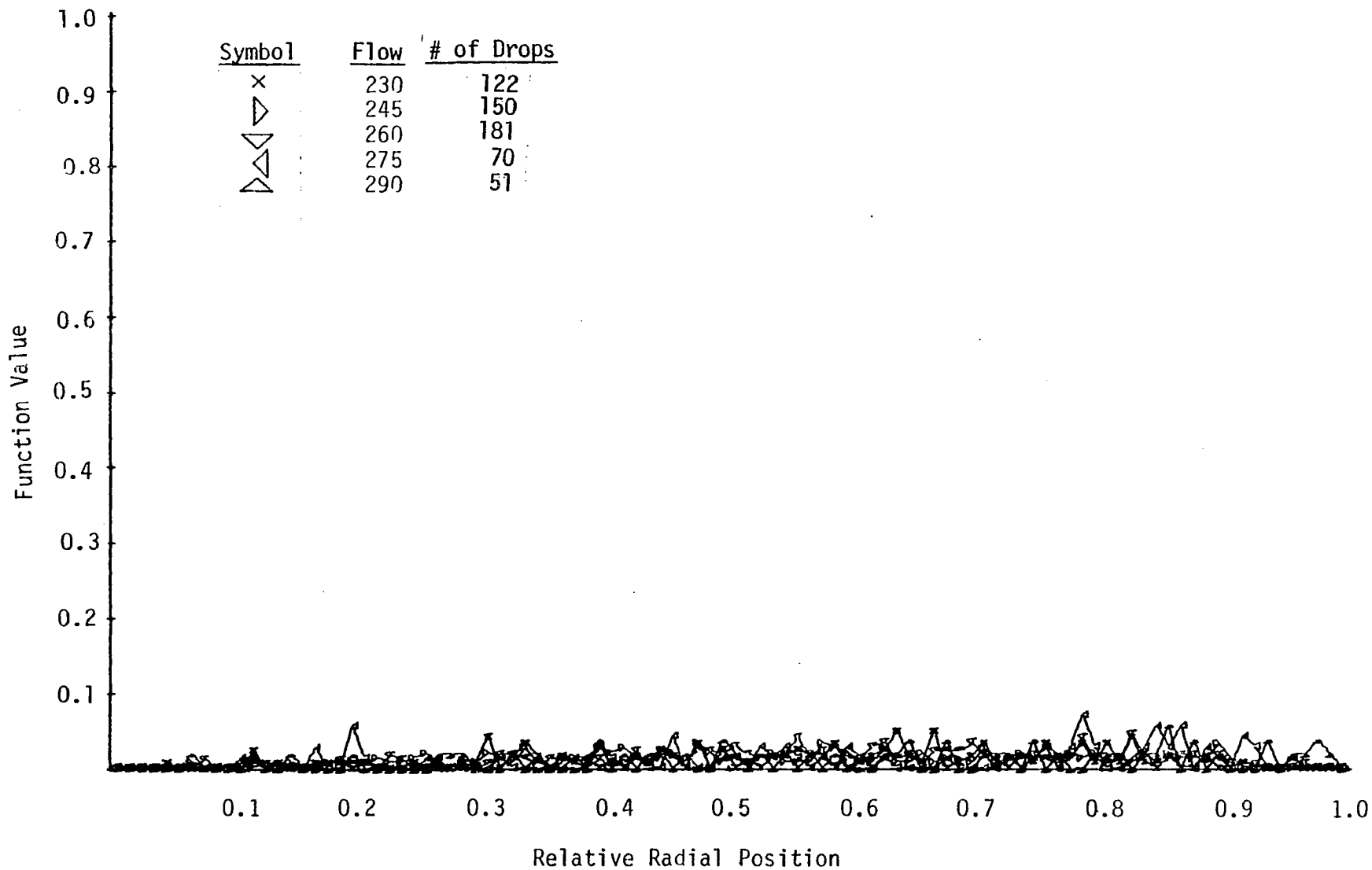
Figure 22a. The Function Value of the Relative Radial Position Distribution (constant radius increments) of Flow Rate 2.
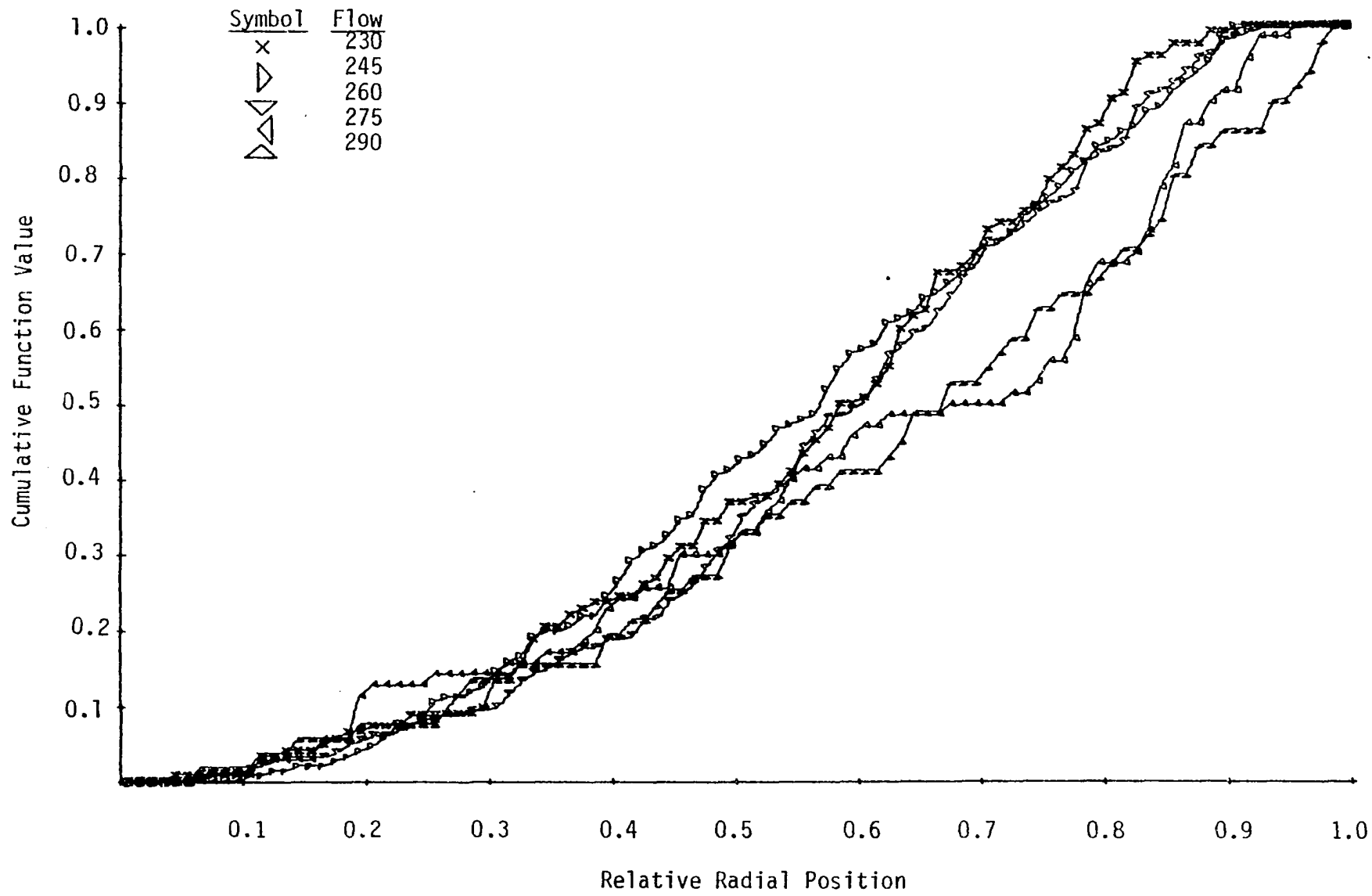
Figure 22b. The Cumulative Function Values of the Relative Radial Position Distribution

(constant radius increments) of Flow Rate 2.
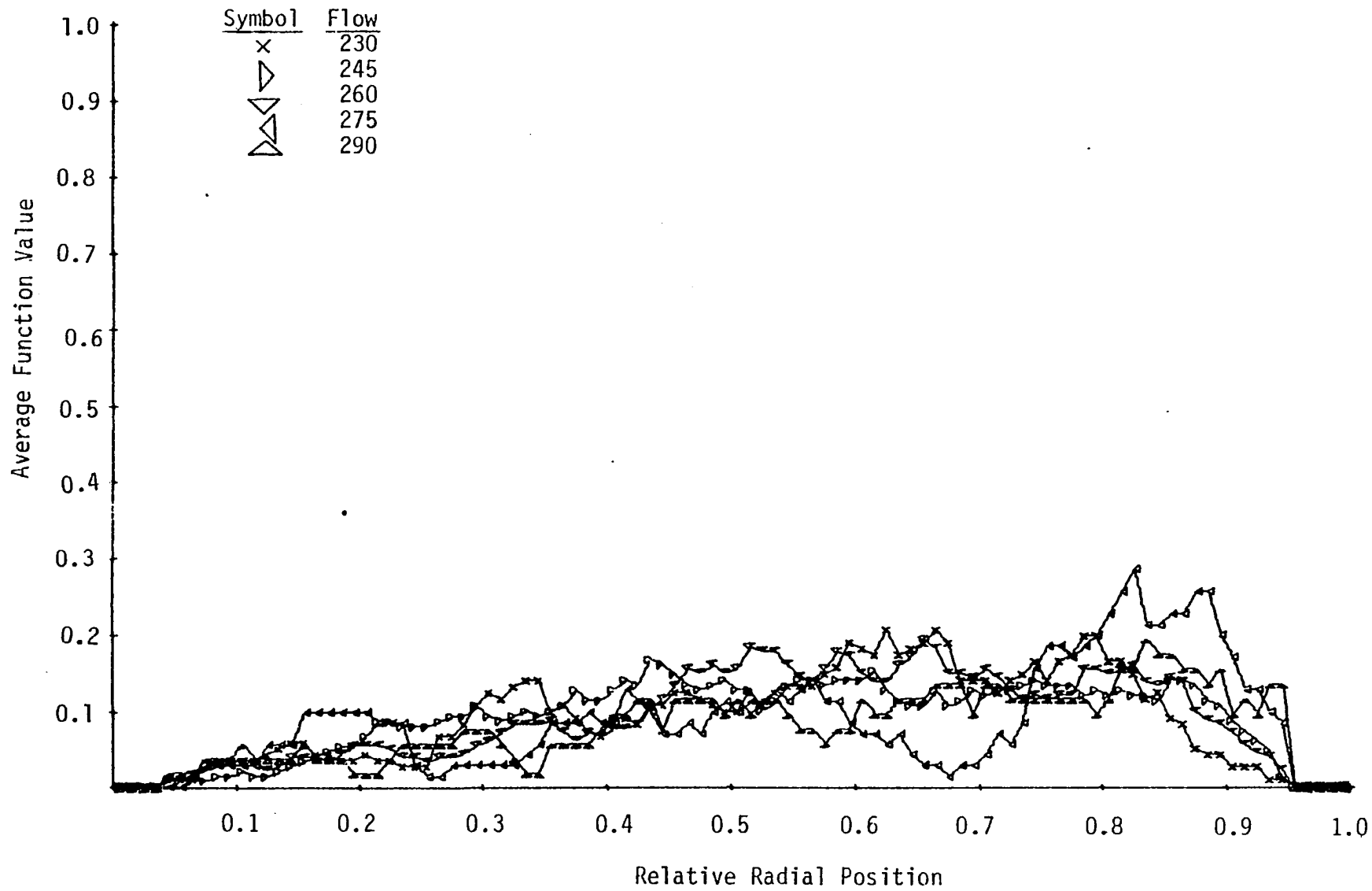
Figure 22c.   The Average Function Value of the Relative Radial Position Distribution

(constant radius increments) of Flow Rate 2.
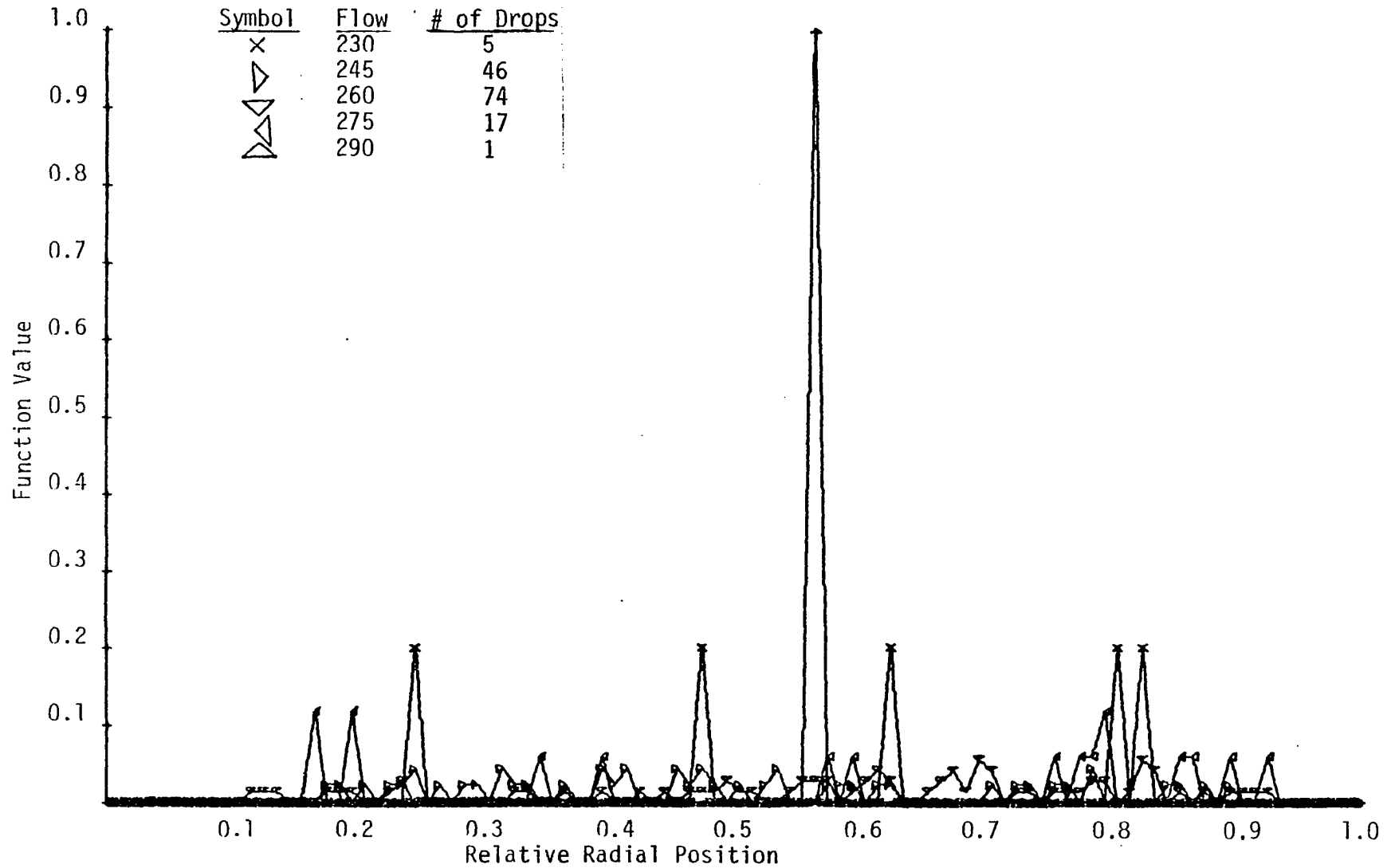
Figure 23a.   The Function Value of the Relative Radial Position Distribution (small droplets)

(constant radius increments) of Flow Rate 2.
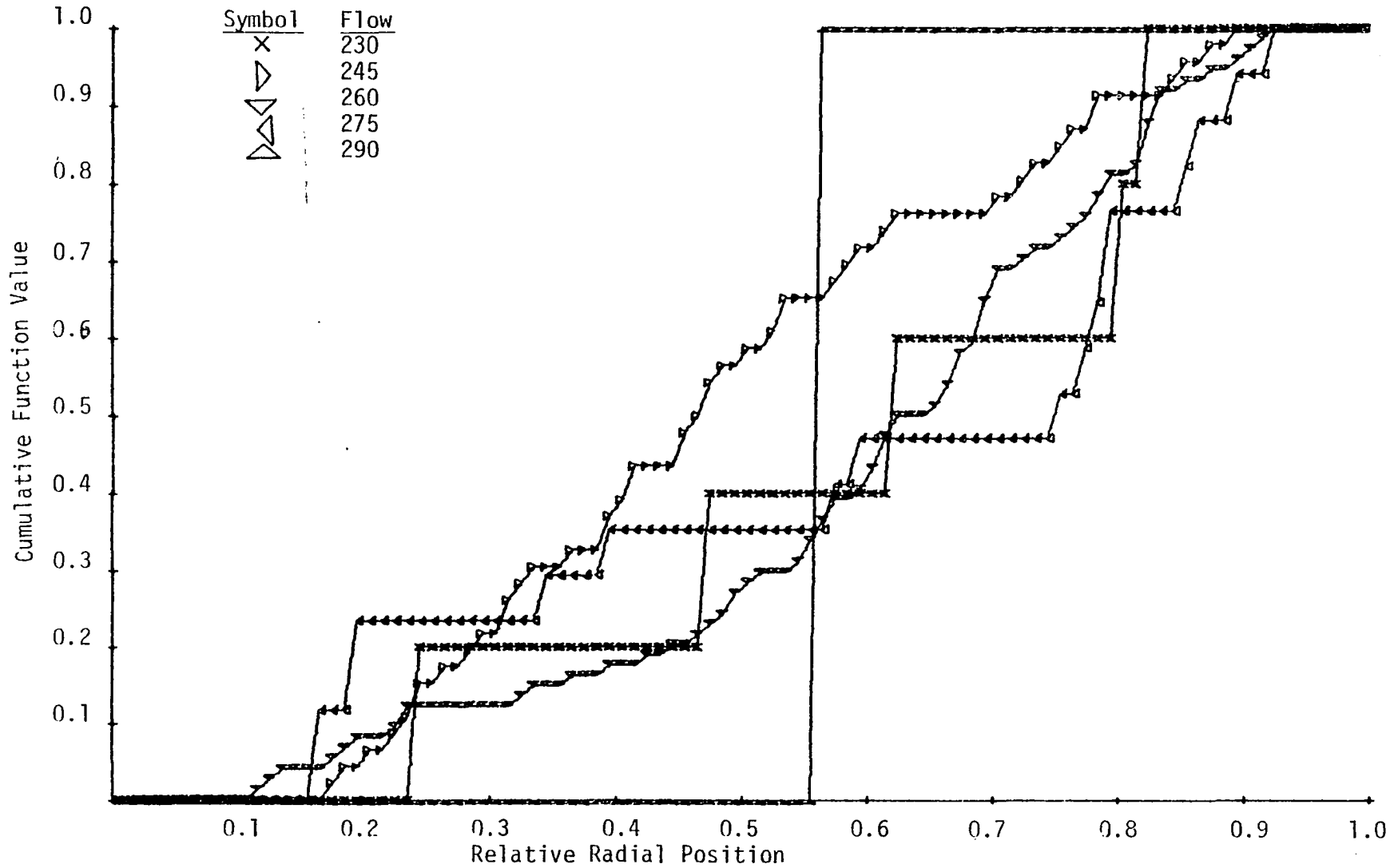
Figure 23b. The Cumulative Function Value of the Relative Radial Position Distribution (small droplets) (constant radius increments) of Flow Rate 2.
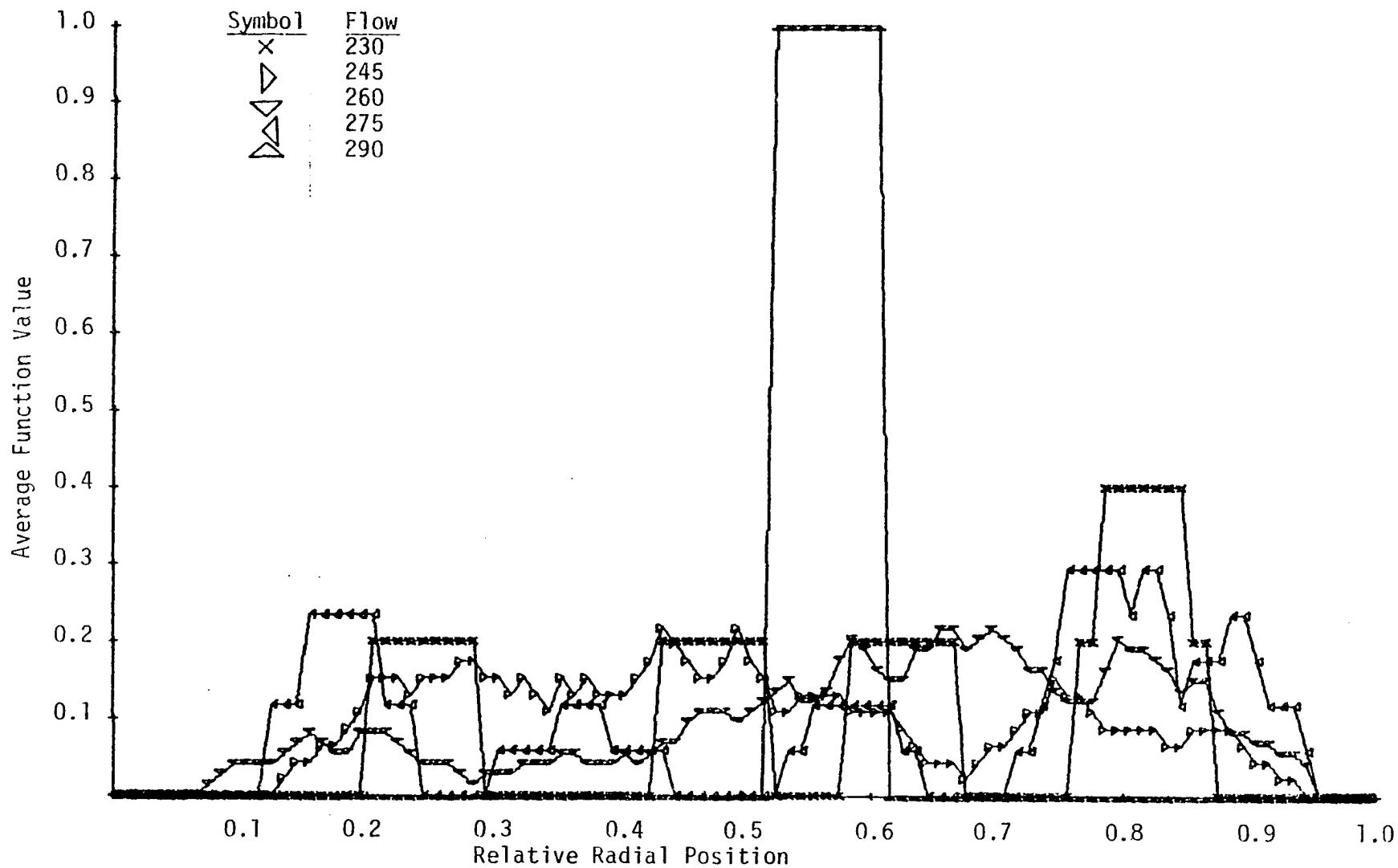
Figure 23c. The Average Function Value of the Relative Radial Position Distribution (small droplets) (constant radius increments) of Flow Rate 2.

Symbol	Flow	# of Drops
✕	230	117
▷	245	104
▽	260	107
◁	275	53
△	290	50

Function Value

0.1   0.2   0.3   0.4   0.5   0.6   0.7   0.8   0.9   0.1

Relative Radial Position
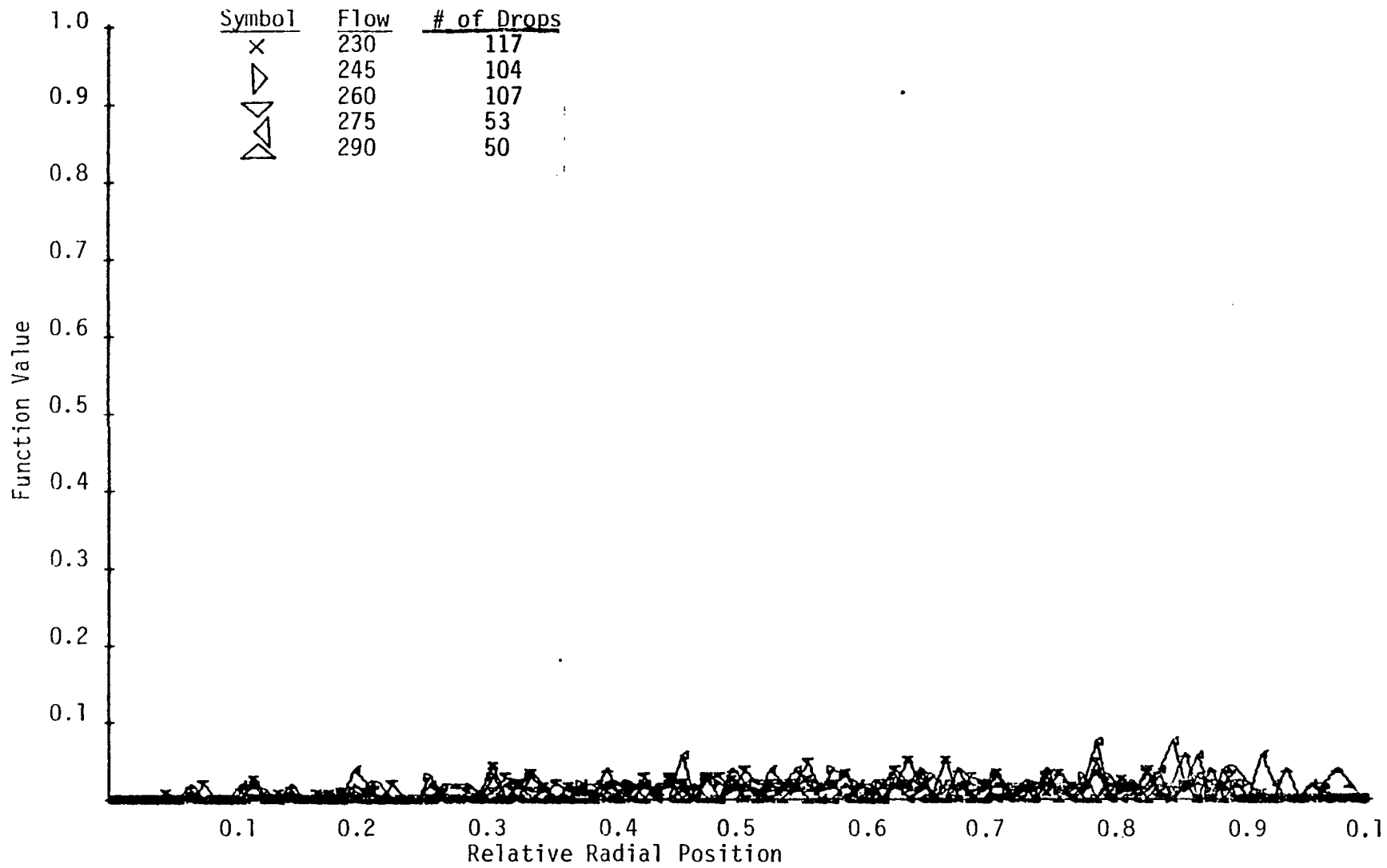
Figure 24a.   The Function Value of the Relative Radial Position Distribution (large droplets) (constant radius increments) of Flow Rate 2.

83
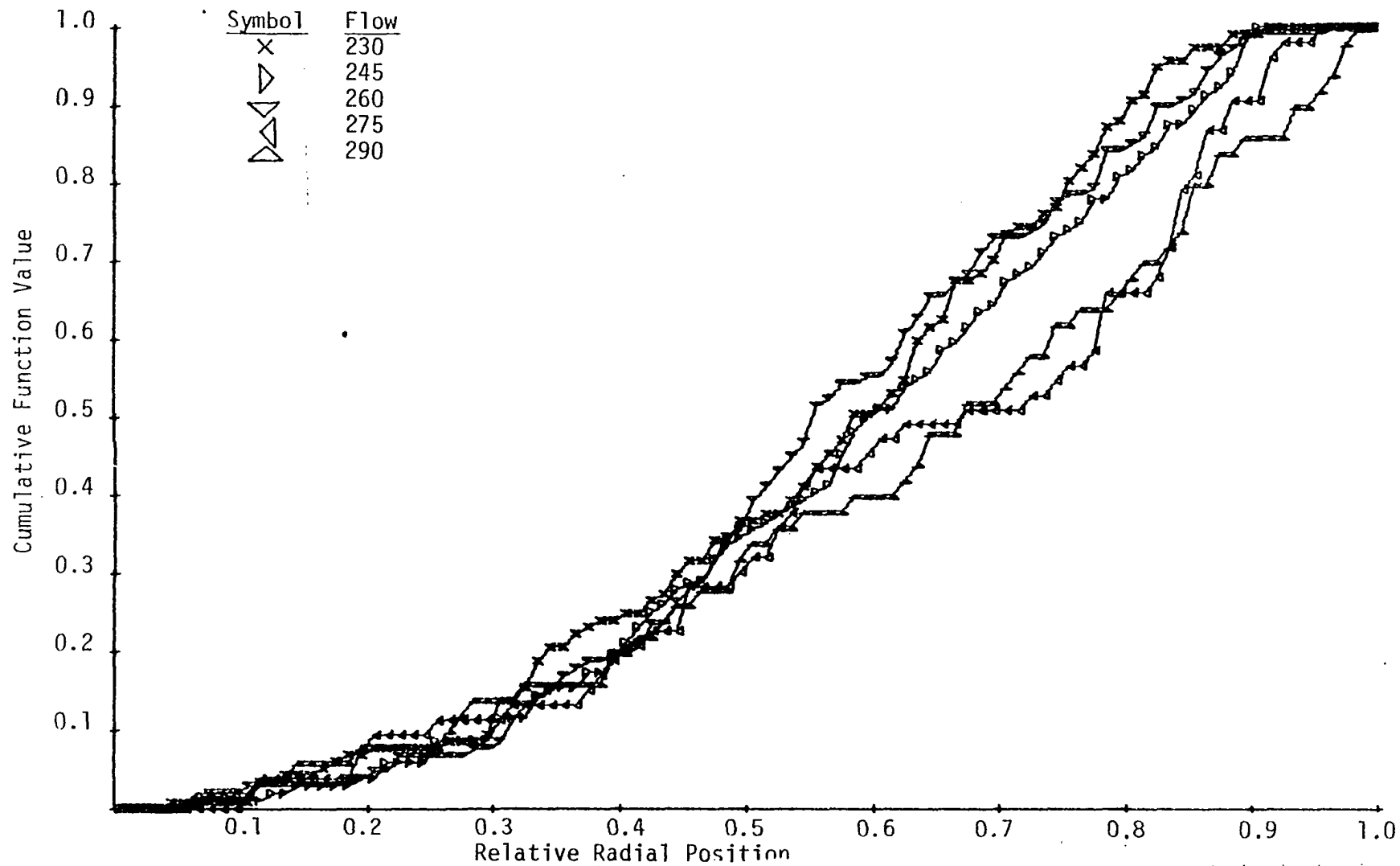
Figure 24b. The Cumulative Function Value of the Relative Radial Position Distribution (large droplets) (constant radius increments) of Flow Rate 2.
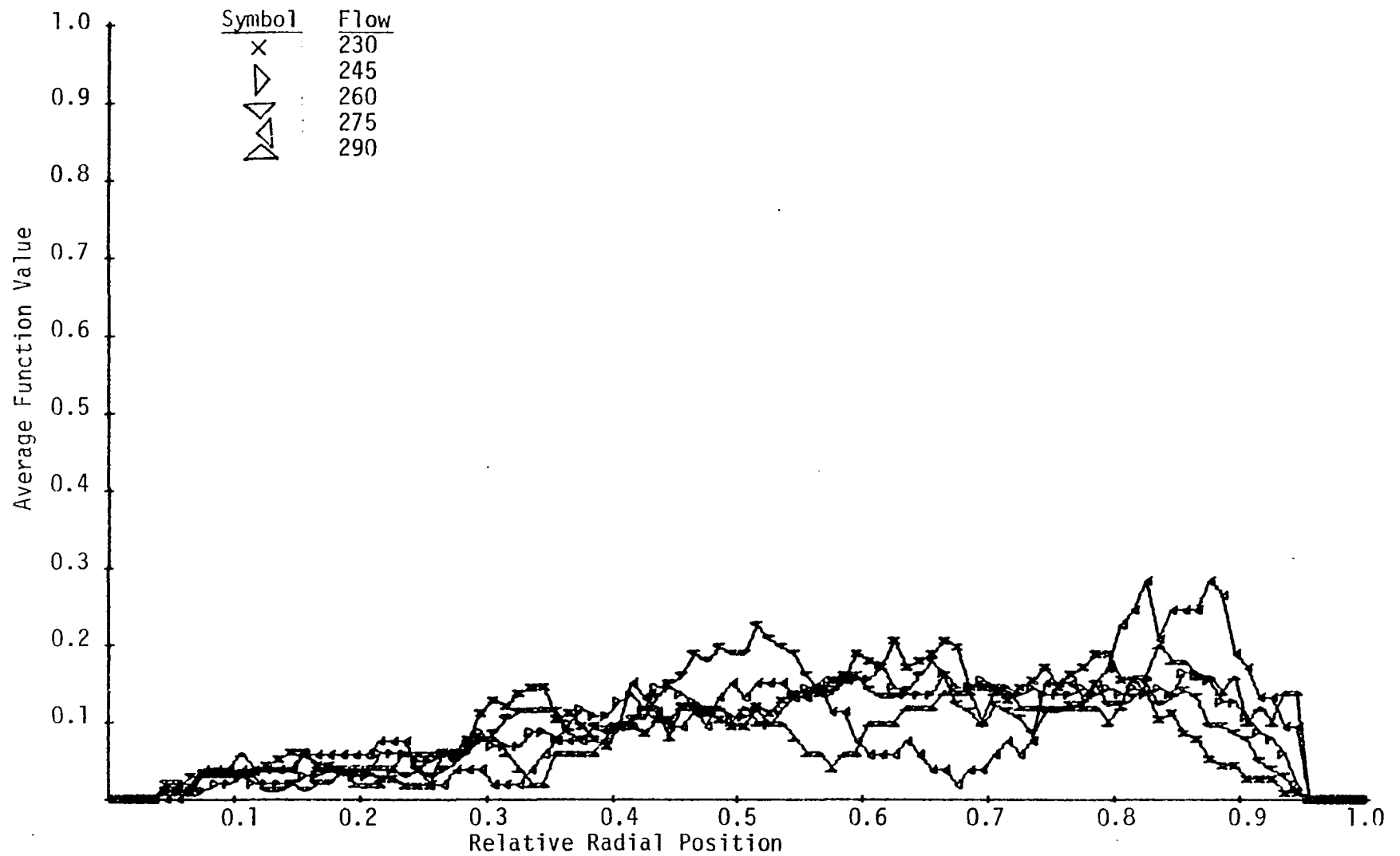
Figure 24c. The Average Function Value of the Relative Radial Position Distribution (large droplets) (constant radius increments) of Flow Rate 2.
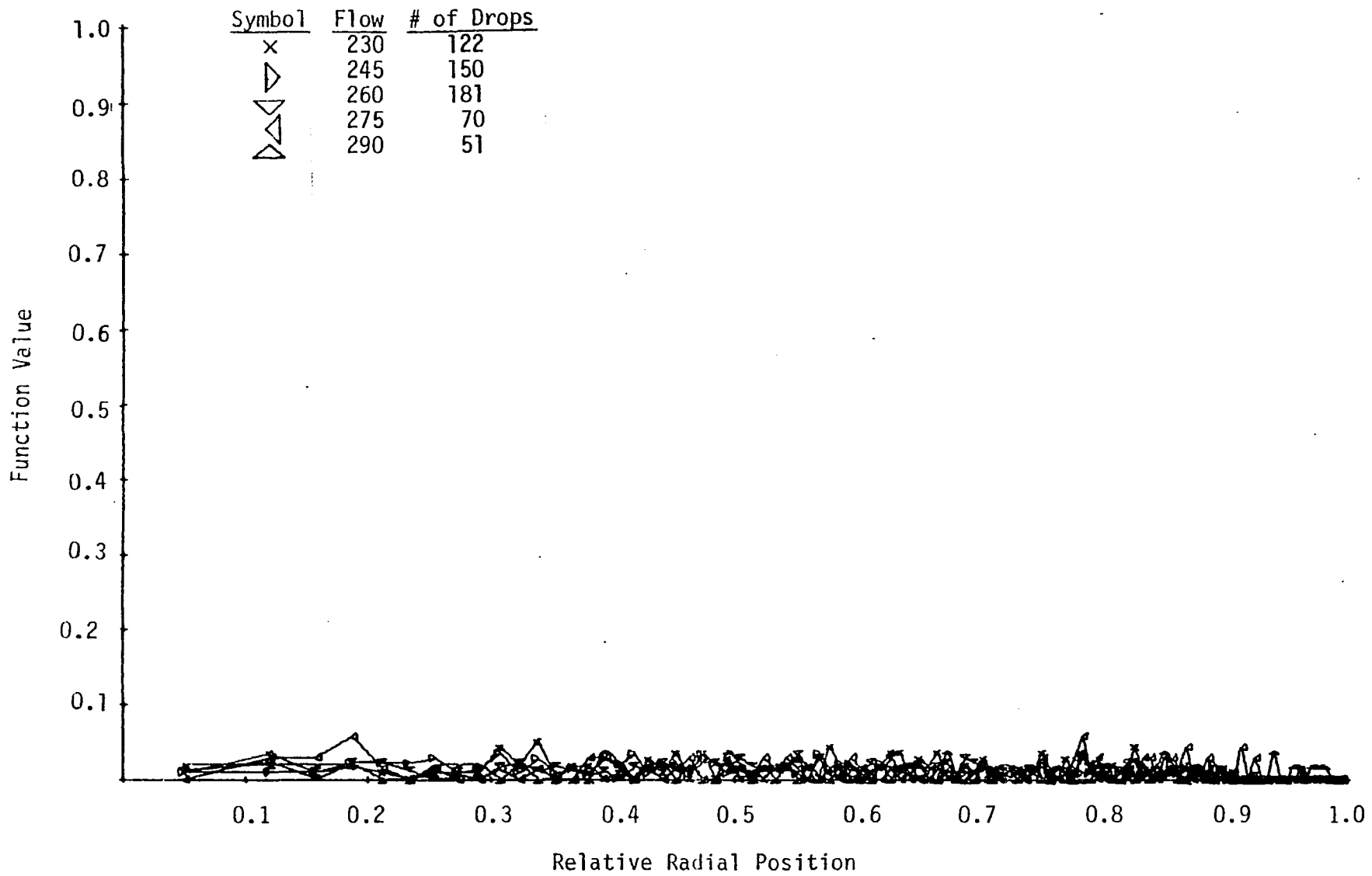
Figure 25a.   The Function Value of the Relative Radial Position Distribution

(constant area increments) of Flow Rate 2.
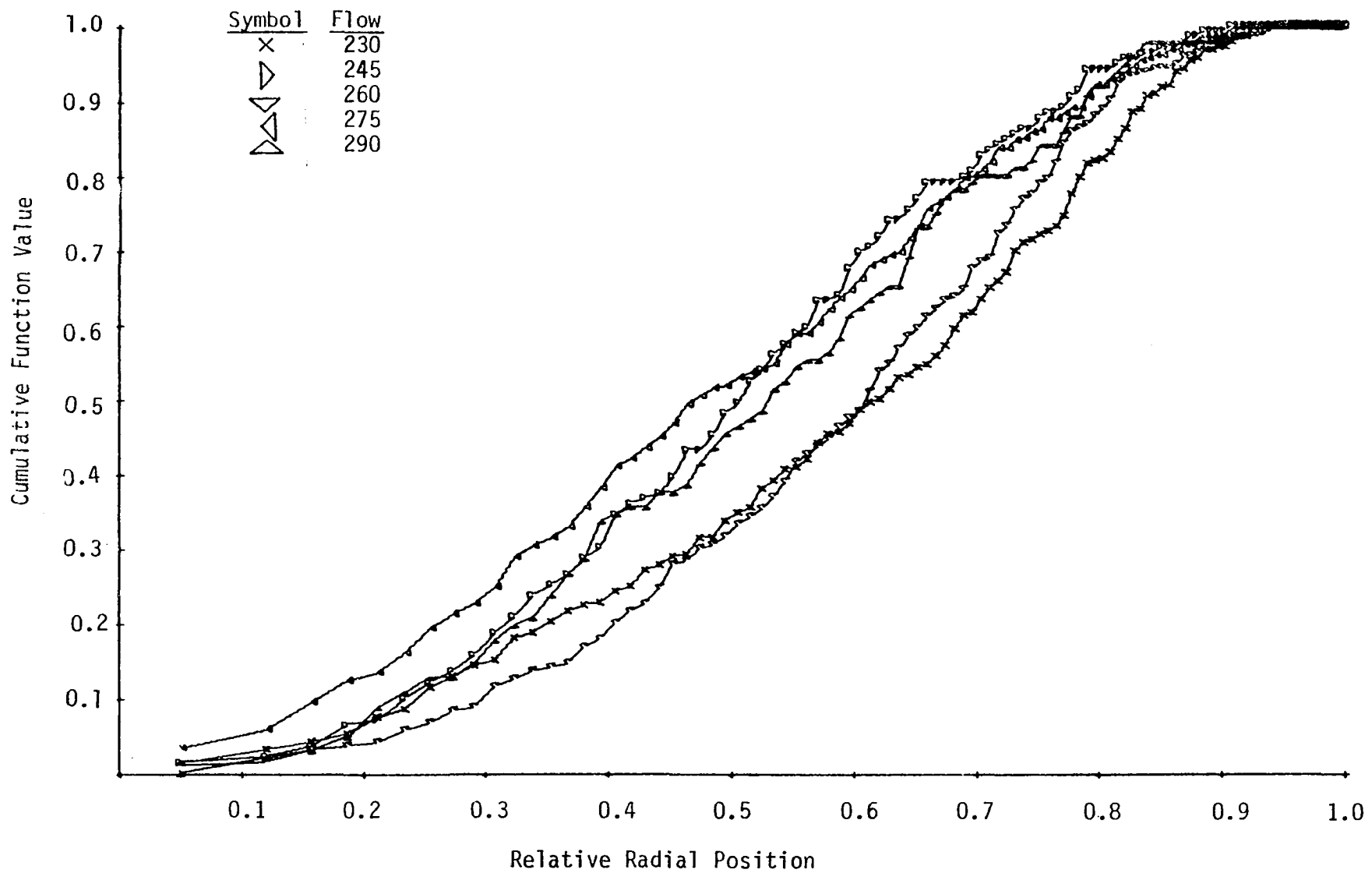
Figure 25b.   The Cumulative Function Value of the Radial Position Distribution
(constant area increments) of Flow Rate 2.
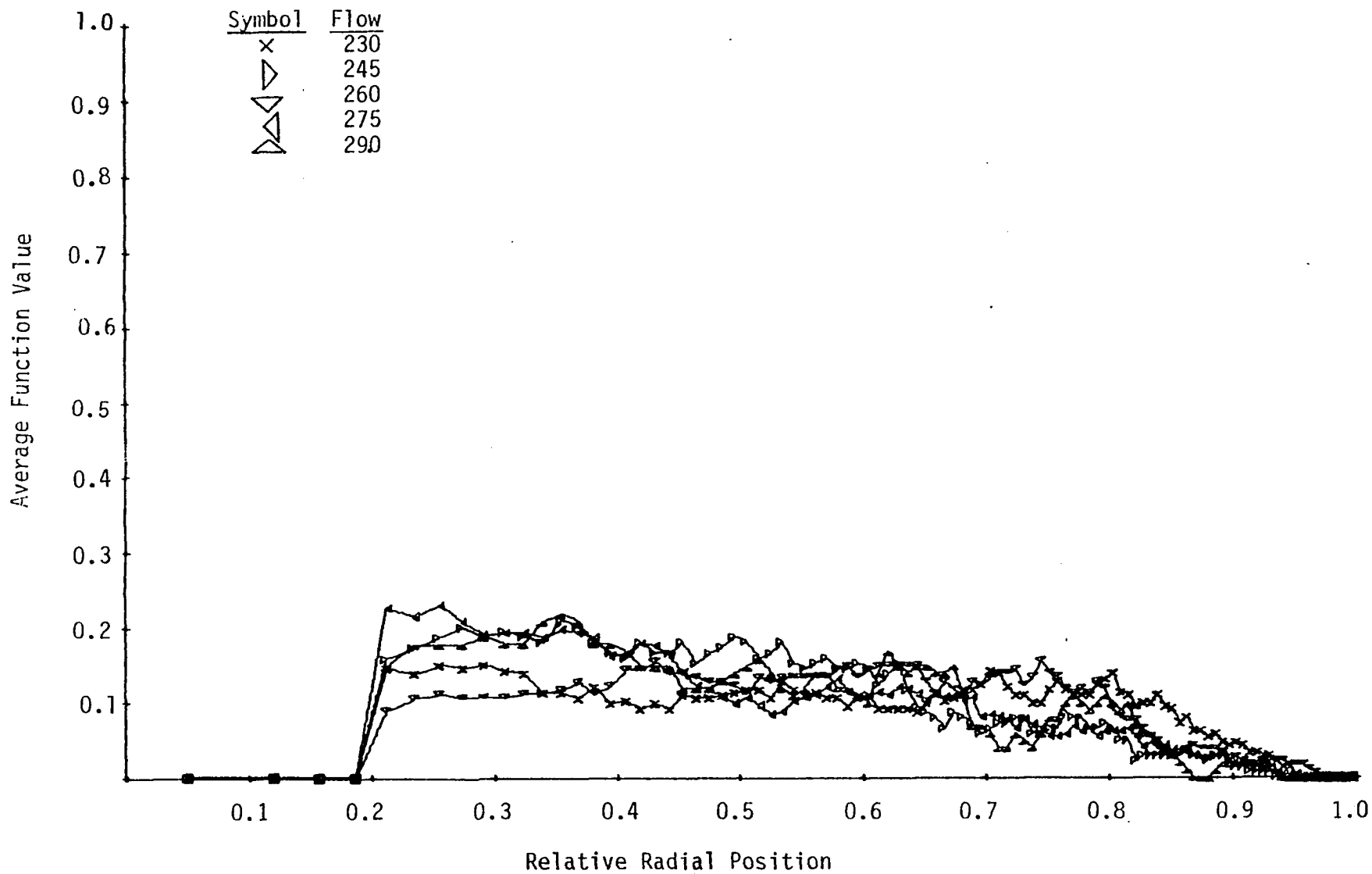
Figure 25c. The Average Function Value of the Relative Radial Position Distribution (constant area increments) of Flow Rate 2.
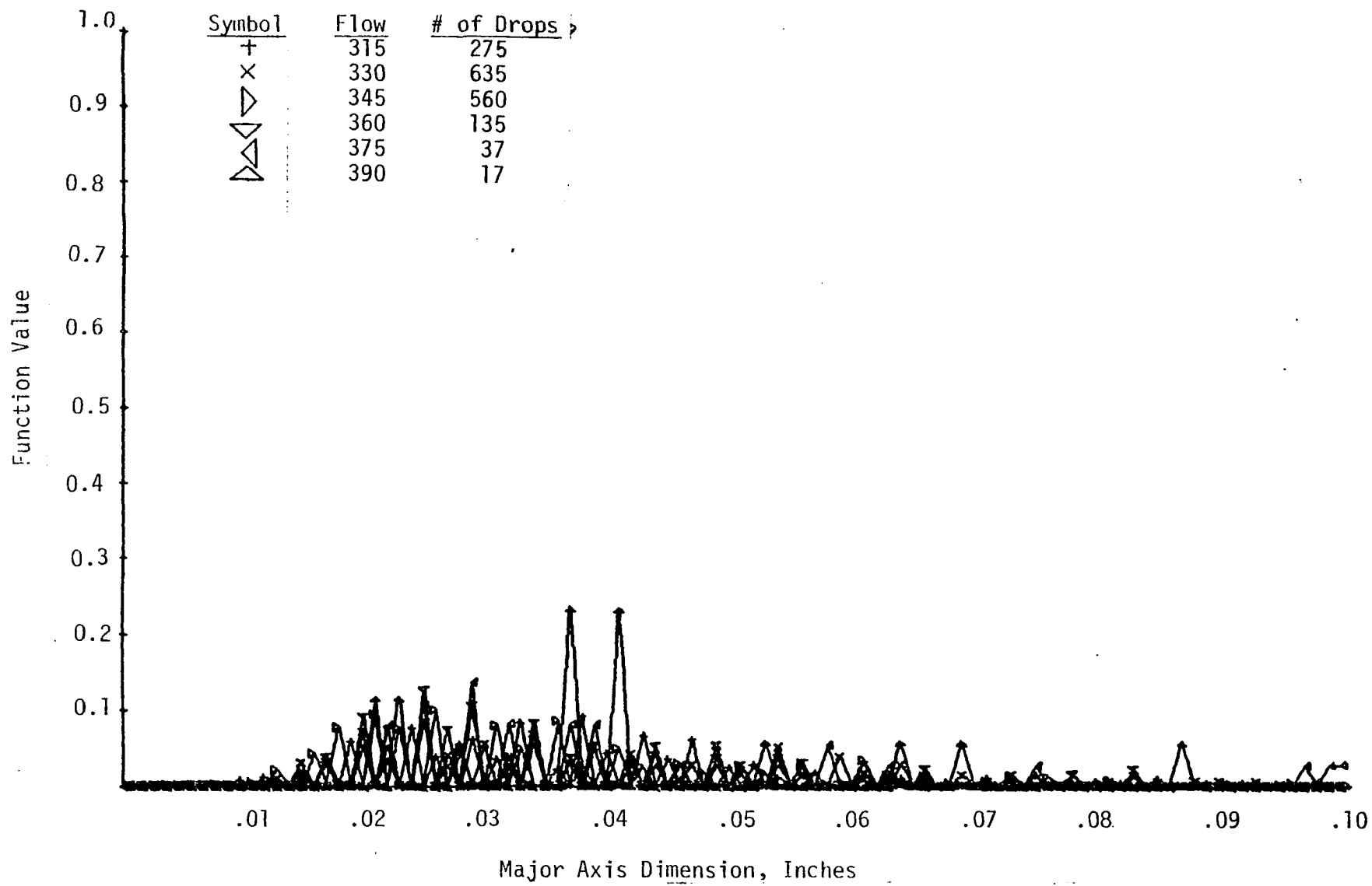
Figure 26a.   The Function Value of the Major Axis Distribution of Flow Rate 3.

The plot legend reads:

Symbol	Flow	# of Drops
+	315	275
×	330	635
▷	345	560
▽	360	135
◁	375	37
△	390	17
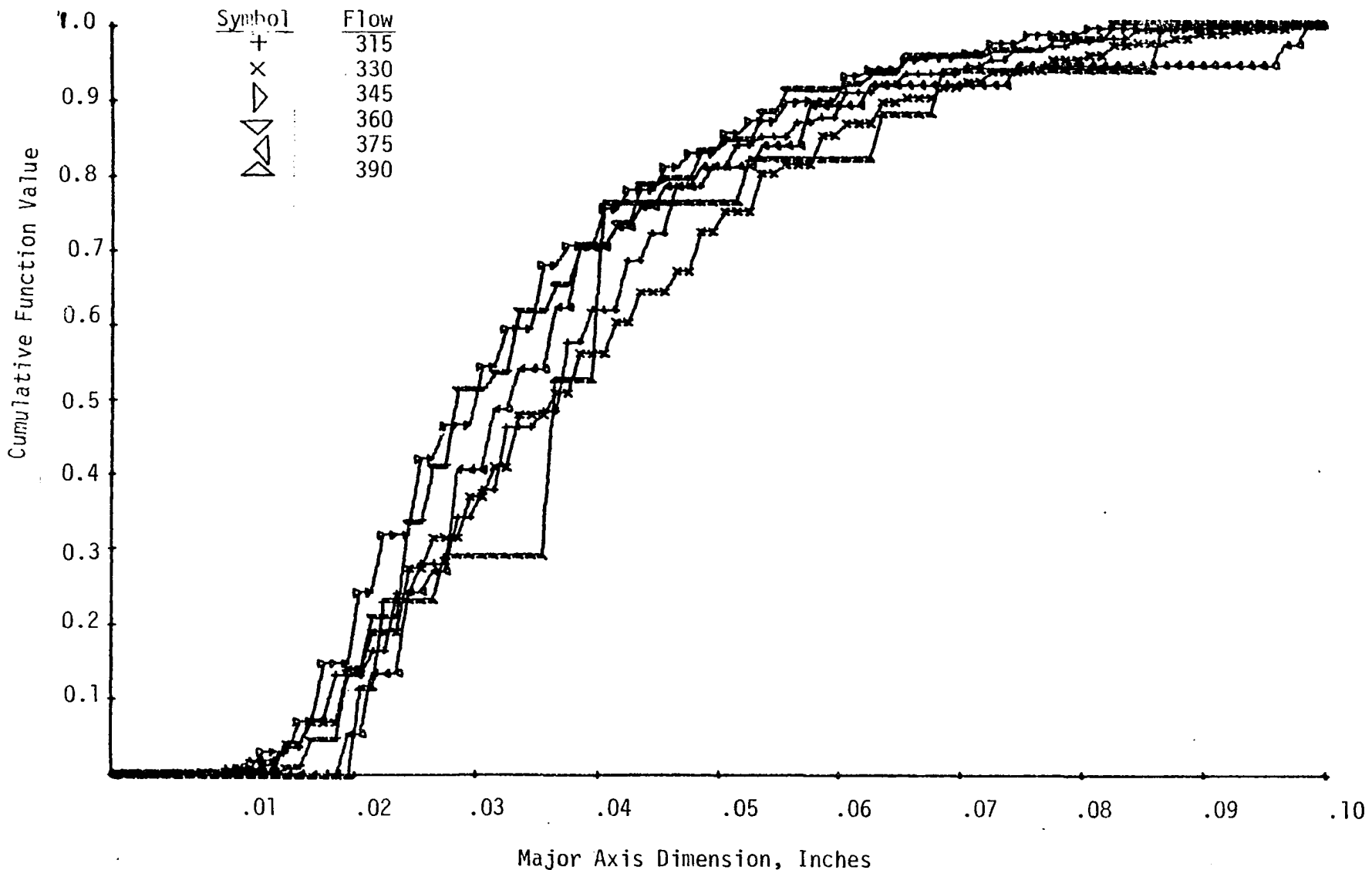
Figure 26b. The Cumulative Function Value of the Major Axis Distribution of Flow Rate 3.
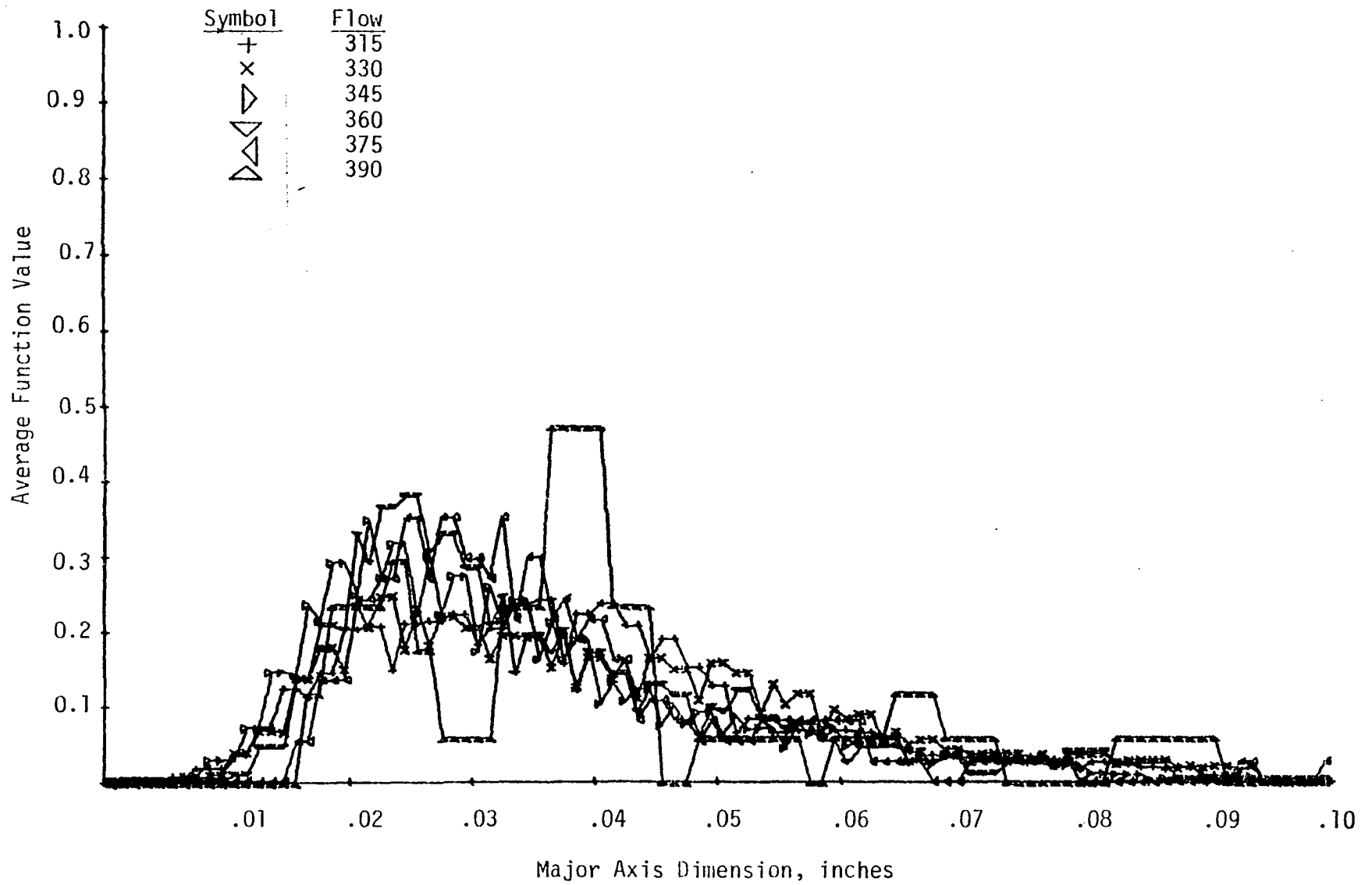
Figure 26c. The Average Function Value of the Major Axis Distribution of Flow Rate 3.

I6
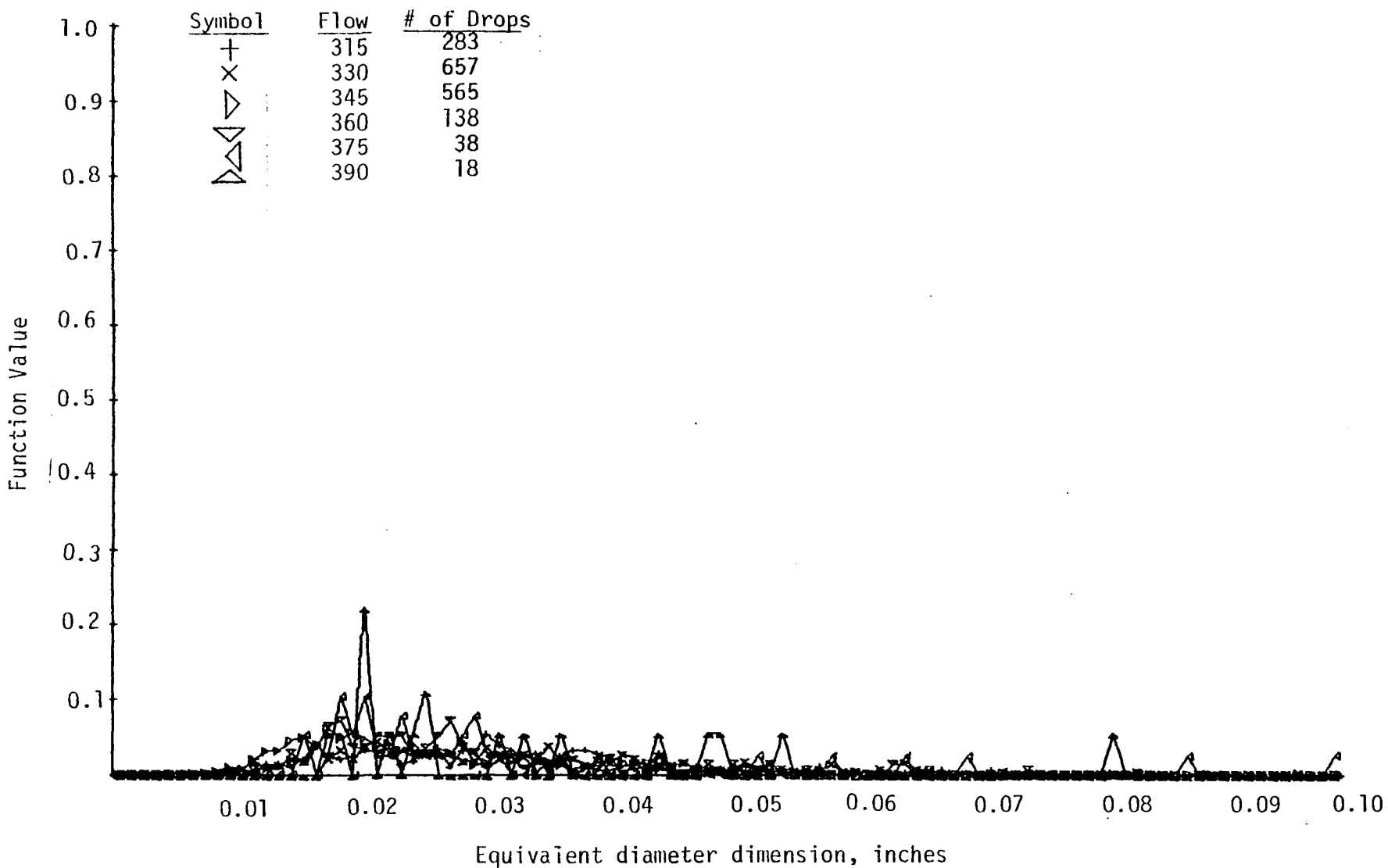
Figure 27a.   The Function Value of the Equivalent Diameter Distribution (small droplets) of Flow Rate 3.
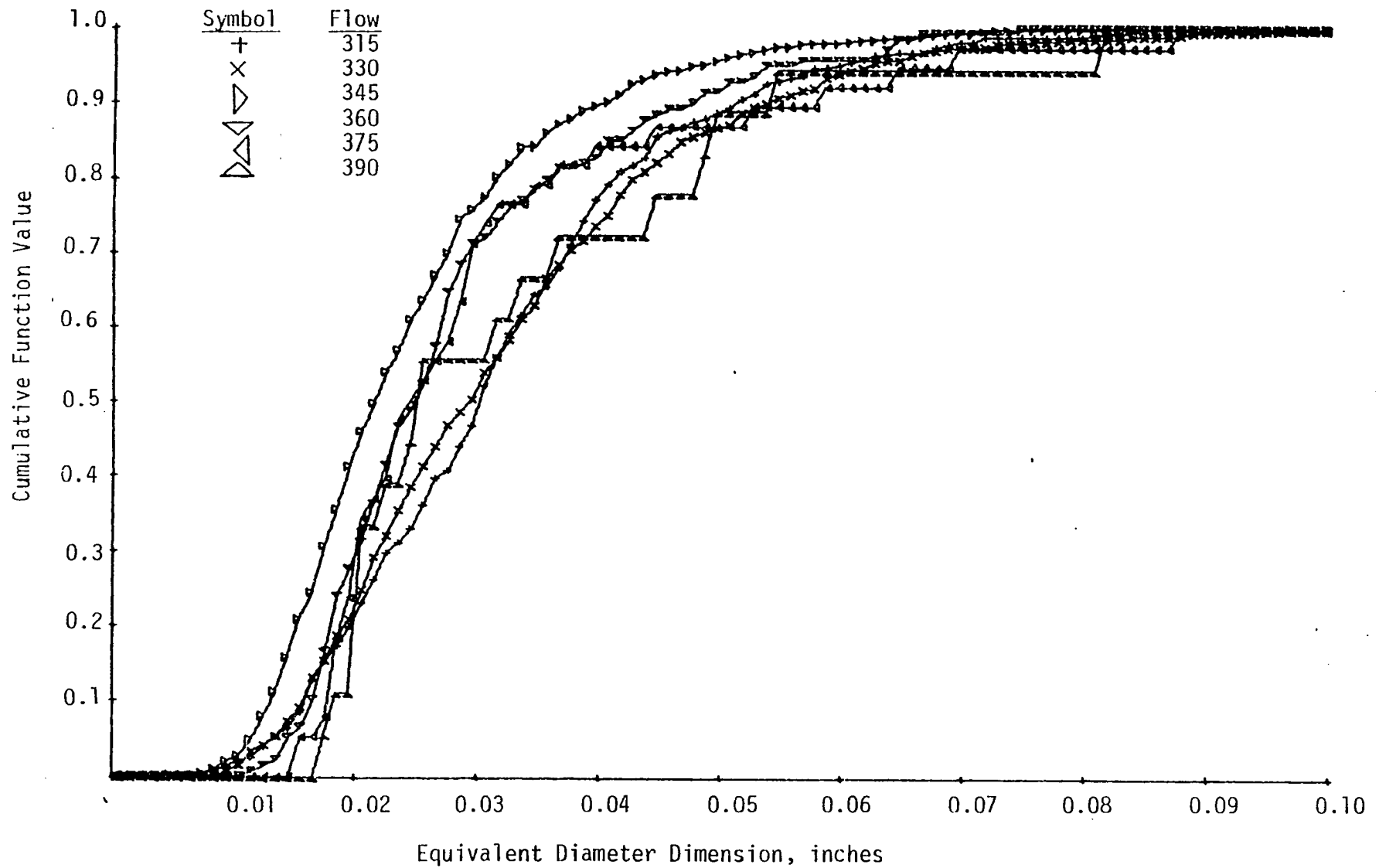
Figure 27b. The Cumulative Function Value of the Equivalent Diameter Distribution (small droplets) of Flow Rate 3.

93
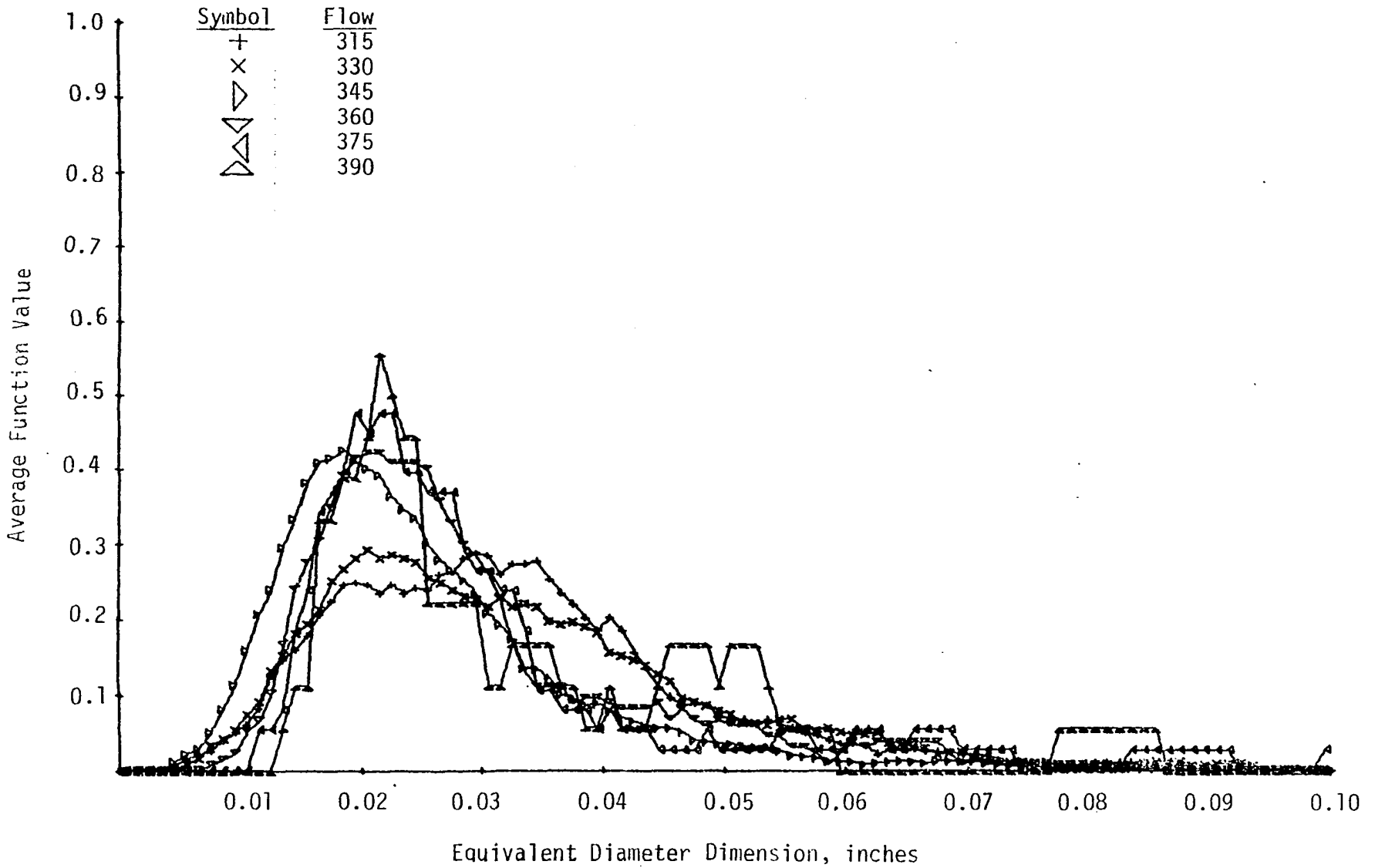
Figure 27c. The Average Function Value of The Equivalent Diameter Distribution (small droplets) of Flow Rate 3.

Symbol	Flow	# of Drops
+	315	277
×	330	647
▷	345	558
▽	360	132
◁	375	37
△	390	16
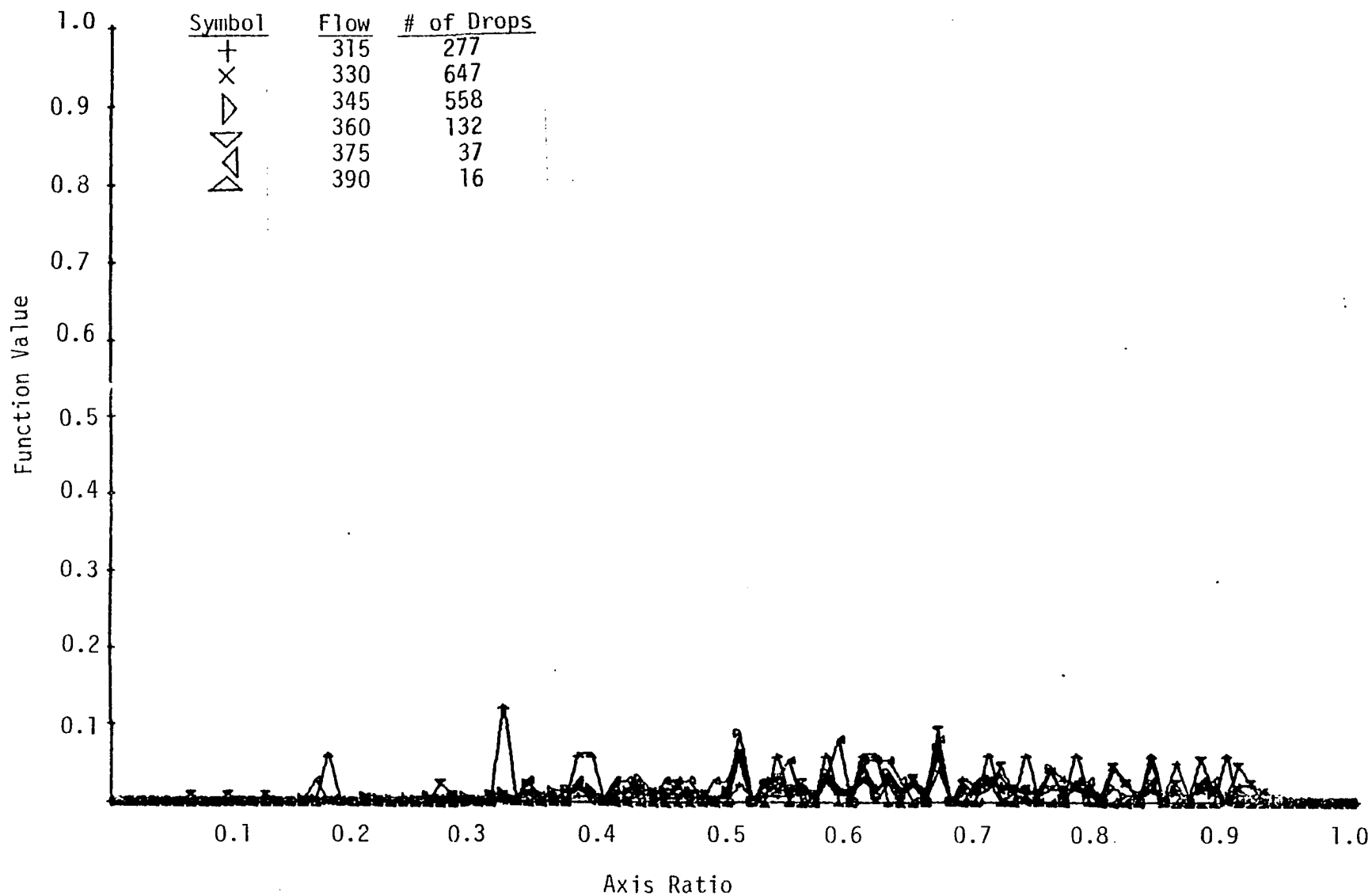
Figure 28a. The Function Value of the Axis Ratio Distribution of Flow Rate 3.
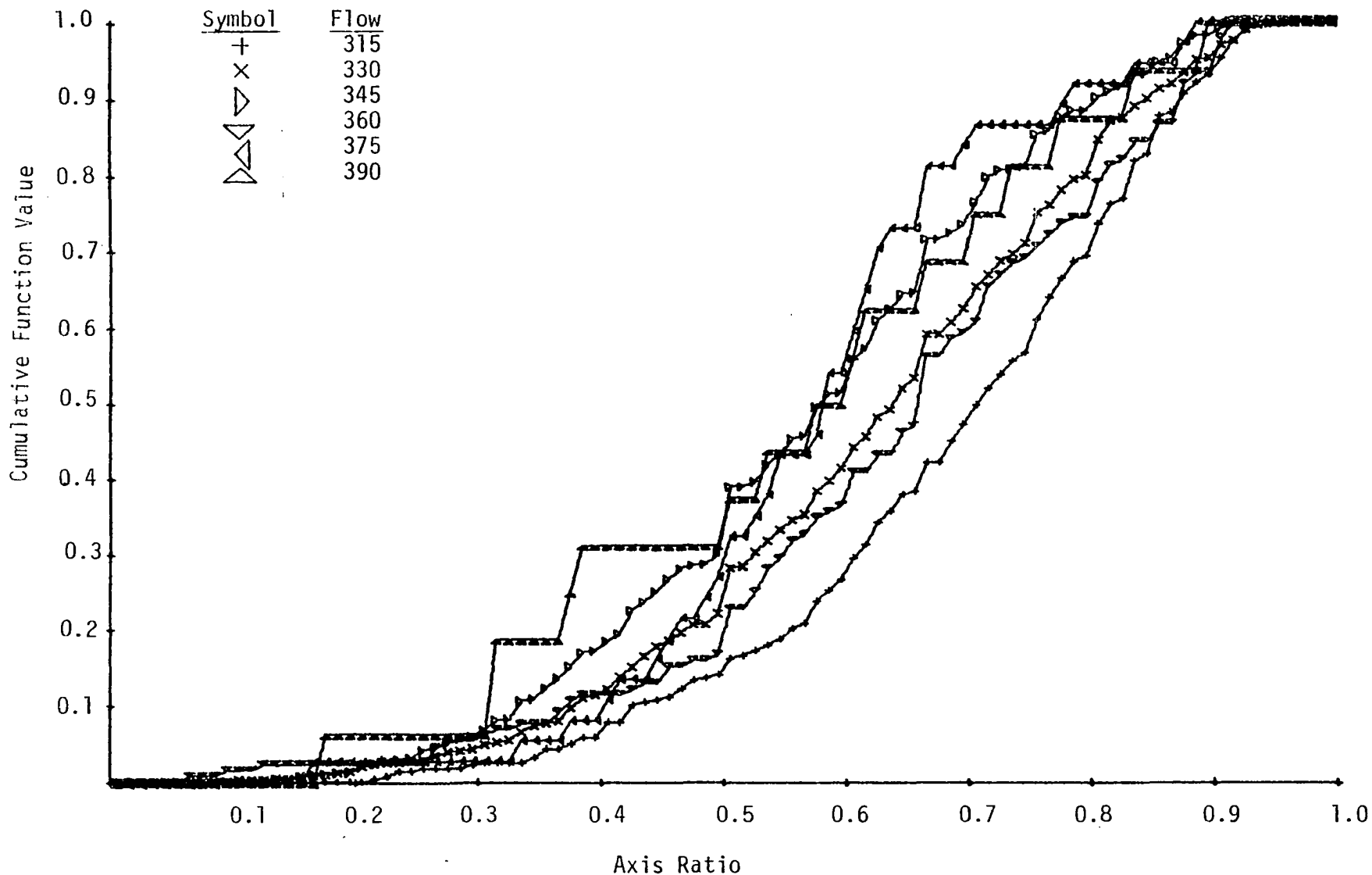
Figure 28b. The Cumulative Function Value of the Axis Ratio Distribution of Flow Rate 3.
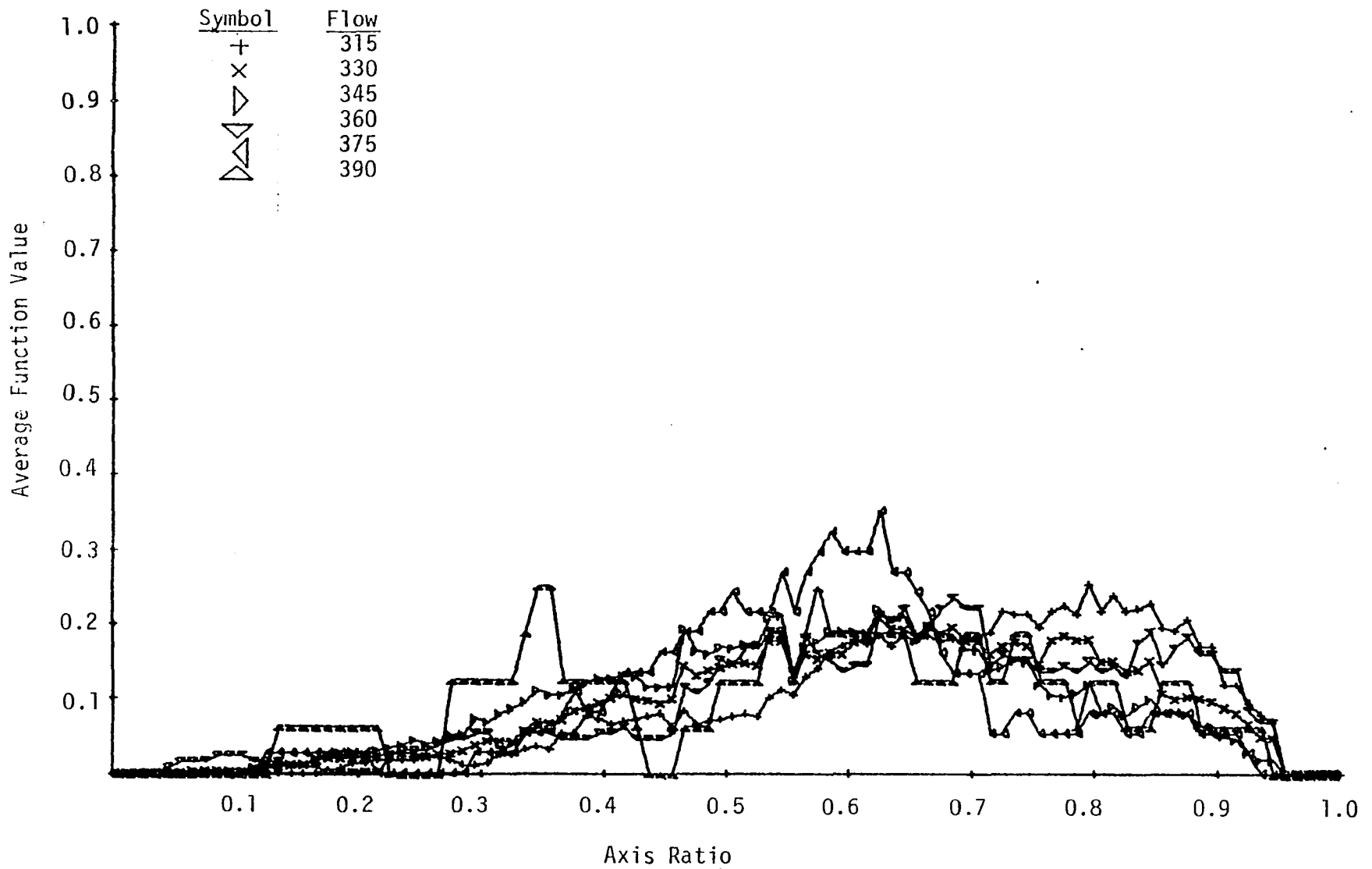
Figure 28c. The Average Function Value of The Axis Ratio Distribution of Flow Rate 3.
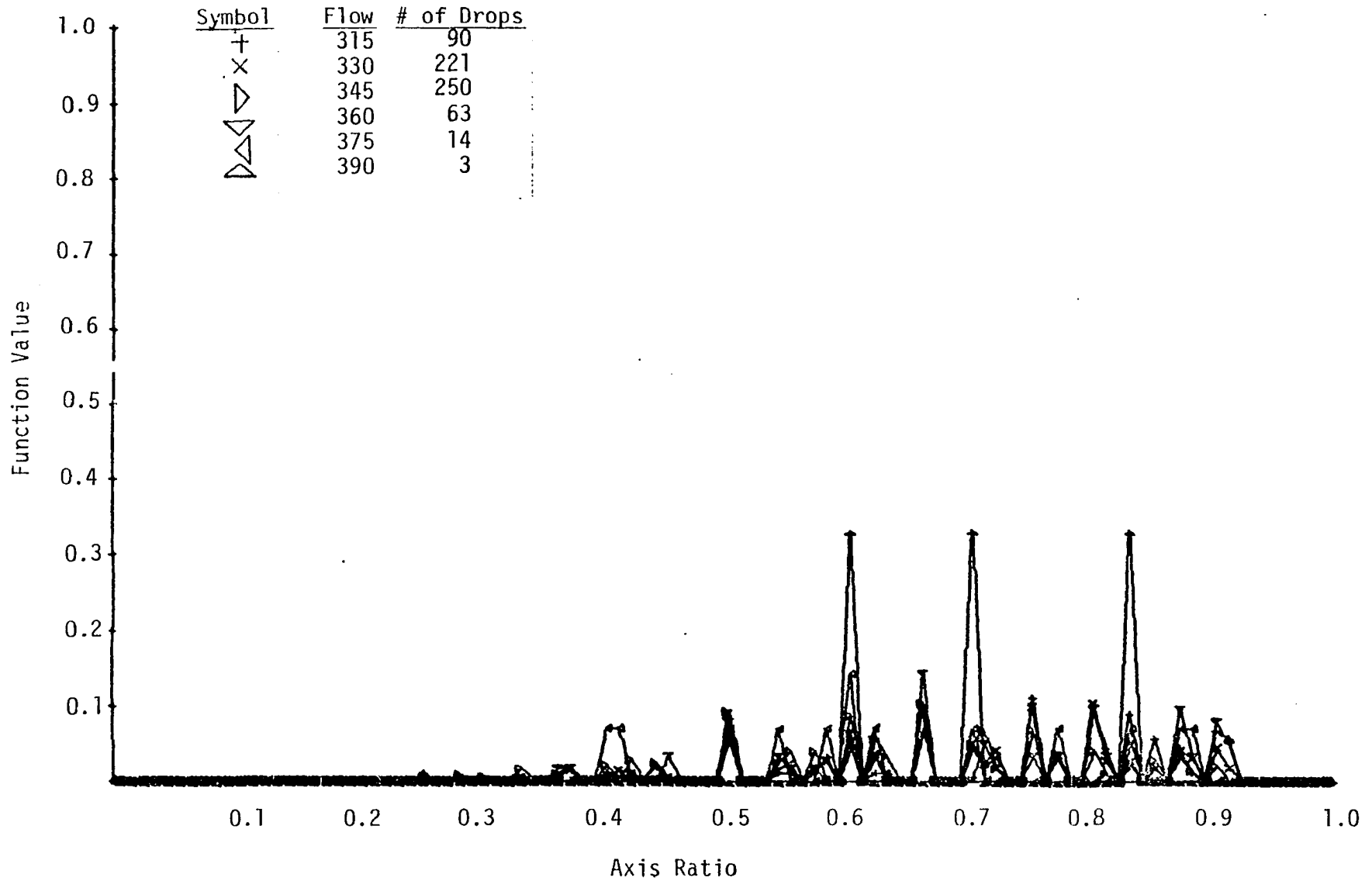
Figure 29a. The Function Value of the Axis Ratio Distribution of Flow Rate 3.
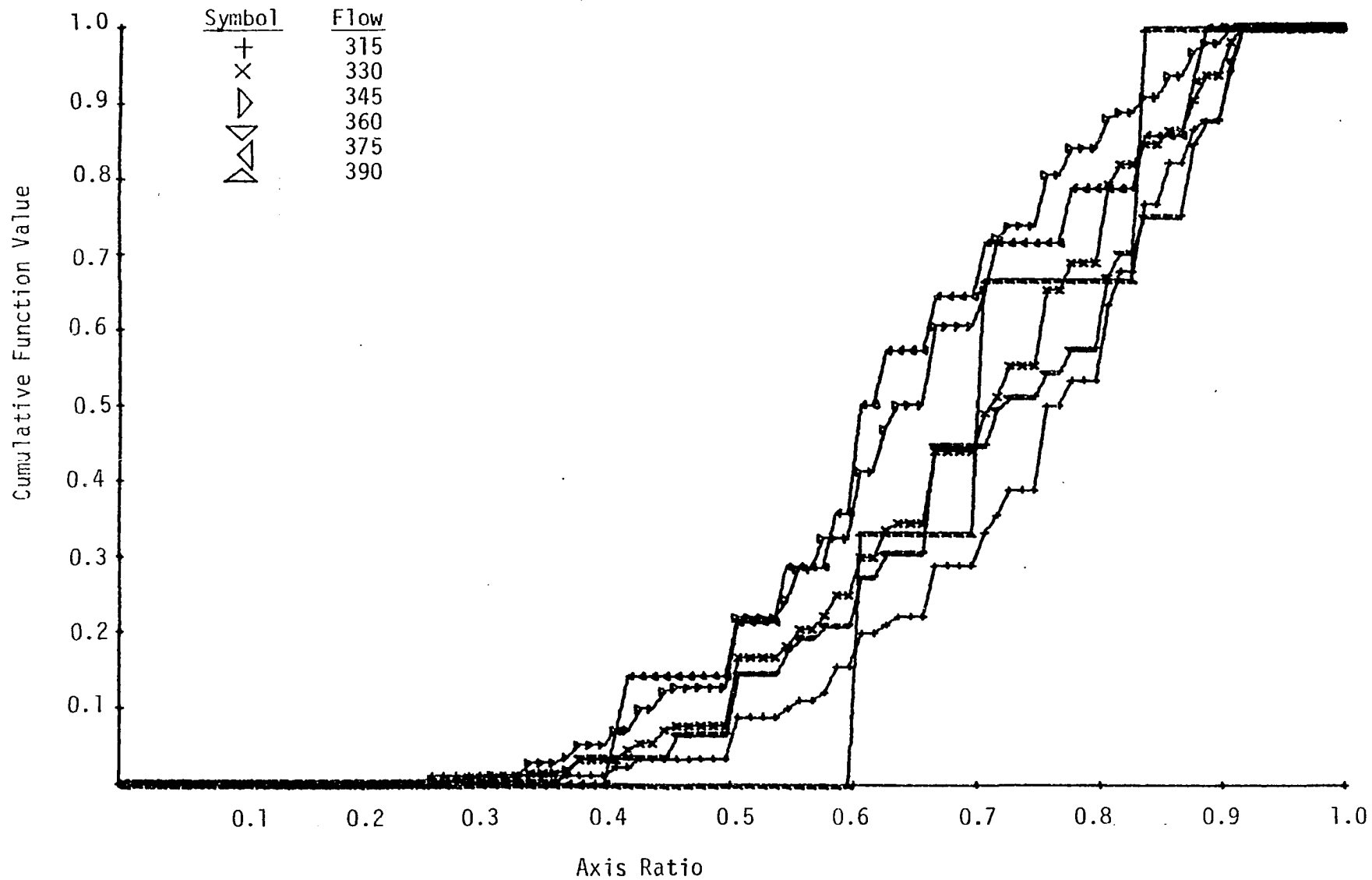
Figure 29b.   The Cumulative Function Value of the Axis Ratio Distribution of Flow Rate 3.
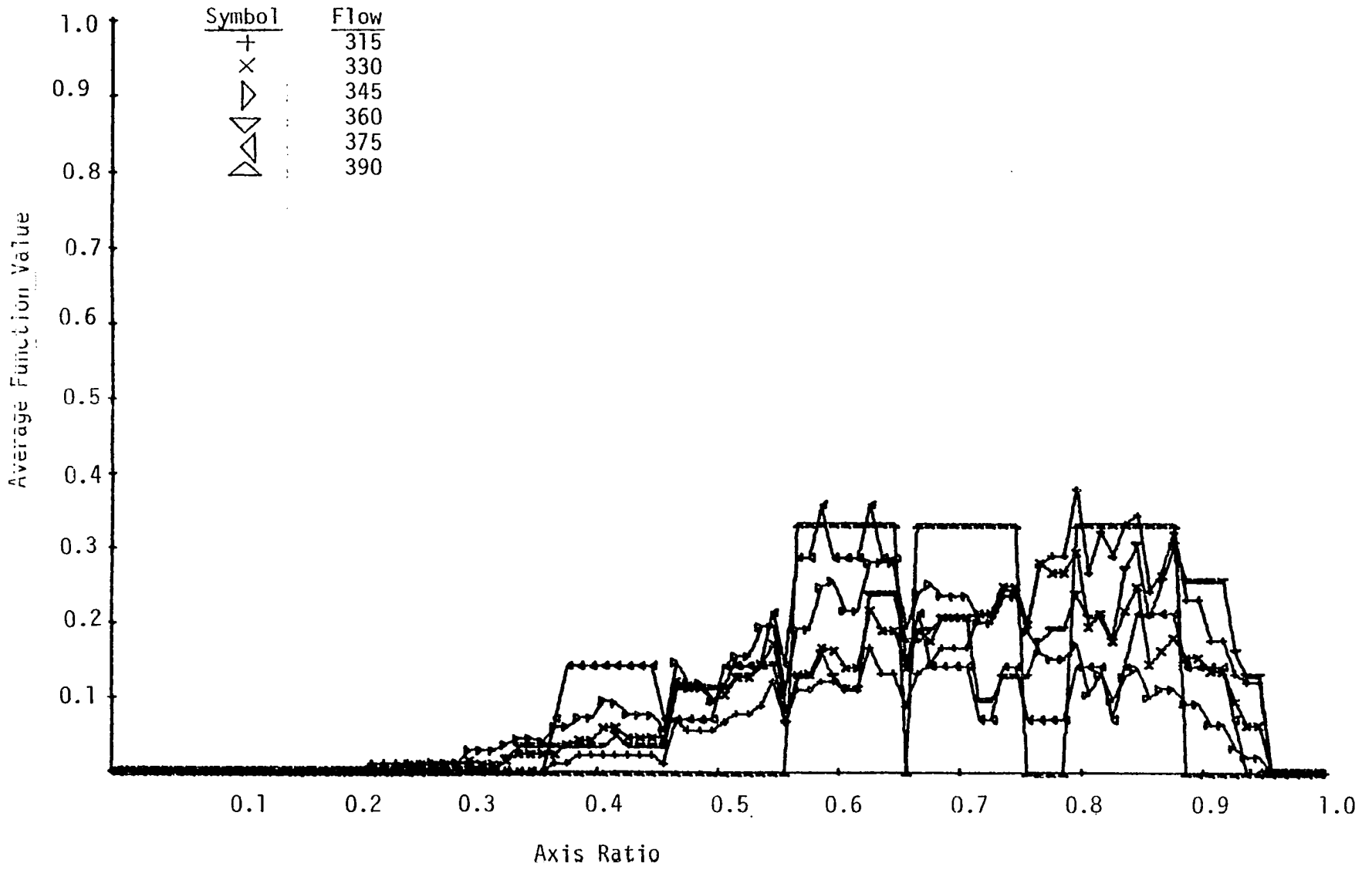
Figure 29c. The Average Function Value of the Axis Ratio Distribution of Flow Rate 3.

Symbol	Flow	# of Drops
+	315	187
×	330	426
▷	345	308
▽	360	69
◁	375	23
△	390	13
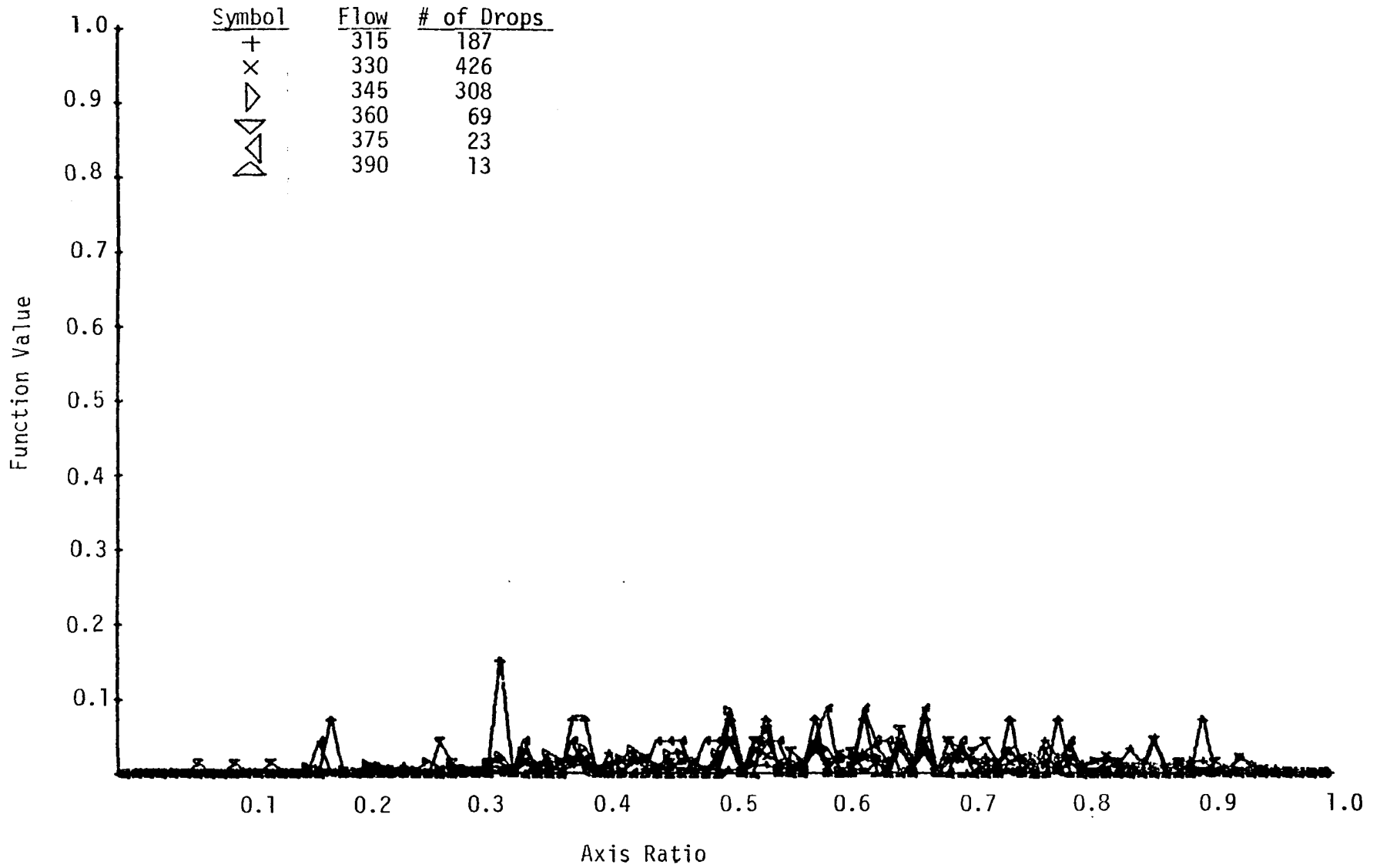
Figure 30a. The Function Value of the Axis Ratio Distribution (large droplets) of Flow Rate 3.
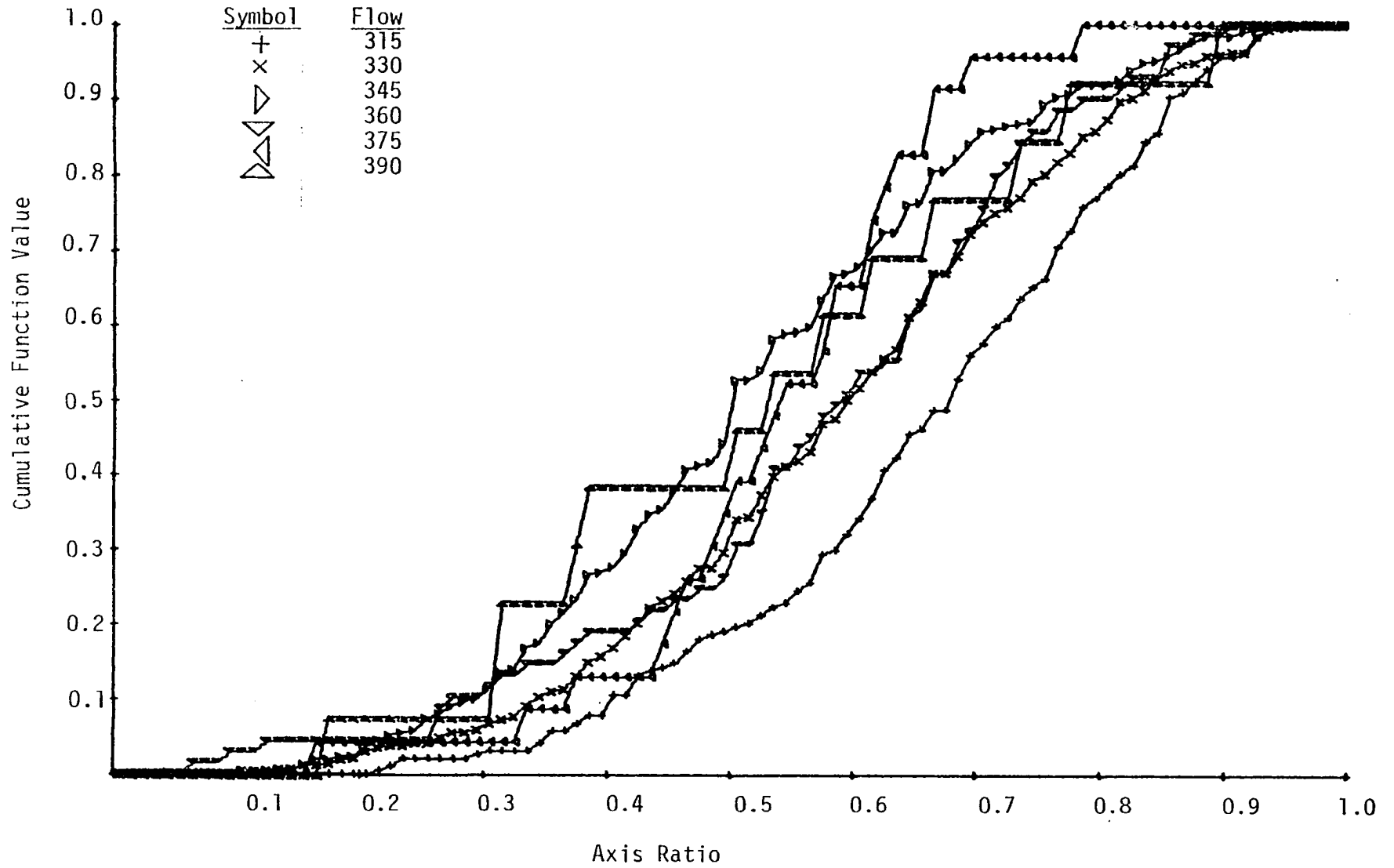
Figure 30b. The Cumulative Function Value of the Axis Ratio Distribution (large droplets) of Flow Rate 3.
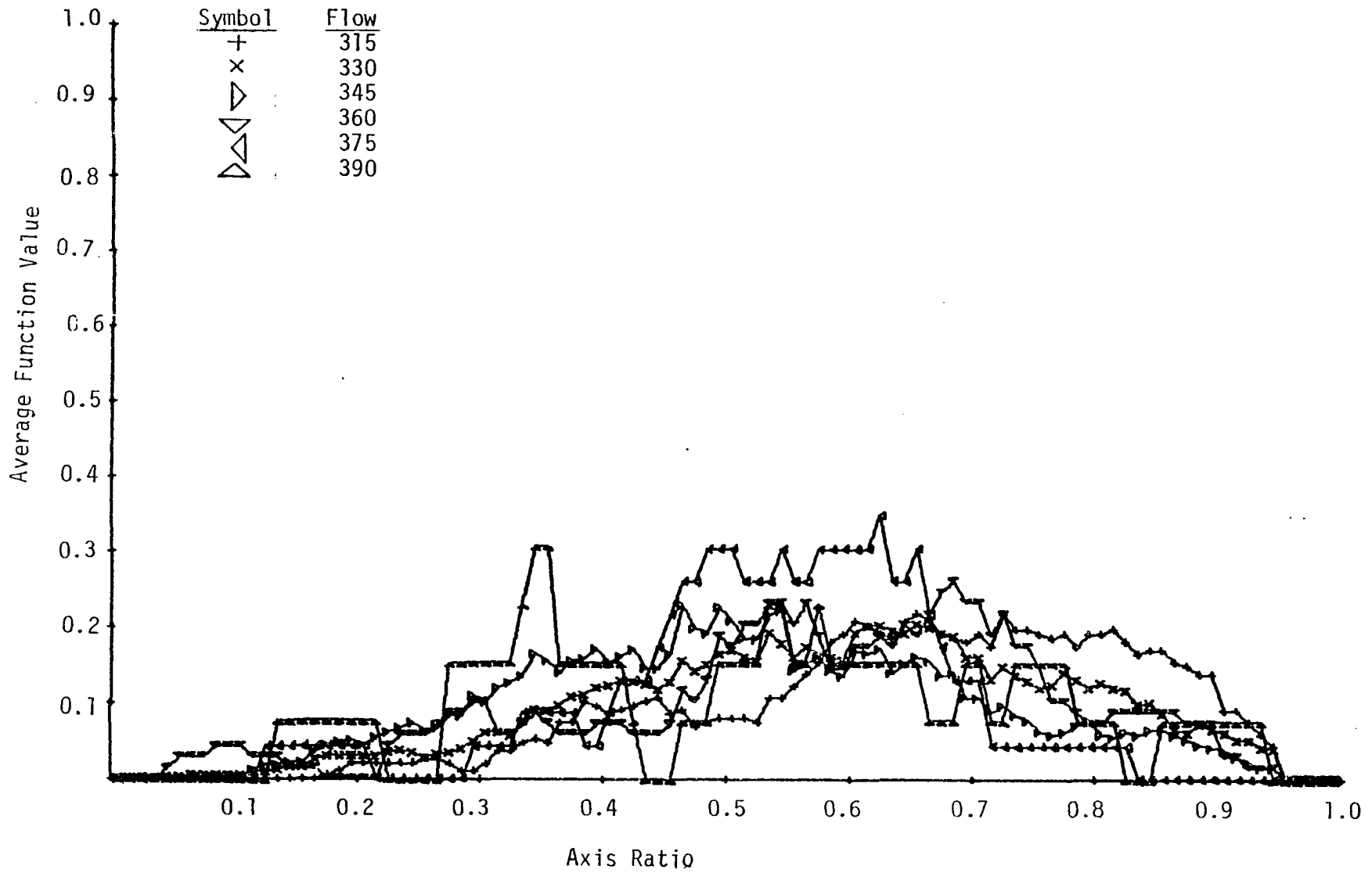
Figure 30c. The Average Function Value of the Axis Ratio Distribution (large droplets) of Flow Rate 3.

Symbol	Flow	# of Drops
+	315	283
×	330	666
▷	345	568
▽	360	138
◁	375	38
△	390	18

Function Value

1.0
0.9
0.8
0.7
0.6
0.5
0.4
0.3
0.2
0.1

0.1 0.2 0.3 0.4 0.5 0.6 0.7 0.8 0.9 1.0

Relative Radial Position
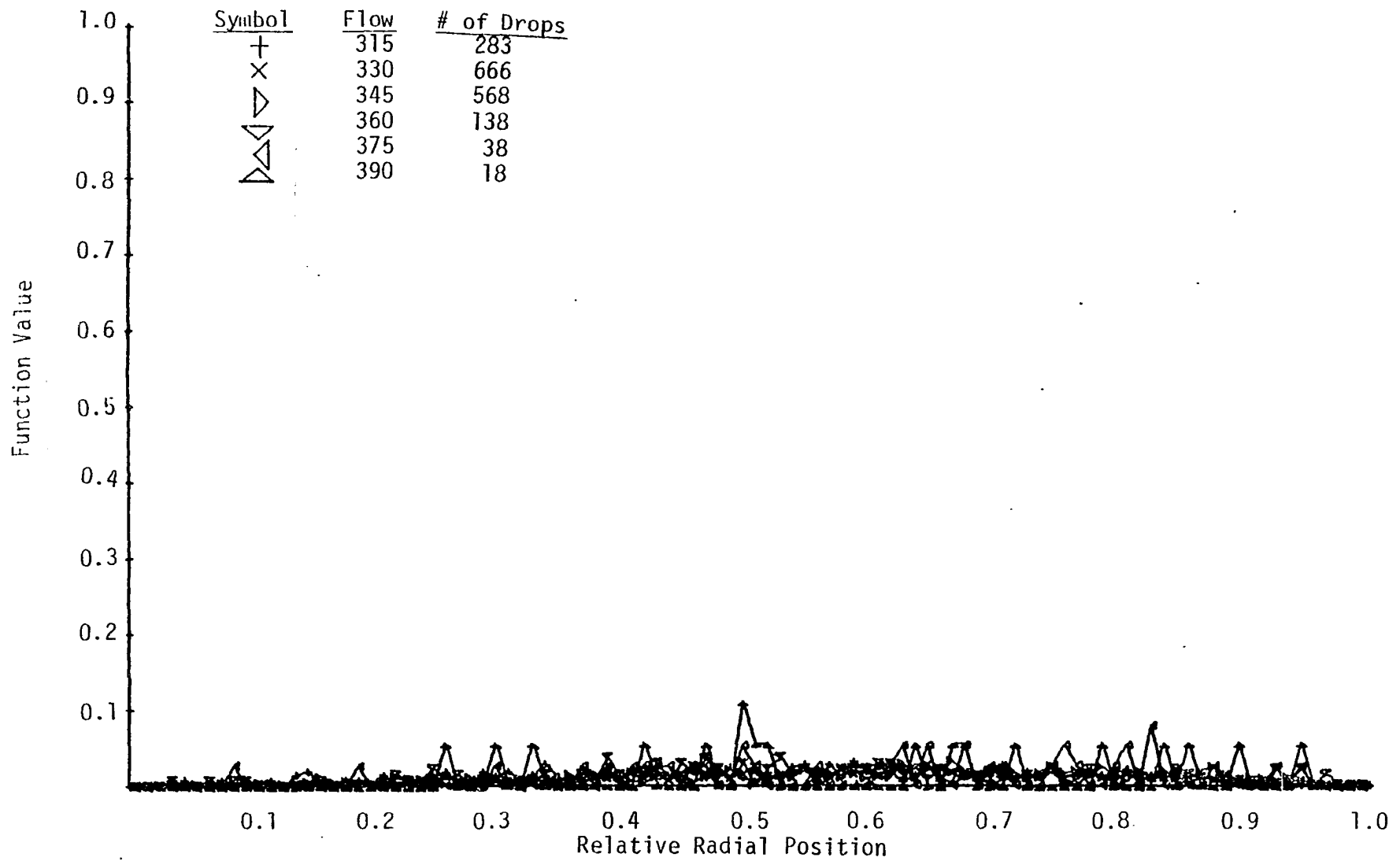
Figure 31a. The Function Value of the Relative Radial Position Distribution (constant radius increments) of Flow Rate 3.
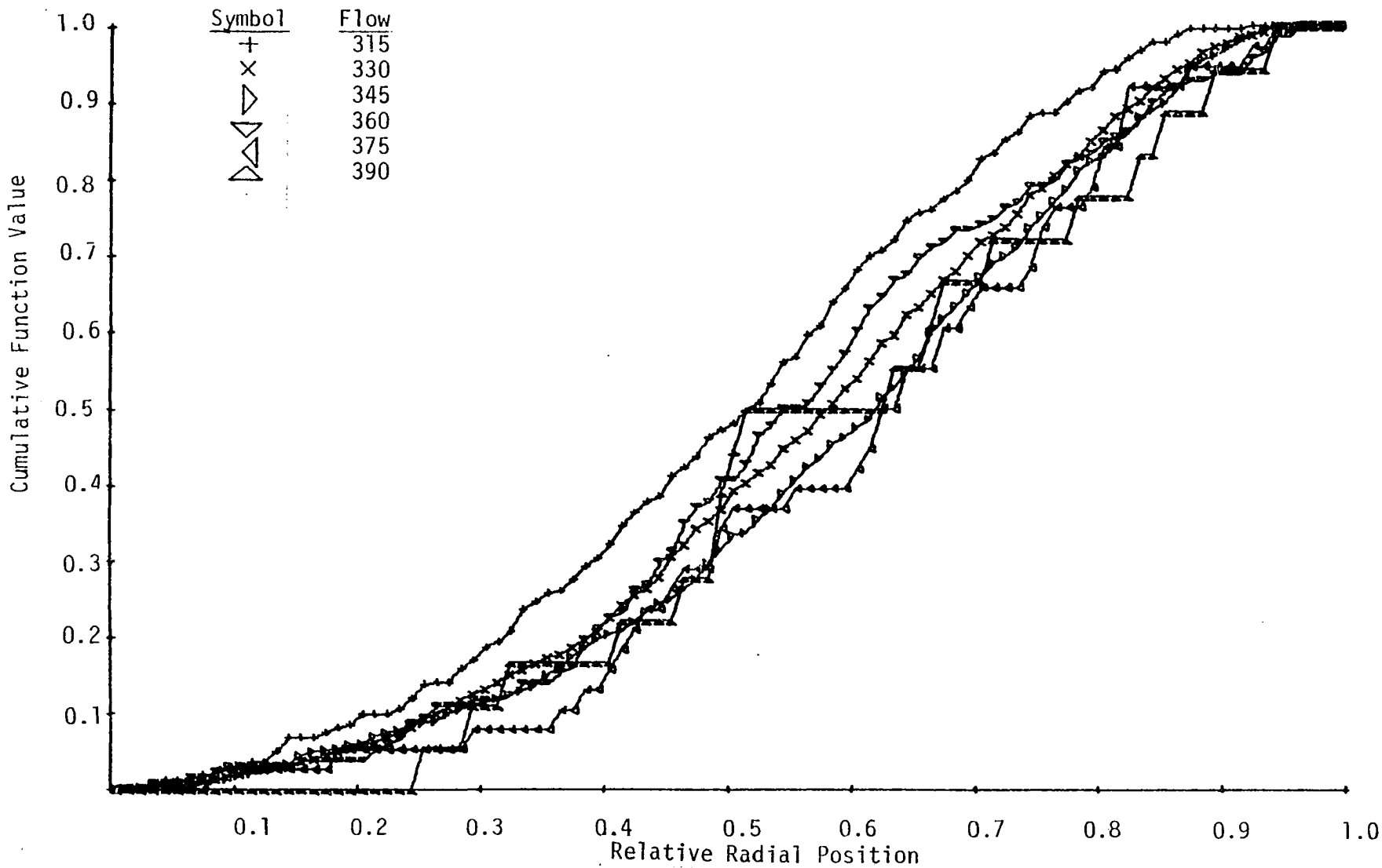
Figure 31b. The Cumulative Function Value of the Relative Position Distribution (constant radius increments) of Flow Rate 3.
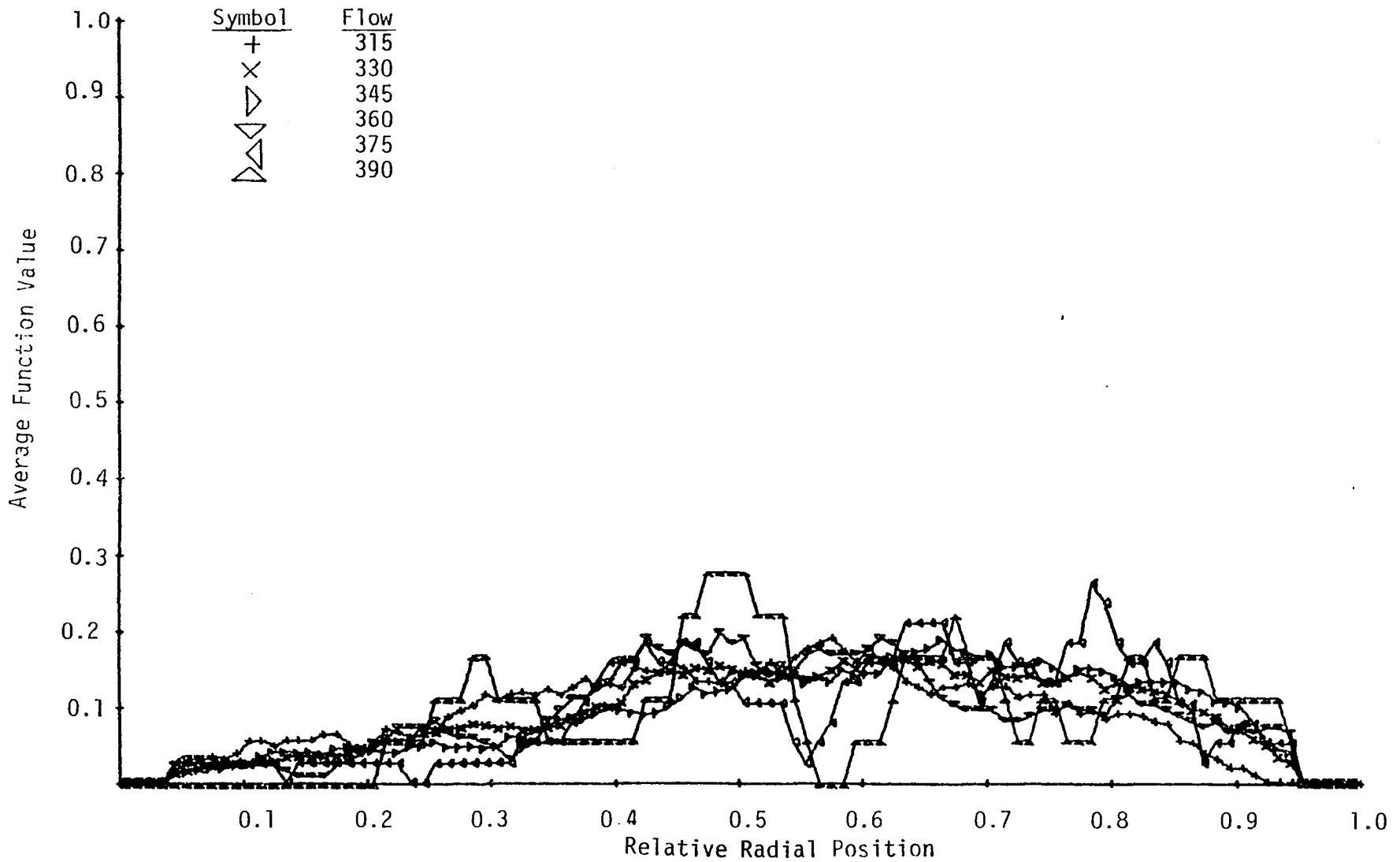
Figure 31c. The Average Function Value of the Relative Radial Position Distribution (constant radius increments) of Flow Rate 3.
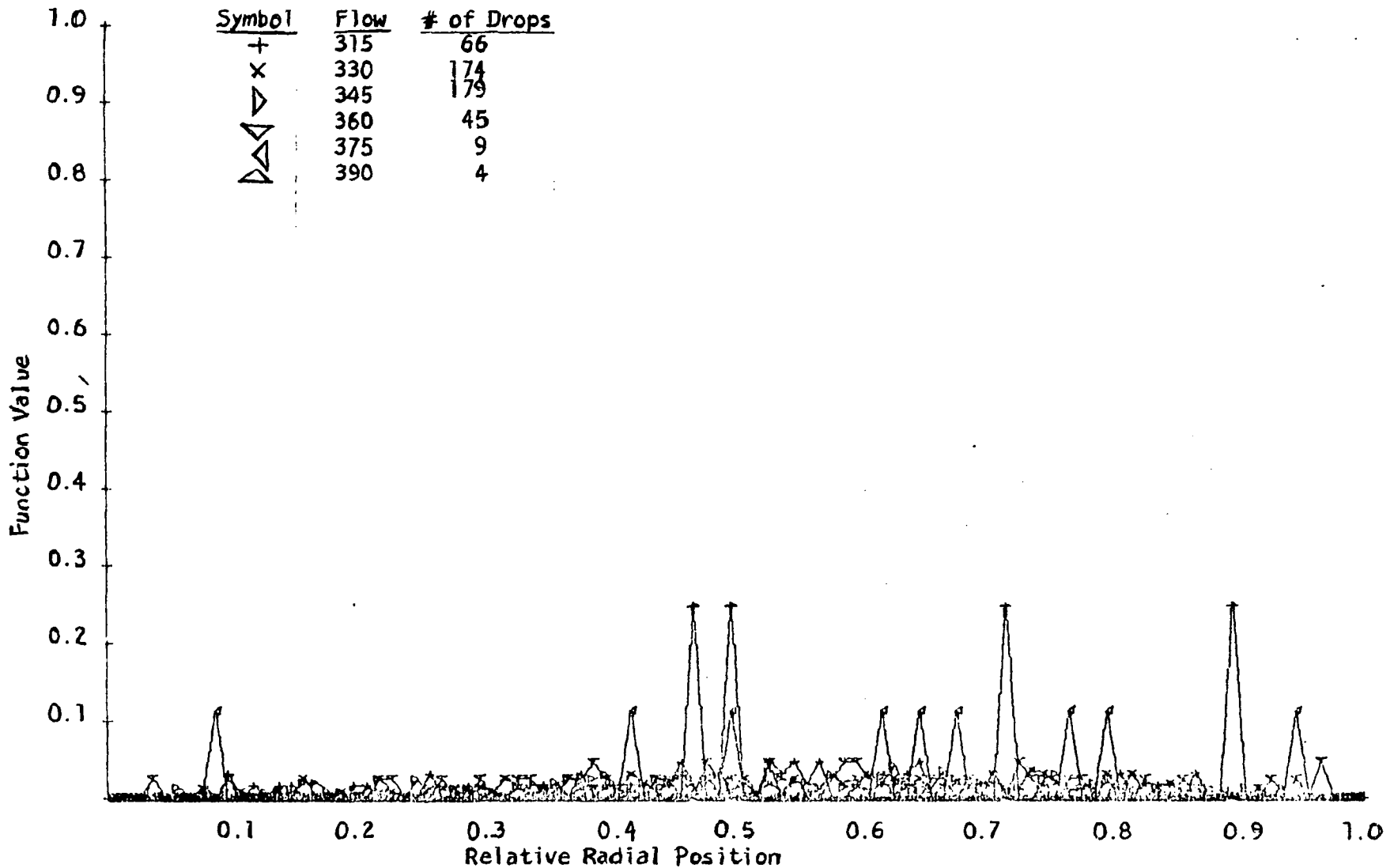
Figure 32a. The Function Value of the Relative Radial Position Distribution (small droplets) (constant radius increments) of Flow Rate 3.
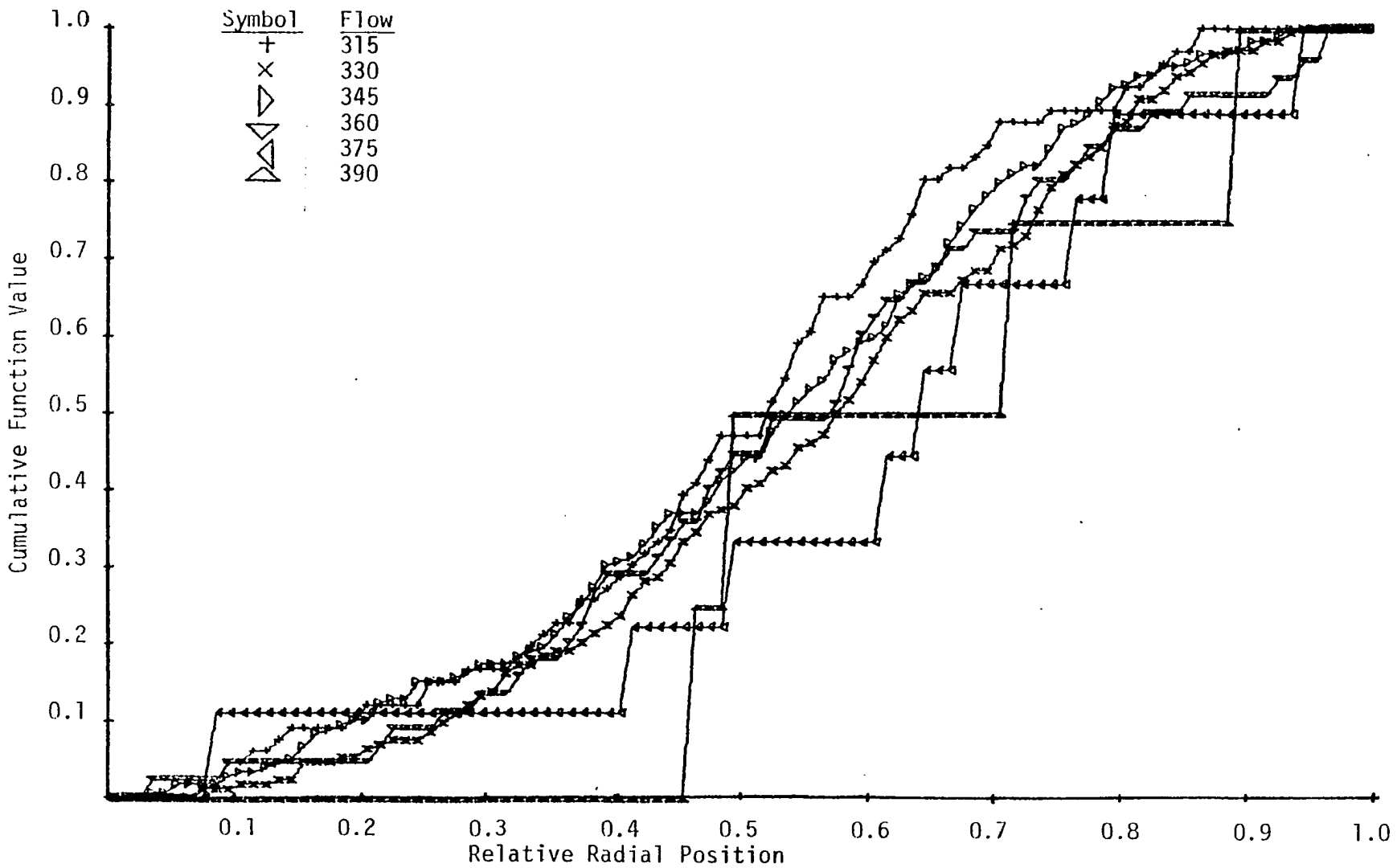
Figure 32b. The Cumulative Function Value of the Relative Radial Position Distribution (small droplets) (constant radius increments) of Flow Rate 3.
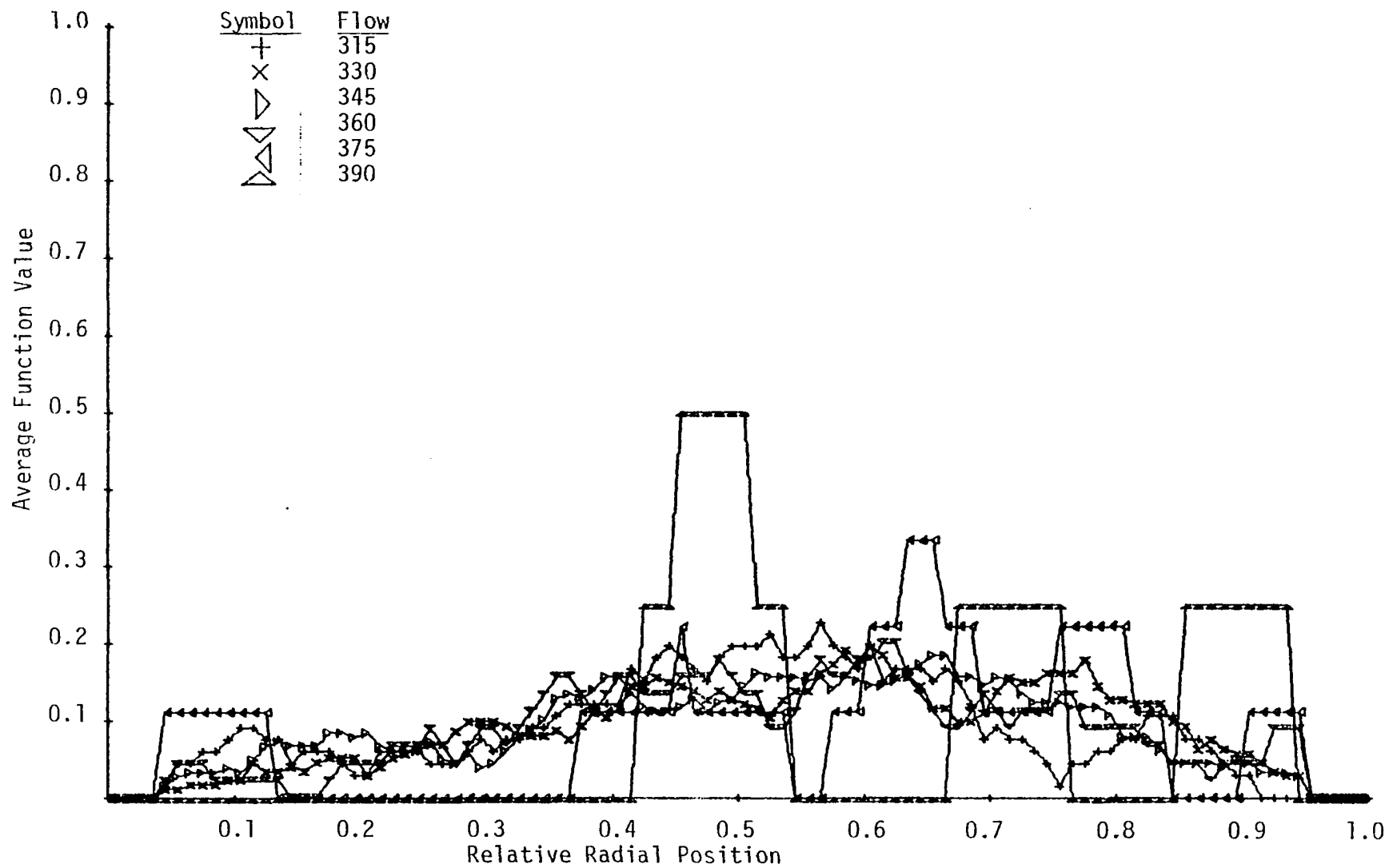
Figure 32c. The Average Function Value of the Relative Radial Position Distribution (small droplets) (constant radius increments) of Flow Rate 3.

Symbol	Flow	# of Drops
+	315	217
×	330	492
▷	345	389
▽	360	93
◁	375	29
△	390	14

Function Value (y-axis: 0.1 to 1.0)

Relative Radial Position (x-axis: 0.1 to 1.0)
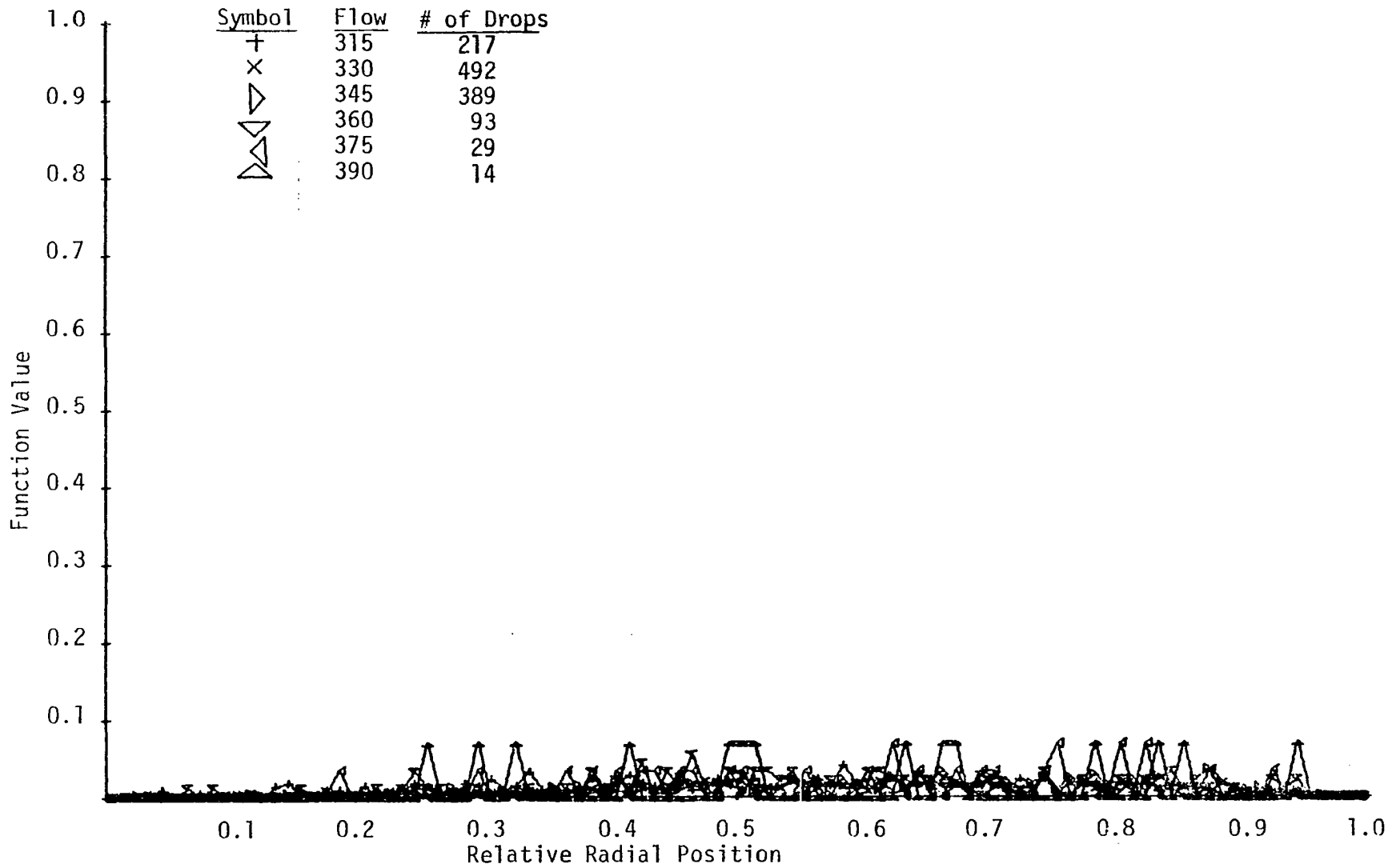
Figure 33a.   The Function Value of the Relative Radial Position Distribution (large droplets) (constant radius increments) of Flow Rate 3.
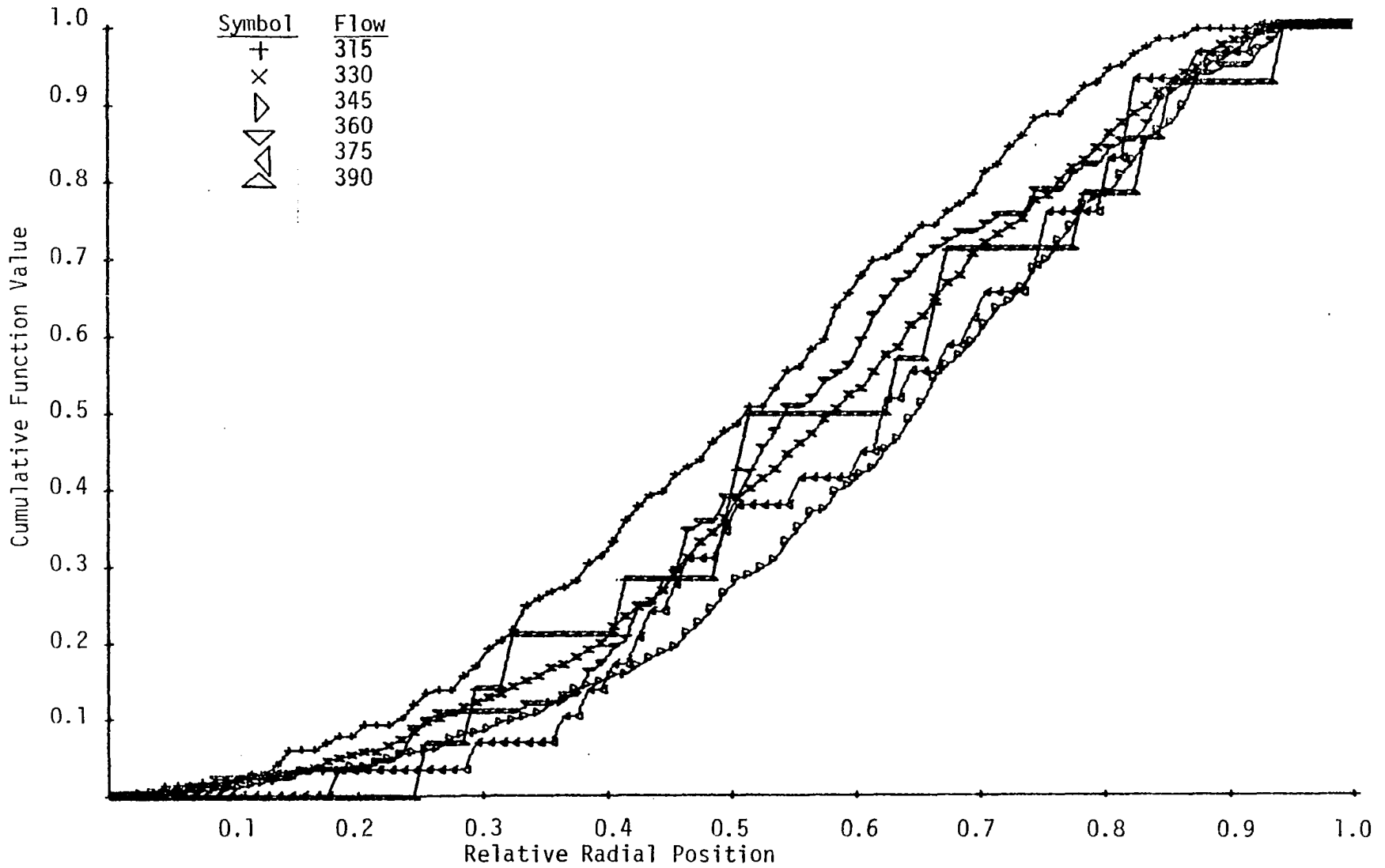
Figure 33b. The Cumulative Function Value of the Relative Radial Position Distribution (large droplets) (constant radius increments) of Flow Rate 3.
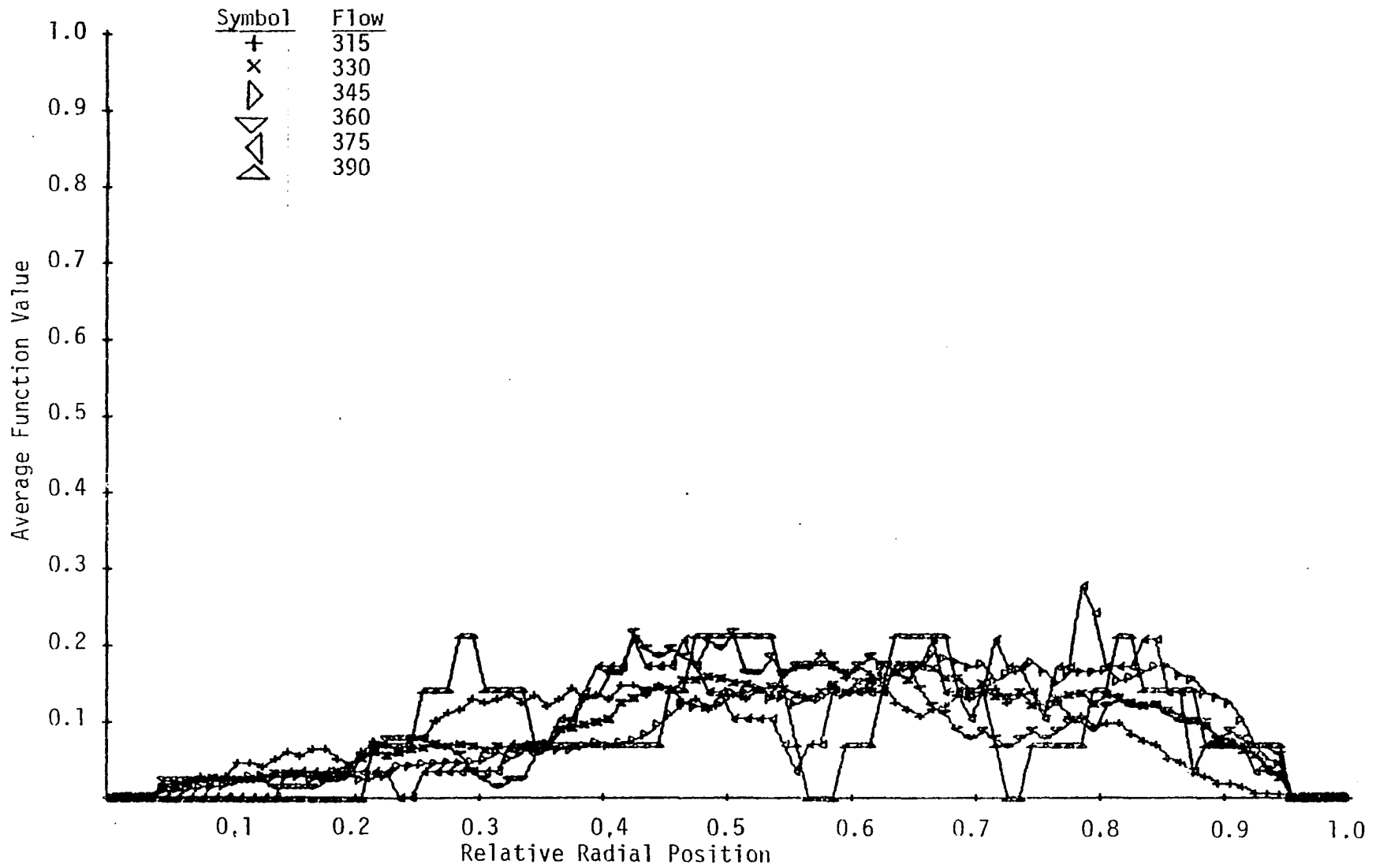
Figure 33c. The Average Function Value of the Relative Radial Position Distribution (large droplets) (constant radius increments) of Flow Rate 3.
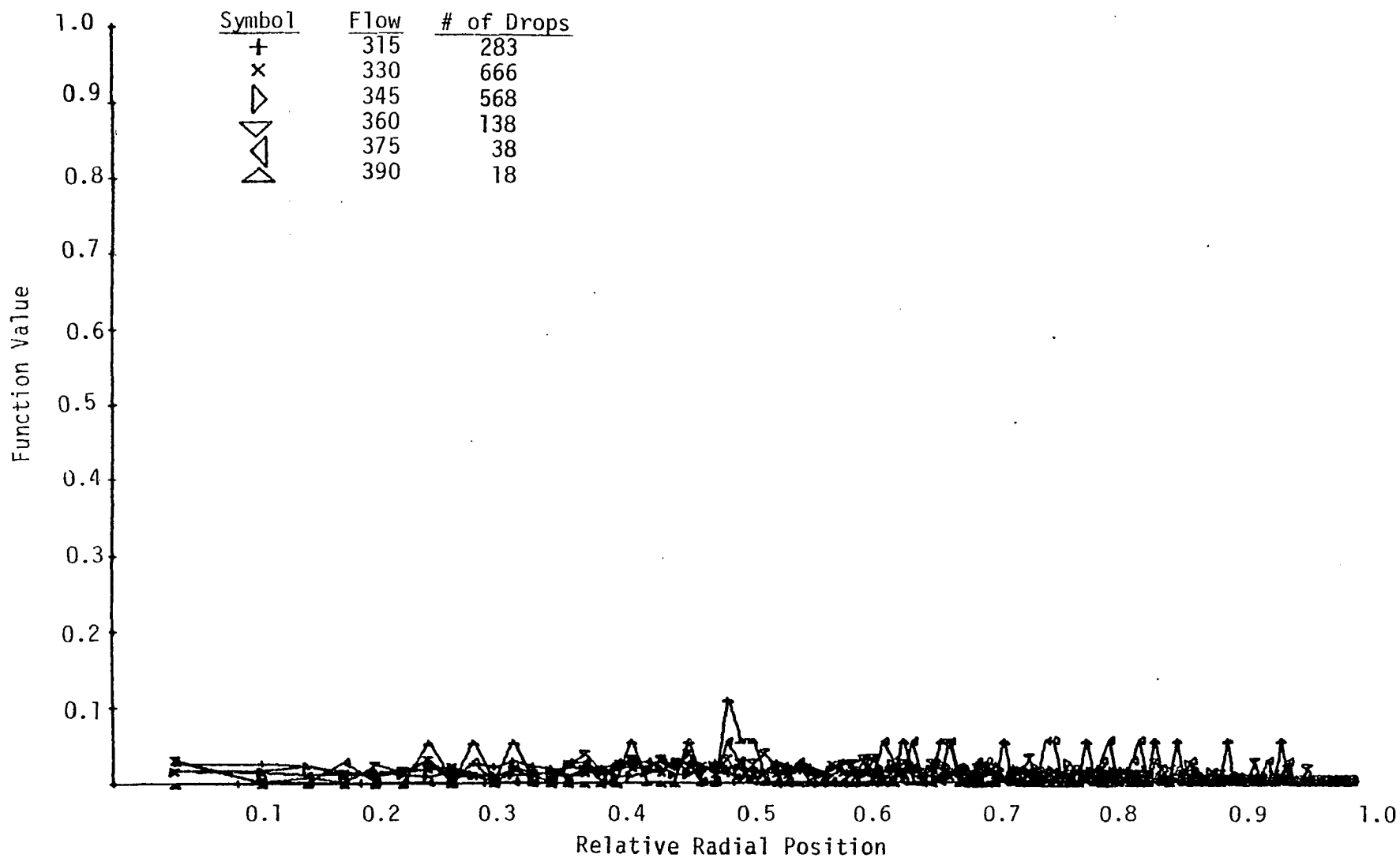
Figure 34a. The Function Value of the Relative Radial Position Distribution (constant area increments) of Flow Rate 3.
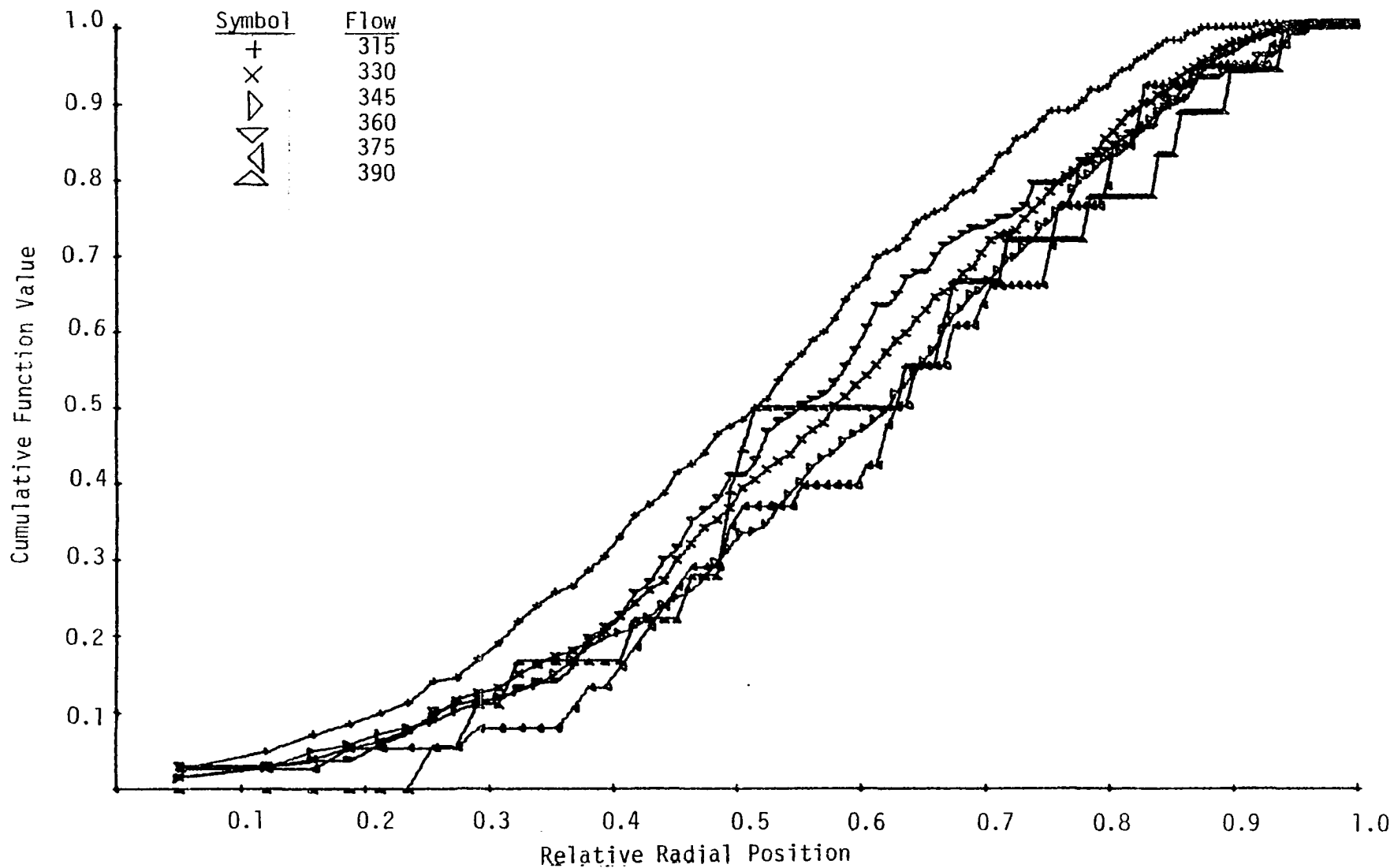
Figure 34b. The Cumulative Function Value of the Relative Radial Position Distribution (constant area increments) of Flow Rate 3.
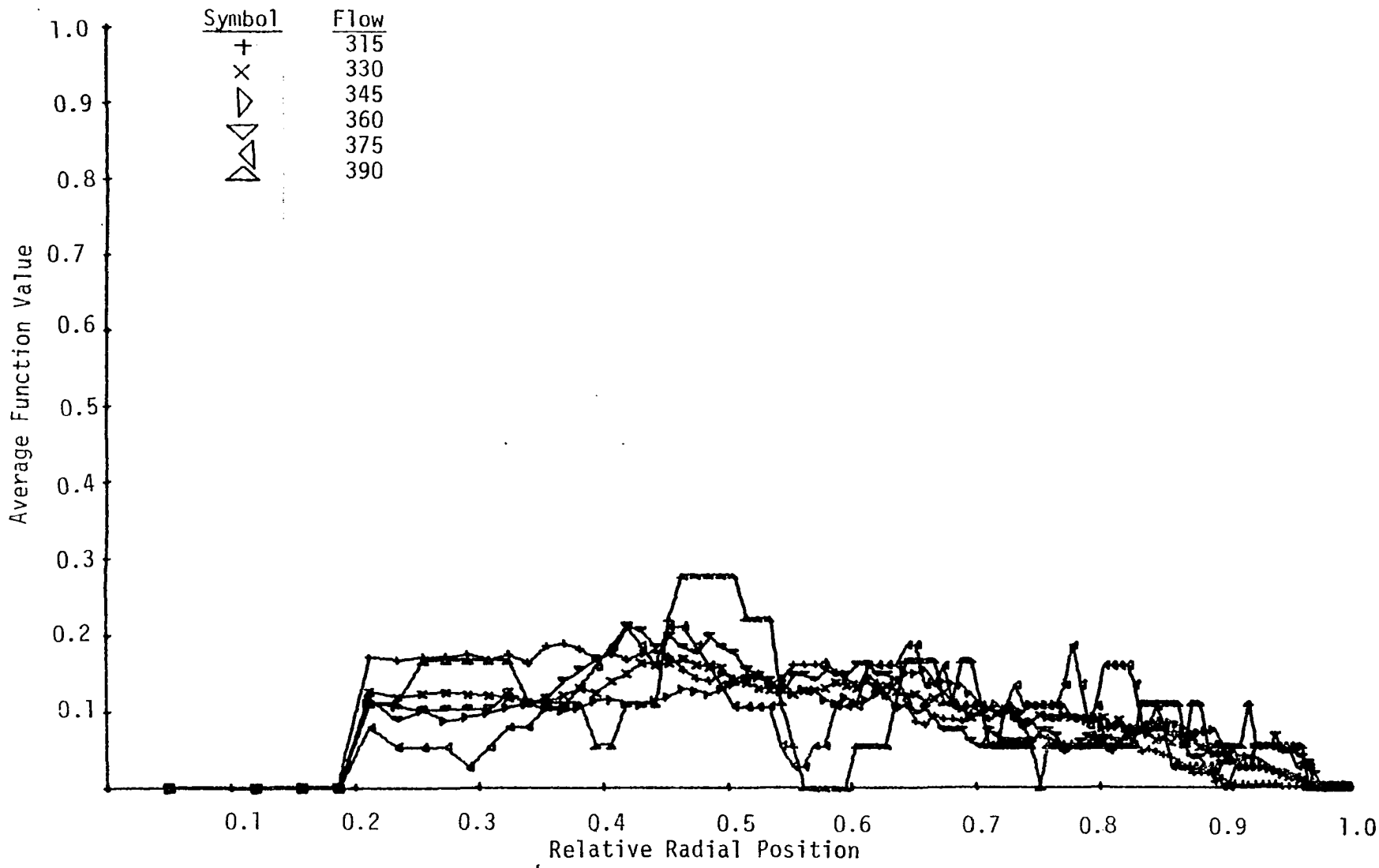
Figure 34c. The Average Function Value of the Relative Radial Position Distribution (constant area increments) of Flow Rate 3.
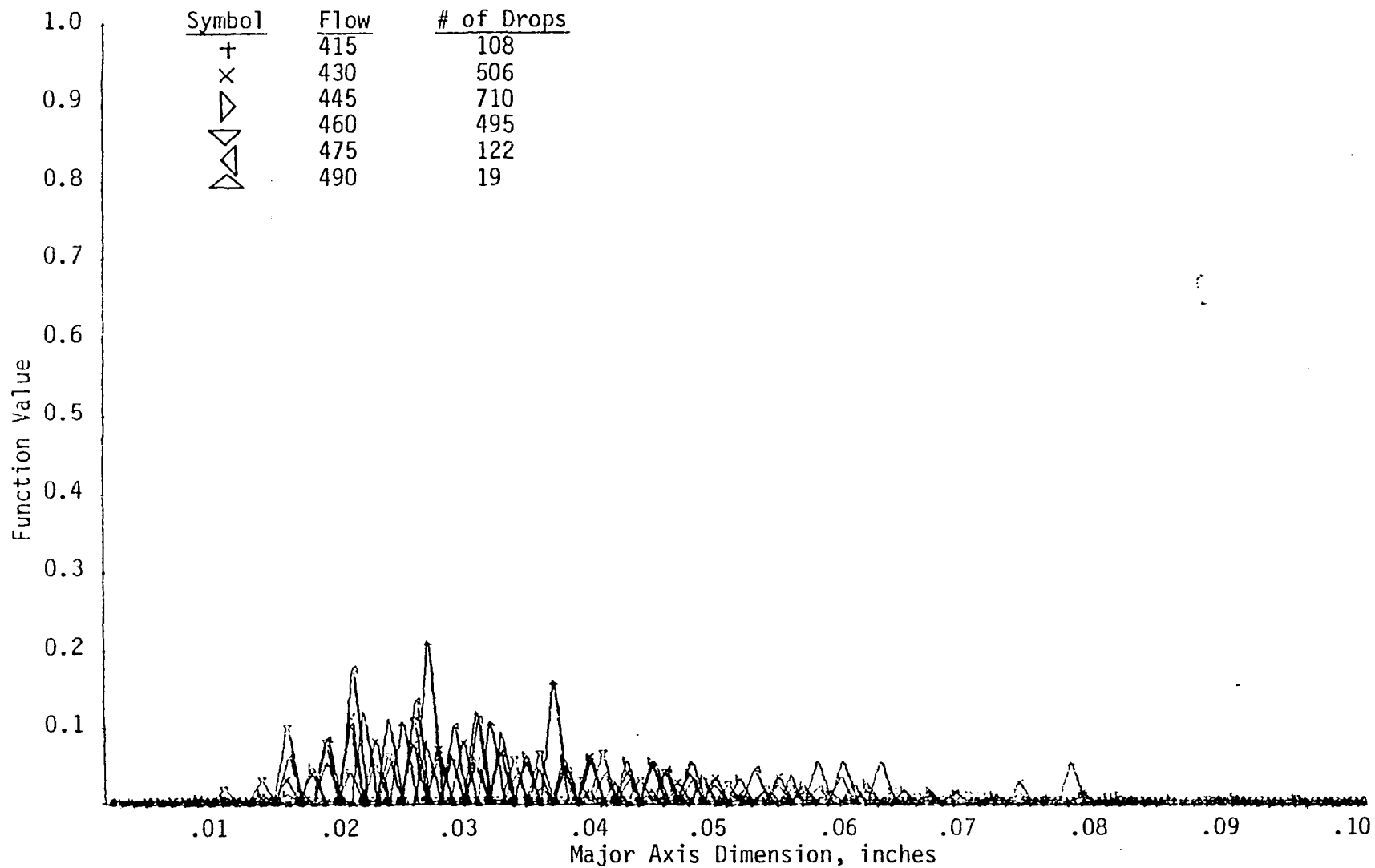
Figure 35a.   The Function Value of the Major Axis Distribution of Flow Rate 4.
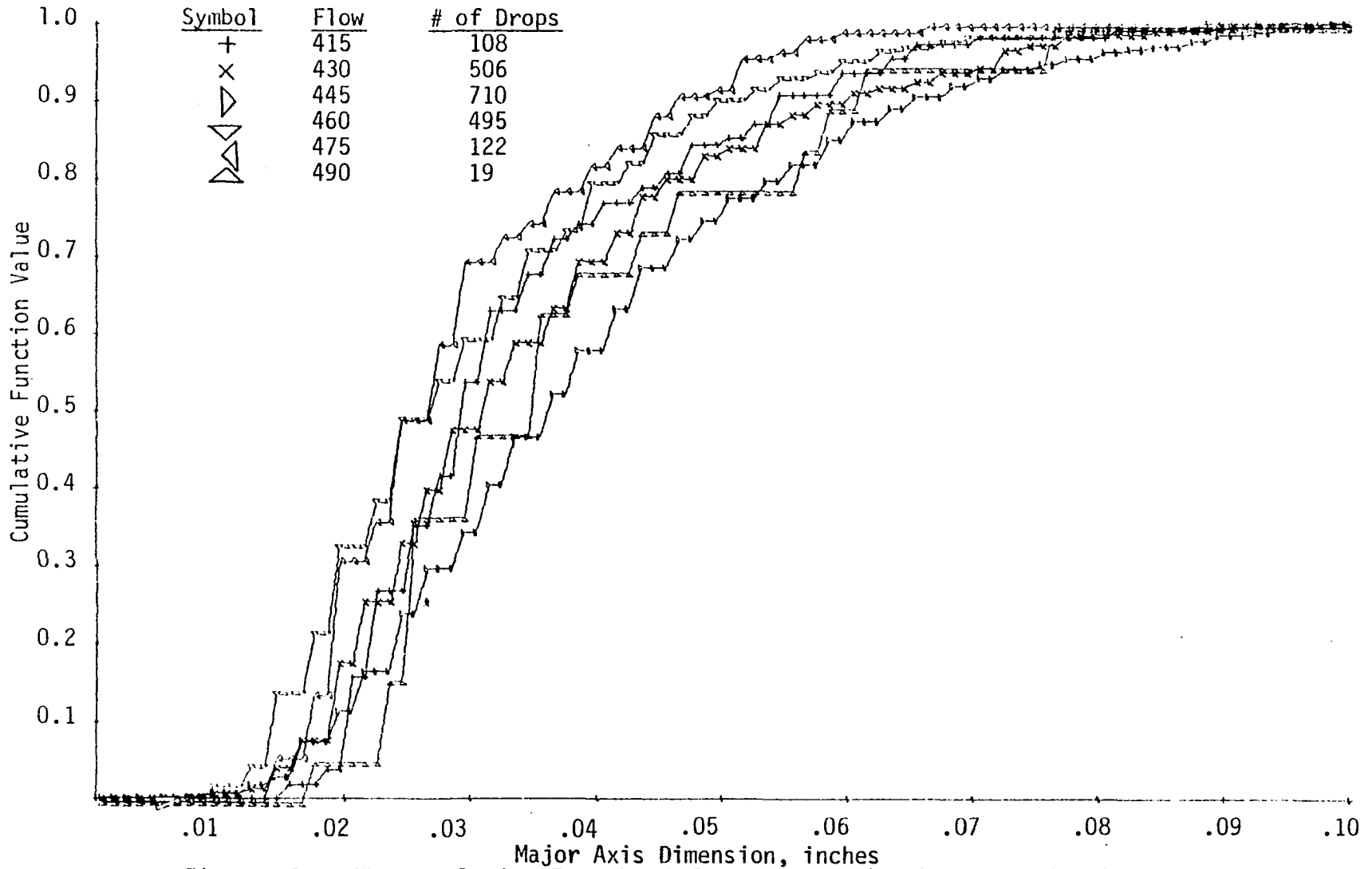
Figure 35b. The Cumulative Function Value of the Major Axis Distribution of Flow Rate 4.

Major Axis Dimension, inches

Cumulative Function Value

Symbol	Flow	# of Drops
+	415	108
×	430	506
▷	445	710
▽	460	495
◁	475	122
△	490	19
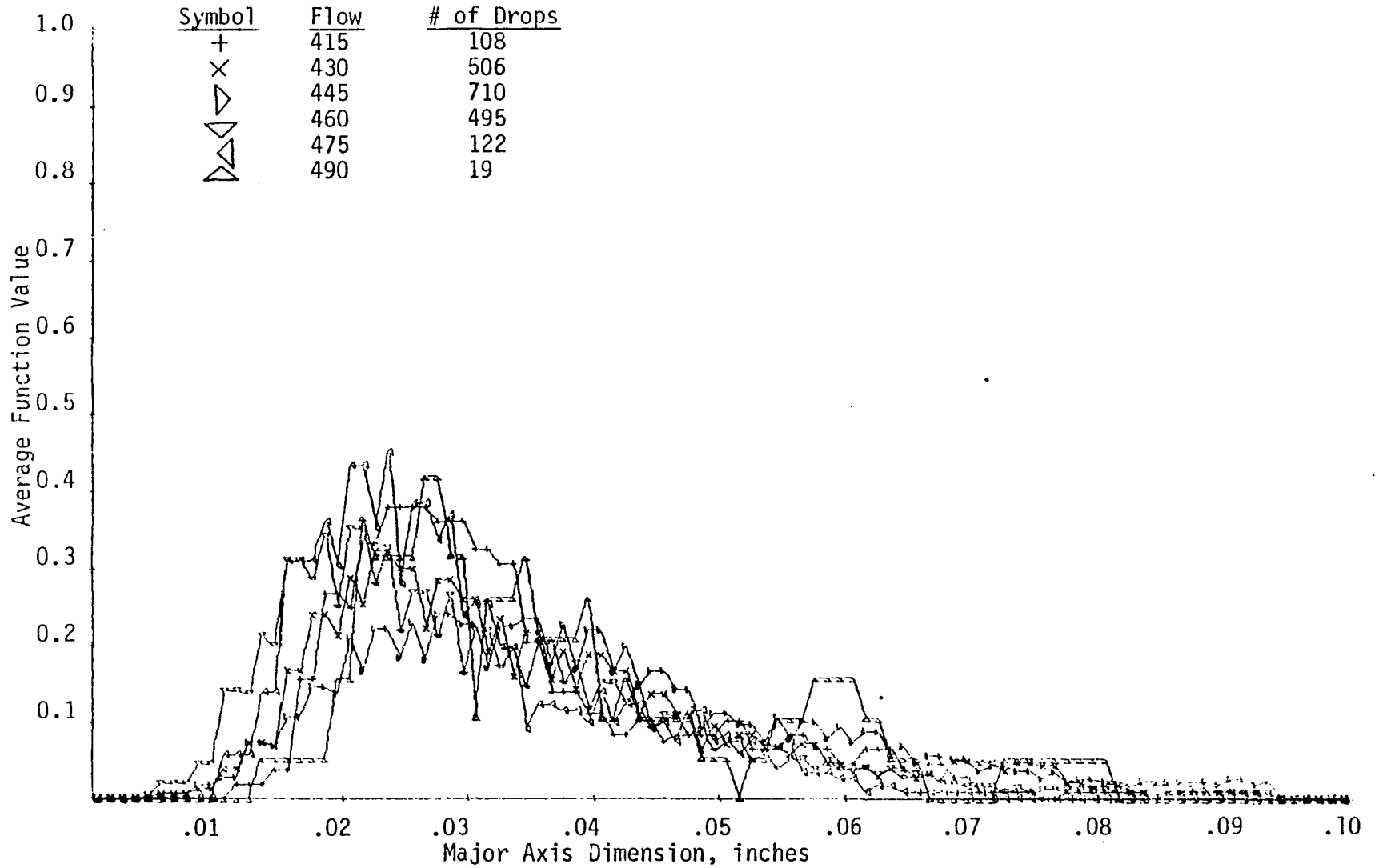
Figure 35c. The Average Function Value of the Major Axis Distribution of Flow Rate 4.
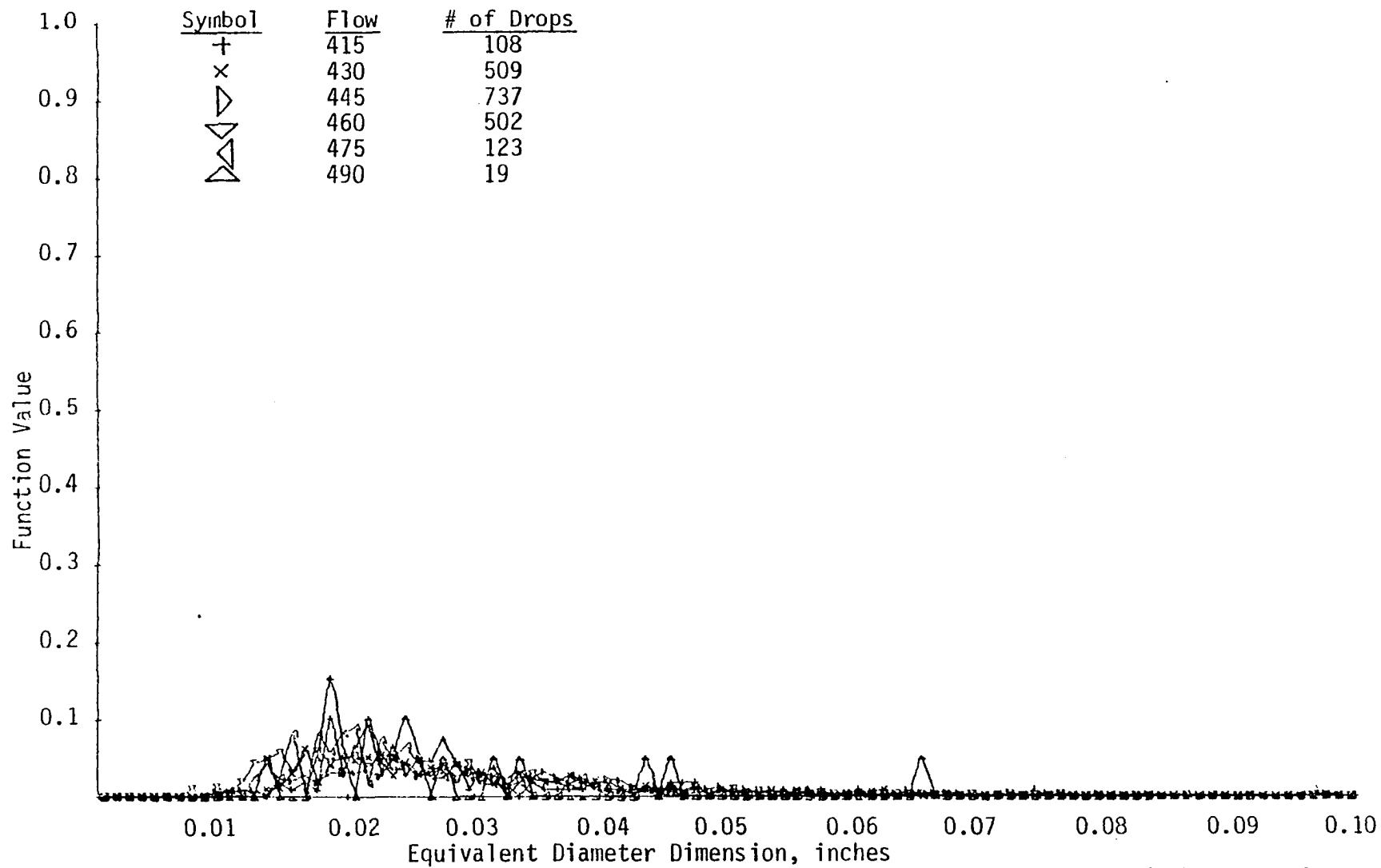
Figure 36a. The Function Value of the Equivalent Diameter Distribution of Flow Rate 4.
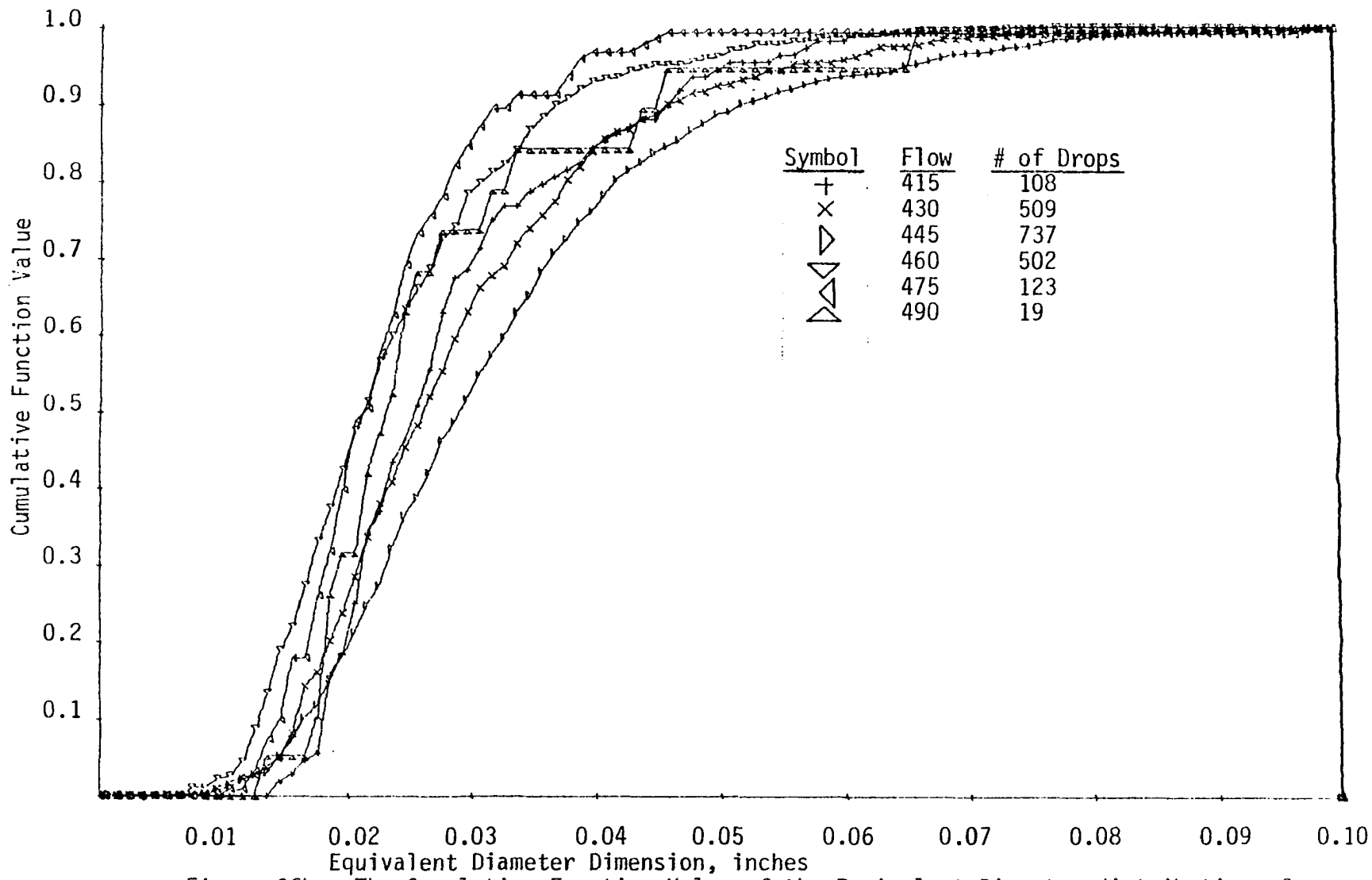
Figure 36b. The Cumulative Function Value of the Equivalent Diameter distribution of Flow Rate 4.
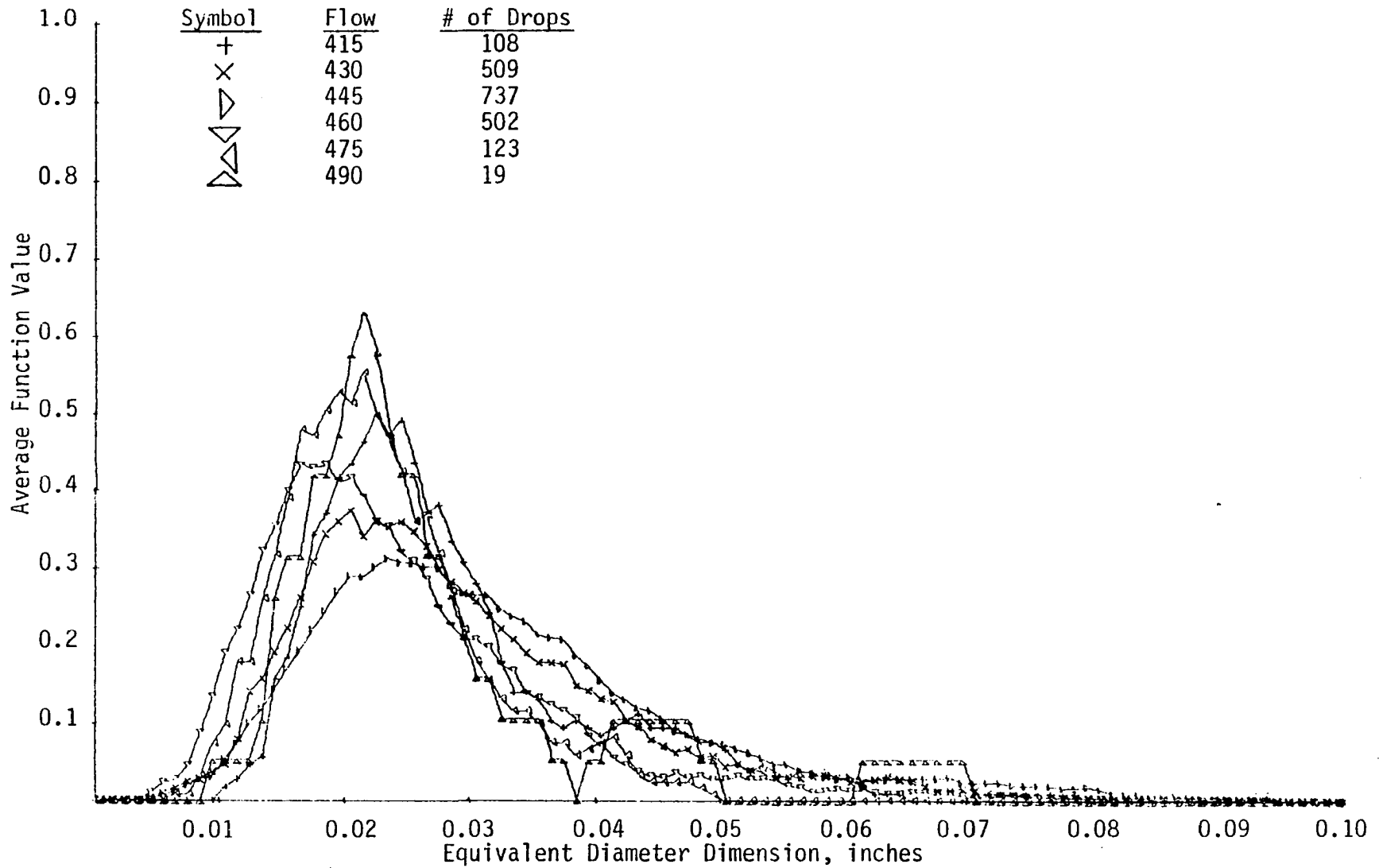
Figure 36c. The Average Function Value of the Equivalent Diameter Distribution of Flow Rate 4.

121
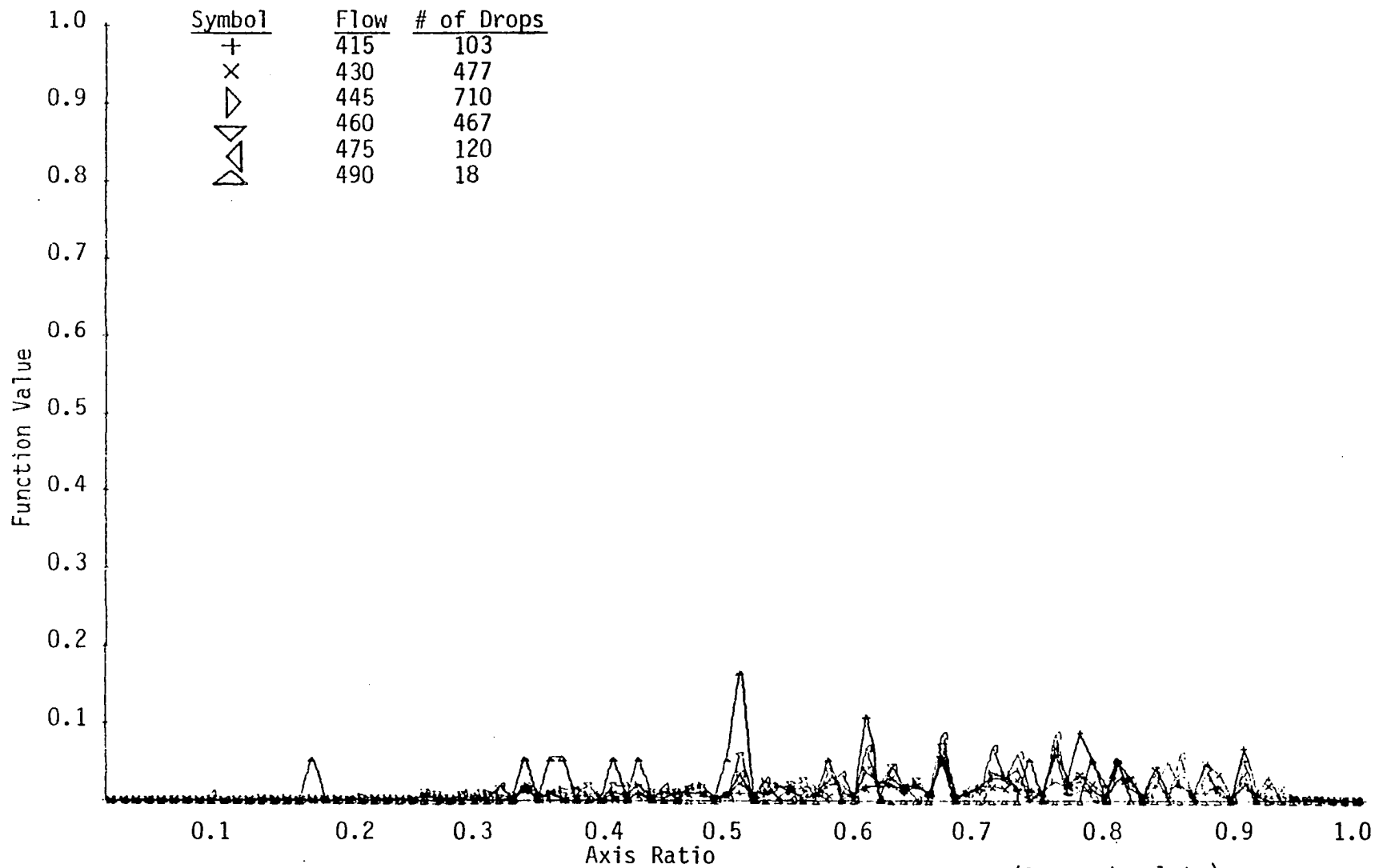
Figure 37a. The Function Value of the Axis Ratio Distribution (large droplets) of Flow Rate 4.
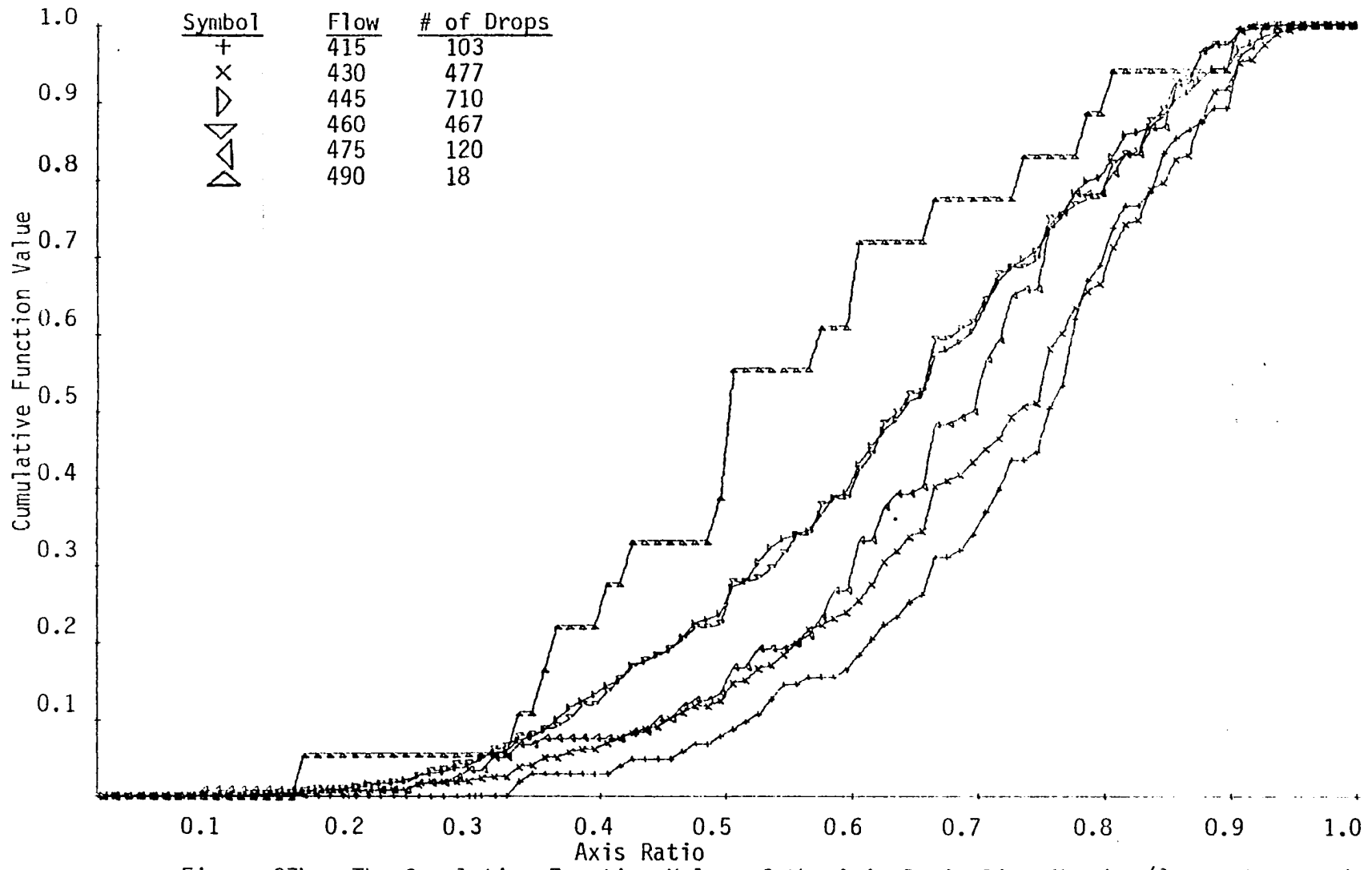
Figure 37b. The Cumulative Function Value of the Axis Ratio Distribution (large droplets) of Flow Rate 4.
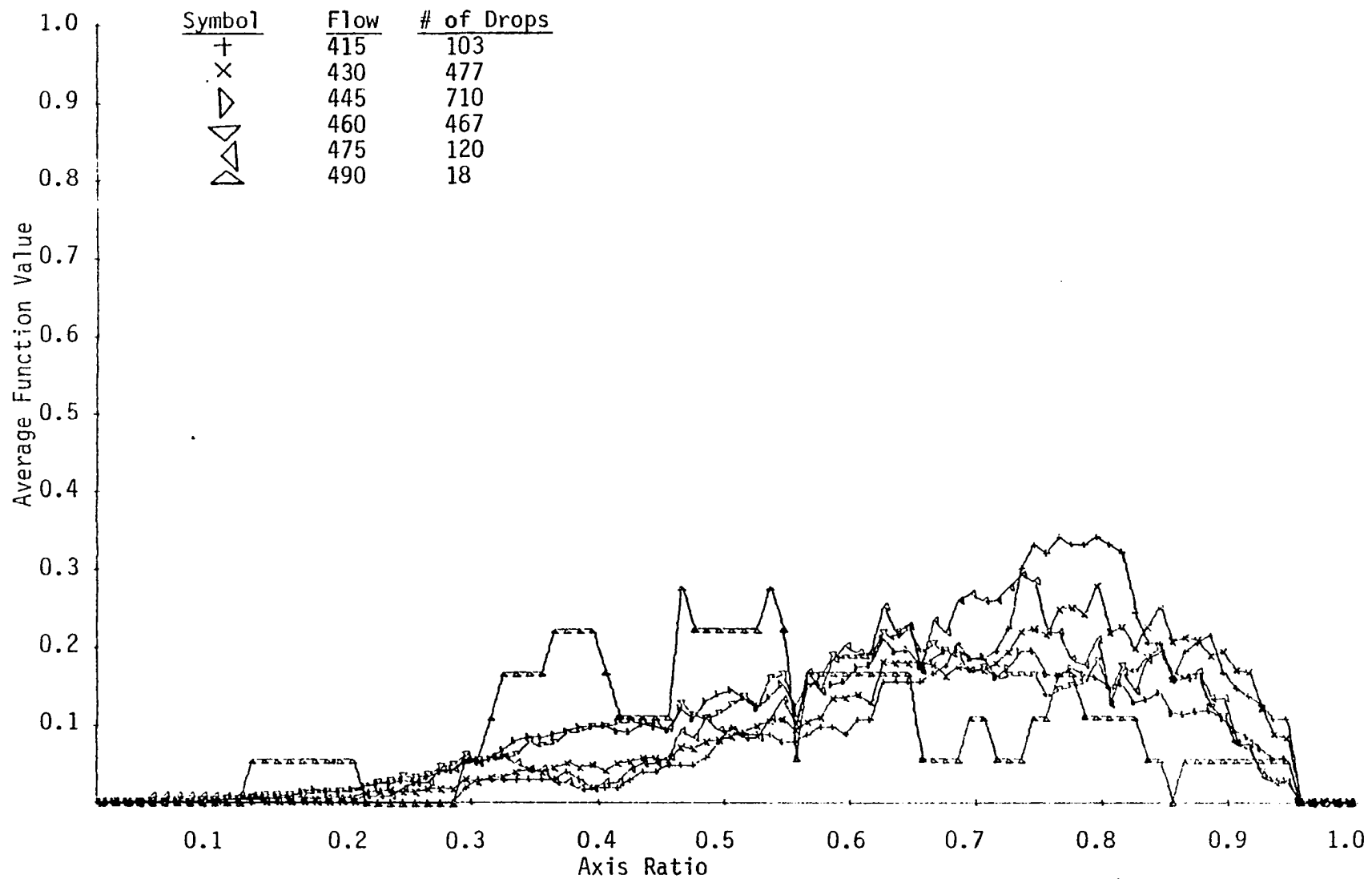
Figure 37c.   The Average Function Value of the Axis Ratio Distribution (large droplets)
of Flow Rate 4.
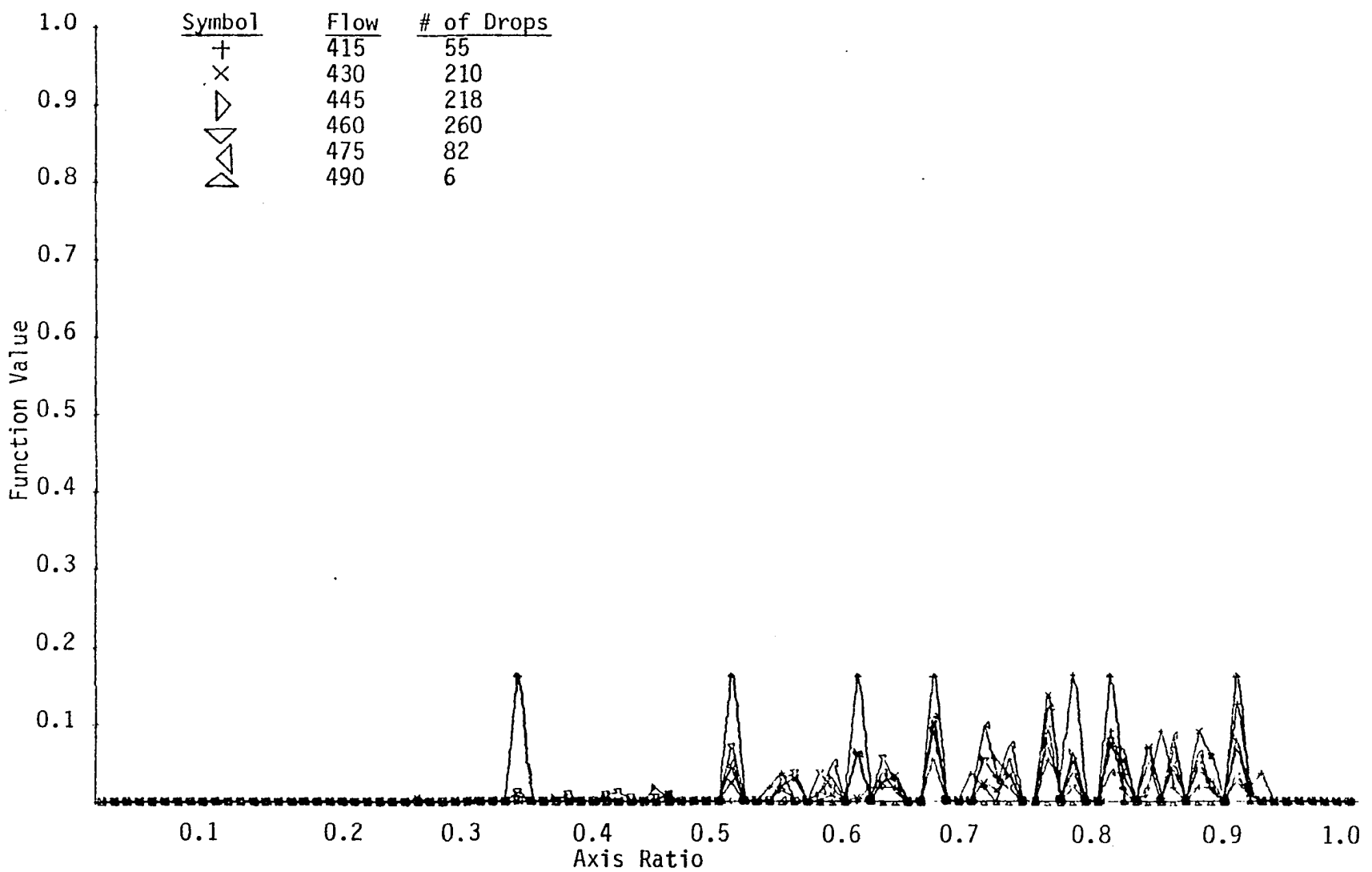
Figure 38a. The Function Value for the Axis Ratio Distribution (small droplets) of Flow Rate 4.
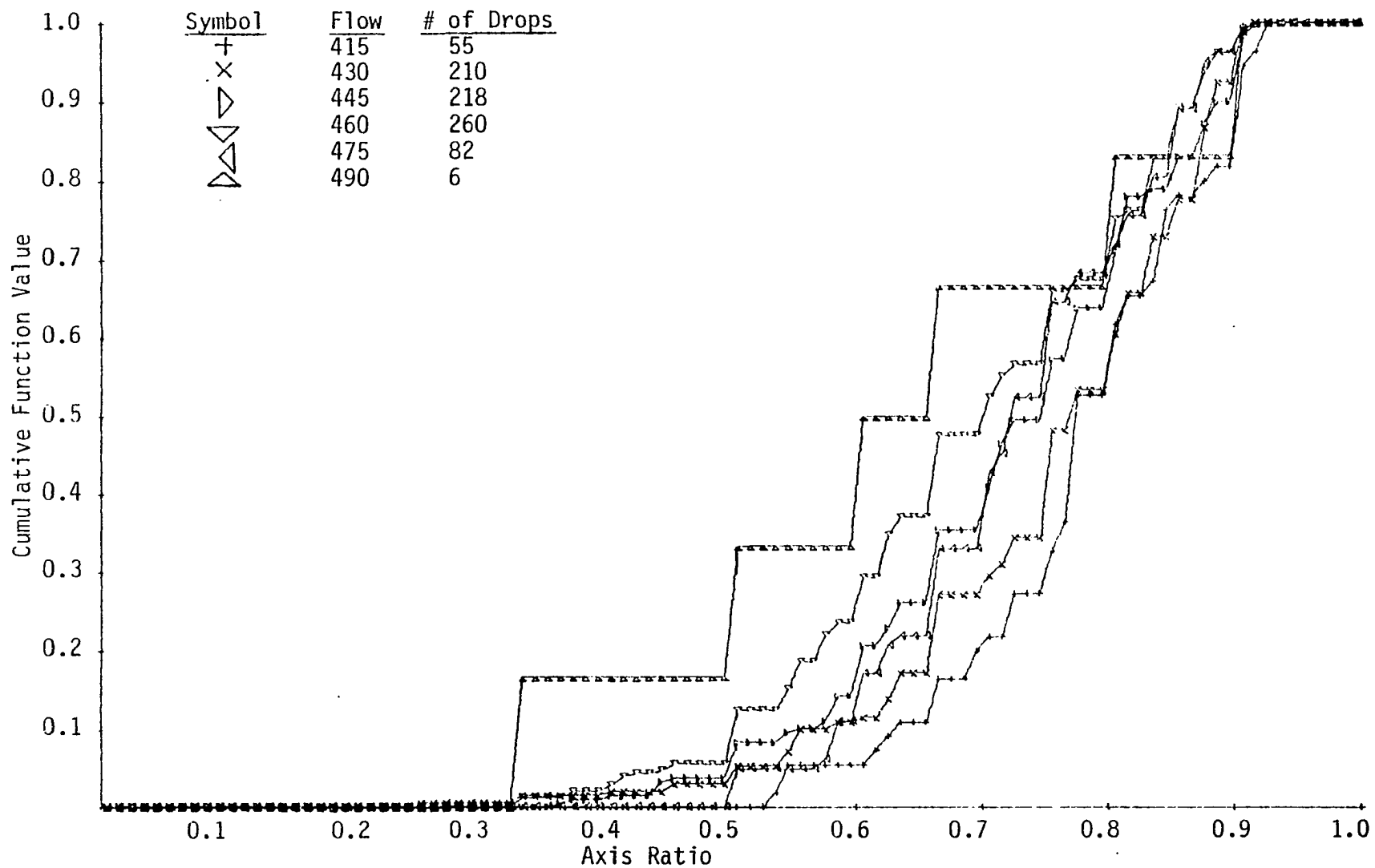
Figure 38b. The Cumulative Function Value of the Axis Ratio Distribution (small droplets) of Flow Rate 4.
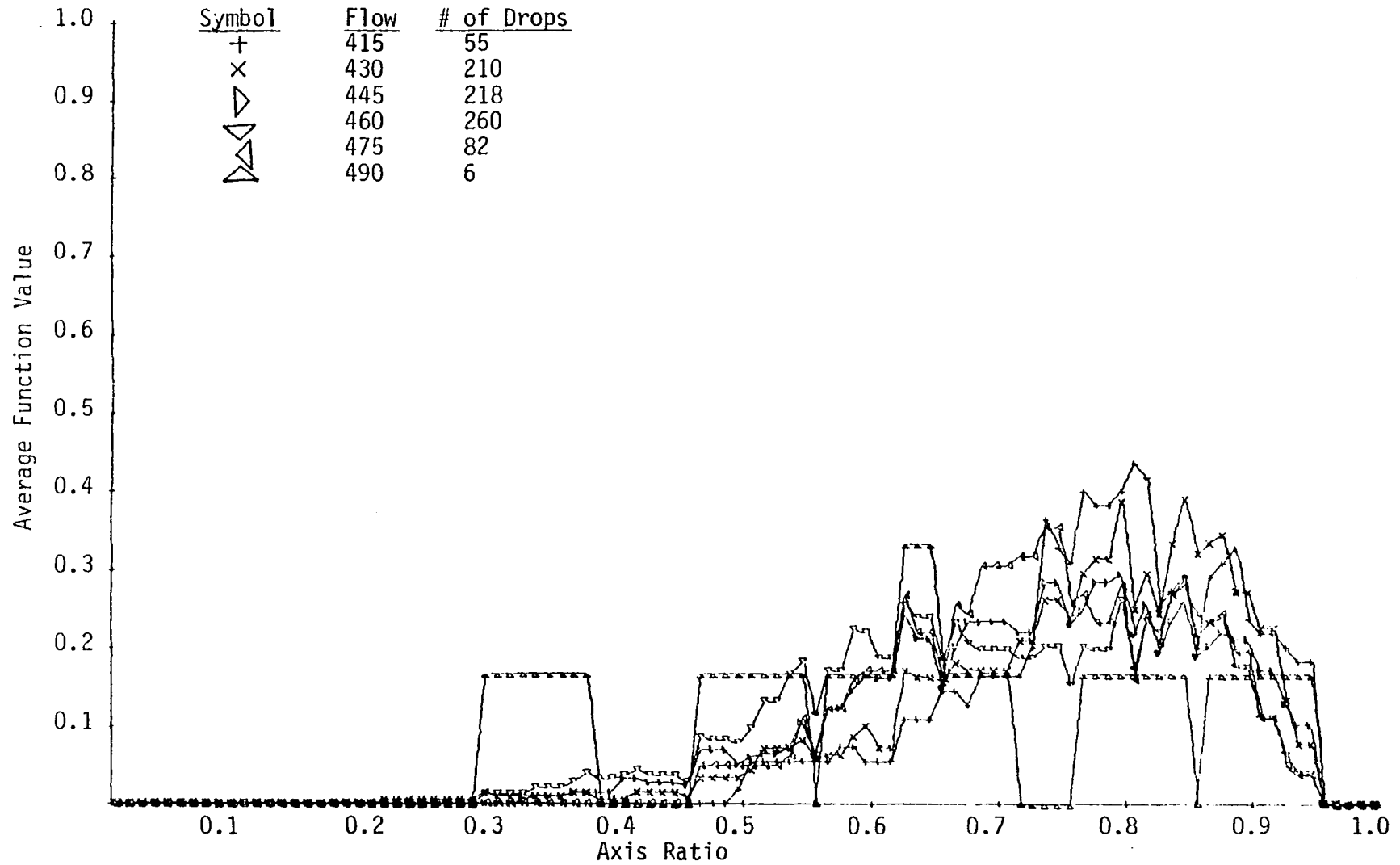
Figure 38c. The Average Function Value of the Axis Ratio Distribution (small droplets) of Flow Rate 4.

Symbol	Flow	# of Drops
+	415	48
×	430	267
▷	445	492
▽	460	207
◁	475	38
△	490	12
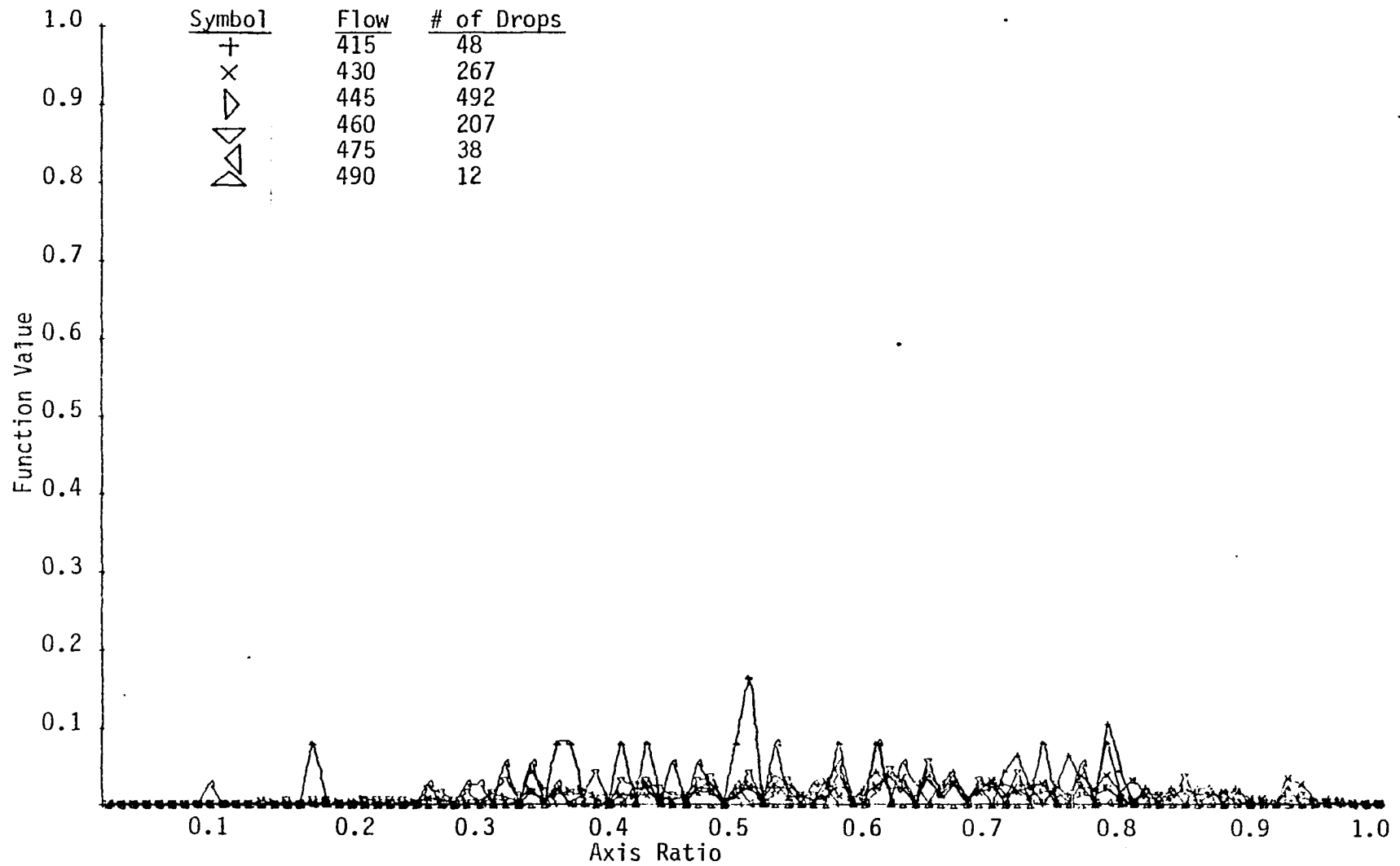
Figure 39a. The Function Value of the Axis Ratio Distribution (large droplets) of Flow Rate 4.
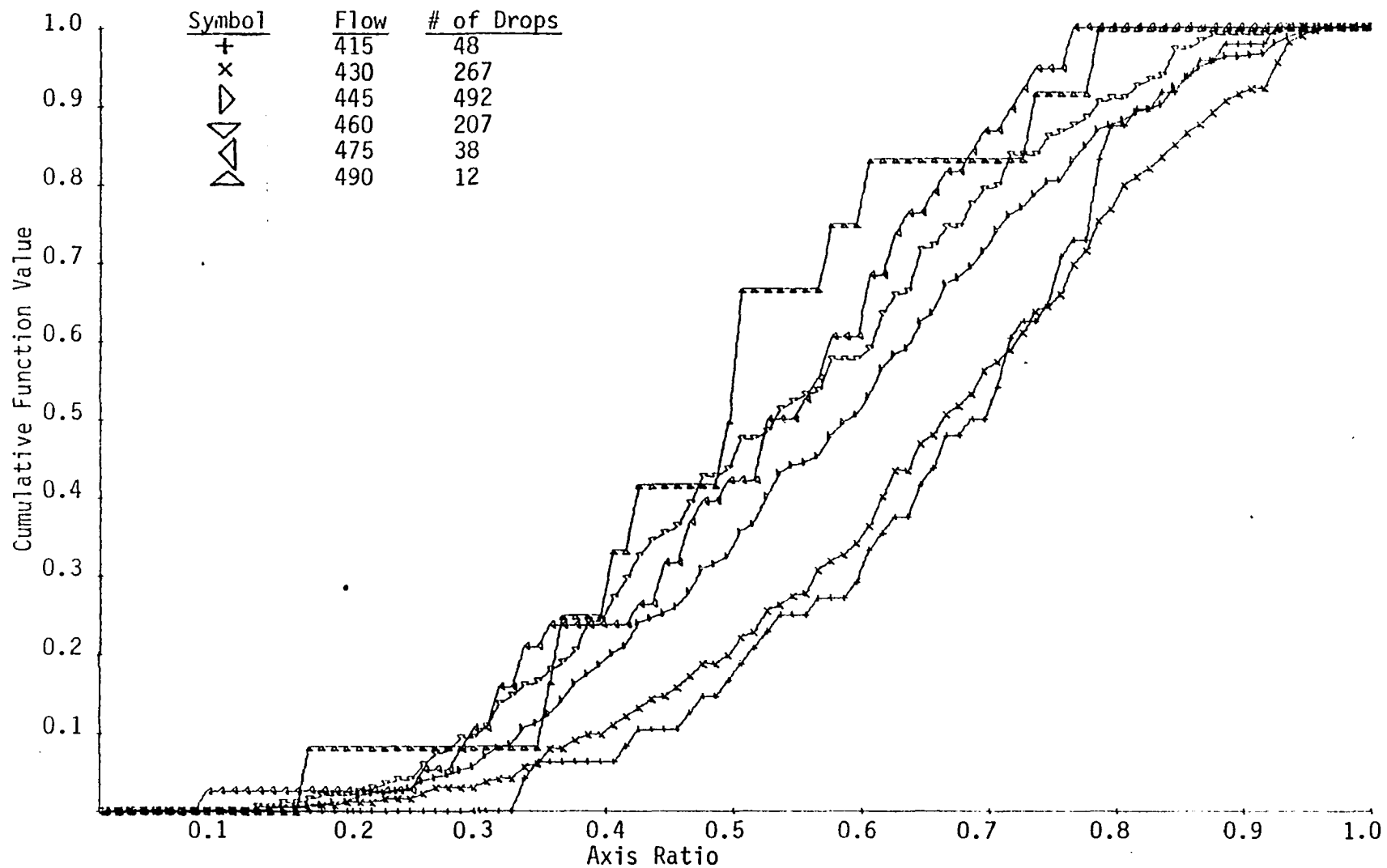
Figure 39b. The Cumulative Function Value of the Axis Ratio Distribution (large droplets) of Flow Rate 4.
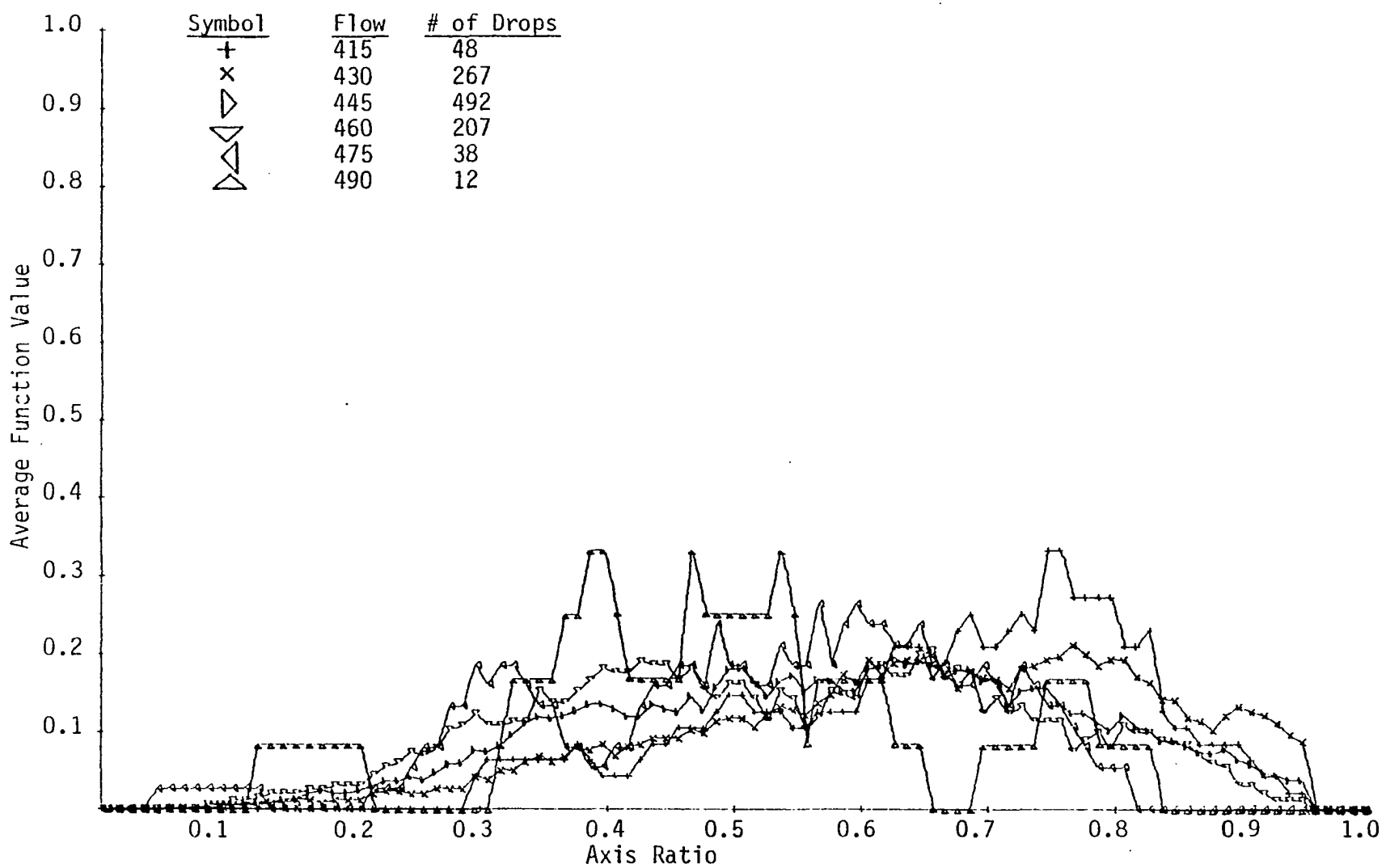
Figure 39c. The Average Function Value of the Axis Ratio Distribution (large droplets)
of Flow Rate 4.

Symbol	Flow	# of Drops
+	415	108
×	430	508
▷	445	737
▽	460	503
◁	475	123
△	490	19

Function Value

Relative Radial Position
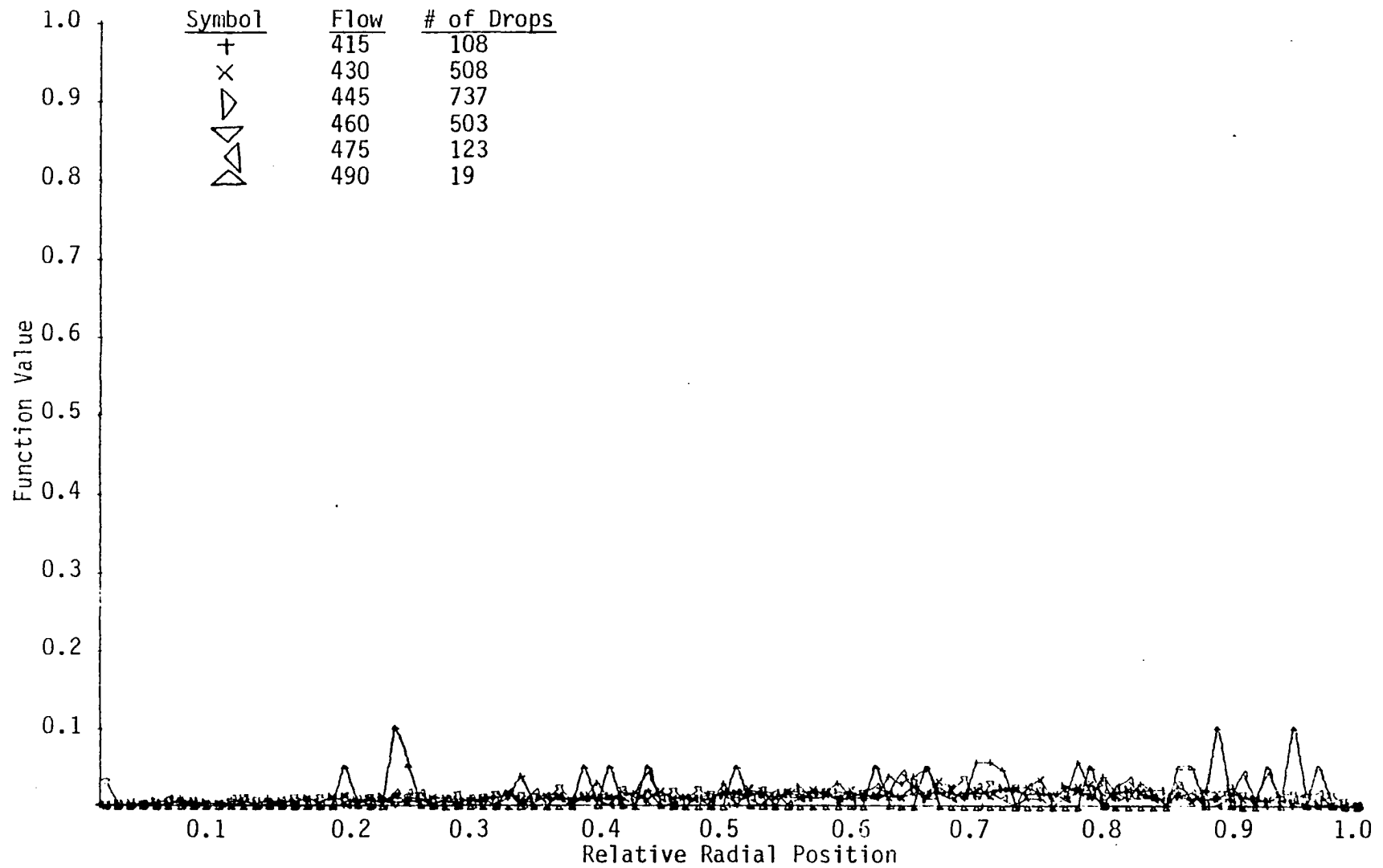
Figure 40a.   The Function Value of the Relative Radial Position Distribution (constant radius increments) of Flow Rate 4.
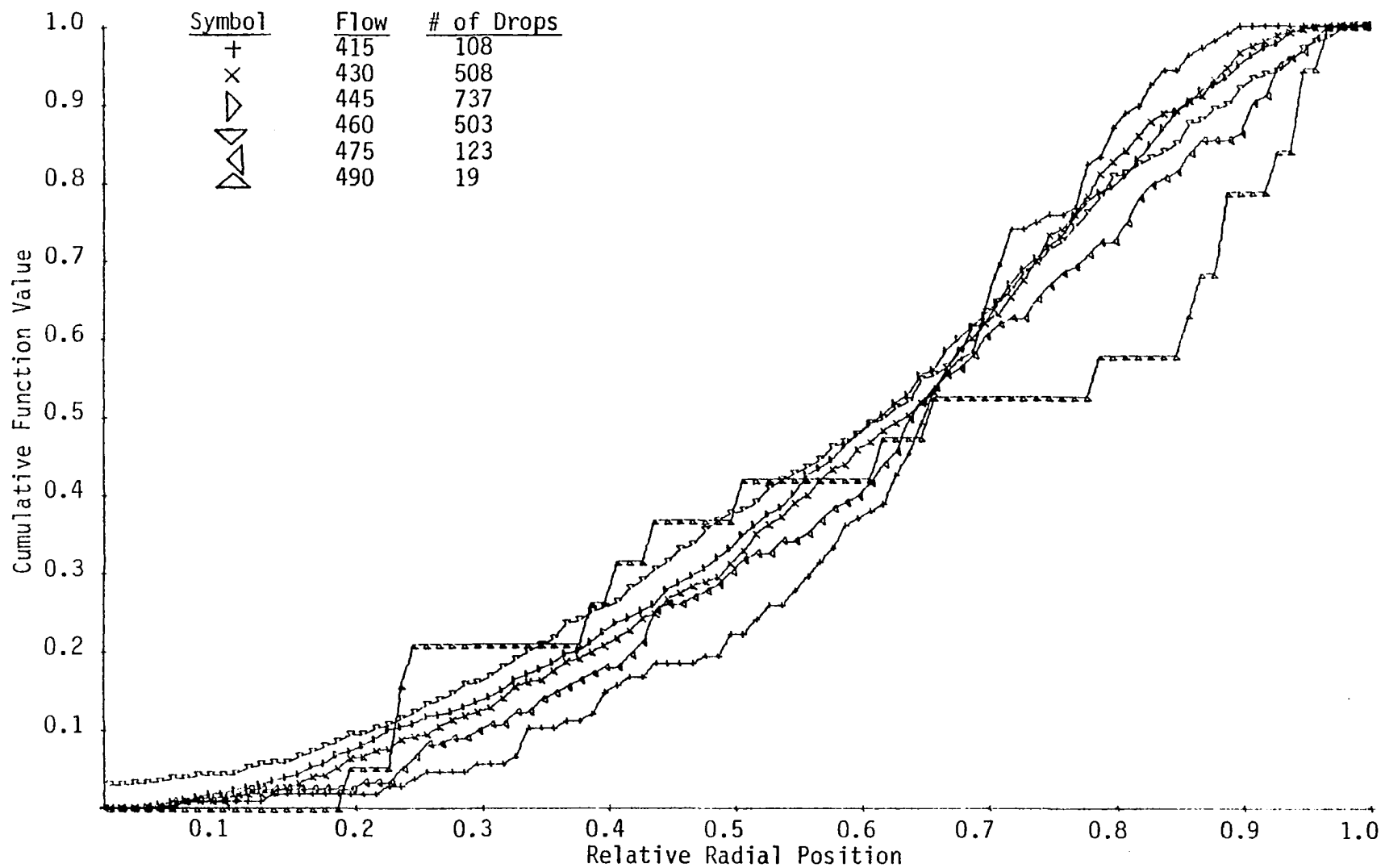
Figure 40b. The Cumulative Function Value of the Relative Radial Position Distribution (constant radius increments) of Flow Rate 4.
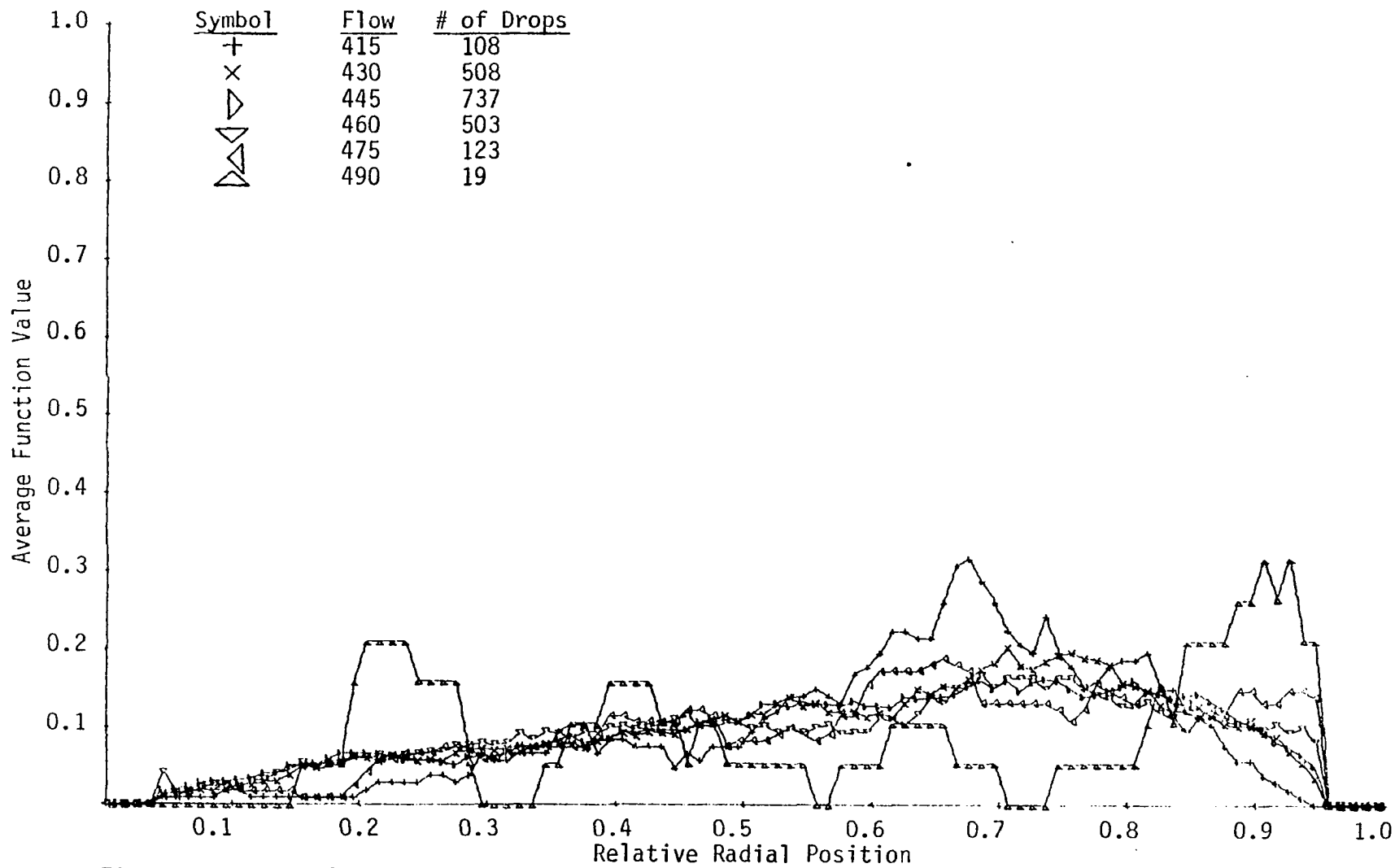
Figure 40c. The Average Function Value of the Relative Radial Position Distribution (constant radius increments) of Flow Rate 4.
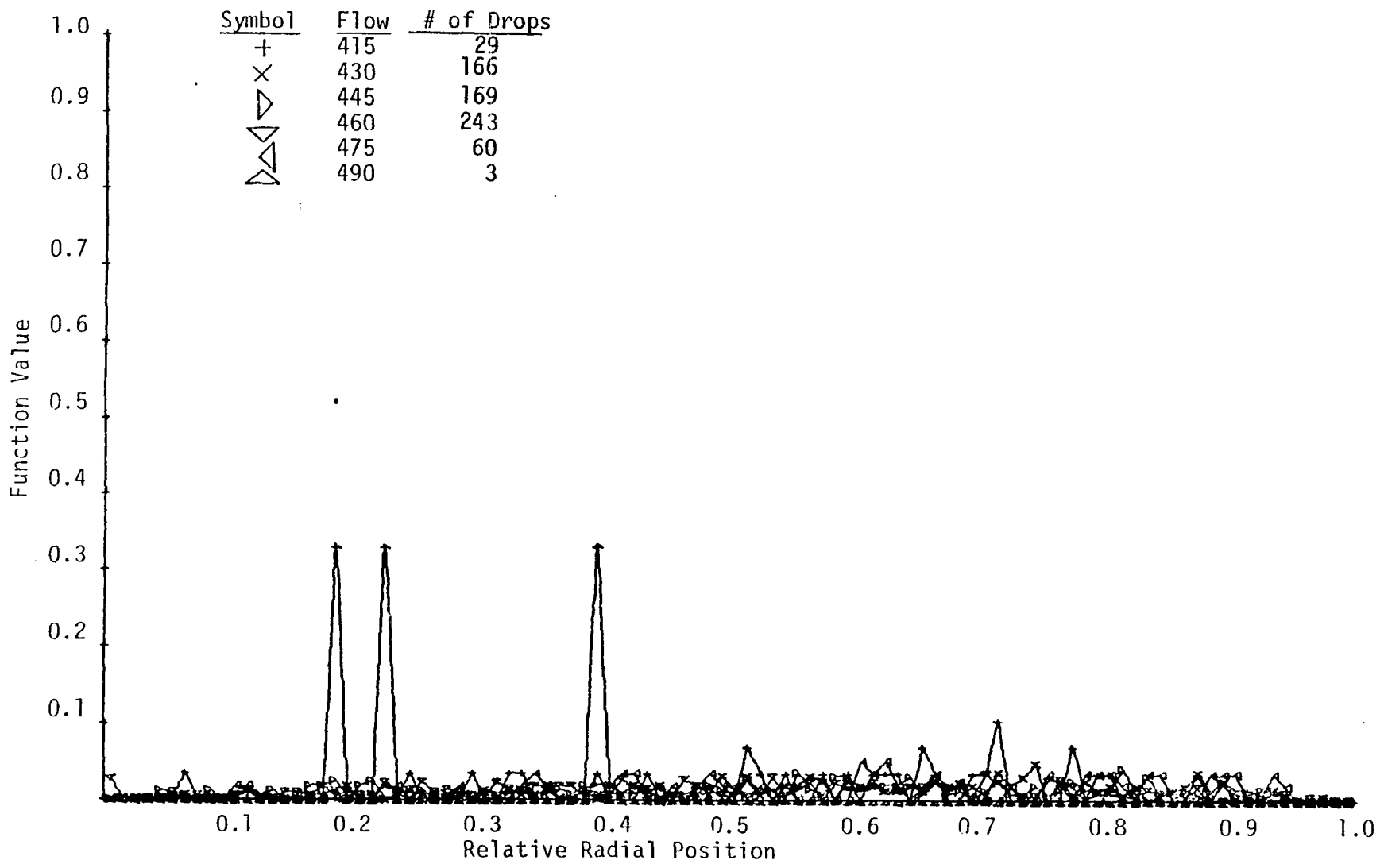
Figure 41a. The Function Value of the Relative Radial Position Distribution (small droplets) (constant radius increments) of Flow Rate 4.
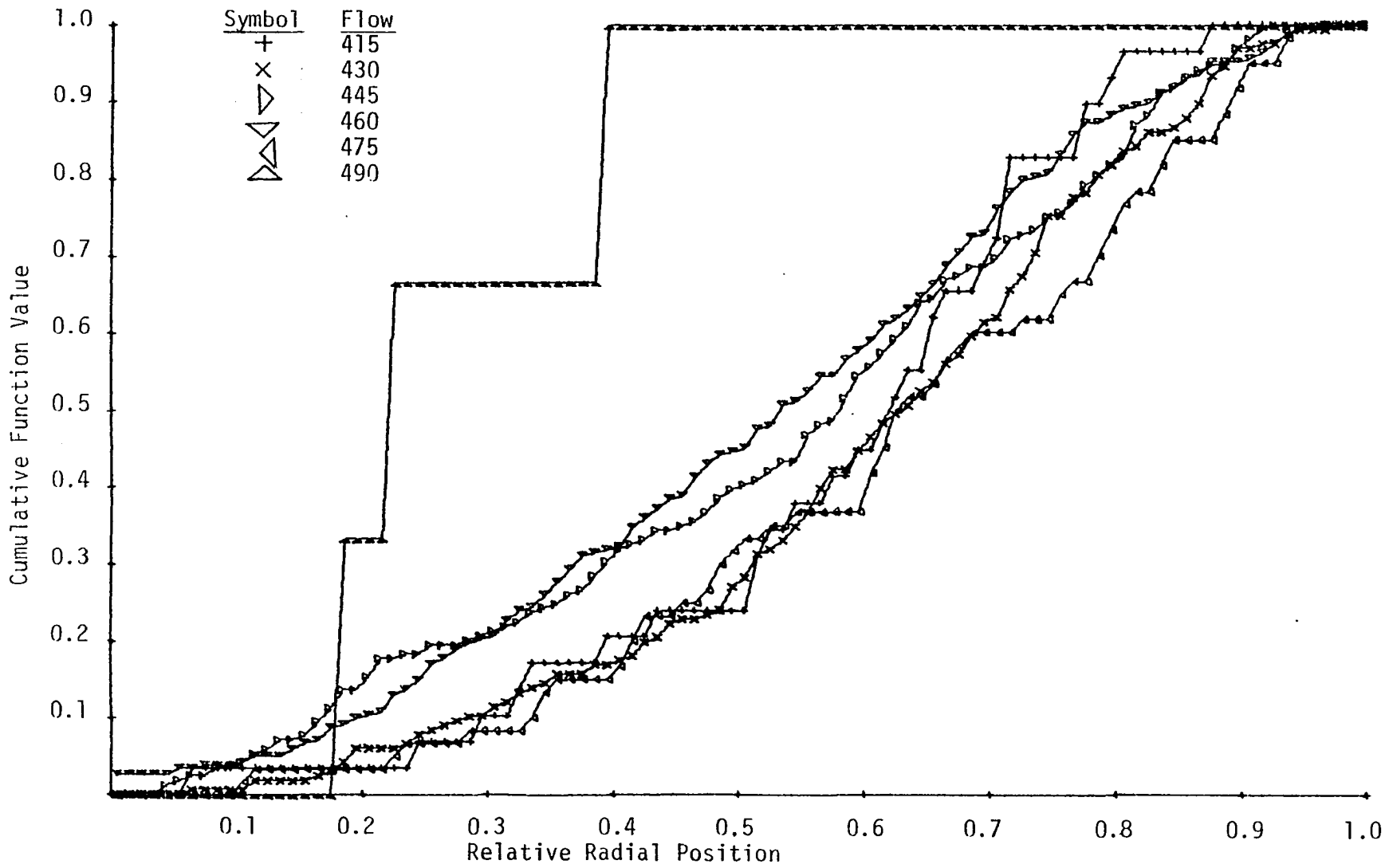
Figure 41b.   The Cumulative Function Value of the Relative Radial Position Distribution (small droplets) (constant radius increments) of Flow Rate 4.

135
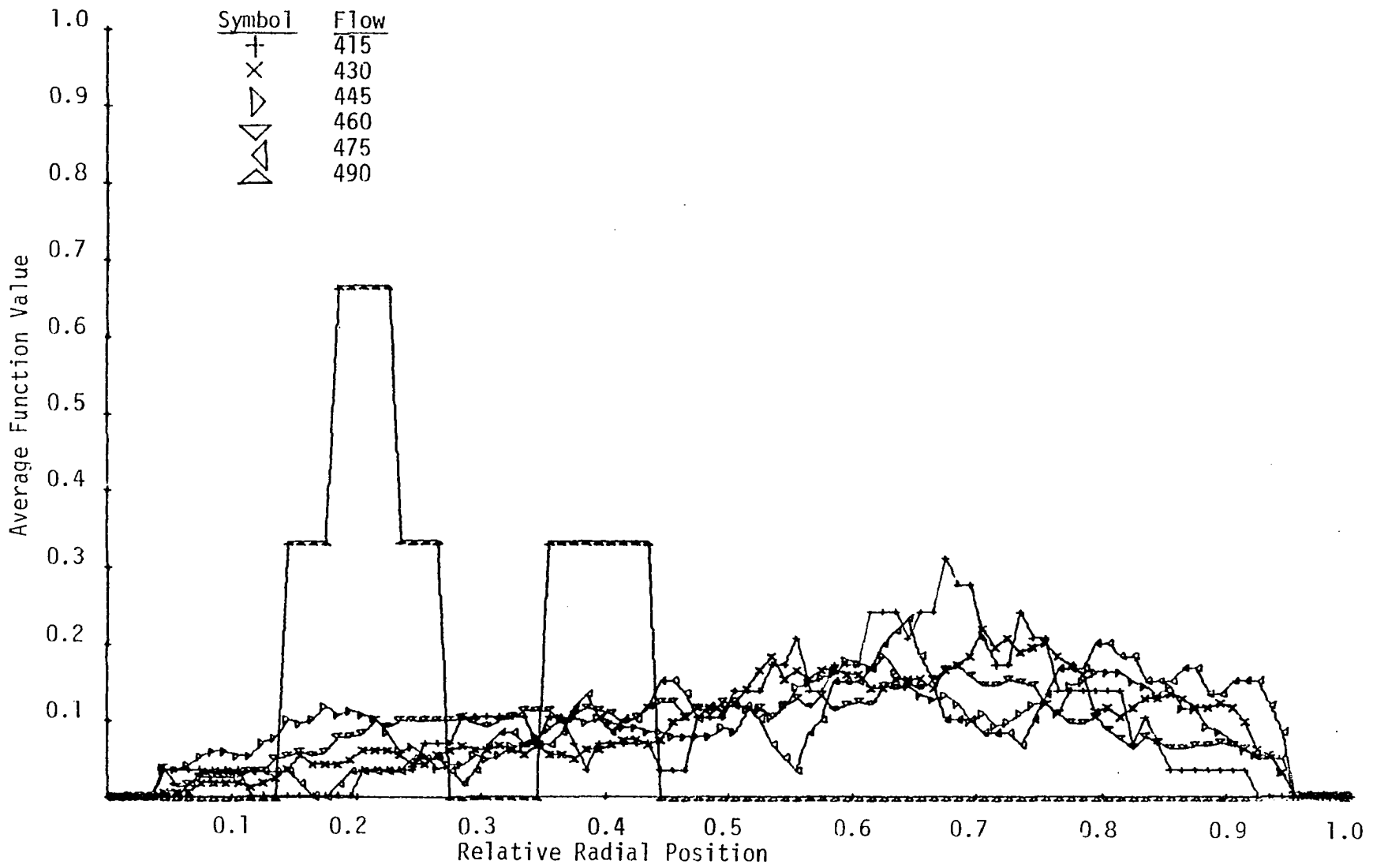
Figure 41c. The Average Function Value of the Relative Radial Position Distribution (small droplets) (constant radius increments) of Flow Rate 4.

Symbol	Flow	# of Drops
+	415	79
×	430	342
▷	445	568
▽	460	260
◁	475	6?
△	490	
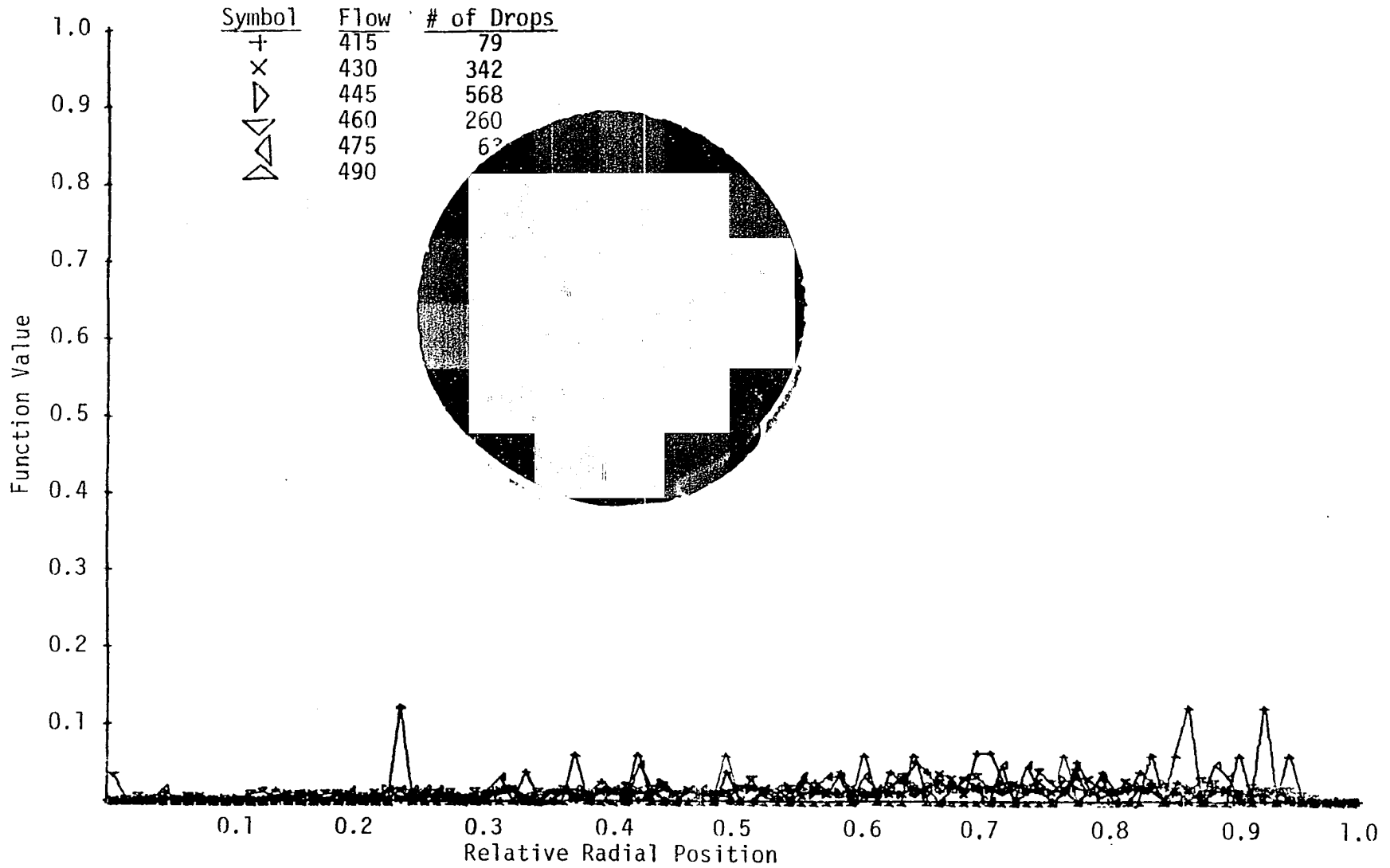
Figure 42a. The Function Value of the Relative Radial Position Distribution (large droplets) (constant radius increments) of Flow Rate 4.
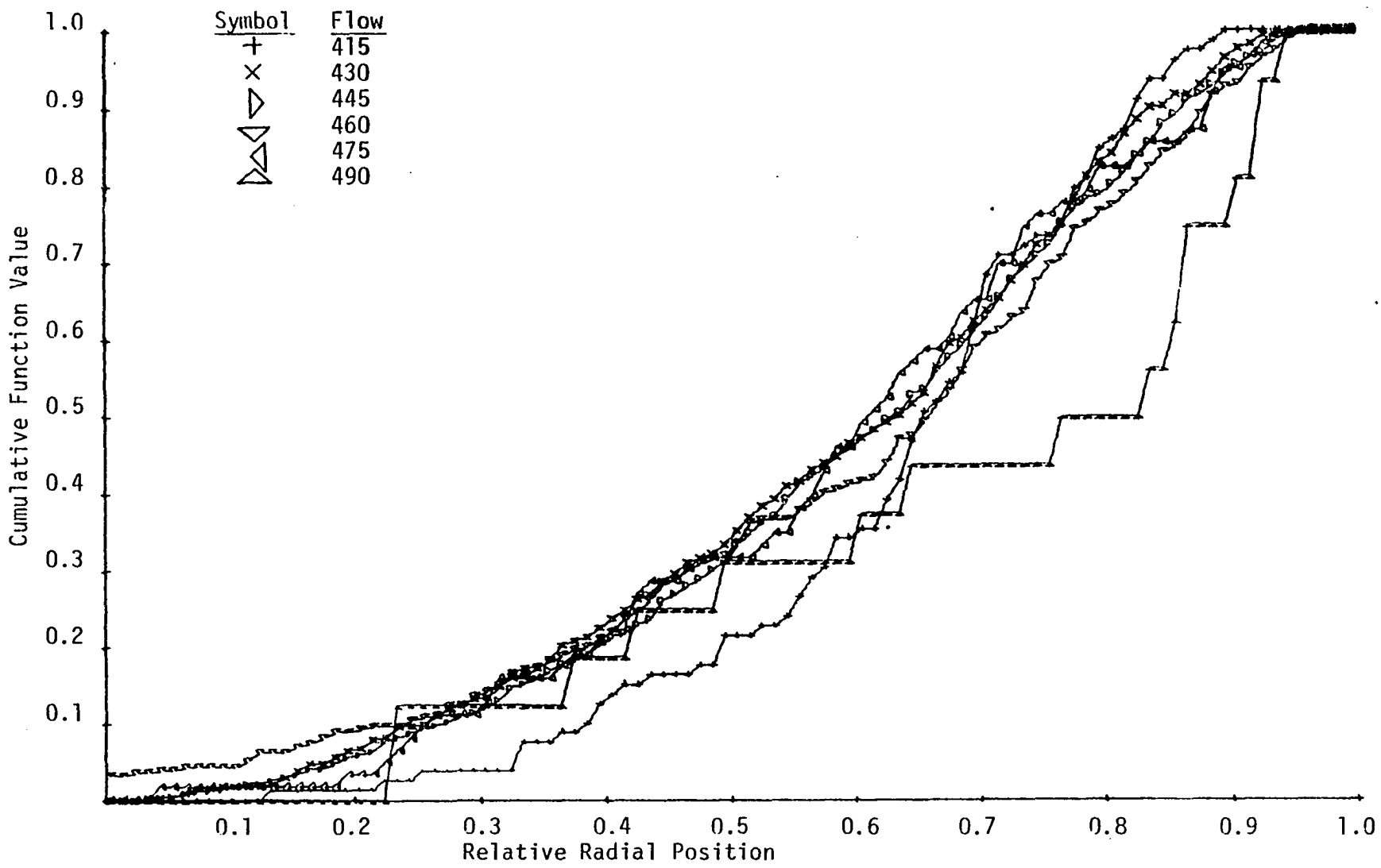
Figure 42b. The Cumulative Function Value of the Relative Radial Position Distribution (large droplets) (constant radius increments) of Flow Rate 4.
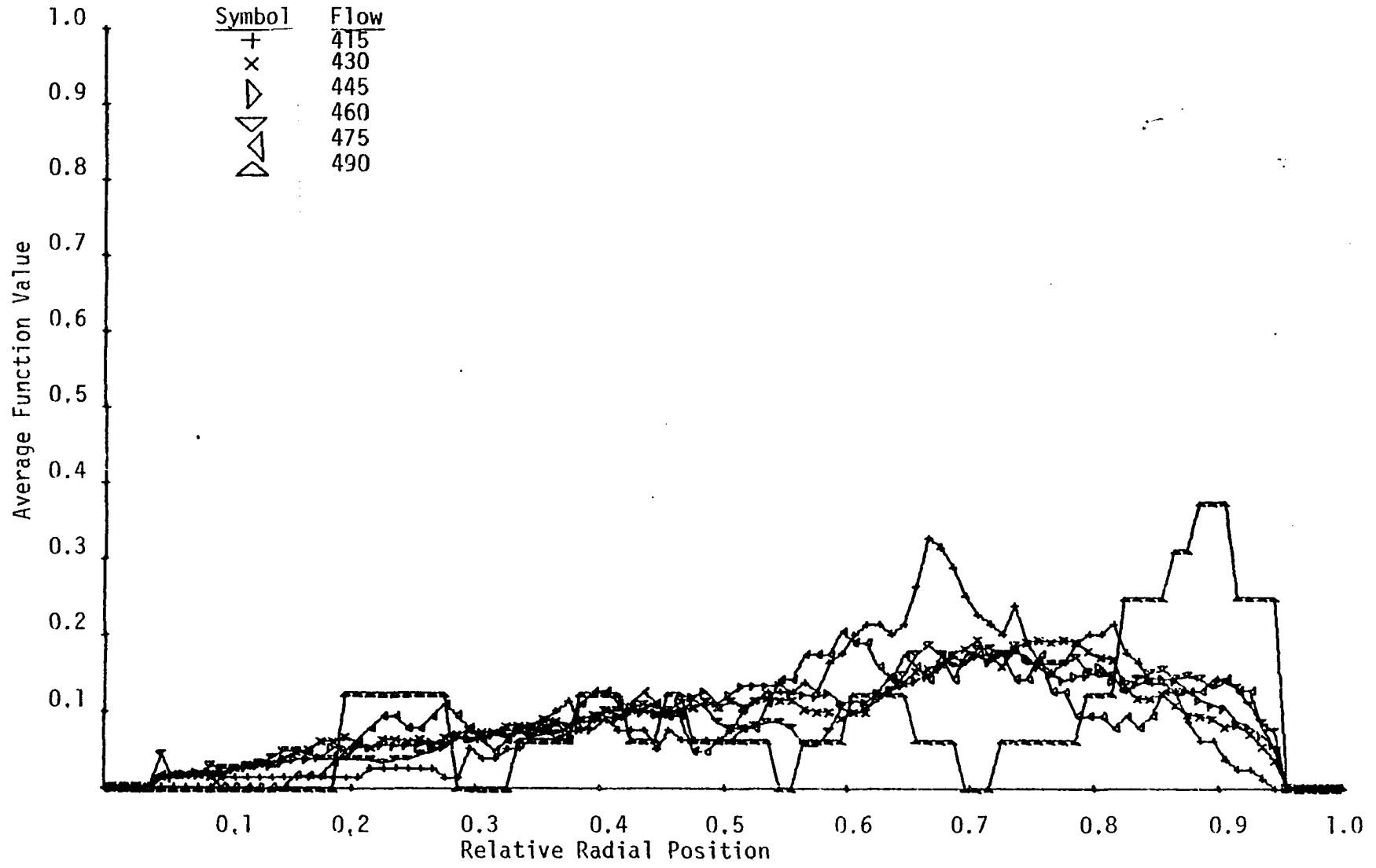
Figure 42c. The Average Function Value of the Relative Radial Position Distribution (large droplets) (constant radius increments) of Flow Rate 4.
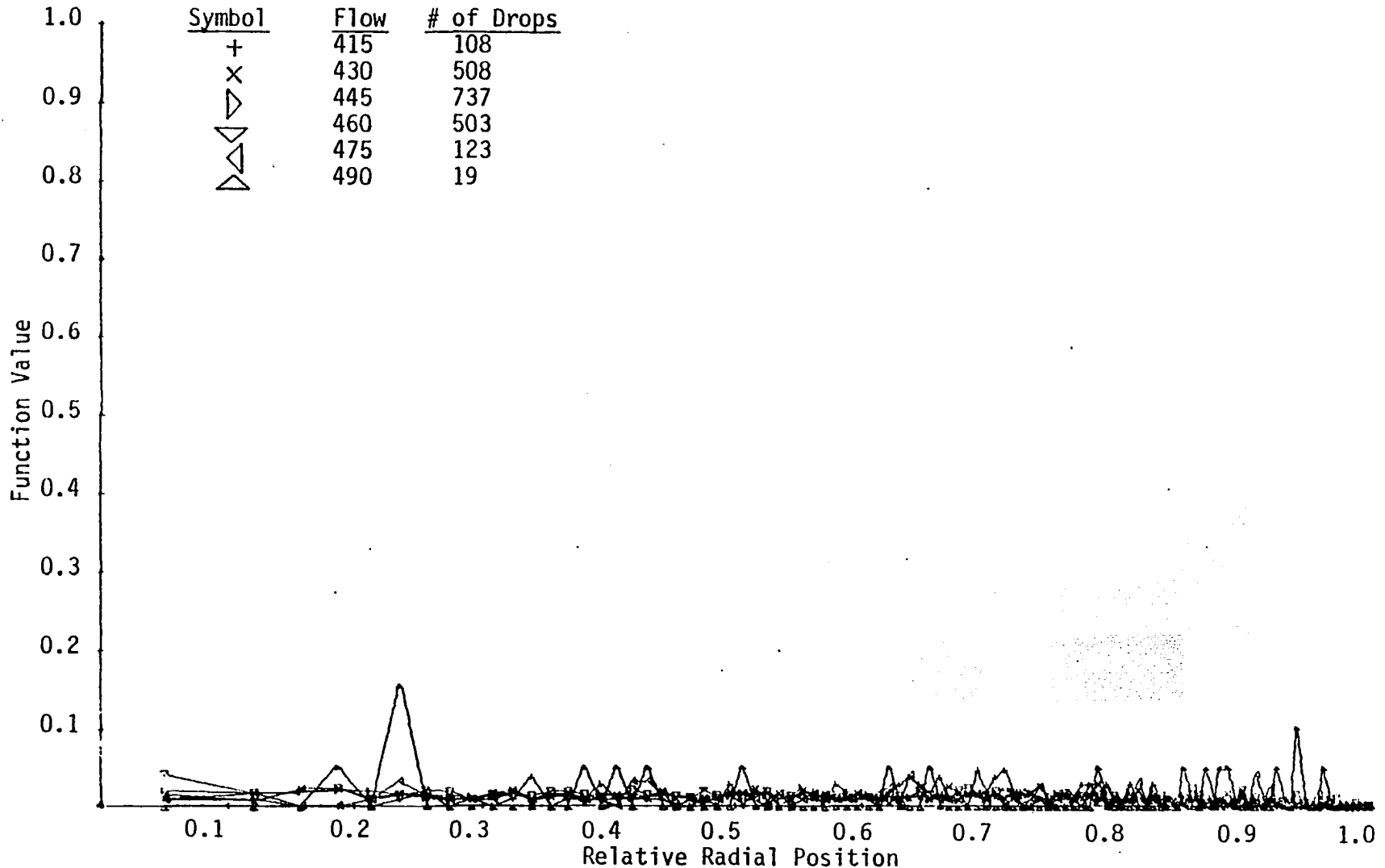
Figure 43a. The Function Value of the Relative Radial Position Distribution (constant area increments) of Flow Rate 4.

Symbol	Flow	# of Drops
+	415	108
×	430	508
▷	445	737
▽	460	503
◁	475	123
△	490	19
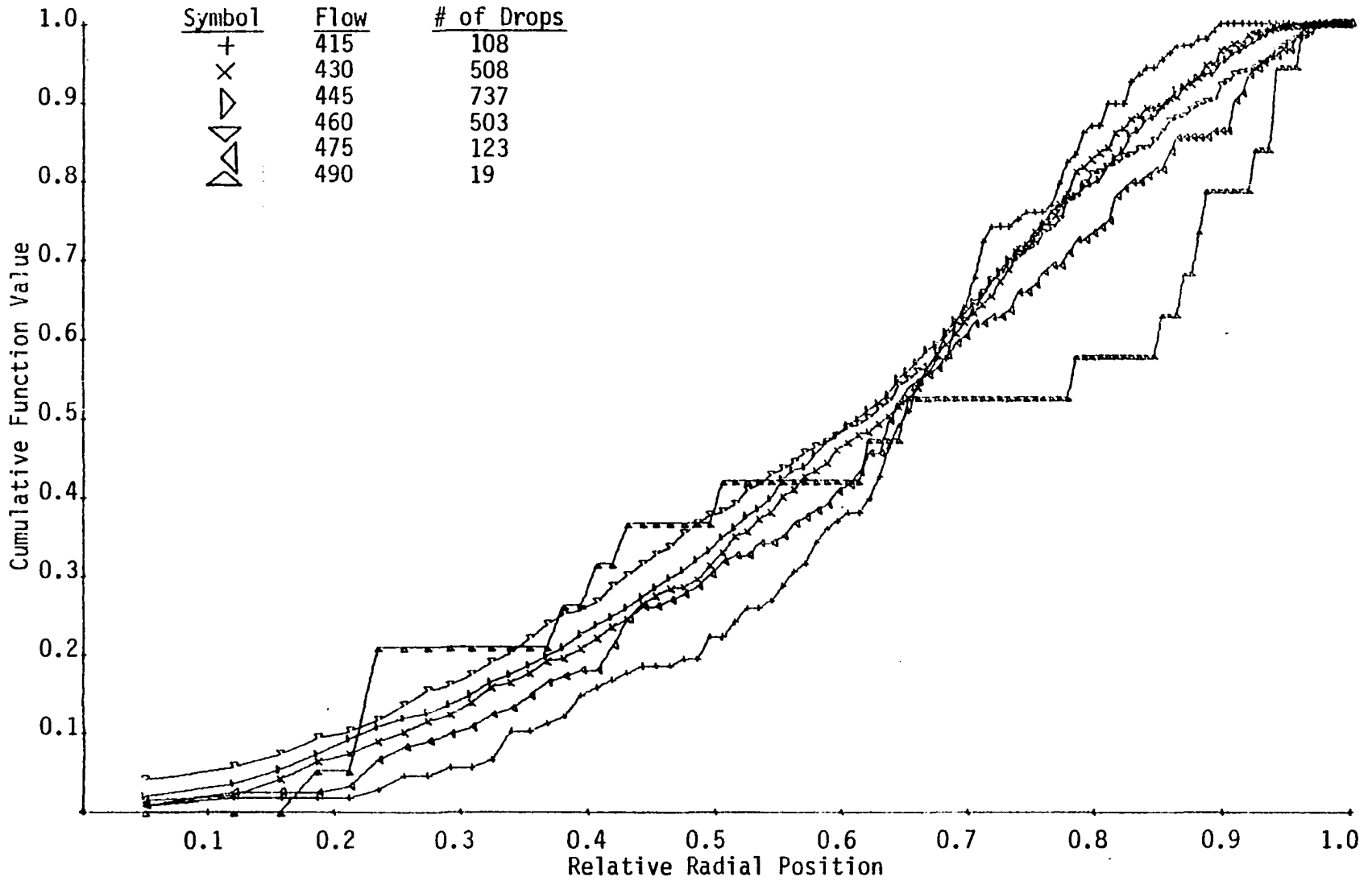
Figure 43b. The Cumulative Function Value of the Relative Radial Position Distribution (constant area increments) of Flow Rate 4.

Symbol	Flow	# of Drops
+	415	108
×	430	508
▷	445	737
▽	460	503
◁	475	123
△	490	19

Average Function Value

Relative Radial Position
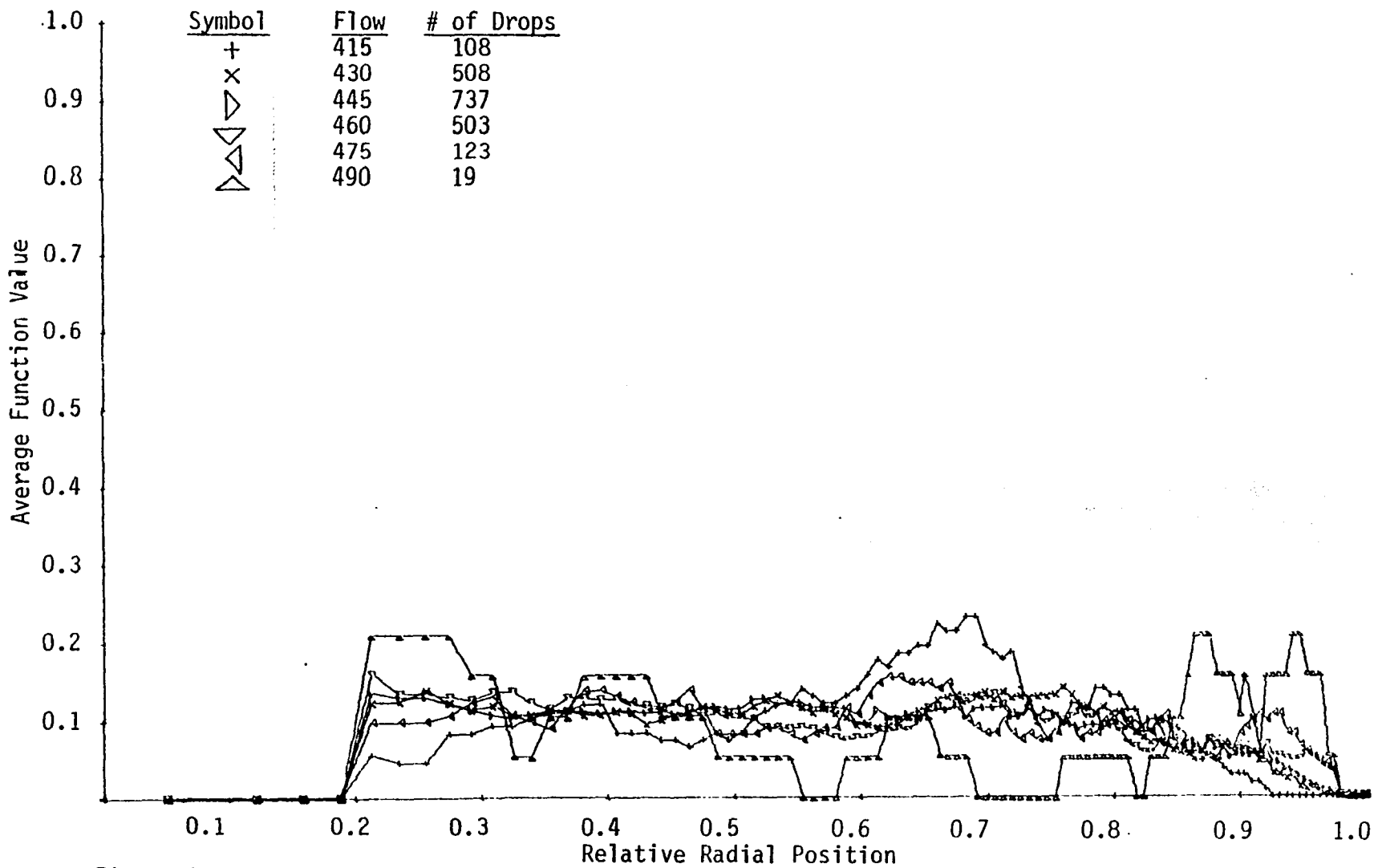
Figure 43c. The Average Function Value of the Relative Radial Position Distribution (constant area increments) of Flow Rate 4.

and Table IV relates the figure numbers for the distribution curves to each of the base variables and for each of the flow rates. When looking at trends from these curves it should be realized that those flow conditions which have the fewest number of droplets in their total droplet population, such as the high quality flows, will tend to show large spikes and steep gradients when incremented along the base variable value.

An example of how Figures 8 through 43 can be used to describe the droplet distribution is shown as follows. Figures 8c, 17c, 26c and 35c show the major axis dimension range of .02 to .04 inches to be the most common for droplets at all flow rates and for all qualities. Table V shows the average major axis and average minor axis for each flow condition. In general, the size of the droplets decreased slightly when both the flow rates and the qualities were increased.

Figures 9c, 18c, 27c and 36c show the most common equivalent diameter range to be from .02 to .03 inches for all flow conditions. A tabulated value of the average equivalent diameter in Table V is seen to be approximately constant for all flow conditions. The equivalent diameter is found by equating the area of an ellipse to the area of a circular droplet as follows,

$$\frac{\pi d_{eq}^2}{4} = \frac{\pi ab}{4} \ .$$

Solving for d_{eq},

Table V. Average Flow and Droplet Data.

Flow Condition Number	Average Major Axis (inches)	Average Minor Axis (inches)	Average Equivalent Diameter (inches)	Average Axis Ratio	Average Radial Position (inches)	Average Relative Radial Position
120	0.048	0.024	0.033	0.535	0.368	0.585
130	0.055	0.031	0.041	0.607	0.367	0.584
145	0.061	0.034	0.044	0.606	0.328	0.524
160	0.063	0.035	0.046	0.634	0.392	0.624
190	0.041	0.024	0.031	0.622	0.353	0.561
230	0.061	0.034	0.044	0.637	0.354	0.564
245	0.039	0.022	0.029	0.594	0.353	0.561
260	0.037	0.023	0.029	0.652	0.367	0.584
275	0.035	0.023	0.028	0.657	0.390	0.620
290	0.066	0.042	0.052	0.661	0.398	0.633
315	0.040	0.026	0.032	0.693	0.318	0.505
330	0.045	0.026	0.034	0.636	0.358	0.569
345	0.035	0.019	0.025	0.582	0.373	0.593
360	0.038	0.023	0.028	0.657	0.354	0.563
375	0.041	0.023	0.030	0.589	0.383	0.608
390	0.046	0.025	0.033	0.610	0.377	0.600
415	0.034	0.024	0.029	0.737	0.389	0.619
430	0.036	0.025	0.030	0.718	0.374	0.594
445	0.044	0.026	0.033	0.646	0.370	0.588
460	0.032	0.019	0.024	0.653	0.362	0.575
475	0.030	0.019	0.023	0.671	0.392	0.624
490	0.038	0.020	0.027	0.564	0.396	0.629

$$d_{eq} = \sqrt{ab}$$

where d_{eq} is the equivalent diameter, a is the major axis and b is the minor axis of the droplets.

It is of interest to compare these values of equivalent diameter to values used for droplet sizes in literature. Due to incomplete droplet data for most flow conditions, typical values are usually assumed rather than calculated. Crowe, et.al.,[44] assume three typical droplet diameters of .0291, .0394 and .0543 inches for use in their models. These values are in excellent agreement with the average equivalent diameter listed for each of the flow conditions in Table V. Using Figures 9b, 18b, 27b and 36b it can be seen that equivalent droplet diameters of .029 to .055 inches account for approximately 40% of all the droplets while increasing the range from .020 to .055 inches would account for approximately 75% of all the droplets.

Figures 10c, 19c, 28c and 37c show the most common axis ratio to range from .6 and .85 for all flow conditions. In addition, a comparison of Figures 11, 20, 29 and 38 for small droplets (i.e., droplets having major axis less than 0.025 inches) and Figures 12, 21, 30 and 39 for large droplets show that small droplets have their most common axis ratio between .7 and .8 while the large droplets have a more even distribution of droplets across all axis ratio values, with the most common axis ratio usually being slightly less

than for the corresponding distribution curve for the small droplets at the same flow conditions. This means that the small droplets tend to be more circular in shape while the larger droplets are more elliptical in shape.

Figures 13c, 22c, 31c and 40c show the relative radial position of all droplets based on constant radius increments. It is not surprising that the most common relative radial position usually occurs between .75 and .95 as with constant radius increments the droplets in a larger flow area are taken into account with each successive increment in the relative radial position. Comparison of Figures 14c, 23c, 32c and 41c for droplets with major axis dimensions less than 0.03 inches with Figures 15c, 24c, 33c and 42c for larger droplets show distributions relating relative radial position do not vary significantly from each other.

Figures 16c, 25c, 34c and 43c show the relative radial position based on constant area increments for all droplets at all flow conditions. In contrast with the constant radial increment distribution curves these Average Function Values are relatively constant for a much wider range of the relative radial position scale. Table V shows the average radial position and the average relative radial position to be approximately a constant for all flow conditions regardless of the gas flow rate and the quality.

Other Droplet and Flow Pattern Data Results

In addition to the distribution functions there are a number of other droplet and flow pattern quantities which are a direct result of the two phase flow data obtained in this study. One such quantity was the average area due to wave blockage inside the gas core area as determined by r_g. Using a computer program the average wave blockage area, A_W, for each slide was determined and the standard deviation, σ_W, of the wave blockage area was calculated for each flow condition as given by

$$\sigma_W = \sum_{i=1}^{n} \sqrt{\frac{A_W^2 - A_{Wi}^2}{n - 1}}$$

where A_{Wi} is the wave area for each individual slide, A_W is the average wave blockage for all the slides at a given flow condition, and n is the total number of slides at each given flow condition. Since there was considerable scatter in the data, as indicated by values of σ_W which are in the range of 50% of the value of A_W, the curves of A_W versus quality for the different flow rates were not clear and distinct from one another. For this reason the results are tabulated in Table VI instead of presented graphically. In general, however, the trend was toward less wave blockage area as the quality increased and also as the gas flow rate increased.

In a similar manner the blockage area caused by each droplet was calculated by assuming each droplet to be an

ellipse with a cross sectional area defined by

$$\text{Area} = \frac{\pi ab}{4}.$$

The total droplet blockage area for each slide can be determined and then an average droplet blockage area as well as the standard deviation of the droplet blockage area can be calculated for each flow condition. Again, the values of A_d and σ_d have been tabulated in Table VI due to the large scatter in the data and the crossing of A_d versus quality curves for the different flow rates. In much the same fashion as the wave blockage, the general trend was observed to be less droplet blockage area as the quality increased and also as the gas flow rate increased.

A total blockage in the gas core area can be described by a summation of the wave blockage area and the droplet blockage area. This combination blockage term was calculated and also tabulated in Table VI. Study of the combination blockage area shows its variation and trend to be well defined as a function of quality and gas flow rate as shown in Figure 44. The standard deviation, given in Table VI, was found to be much lower than the standard deviation for either A_w or A_d. This good correlation in combination blockage area suggested that there is a trade-off between the liquid film on the walls, especially the tips of the waves, and the droplets. This model was also confirmed photographically by Figures 45a, 45b and 46. These axial
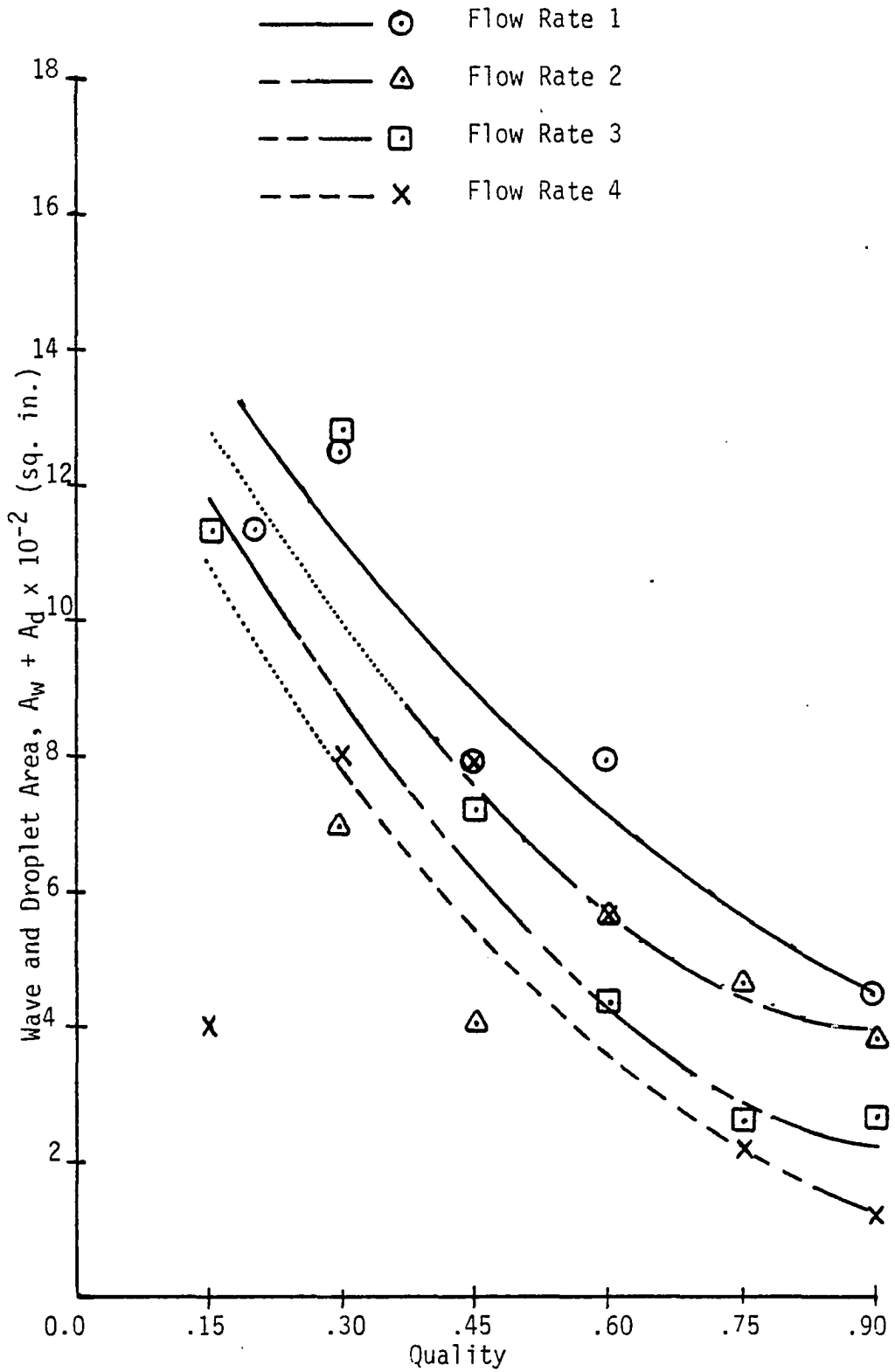
Figure 44. Wave and Droplet Blockage Area as a Function of Quality for Each Gas Flow Rate.

Table VI. Average Wave Blockage Area, Droplet Blockage Area and Combination Wave and Droplet Blockage Area For All Flow Conditions.

Flow Condition Number	Ave Wave Blockage Area - A_w (sq in)	Standard Deviation Of Wave Blockage Area - σ_w	Droplet Blockage Area - A_d (sq in)	Standard Deviation Of Droplet Blockage Area - σ_d	$A_w + A_d$ (sq in)	Standard Deviation of $A_w + A_d$ - σ_{wd}
120	.0636	.0342	.0395	.0228	.1031	.0253
130	.0844	.0233	.0403	.0376	.1247	.0460
145	.0574	.0201	.0214	.0175	.0789	.0260
160	.0606	.0377	.0179	.0121	.0784	.0382
190	.0293	.0107	.0152	.0082	.0446	.0164
230	.0423	.0258	.0265	.0159	.0688	.0352
245	.0315	.0184	.0086	.0083	.0401	.0201
260	.0467	.0166	.0101	.0083	.0568	.0190
275	.0430	.0194	.0038	.0023	.0469	.0188
290	.0307	.0224	.0081	.0087	.0388	.0258
315	.0793	.0280	.0344	.0086	.1136	.0306
330	.0686	.0477	.0591	.0264	.1278	.0482
345	.0476	.0235	.0246	.0135	.0722	.0238
360	.0333	.0183	.0096	.0063	.0429	.0226
375	.0229	.0114	.0035	.0041	.0264	.0129
390	.0254	.0102	.0010	.0017	.0264	.0099
415	.0254	.0131	.0161	.0064	.0415	.0107
430	.0479	.0328	.0328	.0158	.0807	.0229
445	.0270	.0140	.0518	.0311	.0788	.0375
460	.0420	.0161	.0154	.0082	.0574	.0171
475	.0185	.0068	.0035	.0029	.0220	.0071
490	.0122	.0084	.0008	.0010	.0130	.0083

Figure 45a. Axial Photograph Showing the Interchange Between Liquid Film on the Wall and the Droplets in the Core Region for Flow Condition 360, Slide No. 19.

Figure 45b.   Axial Photograph Showing the Interchange Between Liquid Film on the
Wall and the Droplets in the Core Region for Flow Condition 460,
Slide No. 35.
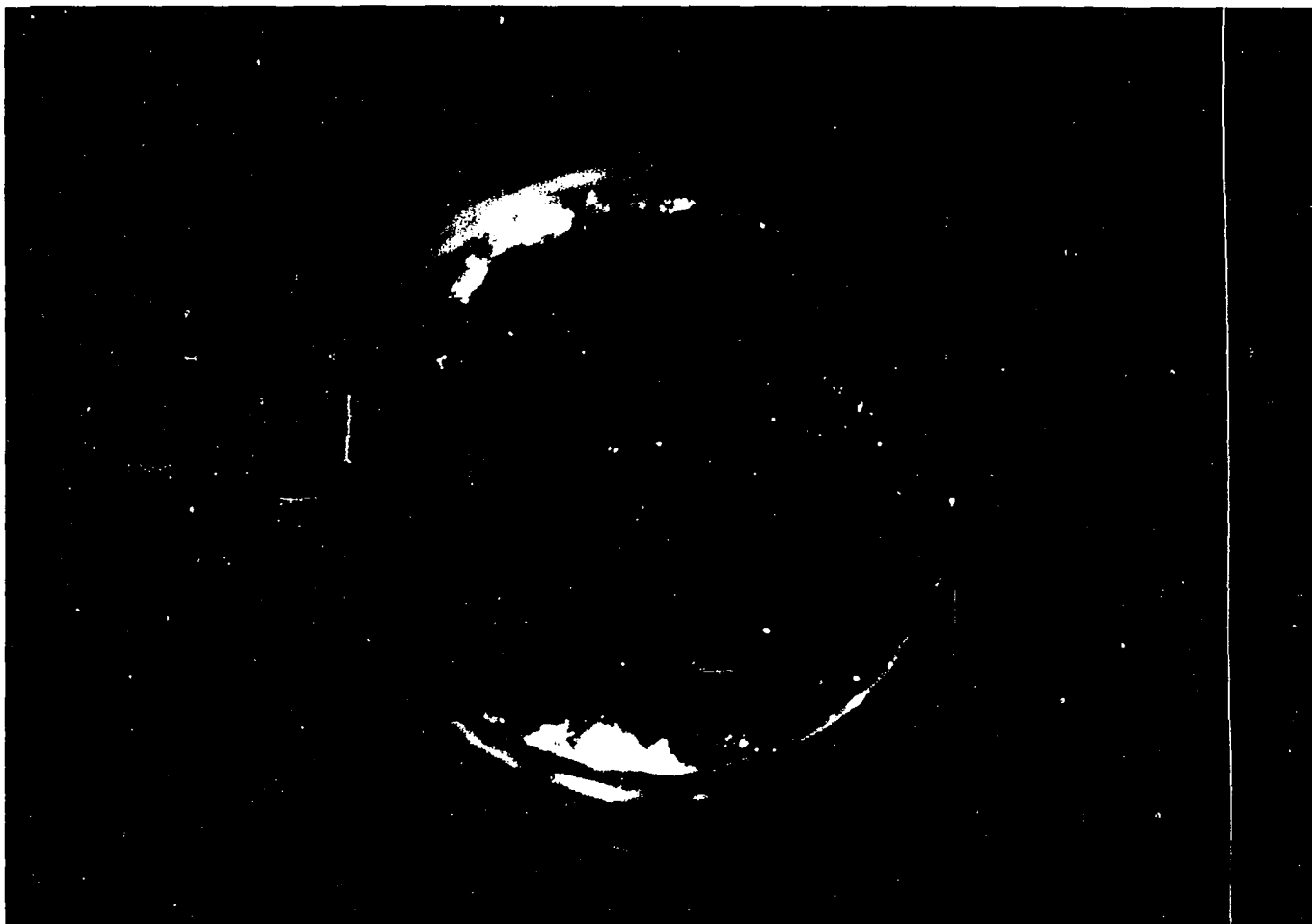
Figure 46. Axial Photograph Showing the Typical Blockage Due to Droplets and Waves in the Flow Tube (Flow Condition 445, Slide No. 4).

photographs for Flow Conditions 360, Slide No. 19, and 460,
Slide No. 35 respectively, show the gas "tearing" liquid
film from the wall and producing droplets in the gas core
area. This concept will be discussed further in Chapter IV
under the concept of the blockage factor. Figure 46 shows
a typical axial view of two phase flow, taken at Flow Condi-
tion 245, Slide No. 4, and shows the blockage that can exist
from the presence of droplets and waves in the flow tube.

Another factor of considerable interest which can be
obtained from axial photographs of two-phase flow data was
the thickness of the liquid film on the wall. In a manner
described earlier, the average liquid film thickness, δ_{ave},
was determined by calculating an equivalent gas core radius
from the gas core area measured by the planimeter. The dif-
ference between this gas core equivalent radius and the flow
tube radius is defined as δ_{ave}. The variation of δ_{ave} as a
function of quality at each of the gas flow rates has been
shown in Figure 47. Additional examination of Figure 6 sug-
gested that another liquid film thickness could be calcu-
lated if the tips of the waves which go inside the equiva-
lent gas core radius are thought of as "droplets" next to
the liquid film. The variation of liquid film thickness
with quality and gas flow rates using this definition will
be denoted by δ_r and has been shown in Figure 48. Figure 49
shows a comparison of δ_{ave} and δ_r for the lowest and highest
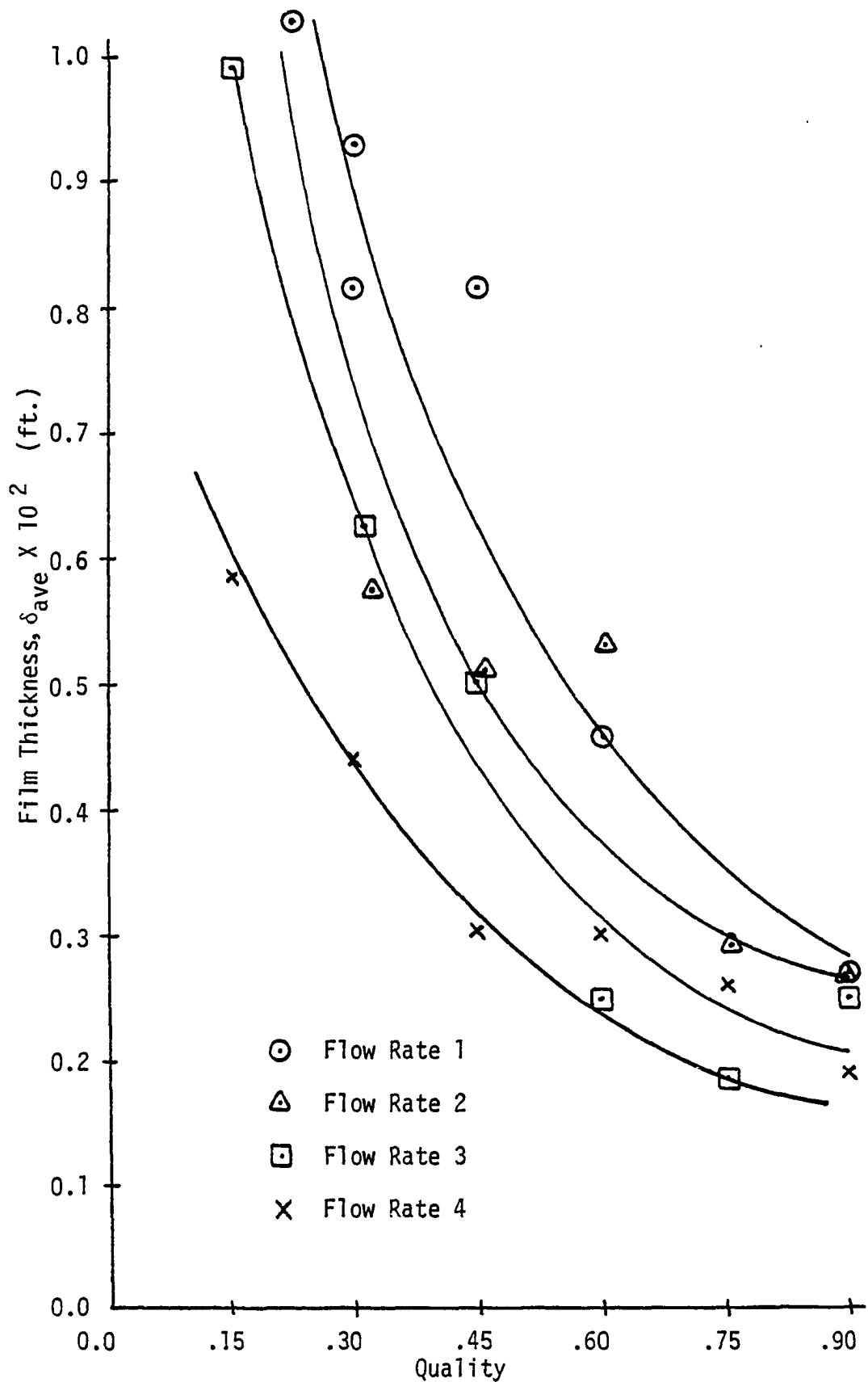
Figure 47. The Variation of Liquid Film Thickness, δ_{ave}, as a Function of Quality for Each Gas Flow Rate.
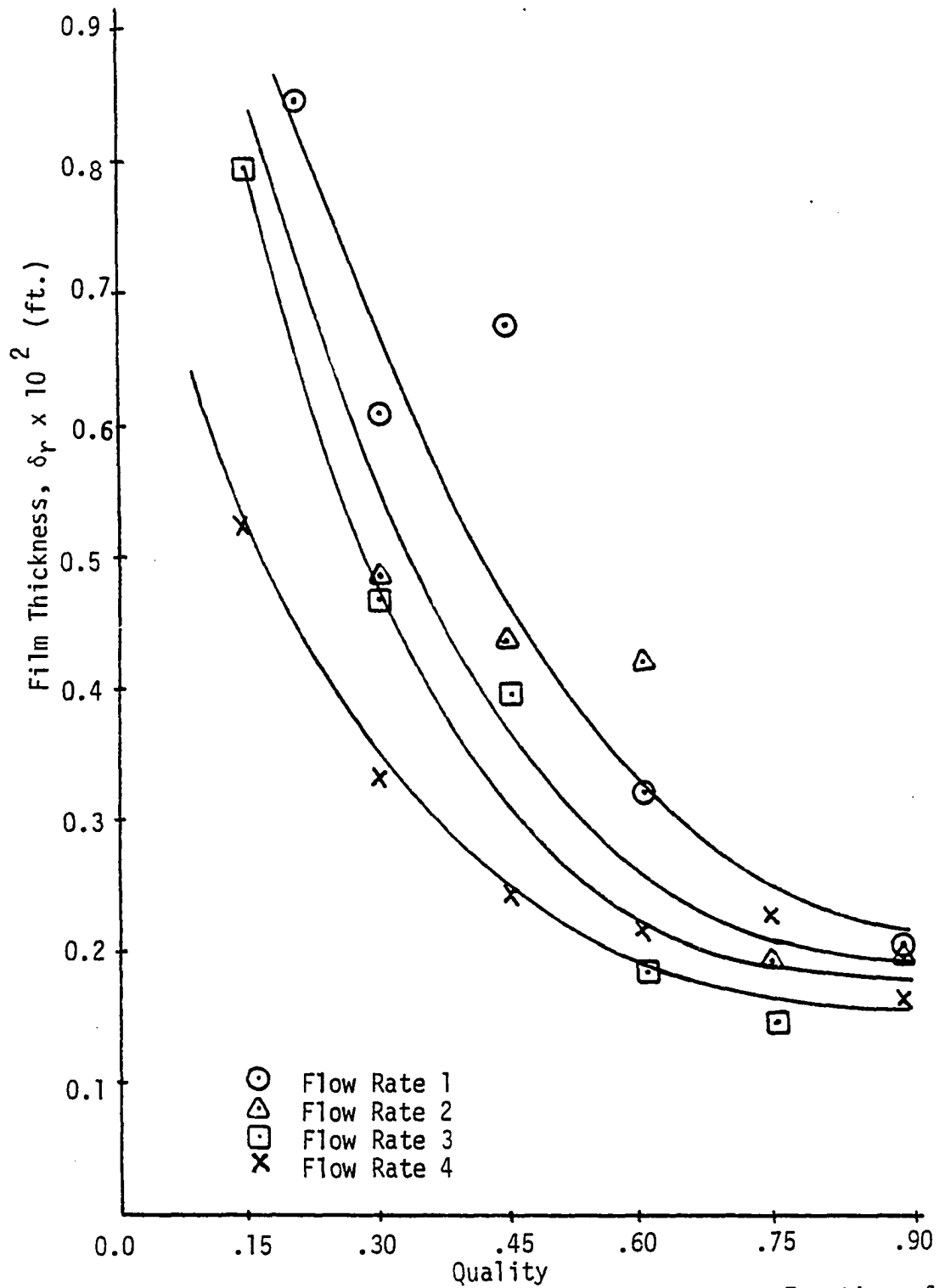
Figure 48. The Variation of Liquid Film Thickness, δ_r, as a Function of Quality for Each Gas Flow Rate.
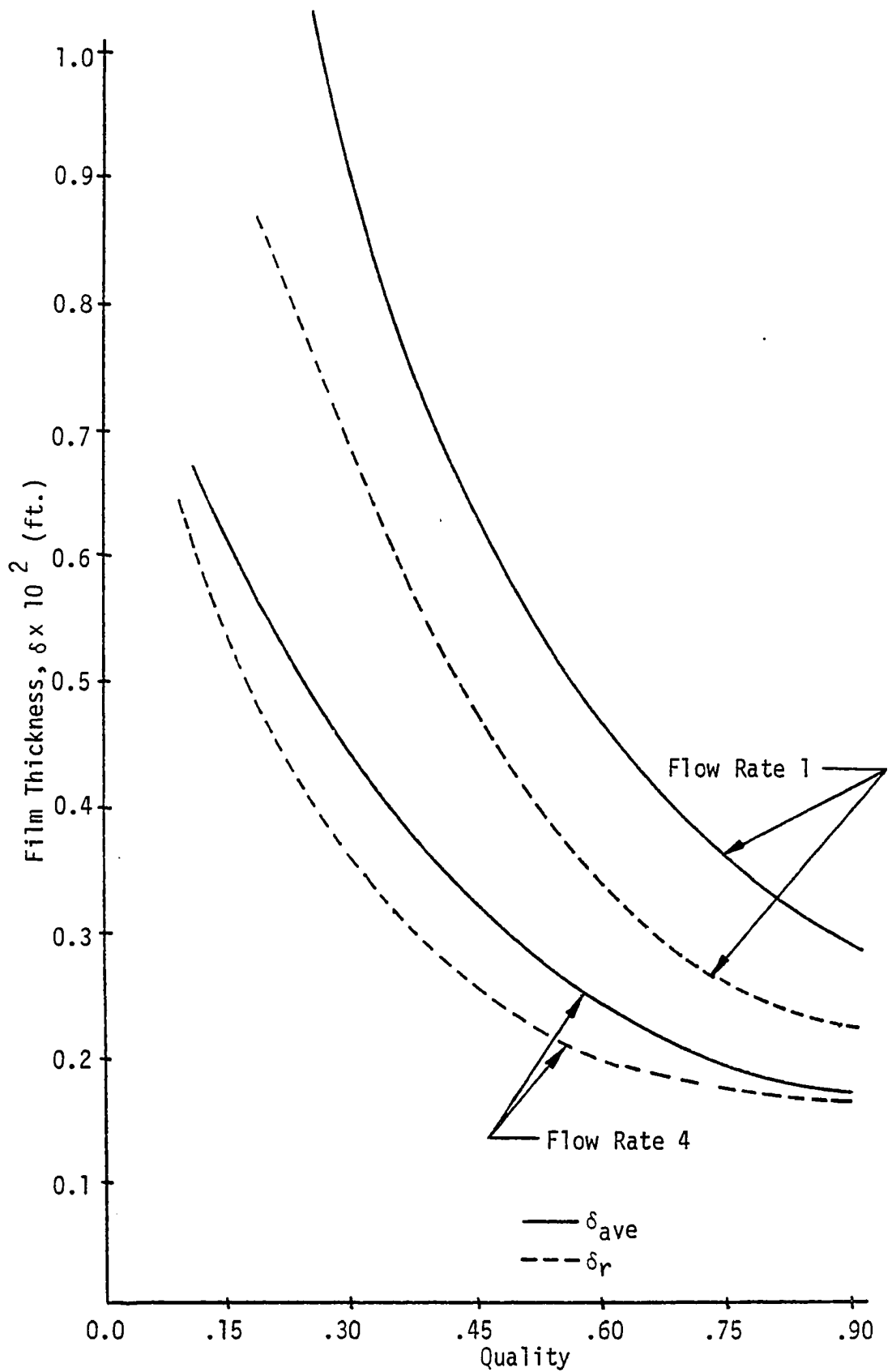
Figure 49. A Comparison of δ_{ave} and δ_r at the Lowest and Highest Gas Flow Rates.

gas flow rates. It should be noticed that δ_{ave} and δ_r approach each other as the gas flow rates and the quality increase.

When comparing δ_{ave} and δ_r with reported values of film thickness in literature several factors should be noted. First, several techniques are in common use for liquid injection into gas for two-phase flow; for example, liquid through a porous medium and liquid through a slot or tube, as used in this study. Secondly, a number of different techniques for measuring film thickness are being used. As a result, there is some variation in the values of film thickness reported in the literature. The values of Chien and Ibele[45] for downward vertical two-phase flow are shown in Figure 50 and in Table VII. Even though interpolation was necessary to compare the results of their study with this present study, values of the liquid film thickness are in very good agreement at the high gas flow rates, especially for moderate to high quality values. Chien and Ibele, using a probe technique for measuring film thickness, show film thickness plotted as a function of flow tube length. In contrast, the values of film thickness reported by Gill, Hewitt, and Lacey[46] are considerably lower. Figure 50 and Table VII shows these values, after interpolation to match the flow conditions of this study. It should be noted that this data was taken using a probe technique, and the film thicknesses are reported for a height above injection
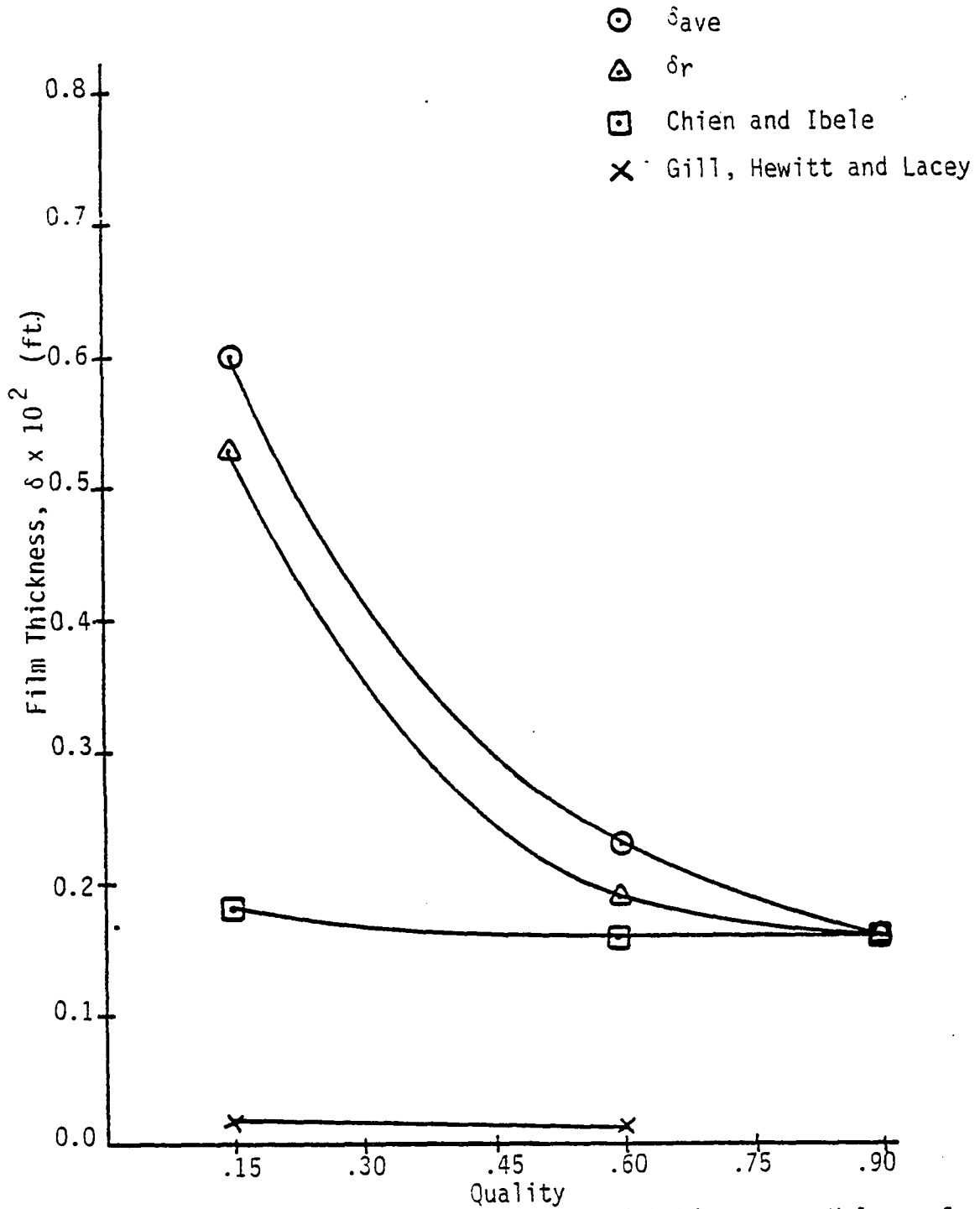
Figure 50. A Comparison of δ_{ave} and δ_r With Literature Values of Liquid Film Thickness Corresponding to Flow Rate 4.

Table VII.   Comparison of δ_{ave} and δ_r To
Literative Values of Liquid Film
Thickness.

Flow Condition Number	$*\delta_{ave}$ X 10^2 (feet)	$*\delta_r$ X 10^2 (feet)	$*\delta$ X 10^2 from Chien and Ibele (feet)	$**\delta$ X 10^2 from Gill, Hewitt and Lacey (feet)
315	1.0	0.78	0.21	0.015
360	0.30	0.21	0.17	0.013
390	0.20	0.17	0.16	—
415	0.60	0.53	0.18	0.013
460	0.23	0.19	0.16	0.012
490	0.16	0.16	0.16	—

* Film thickness evaluated at 38 inches after liquid injection.
** Film thickness evaluated at 200 inches after liquid injection.

of approximately 200 inches, in contrast to a test section which was located 38 inches above water injection level for this study. Hughmark[47] has collected and correlated the film thickness data from a number of investigators. Results from this study are in agreement, at least to the same order of magnitude, when reasonable values of wall shear and interfacial shear stresses are used to convert δ_{ave} and δ_r into a nondimensional form. In general, both δ_{ave} and δ_r are thought to be in reasonable agreement with most reported values of liquid film thickness, especially at the higher values of quality.

Another factor that can be obtained from the axial photographs of two-phase flow is the average number of droplets per sample at each of the flow conditions. These values are given in Table I and are useful in building a physical picture of two-phase flow at various qualities as well as in modeling. At the lower gas flow rates more droplets occur at the lower qualities. As the gas velocity increases, however, the number of droplets at the higher qualities increases as seen by comparing the number of droplets for qualities of 45 and 60% at all gas flow rates. For all gas flow rates the number of droplets decreased for all qualities above 75 percent.

CHAPTER IV

ANALYTICAL CALCULATIONS AND MODELING

Introduction

When building separated two-phase flow models it
is generally recognized that the first step is to establish
a model for the flow pattern. Once a flow pattern has been
set, other quantities and factors of interest, such as in-
terface processes, can be evaluated. As a result, the
analysis section of this study will first address the prob-
lem of finding reasonable velocity profiles to describe the
liquid film and the gas core regions. Next, these velocity
profiles will be used in calculating blockage factors based
on mass flow. Blockage factors based on geometry, both
area and volume, will also be calculated. Finally, the
flow pattern velocity profile will be used to predict inter-
face shear stresses, showing a possible application of
building flow patterns by using droplet and wave data ob-
tained from axial photographs of two-phase flow.

Velocity Profiles in Two-Phase Flow

The physical description of annular, vertical two-
phase flow consists of the liquid flowing in an annulus

162

along the wall with the gas ·phase flowing inside this annulus. The interface between the two phases is rough due to the wave action of the liquid film being moved by the gas. In addition, liquid from the film on the wall is torn from the tips of the waves which extend into the gas core, and droplets are entrained in the gas core region. In steady flow there is a balance between the formation of droplets and the collapse of droplets back into the liquid layer on the wall.

This simplified physical picture of the flow pattern suggests two separate velocity profiles. The first velocity profile describes the velocity of the liquid film which varies from zero at the wall to some value of velocity at the liquid-gas interface. This interfacial velocity must be the same for both the liquid and the gas. The second profile, describing the gas core, varies from this interfacial velocity to a maximum velocity at the center of the flow tube.

Several ways have been suggested in literature for handling the gas core region.[48] One way has been to assume a homogeneous mixture of gas and droplets. As already discussed in the introduction of this study, only limited success, as well as a limited possibility for correcting for additional effects, has been obtained from models using this technique. A second approach[49] is to assume the gas core region to be comprised of only gas, ignoring, for the

present, the droplets. Later, the droplets could be accounted for by using some typical droplet distribution and sizes and calculating the blockage or drag due to this entrainment.

Converting this physical model into mathematical form, the continuity equation may be written in vector form as:

$$\frac{\partial \rho}{\partial t} + \text{div}(\rho \vec{V}) = 0$$

where ρ is density, t is time and $\vec{V}$ is the velocity. Expanding in cylindrical coordinates

$$\frac{\partial \rho}{\partial t} + \frac{1}{r}\frac{\partial}{\partial r}(\rho r V_r) + \frac{1}{r}\frac{\partial}{\partial \theta}(\rho V_\theta) + \frac{\partial}{\partial z}(\rho V_z) = 0$$

where V_r, V_θ and V_z are the velocity components in r, θ and z directions respectively. Now assume:

1) fully developed flow

2) steady state flow

3) one-dimensional flow.

Therefore:

$$\frac{\partial}{\partial z}(\rho V_z) = 0 .$$

Furthermore, if the flow in the gas core is assumed to be incompressible, then

$$\frac{\partial V_z}{\partial z} = 0 . \tag{1}$$

Now consider the momentum equation applied to the gas core and expressed in terms of vectors as follows:[50]

$$\rho \, \frac{D\vec{V}}{Dt} = -\nabla \vec{P} + \vec{B} + \vec{\nabla} \cdot \overleftrightarrow{\tau}$$

where the term on the left hand side represents the time rate of change of momentum expressed in terms of the substantial derivative, and terms on the right hand side of the equation represent the forces due to pressure, gravity (body forces) and viscous shear respectively. Expanding in cylindrical coordinates for the z component of momentum only:

$$\rho \left\{ \frac{\partial V_z}{\partial t} + V_r \, \frac{\partial V_z}{\partial r} + \frac{V_\theta}{r} \, \frac{\partial V_z}{\partial \theta} + V_z \, \frac{\partial V_z}{\partial z} \right\} =$$

$$-\frac{\partial P}{\partial z} + B_z + \frac{1}{r} \, \frac{\partial}{\partial r} \, (r\tau_{rz}) + \frac{1}{r} \, \frac{\partial}{\partial \theta} \, (\tau_{\theta z}) + \frac{\partial}{\partial z} \, (\tau_{zz}) .$$

Again assuming:

1) fully developed flow

2) steady state flow

3) one-dimensional flow

4) constant properties

5) no θ or r variation in V_z,

the momentum equation can be reduced as follows:

$$\rho V_z \, \frac{\partial V_z}{\partial z} = -\frac{\partial P}{\partial z} + B_z + \frac{1}{r} \, \frac{\partial}{\partial r} \, (r\tau_{rz})$$

where:

$$\tau_{rz} = \mu \, \frac{\partial V_z}{\partial r} .$$

Now let

$$\tilde{P} = zB_z - P$$

and from the continuity equation

$$\frac{\partial V_z}{\partial z} = 0 \ .$$

Therefore:

$$\frac{\mu}{r} \frac{\partial}{\partial r} \left(r \frac{\partial V_z}{\partial r} \right) = -\frac{\partial \tilde{P}}{\partial z} \qquad (2)$$

for constant properties. Using similar assumptions, the r and θ component of the momentum equation reduce to

$$0 = \frac{\partial \tilde{P}}{\partial r} \quad \text{and} \quad 0 = \frac{\partial \tilde{P}}{\partial \theta} \ , \text{respectively.}$$

Now solving equation (2) to obtain the velocity in the z direction as follows:

$$V_z = -\frac{\partial \tilde{P}}{\partial z} \frac{r^2}{4\mu} + c_1 \ln r + c_2 \ . \qquad (3)$$

Inspection of equation (3) shows that for the gas core region defined as

$$R - \delta \geq r \geq 0,$$

the general form of the velocity equation can be expressed as

$$U_g = a_1 r^2 + a_2 \ ^* \qquad (4)$$

---

*Note: The velocity profiles will be determined from these general forms so the development of the future models can be treated in a similar manner.

where a_1 and a_2 are constants to be determined by the boundary conditions, since $c_1 \ln r$ at $r = 0$ would be undefined and therefore, c_1 must be zero.

. Likewise, by inspection of equation (3) for the liquid film region, defined as

$$R \geq r \geq R - \delta$$

and for the case when the body and the pressure forces are small in the thin liquid layer, and as well approximately balance each other,* the general form of the liquid velocity profile becomes

$$V_\ell = a_3 \ln r + a_4 \tag{5}$$

Using equations (4) and (5) to describe the velocity profiles in the gas and liquid regions, respectively, a flow pattern model called ln-parabolic can be determined. The four constants can be determined by the following boundary conditions:

$$
\begin{aligned}
&\text{BC 1)} \quad r = R, \ V_\ell = 0 \\[6pt]
&\text{BC 2)} \quad r = R - \delta, \ V_\ell = U_g \\[6pt]
&\text{BC 3)} \quad r = R - \delta, \ \mu_\ell \frac{\partial V_\ell}{\partial r} = \mu_g \frac{\partial U_g}{\partial r} \\[6pt]
&\text{BC 4)} \quad r = 0, \ U_g = U_{max-a}
\end{aligned}
\tag{6}
$$

where μ_ℓ and μ_g are the viscosity of the liquid and gas, respectively, and U_{max-a} is the maximum velocity.

Some investigators[51,52] have suggested that a slip ratio, S, exists between the liquid and gas interface such

---

*It should be noted that the balance of these forces in the liquid layer is not true in general for all flow conditions.

that BC 2 in equation (6) can be written

$$V_\ell = \frac{U_g}{S} .$$

The slip ratio will be included in the development of the ln-parabolic model as an example of how a slip ratio may be included. However, a slip ratio equal to one will be used for all calculations in this study.

Now, applying BC 1:

$$0 = a_3 \ln R + a_4 , \text{ yielding}$$

$$a_4 = -a_3 \ln R .$$

Therefore:

$$V_\ell = a_3 \ln\left(\frac{r}{R}\right) . \tag{7}$$

Applying BC 4,

$$U_{max-a} = a_1(0) + a_2 , \text{ yielding}$$

$$a_2 = U_{max-a} .$$

Therefore:

$$U_g = U_{max-a} + a_1 r^2 . \tag{8}$$

Applying BC 3,

$$\mu_\ell a_3 (1/r)\bigg|_{R-\delta} = \mu_g (2a_1 r)\bigg|_{R-\delta} .$$

Therefore:

$$a_3 = \frac{2a_1}{\mu_r} (R - \delta)^2 \tag{9}$$

where

$$\mu_r = \mu_\ell / \mu_g \ .$$

Now applying BC 2,

$$a_3 \ln(r/R)\bigg|_{R-\delta} = \frac{(a_1 r^2 + U_{max-a})}{S}\bigg|_{R-\delta} \ . \qquad (10)$$

Placing the expression for a_3 from equation (9) into equation (10) and solving for a_1 yields:

$$a_1 = \frac{U_{max-a}}{\left[\dfrac{2S}{\mu_r}(R-\delta)^2 \ln\left(\dfrac{R-\delta}{R}\right) - (R-\delta)^2\right]} \ . \qquad (11)$$

If the void fraction is defined as:

$$\alpha = \frac{A_{gc}}{A_t}$$

where A_{gc} is the area of the gas core and A_t is the area of the flow tube then

$$\alpha = \frac{\pi(D-2\delta)^2/4}{\pi D^2/4} = \left(1 - \frac{\delta}{R}\right)^2 \ .$$

Also define

$$\eta = \frac{\delta}{R} \quad \text{and} \quad \xi = \frac{r}{R} \ .$$

Substitute these variables into equation (11) and

$$a_1 = \left\{\frac{U_{max-a}}{\dfrac{2SR^2\alpha}{\mu_r}\ln\sqrt{\alpha} - \alpha}\right\} \ .$$

By putting these expressions into equation (8), the gas core velocity can be expressed as

$$U_g = U_{max-a} \left\{ 1 + \frac{\xi^2}{\left(\frac{2S}{\mu_r} \alpha \ln\sqrt{\alpha} - \alpha \right)} \right\} \qquad \text{for } 1 - \eta \geq \xi \geq 0.$$

$$(12)$$

Returning now to equation (9) and substituting for a_1, the liquid velocity profile becomes

$$V_\ell = \left\{ \frac{U_{max-a}}{S\ln\sqrt{\alpha} - \frac{\mu_r}{2}} \right\} \ln\xi \qquad \text{for } 1 \geq \xi \geq 1 - \eta . \quad (13)$$

Equations (12) and (13) now describe the flow pattern for gas core and liquid film regions respectively, provided a value of U_{max} can be determined or measured experimentally. One method for determining U_{max} is to use a mass balance on the gas flow rate and assume all the gas flows in the core region. Therefore:

$$\dot{m}_g = \int_0^{R-\delta} \rho_g 2\pi r U_g dr \qquad (14)$$

where $\dot{m}_g$ is the gas (mass) flow rate. Now substituting the gas core velocity profile given in equation (12) into equation (14) yields:

$$\dot{m}_g = 2\pi\rho_g U_{max-a} R^2 \int_0^{1-\eta} \left[\xi + \frac{\xi^3}{\left(\frac{2S}{\mu_r} \alpha \ln\sqrt{\alpha} - \alpha \right)} \right] d\xi$$

$$\dot{m}_g = 2\pi\rho_g U_{max-a} R^2 \left[\frac{\xi^2}{2} - \frac{\xi^4}{4\left(\frac{2S}{\mu_r}\alpha\ln\sqrt{\alpha} - \alpha\right)}\right]_0^{1-\eta}$$

$$\dot{m}_g = \pi\rho U_{max-a} R^2 \alpha \left[1 + \frac{\mu_r/4}{S\ln\sqrt{\alpha} - \mu_r/2}\right] \cdot \quad (15)$$

Solving for U_{max-a},

$$U_{max-a} = \frac{\dot{m}_g}{\pi\rho_g R^2 \alpha \left[1 + \frac{\mu_r/4}{S\ln\sqrt{\alpha} - \mu_r/2}\right]} \cdot \quad (16)$$

Using equations (12) and (13) along with (16), a curve for U/U_{max} versus y/R, where $y = R-r$, is shown in Figure 51. A comparison of Figures 51 and 52 show the difference in the profiles using δ_{ave} and δ_r respectively. As expected, it was found that these values of U/U_{max} remained nearly constant for a given value of y/R at all values of the gas flow rate but were found to be a function of the quality as shown by the family of quality curves.

Tables VIII and IX give the values of U_{max} for δ_{ave} and δ_r, respectively, and, by using these values of maximum velocity, the actual velocity can be determined for any value of y/R.

Figures 53 and 54 show U_{max} from the ln-parabolic model as a function of quality for each of the four gas flow
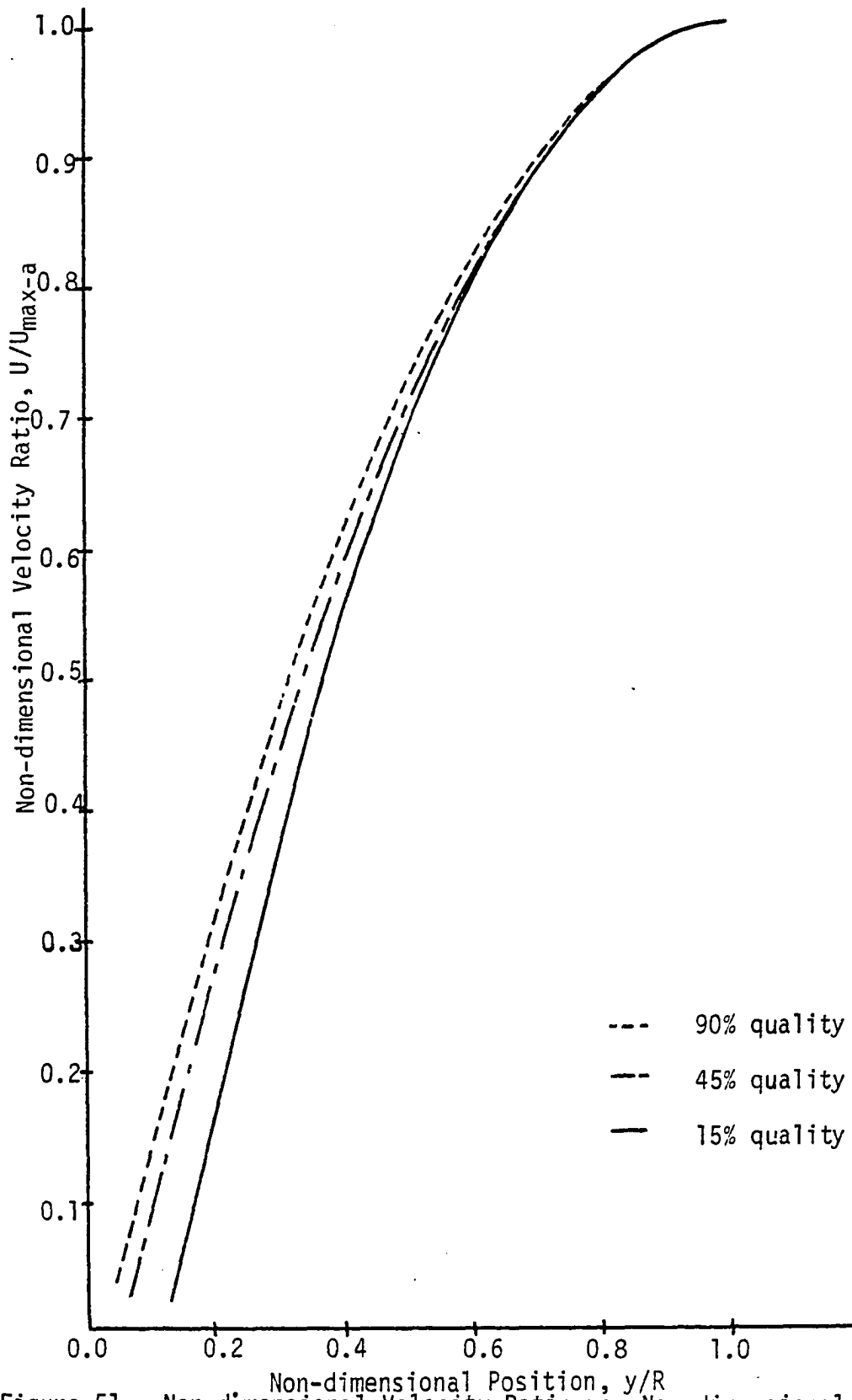
Figure 51. Non-dimensional Velocity Ratio vs. Non-dimensional Position
for the Ln-Parabolic Model Using δ_{ave}.

Figure 52. Non-dimensional Velocity Ratio vs. Non-dimensional Position, y/R for the Ln-Parabolic Model Using δr

15% quality
45% quality
90% quality
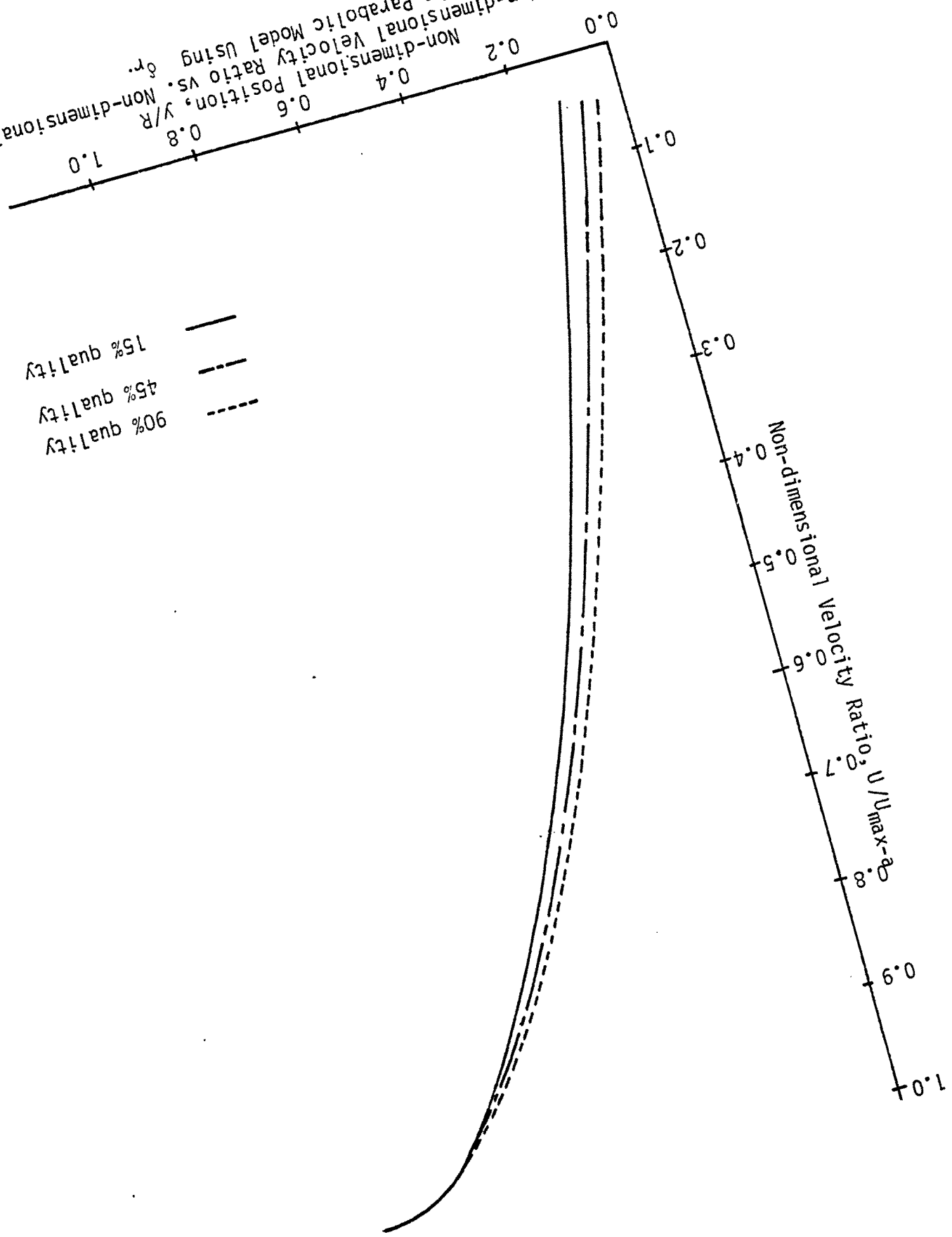
Table VIII. Maximum Velocities for Various Liquid - Gas
Velocity Profile Models Using δ_{ave}.

Liquid Velocity Form - Gas Vel. Form	ln - parabolic U_{max-a}	ln - ln U_{max-b}	linear - ln U_{max-c}	ln - cosine U_{max-d}	ln - ln (parabolic) U_{max-e}
Flow Condition Number	All Velocities Given in Feet/Sec				
120	75.33	71.26	71.22	81.44	55.52
130	83.65	83.79	83.72	90.45	67.04
145	82.85	83.00	82.94	89.59	67.52
160	71.35	65.18	65.16	77.13	49.71
190	66.91	56.72	56.71	72.32	41.97
230	101.81	96.53	94.49	100.07	75.97
245	98.98	91.84	91.81	107.00	71.57
260	99.57	92.85	92.81	107.63	72.14
275	89.80	76.86	76.85	97.06	56.93
290	89.07	75.51	75.50	96.28	55.84
315	152.08	157.93	157.74	164.46	129.84
330	132.47	127.00	126.94	143.22	99.50
345	124.57	115.30	115.26	134.67	88.99
360	111.44	93.71	93.70	120.45	69.04
375	108.28	88.21	88.20	117.03	64.42
390	112.71	94.76	94.77	121.82	69.94
415	176.26	167.11	167.04	190.56	132.55
430	169.43	153.92	153.88	183.15	117.44
445	160.59	138.38	138.36	173.58	103.25
460	158.29	136.34	136.33	171.09	101.26
475	155.40	131.21	131.20	167.97	97.22
490	151.05	122.42	122.42	163.26	89.54

Table IX. Maximum Velocities for Various Liquid - Gas

Velocity Profile Models Using δ_r.

Liquid Velocity Form - Gas Vel. Form	ln - parabolic U_{max-a}	ln - ln U_{max-b}	linear - ln U_{max-c}	ln - cosine U_{max-d}	ln - ln (parabolic) U_{max-e}
Flow Condition Number	All Velocities Given in Feet/Sec				
120	70.84	64.03	64.02	76.58	49.66
130	76.52	72.97	72.94	82.72	58.89
145	77.91	75.56	75.51	84.23	61.91
160	67.48	53.59	58.58	72.94	44.27
190	65.23	53.46	53.45	70.50	39.32
230	97.69	89.97	89.94	105.60	70.65
245	96.05	87.08	87.05	103.83	67.62
260	95.24	85.79	85.77	102.94	66.34
275	86.51	70.50	70.50	93.50	51.76
290	86.74	70.96	70.95	93.75	52.14
315	138.87	138.49	138.38	150.15	116.20
330	123.82	113.30	113.26	133.85	88.55
345	119.11	106.28	106.26	128.75	81.57
360	108.30	87.43	87.42	117.05	64.00
375	106.21	83.78	83.73	114.79	60.97
390	110.27	89.95	89.95	119.18	66.04
415	171.91	160.24	160.18	185.84	126.96
430	162.12	141.48	141.46	175.24	107.14
445	156.83	131.38	131.37	169.51	97.46
460	152.59	125.52	125.51	164.92	92.42
475	152.93	126.43	126.42	165.29	93.30
490	149.50	119.08	119.08	161.58	86.93
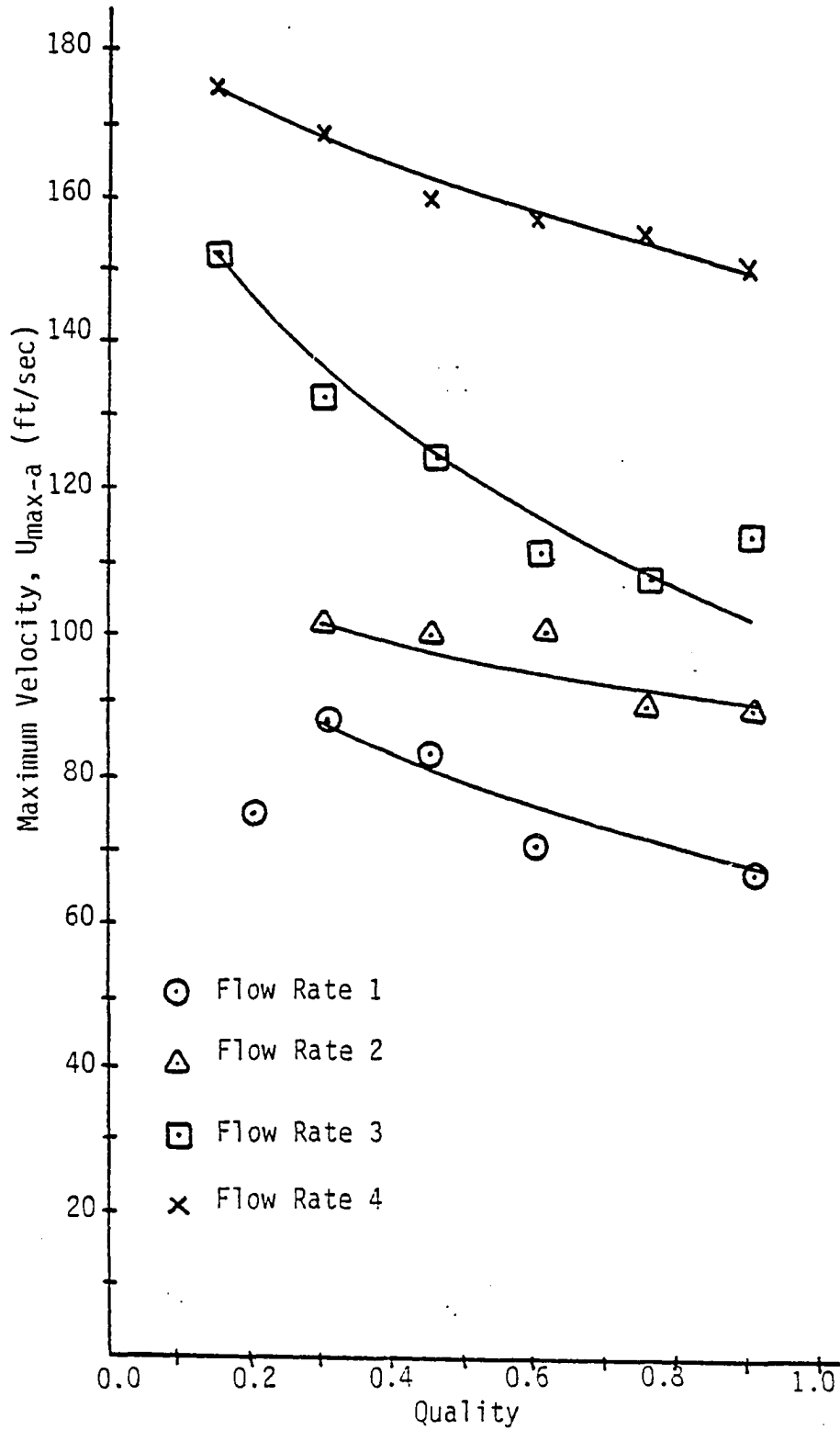
Figure 53. Maximum Velocity vs. Quality for Various Flow Rates
Using the Ln-Parabolic Model with δ_{ave}.
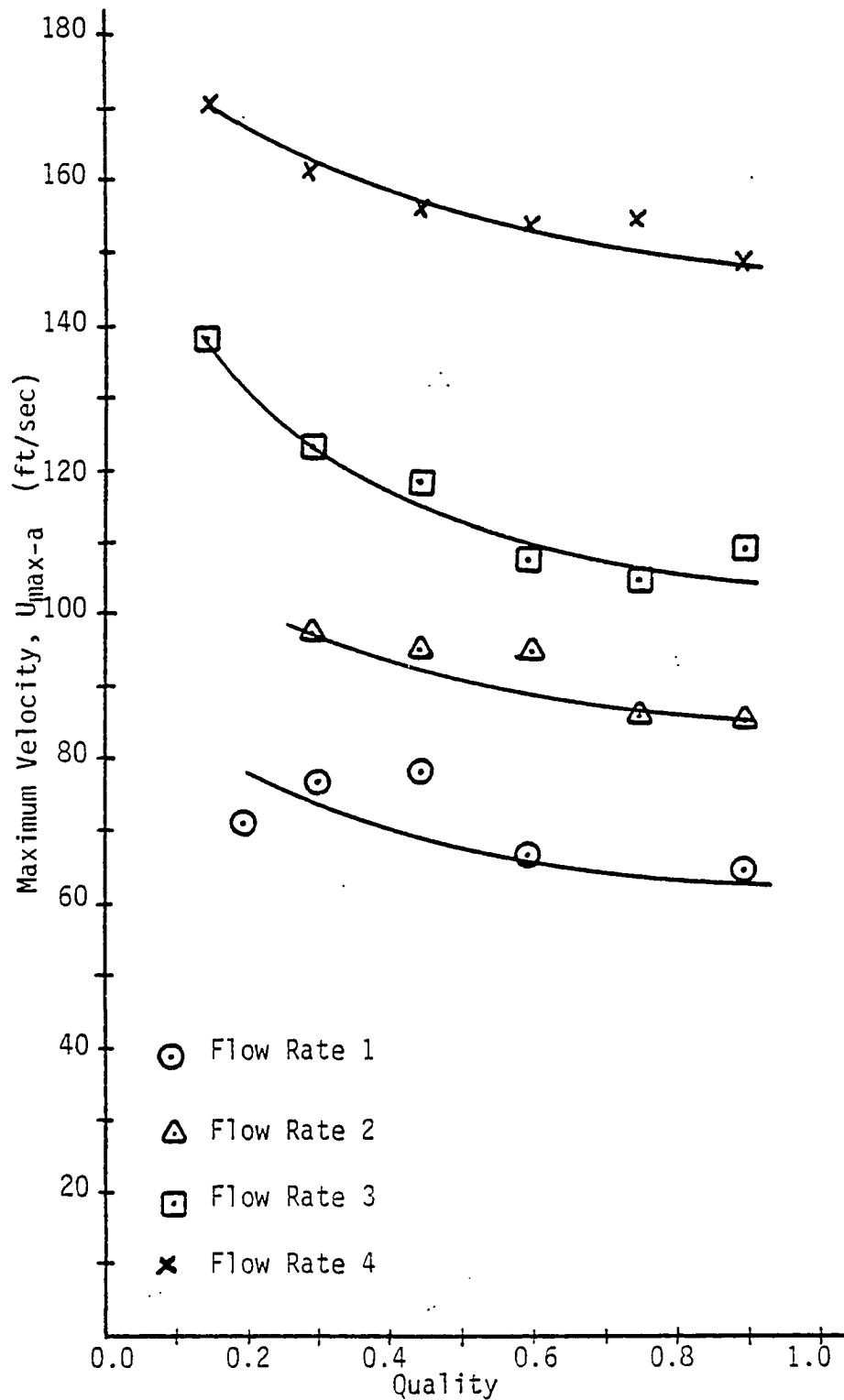
Figure 54. Maximum Velocity vs. Quality for Various Flow Rates Using the Ln-Parabolic Model with δ_r.

rates. When comparing these values of U_{max} to experimental values of U_{max}, the values from the ln-parabolic model were higher in every case. The parabolic gas velocity profile is normally associated with laminar flow. However, a check of the superficial gas Reynolds number (i.e., assuming the gas to be flowing alone in the flow tube) produced values that were in the turbulent range. Thus, assuming a turbulent gas core velocity profile would be more reasonable. As a result several different flow pattern models were tried, solving each time for a liquid velocity profile, a gas core velocity profile and then, using a gas mass balance, an expression for U_{max} was determined.

The second model, referred to as the ln-ln model, assumes a log profile in the gas core region (in keeping with turbulent flow forms) as well as a log profile in the liquid layer. Therefore the equations become:

$$V_\ell = b_1 + b_2 \ln (1 - \frac{y}{R}) \qquad \text{for } 0 \leq y \leq \delta \qquad (17)$$

and

$$U_g = b_3 + b_4 \ln y \qquad \text{for } \delta \leq y \leq R \qquad (18)$$

with the boundary conditions of:

$$
\begin{aligned}
&\text{BC 1)} \quad y = 0, \quad V_\ell = 0 \\[4pt]
&\text{BC 2)} \quad y = \delta, \quad V_\ell = U_g \\[4pt]
&\text{BC 3)} \quad y = \delta, \quad \mu_\ell \frac{\partial V_\ell}{\partial y} = \mu_g \frac{\partial U_g}{\partial y} \\[4pt]
&\text{BC 4)} \quad y = R, \quad U_g = U_{max-b}
\end{aligned}
\qquad (19)
$$

Now, solving for b_1 through b_4 in a manner similar to the ln-parabolic model, expressions for the velocities can be obtained as follows:

$$U_g = U_{max-b} \left\{ 1 + \frac{\ln(y/R)}{\Lambda_1} \right\} \qquad \text{for } 0 \leq y \leq \delta \qquad (20)$$

$$V_\ell = \left\{ \frac{U_{max-b}}{-\frac{\mu_r \eta}{\sqrt{\alpha}} \Lambda_1} \right\} \ln(1 - y/R) \qquad \text{for } \delta \leq y \leq R \qquad (21)$$

where:

$$\Lambda_1 = -\left[\frac{\sqrt{\alpha}}{\eta \mu_r} \ln\sqrt{\alpha} + \ln\eta \right].$$

A gas mass balance can be used to find the maximum velocity as follows:

$$\dot{m}_g = \int_\delta^R \rho_g 2\pi (R - y) U_g dy$$

Let $\omega = y/R$, therefore:

$$\dot{m}_g = 2\pi \rho_g R^2 U_{max-b} \int_\eta^1 \left[1 + \frac{1}{\Lambda_1} \ln\omega - \omega - \frac{1}{\Lambda_1} \omega \ln\omega \right] d\omega .$$

Now integrating and solving for U_{max-b}:

$$U_{max-b} = \frac{\dot{m}_g / 2\pi \rho_g R^2}{\left\{ \frac{1}{2} - \frac{3}{4\Lambda_1} + \eta \left(\frac{1}{\Lambda_1} - \frac{1}{\Lambda_1} \ln\eta - 1 \right) + \frac{\eta^2}{2} \left(1 + \frac{1}{\Lambda_1} \ln\eta - \frac{1}{2\Lambda_1} \right) \right\}} \qquad (22)$$

Using equations (20) and (21) along with (22), a curve for U/U_{max} versus y/R has been shown in Figure 55 for δ_{ave} and Figure 56 for δ_r, respectively. The values of U_{max-b} have been tabulated in Tables VIII and IX so the velocity profiles at each flow rate and quality can be determined. In addition, the variation of U_{max-b} with quality and flow rate has been shown in Figures 57 and 58 for δ_{ave} and δ_r respectively.

Figures 59 and 60 show a comparison of the values of U_{max} for the ln-parabolic and ln-ln models with experimental data. Using a pitot tube, experimental data was obtained only for values of high quality due to interference of the liquid in the pitot tube. The experimental values of U_{max} were all between the values of U_{max-a} and U_{max-b}. In general, excellent agreement was found between the values of U_{max} (experimental) and U_{max-b} (using the ln-ln model) at the high quality values of each flow rate.

Additional velocity profile models were also investigated, the first being a linear-ln model. A linear profile was used to describe the liquid film layer as an approximation to a log profile for small distances. This approximation is in agreement with the laminar sublayer region description for the many turbulent models which used the well known "law of the wall". The general form of the assumed velocity profile becomes:

$$V_z = c_1 + c_2 y \qquad \text{for } 0 \le y \le \delta \qquad (23)$$
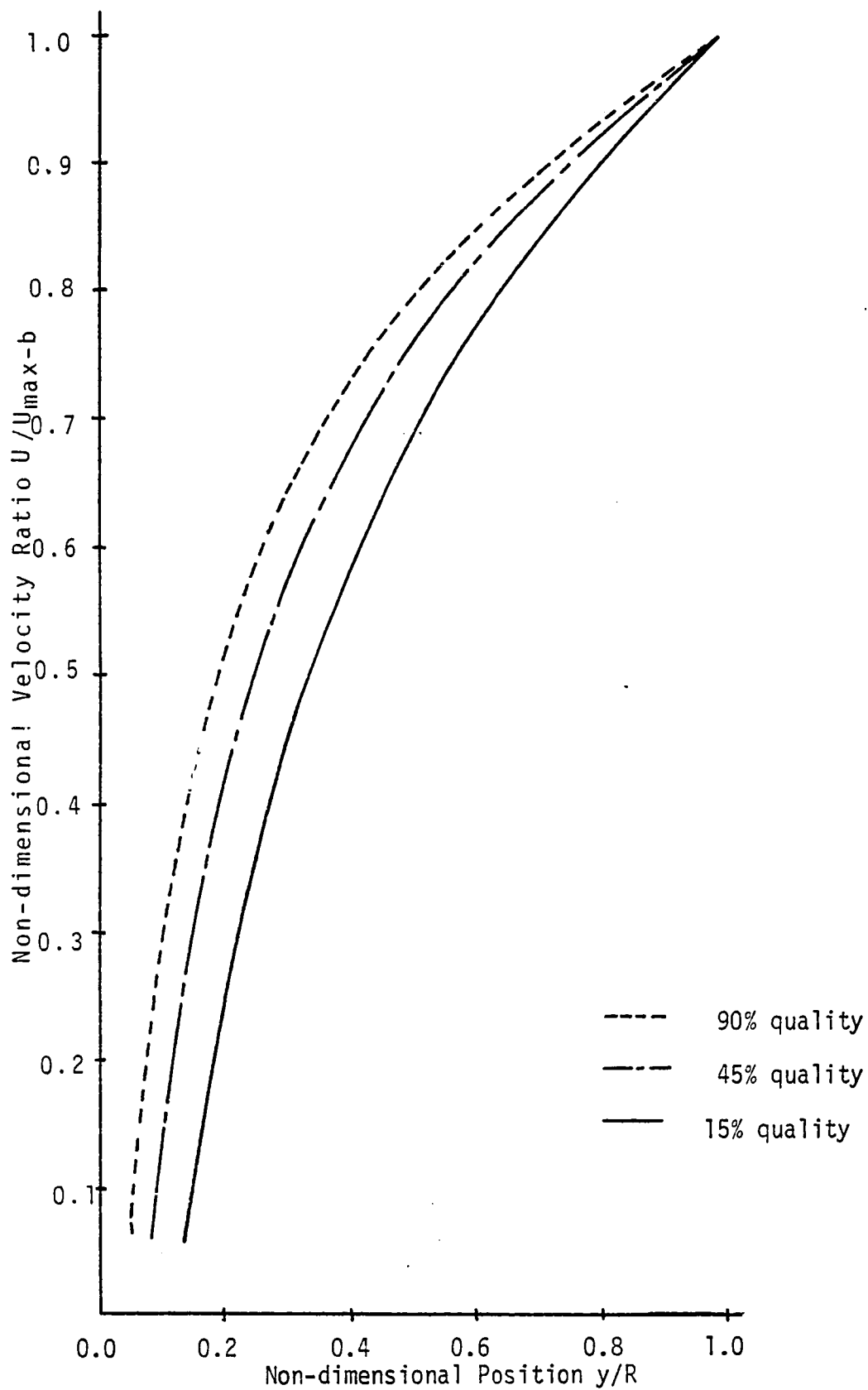
Figure 55. Non-dimensional Velocity Ratio vs. Non-dimensional
Position for the Ln-Ln Model Using δ_{ave}.
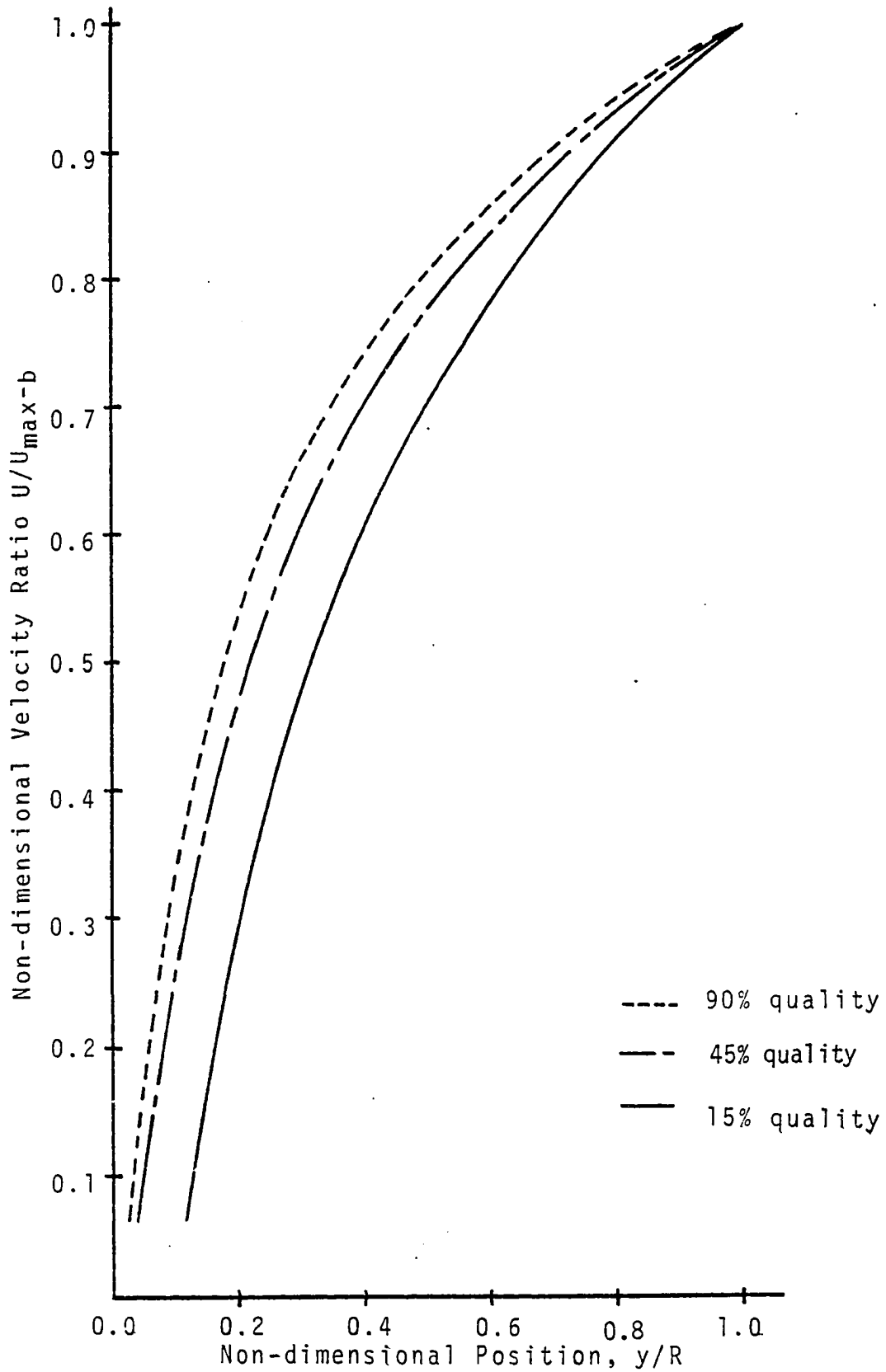
Figure 56. Non-dimensional Velocity Ratio vs. Non-dimensional Position for the Ln-Ln Model Using δ_r.
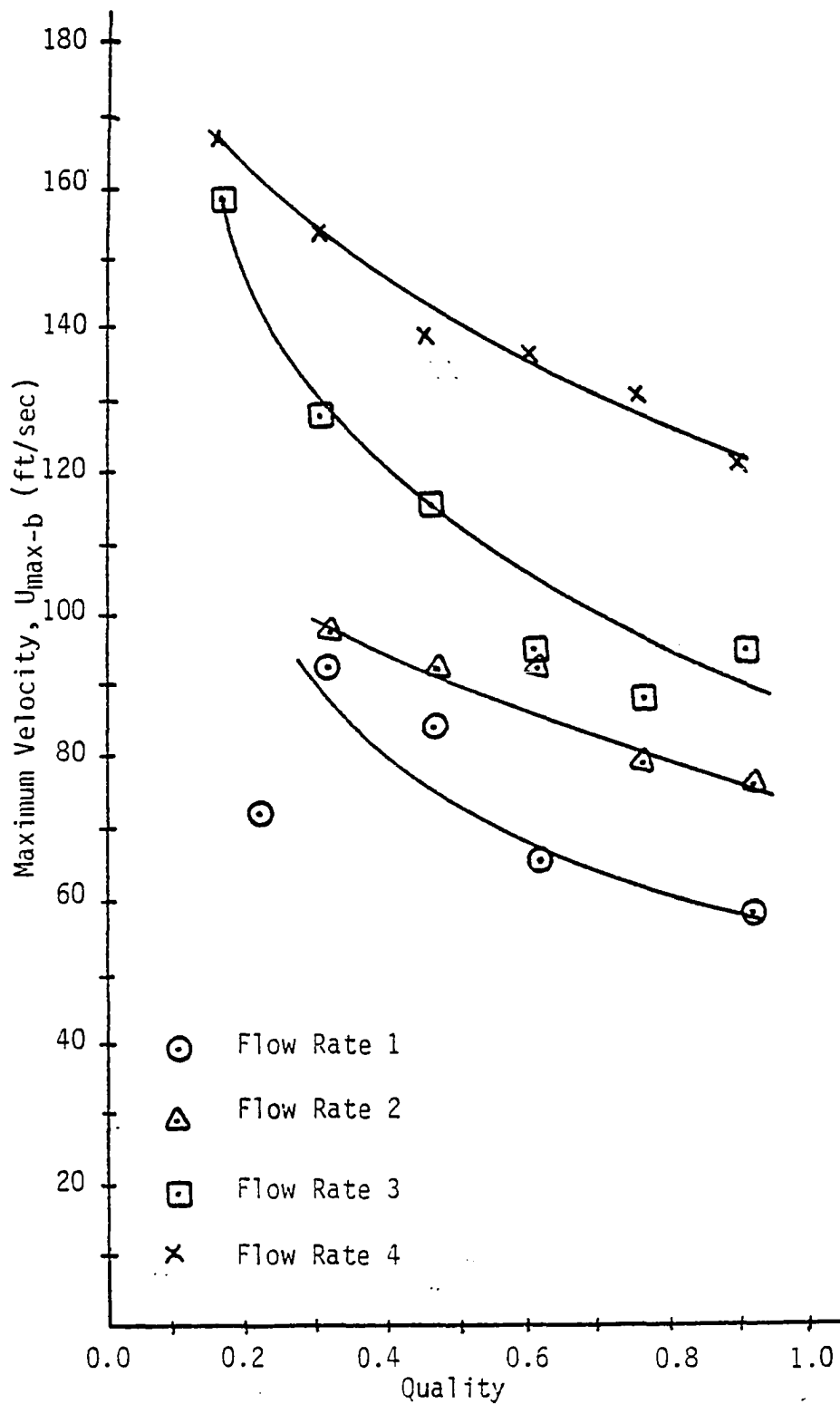
Figure 57. Maximum Velocity vs. Quality for Various Flow Rates Using the Ln-Ln Model with δ_{ave}.
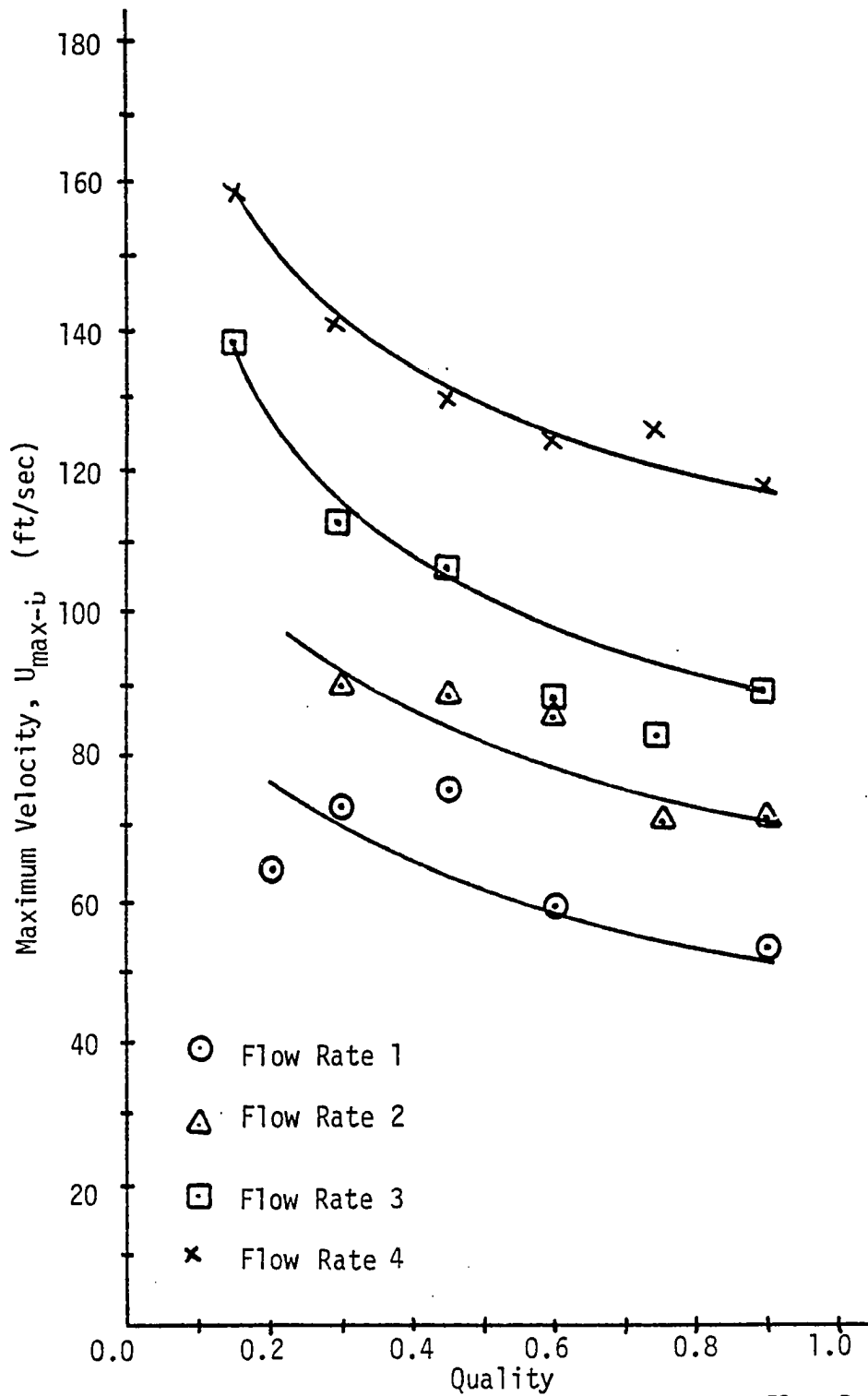
Figure 58.   Maximum Velocity vs. Quality for Various Flow Rates
Using the Ln-Ln Model with δ_r.
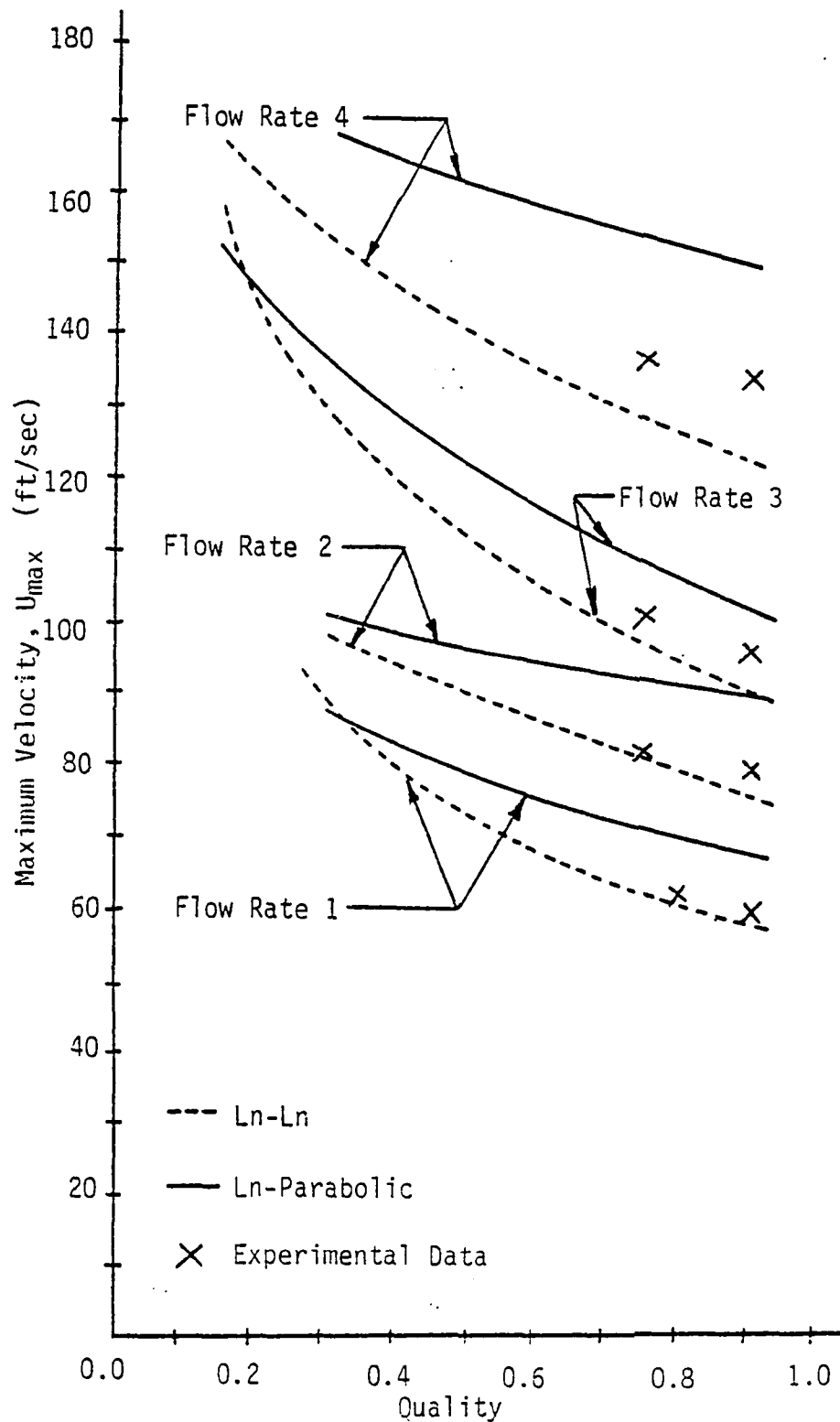
Figure 59. A Comparison of Experimental Values of U_{max} with the Ln-Parabolic Model and the Ln-Ln Model Using δ_{ave}.
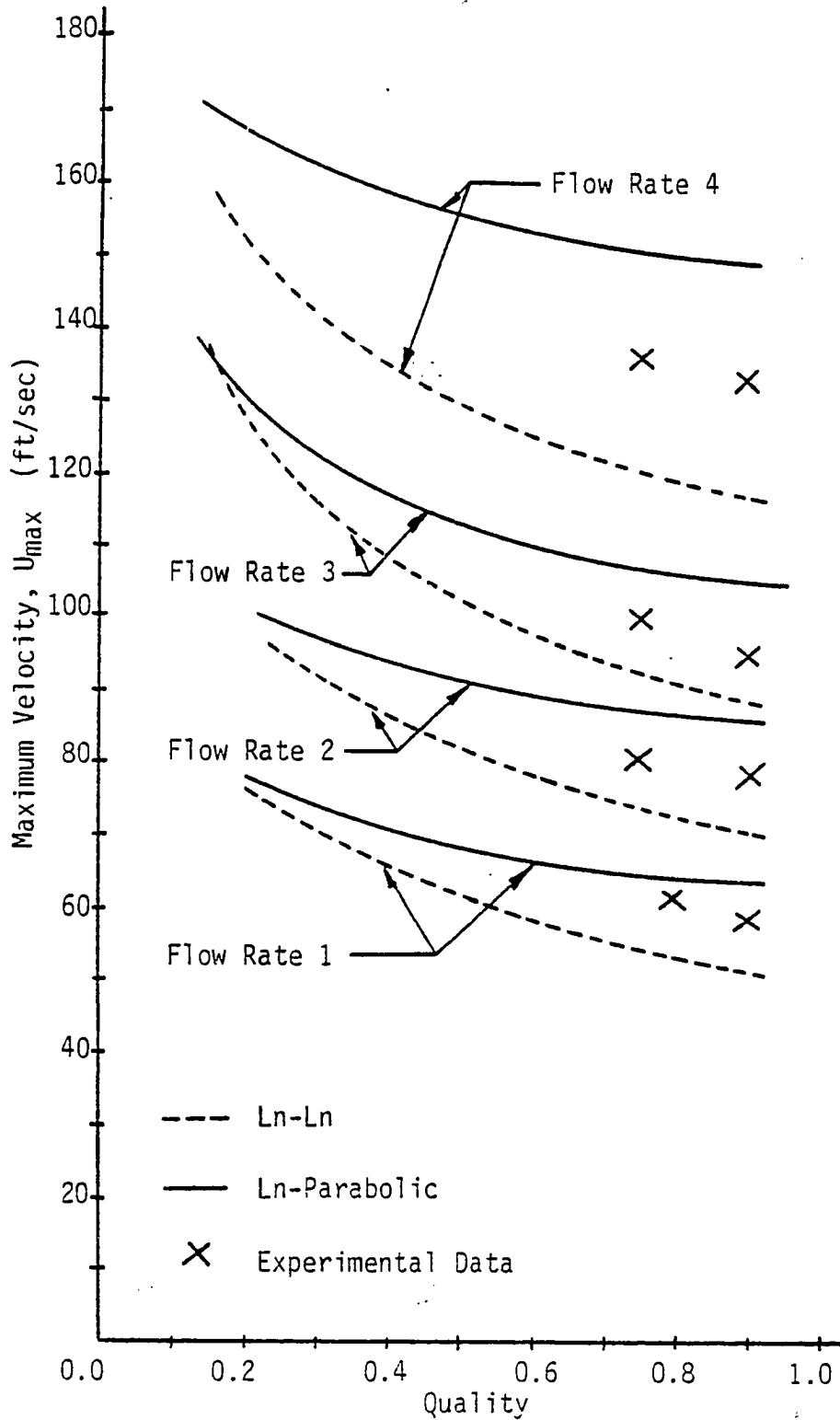
Figure 60. A Comparison of Experimental Values of U_{max} with the Ln-Parabolic Model and the Ln-Ln Model Using δ_r.

and

$$U_g = c_3 + c_4 \ln y \qquad \text{for } \delta \leq y \leq R \qquad (24)$$

with boundary conditions of:

$$
\begin{aligned}
&\text{BC 1)} \quad y = 0, \quad V_\ell = 0 \\
&\text{BC 2)} \quad y = \delta, \quad V_\ell = U_g \\
&\text{BC 3)} \quad y = \delta, \quad \mu_\ell \frac{\partial V_\ell}{\partial y} = \mu_\ell \frac{\partial U_g}{\partial y} \\
&\text{BC 4)} \quad y = R, \quad U_g = U_{max-c} \, .
\end{aligned}
\qquad (25)
$$

Using the same technique as described for the previous velocity profile models, values for c_1 through c_4 can be obtained and the velocity profiles are written as:

$$V_\ell = \frac{\Lambda_2 U_{max-c}}{R \mu_r} \left(\frac{y}{\eta} \right) \qquad \text{for } 0 \leq y \leq \delta \qquad (26)$$

and

$$U_g = U_{max-c}[1 + \Lambda_2 \ln(y/R)] \qquad \text{for } \delta \leq y \leq R \qquad (27)$$

where

$$\Lambda_2 = \frac{\mu_r}{1 - \mu_r \ln \eta} \, .$$

Now a mass balance of the gas flow yields an expression for U_{max-c} as follows:

$$U_{max-c} = \frac{\dot{m}_g / 2\pi \rho_g R^2}{\left\{ \frac{1}{2} - \frac{3}{4}\Lambda_2 + \eta(-1 - \Lambda_2 \ln \eta + \Lambda_2) + \frac{\eta^2}{2}\left(1 + \Lambda_2 \ln \eta - \frac{\Lambda_2}{2}\right) \right\}} \cdot (28)$$

As expected, the values of U_{max-c} (shown in Tables VIII and IX) from this technique were almost identical to values obtained from the ln-ln model. In addition, values of U/U_{max} versus y/R were so close to the case of the ln-ln model that separate curves were not warranted.

Due to the similarity between the general shape of these profiles and a cosine profile, an additional model was proposed. This model uses a log profile to describe the liquid film velocity and incorporates a cosine profile to describe the gas core region as follows:

$$V_\ell = d_1 \ln r + d_2 \qquad \text{for } R \geq r \geq R - \delta \qquad (29)$$

and

$$U_g = d_3 \cos\left(\frac{\pi}{2} [r/(R-\delta)]\right) + d_4 \qquad \text{for } R - \delta \geq r \geq 0 \qquad (30)$$

with the boundary conditions of:

$$
\begin{aligned}
&\text{BC 1)} \quad r = R, \ V_\ell = 0 \\[4pt]
&\text{BC 2)} \quad r = R - \delta, \ V_\ell = U_g \\[4pt]
&\text{BC 3)} \quad r = R - \delta, \ \mu_\ell \frac{\partial V_\ell}{\partial r} = \mu_g \frac{\partial U_g}{\partial r} \\[4pt]
&\text{BC 4)} \quad r = 0, \ U_g = U_{max-d} \ .
\end{aligned}
\qquad (31)
$$

Solving for d_1 through d_4 as well as U_{max-d}, the ln-cos velocity model becomes:

$$V_\ell = -\frac{\pi U_{max-d}}{2\mu_r \Lambda_3} \ln \xi \qquad \text{for } 1 \geq \xi \geq 1 - \eta \qquad (32)$$

and

$$U_g = \frac{U_{max}}{\Lambda_3} \left\{ \cos\left(\frac{\pi}{2}[r/(R-\delta)]\right) + \Lambda_3 - 1 \right\} \qquad \text{for } R - \delta \geq r \geq 0$$

(33)

where

$$\Lambda_3 = 1 - \frac{\pi \ln\sqrt{\alpha}}{2\mu_r} .$$

The expression for the maximum velocity is given by:

$$U_{max-d} = \frac{\dot{m}_g}{\Lambda_4 \left[\frac{\pi}{2} - 1 + \frac{\pi^2}{8}(\Lambda_3-1)\right]}$$

(34)

where

$$\Lambda_4 = \frac{8\rho_g R^2 \alpha}{\Lambda_3 \pi} .$$

Figure 61 shows U/U_{max} versus y/R for the ln-cos model for δ_{ave}. The values of U_{max-d} are tabulated in Tables VIII and IX for δ_{ave} and δ_r respectively, at the various flow conditions. The values of U_{max-d} produced by this model were the highest for any of the models studied, and, in general, were not in as close agreement with the experimental values of U_{max} as the other models.

Another technique for obtaining velocity profiles in two-phase flow was investigated by replacing BC 3, which equates the shear stress of the gas and liquid phases at the interface for each of the previous models, with

$$\tau_i = \mu_g \left.\frac{\partial U_g}{\partial y}\right|_{y=\delta}$$

(35)
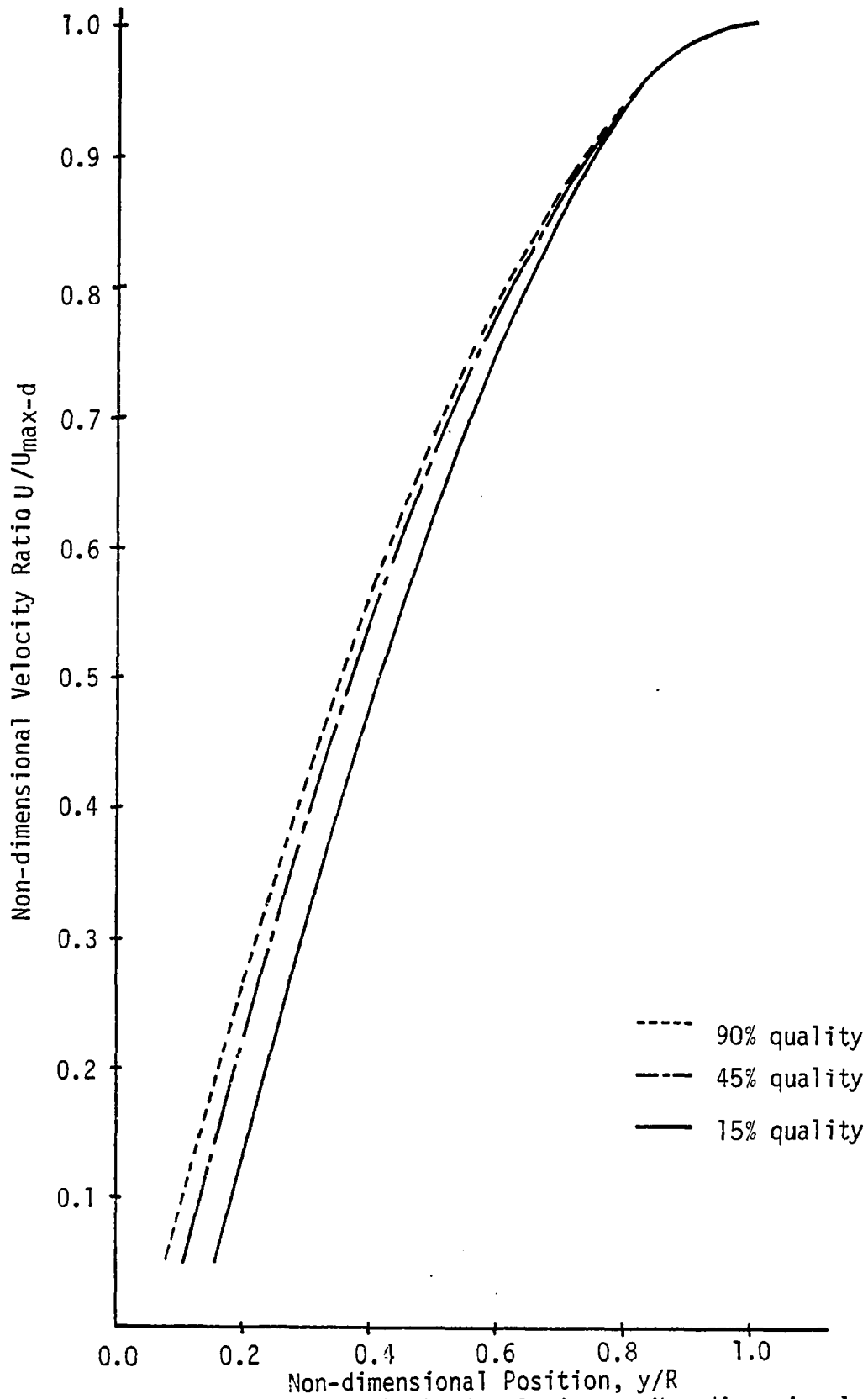
Figure 61. Non-dimensional Velocity Ratio vs. Non-dimensional Position for the Ln-Cosine Model Using δ_{ave}.

where values of τ_i can be obtained from analytical models or from experimental data for the pressure drop, body forces and void fraction as expressed by Wallis[53] in the form of

$$\tau_i = -\frac{D\sqrt{\alpha}}{4}\left[\frac{dp}{dz} + \rho_g g\right] . \qquad (36)$$

Here dp/dz is the pressure gradient, $\rho_g g$ is the gas body force and D is the flow tube diameter.

In order to demonstrate this technique, a ln-ln model will be assumed in both the liquid and gas regions with τ_i values known and defined by the expression:

$$\tau_i = -\mu_g \left.\frac{\partial U_g}{\partial r}\right|_{r = R-\delta} . \qquad (37)$$

Therefore, the general form of the assumed velocity profiles become:

$$V_\ell = e_1 + e_2\ln(1 - y) \qquad \text{for } 0 \leq y \leq \delta \qquad (38)$$

$$U_g = e_3 + e_4\ln y \qquad \text{for } \delta \leq y \leq R \qquad (39)$$

with the following boundary conditions:

$$
\begin{aligned}
&\text{BC 1)} \quad y = 0, \quad V_\ell = 0 \\
&\text{BC 2)} \quad y = \delta, \quad V_\ell = U_g \\
&\text{BC 3)} \quad y = \delta, \quad \tau_i = \mu_g \frac{\partial U_g}{\partial y} \\
&\text{BC 4)} \quad y = R, \quad U_g = U_{max-e} .
\end{aligned}
\qquad (40)
$$

Solving for e_1 through e_4, the velocity profiles can be expressed as:

$$V_\ell = \left\{ \frac{U_{max-e}}{\ln\sqrt{\alpha}} + \left(\frac{\tau_i R\eta}{\mu_g}\right)\frac{\ln\eta}{\ln\sqrt{\alpha}} \right\} \ln(1 - y/R) \qquad \text{for } 0 \leq y \leq \delta$$

$$(41)$$

and

$$U_g = U_{max-e} + \left(\frac{\tau_i R\eta}{\mu_g}\right) \ln(y/R) \qquad \text{for } \delta \leq y \leq R. \qquad (42)$$

Again, using a gas mass balance in the core region, the expression for U_{max-e} becomes:

$$U_{max-e} = \frac{\dot{m}_g}{\pi \rho_g R^2 \alpha} + \frac{2\tau_i R\eta}{\mu_g \alpha}\left(\frac{3}{4} - \eta + \frac{\eta^2}{4} + \eta\ln\eta - \frac{\eta^2}{2}\ln\eta\right). \qquad (43)$$

As an illustration of how this technique may be evaluated, let values of the interfacial shear stress predicted by the ln-parabolic model be used to supply the known τ_i values as expressed in equation (40), BC 3. Figure 62 shows U/U_{max} versus y/R for the ln-ln, parabolic τ_i model (hereafter referred to as ln-ln (parabolic) model) for δ_{ave}. The values of U_{max-e} are tabulated in Tables VIII and IX for both δ_{ave} and δ_r respectively, for the various conditions.

Figure 63 compares all five velocity profile models at the 460 Flow Condition. The ln-ln and linear-ln models were so close together that only one line has been shown. It is interesting to note that the ln-cos model has the highest U_{max} value. It should also be noted that the ln-ln (parabolic) model has the flattest gas core velocity profile
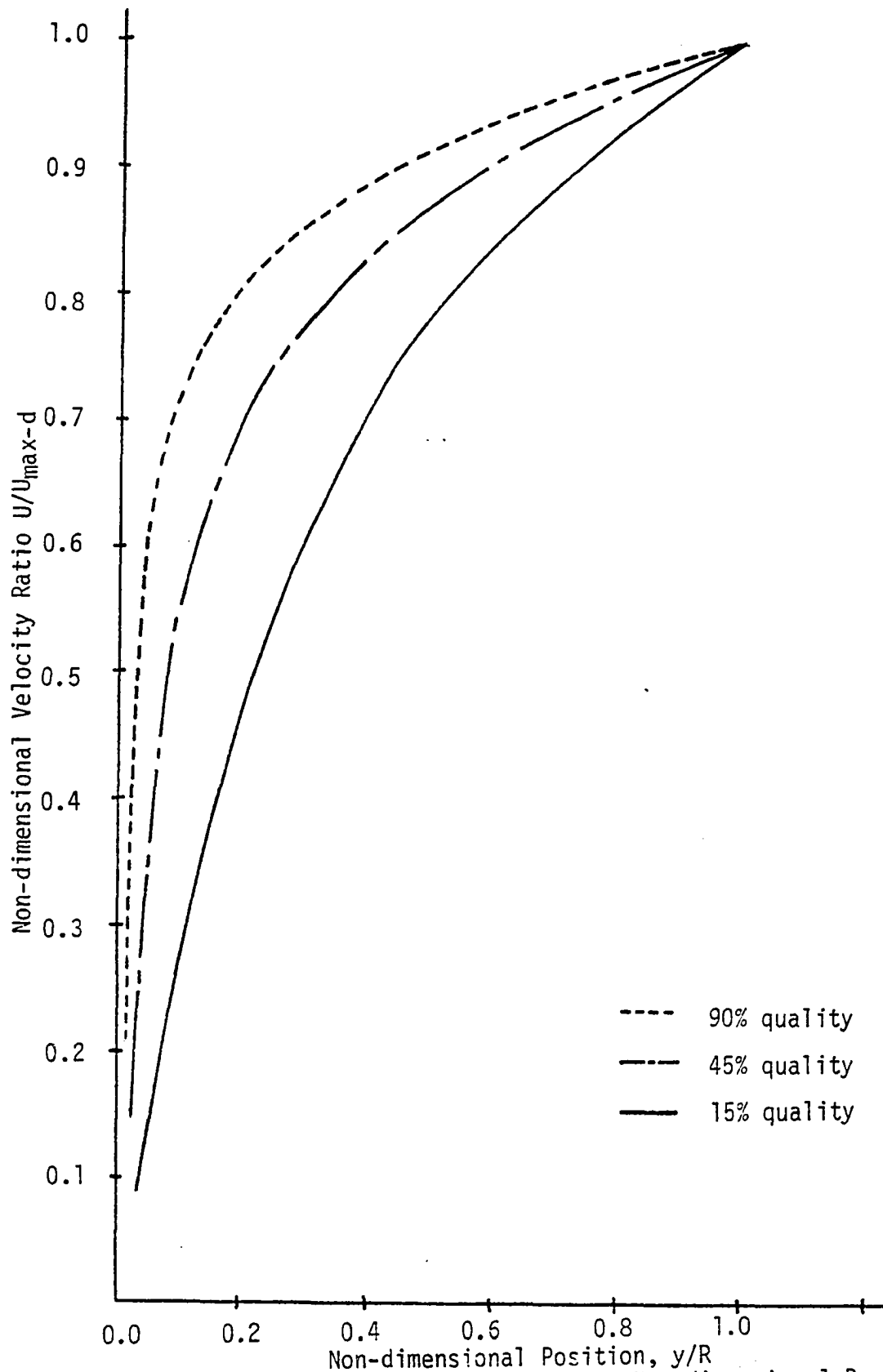
Figure 62. Non-dimensional Velocity Ratio vs.Non-dimensional Position
for the Ln-Ln (Parabolic) Model Using δ_{ave}.
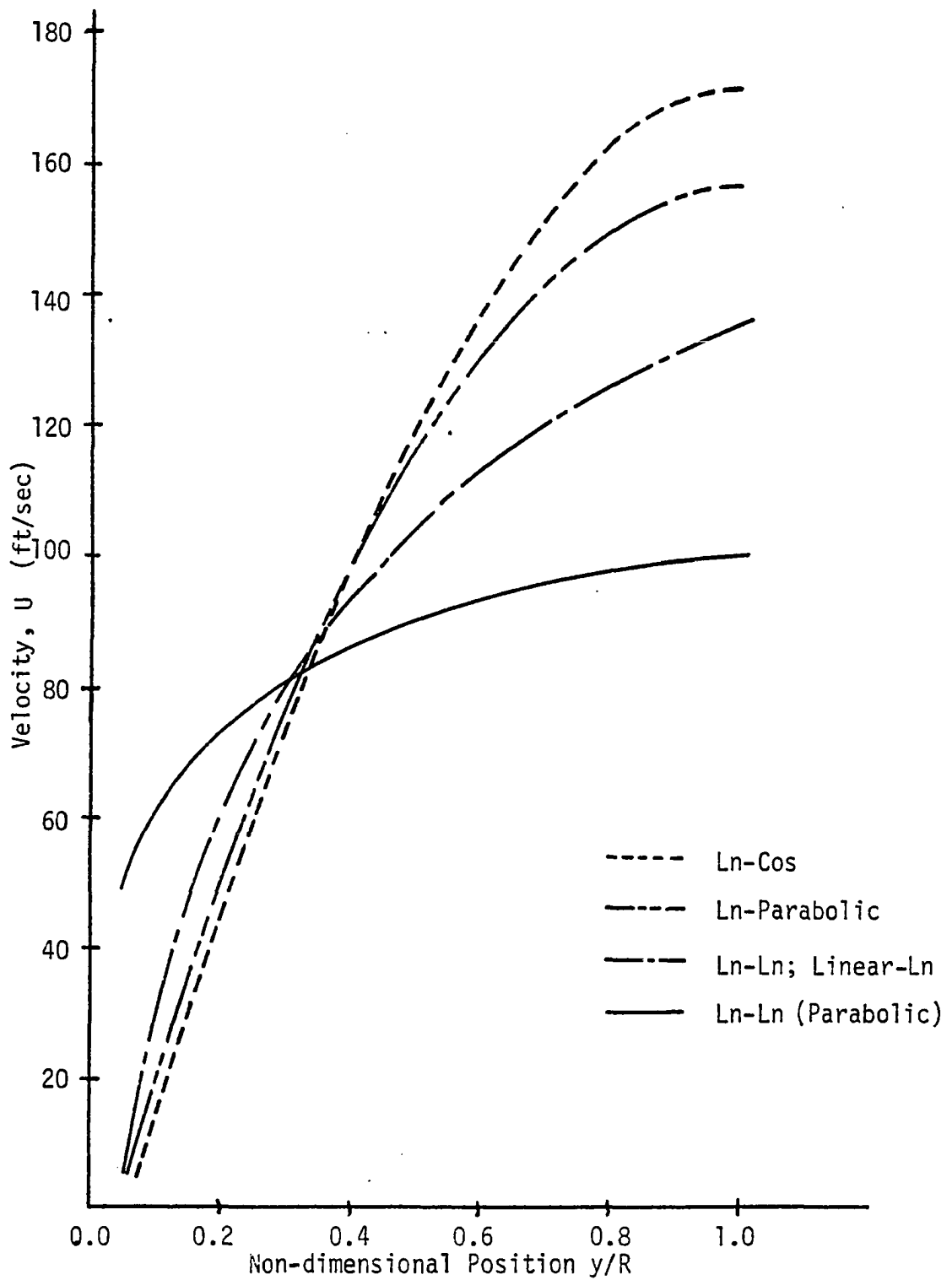
Figure 63. Gas Velocity Profiles For All Models at Flow Condition 460 Using δ_{ave}.

and also the steepest rise in velocity as a function of y/R
for small values of y/R. Figure 64 shows that similar trends
also exist at the 160 Flow Condition.

Since the values of velocity in the liquid layer are
usually much smaller than the velocity in the gas core,
liquid velocities on an expanded scale have been plotted in
Figures 65 and 66 for Flow Conditions 460 and 160, respec-
tively, using δ_{ave}. For small values of y/R, no distinction
could be made between the linear-ln and ln-ln models or be-
tween the ln-parabolic and ln-cos models. All the models
are in fair agreement with the exception of the ln-ln (para-
bolic) model which shows a much sharper rise in velocity for
values of y/R less than δ.

In general, for the flow conditions in this study,
the ln-ln and ln-parabolic models show the best correlation
with experimental values of maximum velocity. In addition,
the shape of these velocity profiles are in reasonable agree-
ment with the published values of Cousins and Hewitt.[54]

Blockage Factors

Another factor which can be used to describe the flow
pattern in two-phase flow is a blockage factor. In general,
a blockage factor will be described as the blockage of the
gas core region by the liquid. Smith[55,56] used a "correc-
tion factor", which represented the ratio of the effective
gas flow area to the total flow area available for the en-
tire two-phase flow mixture, to predict critical flow in an
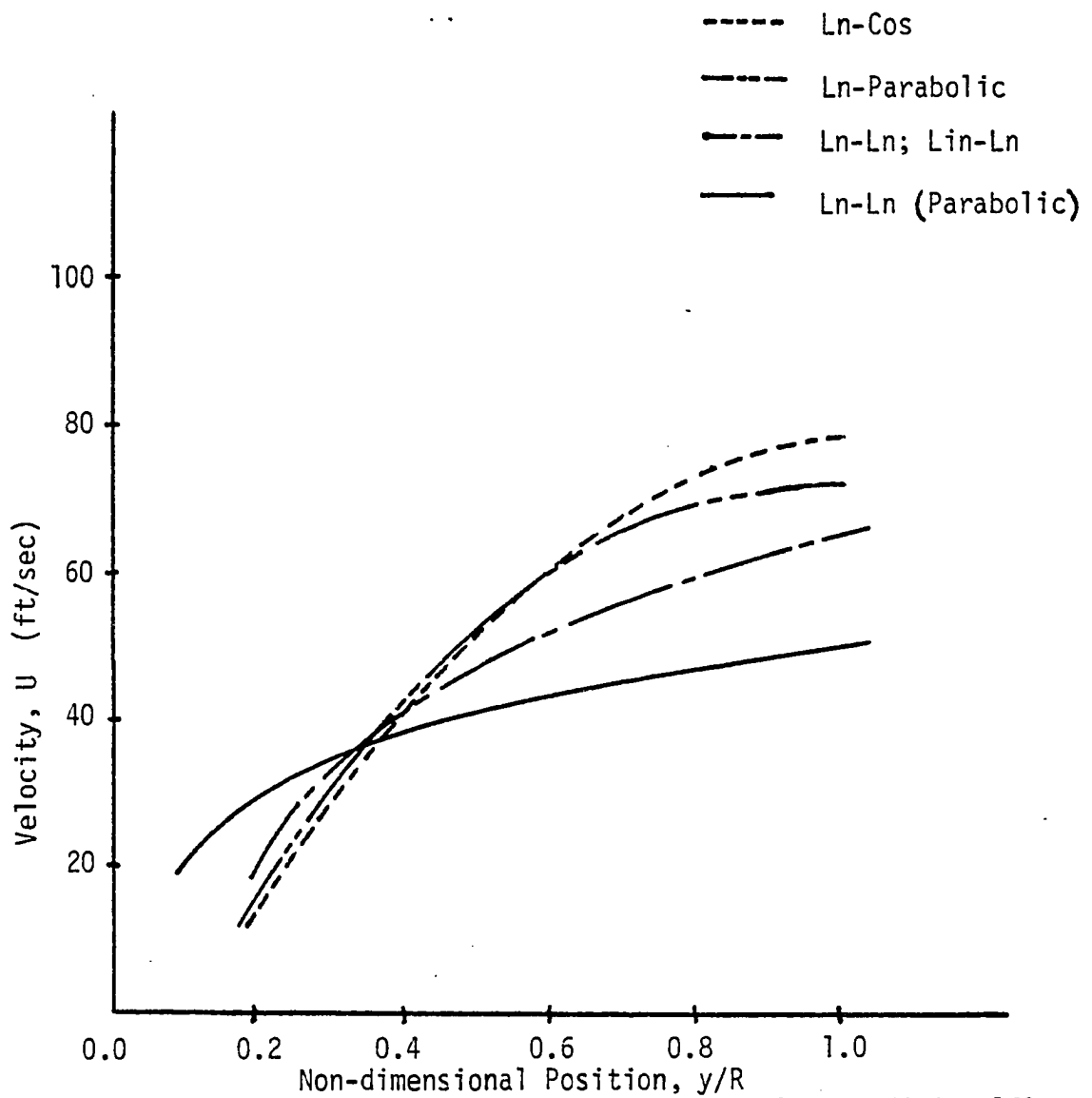
Figure 64. Gas Velocity Profiles for All Models at Flow Condition 160 Using δ_{ave}.
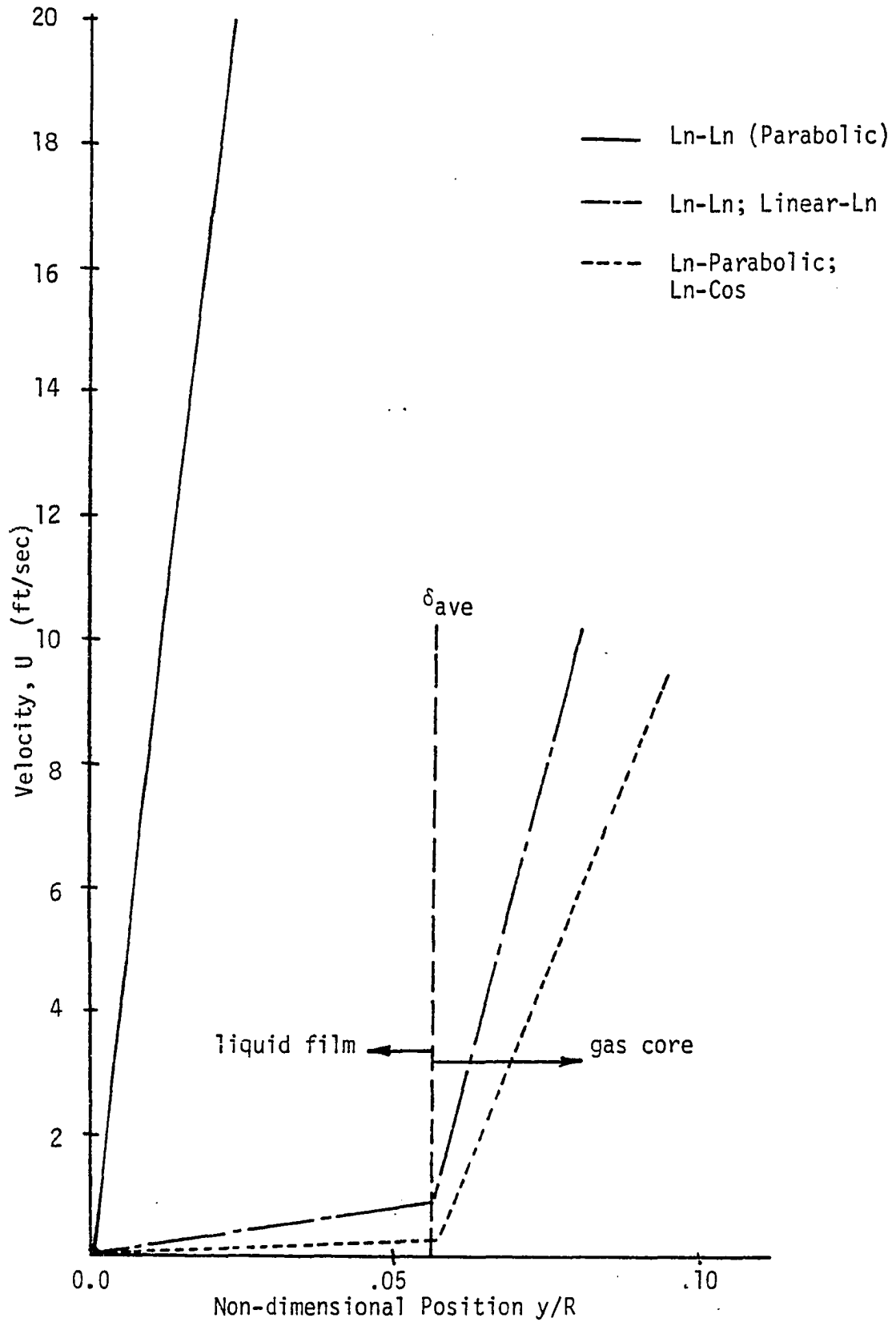
Figure 65. Liquid Velocity Profiles for All Models at Flow Condition 460 Using δ_{ave}.
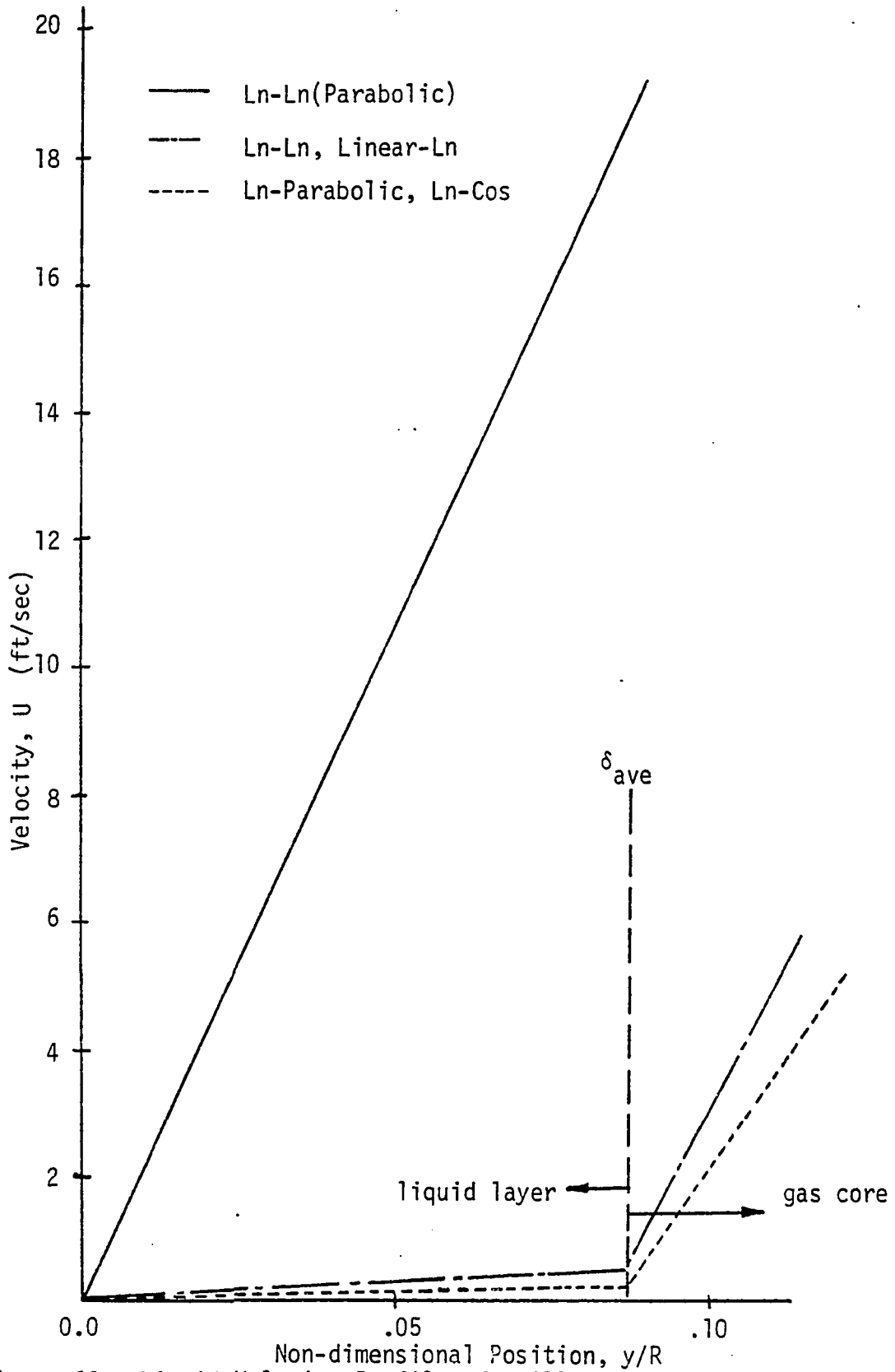
Figure 66. Liquid Velocity Profiles for All Models at Flow Condition 160 Using δ_{ave}.

air-water system. This correction factor was applied to critical two-phase flow using hydrogen and nitrogen with good success.[57] Sullivan[58] and Wallis and Sullivan[59] have also used a geometric blockage factor to modify separated flow theory equations with good success in describing gas-liquid nozzle flow.

In addition to a geometric blockage factor, a blockage based on mass flow has been implied by Wallis[60] in the calculation of an average core density as well as in calculating an interfacial shear stress. In both cases Wallis modifies normal separated flow expressions by the equivalent of a mass blockage factor in the form of $\dot{m}_g/\dot{m}_c$, where $\dot{m}_c$ is the core mass flow rate and $\dot{m}_g$ is the gas mass flow rate. As a result, both geometric and mass blockage factors for use in modifying separated two-phase flow expressions will be investigated for the flow conditions of this study.

First, consider blockage factors due to geometry. Defining the blockage factor as the ratio of the gas flow area to the total flow area, the blockage factor can be expressed as:

$$B_a = \frac{A_t - A_\delta - A_d - A_w}{A_t - A_\delta} \qquad (44)$$

where:

A_t is the cross sectional area of the flow tube

A_δ is the cross sectional area of the liquid film on the wall

A_d is the total cross sectional area of the droplets

A_w is the total cross sectional area of the wave tips

that extend into the gas core region

Physically, $A_t - A_\delta$ represents the gas core region, A_{gc}. In this blockage factor model of two-phase flow it is assumed that the gas flow does not have time to expand and completely fill the areas between the actual liquid film boundary and δ_{ave}, thus creating areas of backflow and re-circulation. It should also be noted that A_w is accounted for in A_δ as well as subtracted from A_{gc}, thus appearing to give a double count to the tips of the waves extending inside the gas core region. This method of calculation is justified by viewing this portion of the waves as causing a sudden, abrupt change in the gas flow area and similar to a "vena contracta" effect, making an even smaller cross sectional area available for gas flow. Therefore, the blockage factor can also be expressed as:

$$B_a = \frac{A_{gc} - A_d - A_w}{A_{gc}} \qquad (45)$$

or

$$B_a = 1 - \frac{A_{wd}}{A_{gc}} , \qquad (46)$$

where A_{wd} is the combination of wave and droplet area. Thus, this blockage factor should reflect the wave and droplet combination area as tabulated in Table VI and shown in Figure 44. Figure 67 shows B_a plotted as a function of quality
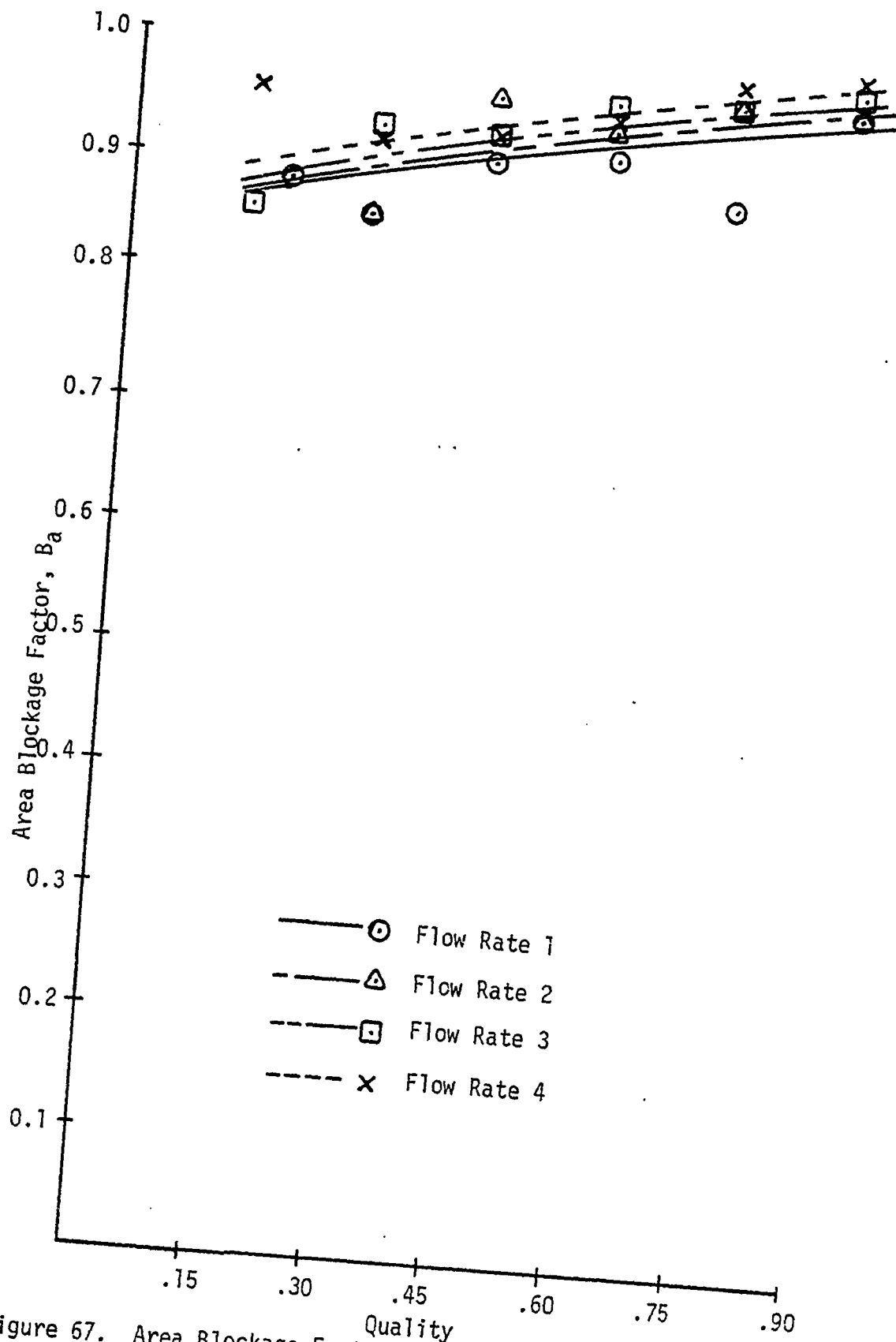
Figure 67. Area Blockage Factor as a Function of Quality for Each Flow Rate.

for each of the flow rates. It was noticed that the scatter around a single best fit curve for all flow rates was approximately the same as the scatter of B_a for all slides at a given flow condition. As a result, a single, average curve will be used to summarize the area blockage factor as shown in Figure 68.

Another geometric blockage factor can be calculated based on a volume blockage due to the liquid. Defining this blockage factor as the ratio of the gas flow volume to the total flow volume in the control volume region, B_v can be expressed as follows:

$$B_v = \frac{V_r - V_d - V_w}{V_r} . \tag{47}$$

V_r represents the control volume defined as the height of the illuminated slit times the flow tube cross sectional area. V_d and V_w represent the volume blockage due to the droplet and waves respectively. The blockage volume of the droplets was calculated as a wake in the form of a cone having a circular base with an area equal to the cross sectional area of each droplet. The height of the cone was chosen to be five times the equivalent droplet diameter, but not exceeding 0.3 inches, although an assumed height ranging from three to ten times the equivalent diameter would be considered just as reasonable. Thus the volume blockage for each droplet was calculated by

$$V_d = A_d \frac{h}{3} = \frac{\pi abh}{12} .$$
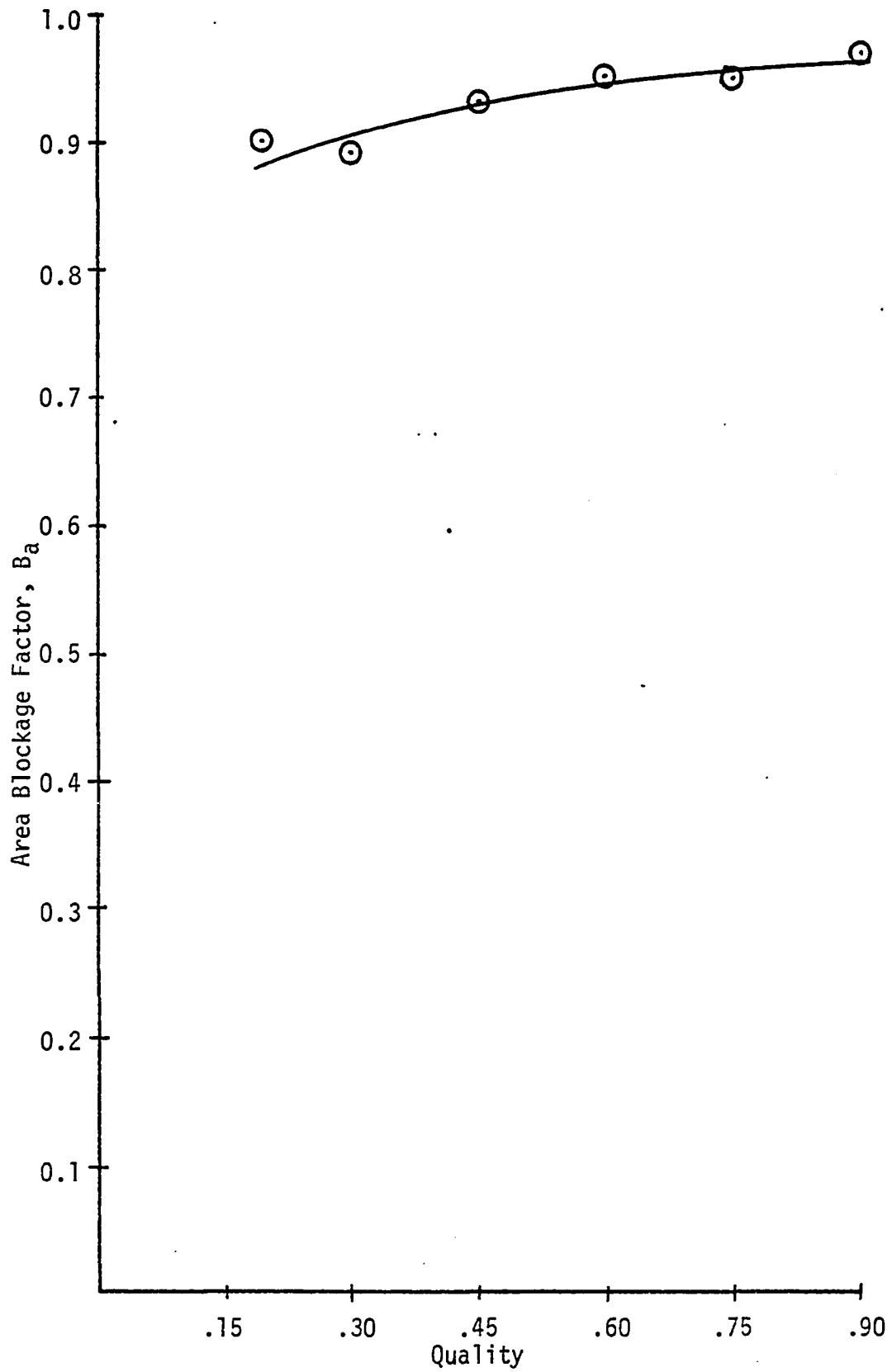
Figure 68. Average Value of the Area Blockage Factor as a Function of Quality.

The volume blockage due to the waves was calculated
by taking the wave blockage area, A_w, times the height of
the control volume, 0.3 inches. Figure 69 shows the volume
blockage factor as a function of quality, using an average
value of B_v from all four gas flow rates. It should be
noted that as the droplets grow larger and the cones become
more like cylinders, or if the height of the cone is chosen
to be ten to twenty times the equivalent droplet diameter,
the values of B_v should approach B_a.

Figures 70 and 71 show the effect on B_a and B_v, re-
spectively, when the blockage due to the waves is neglected
and only the blockage due to the droplets in the core is
considered.

Additional blockage factors can be calculated based
on mass flow and defined in general as

$$B = \frac{\dot{m}_g}{\dot{m}_c} .$$

(48)

Assuming a constant, but different, velocity profile in
both the liquid and gas regions as shown in Figure 72,
equation (48) can be written as

$$B_1 = \frac{x\dot{m}_t}{\dot{m}_t - \dot{m}_r}$$

(49)

where $\dot{m}_t$ is the total mass flow, x is the quality, and $\dot{m}_r$
is the mass flow in the liquid ring on the wall of the tube.
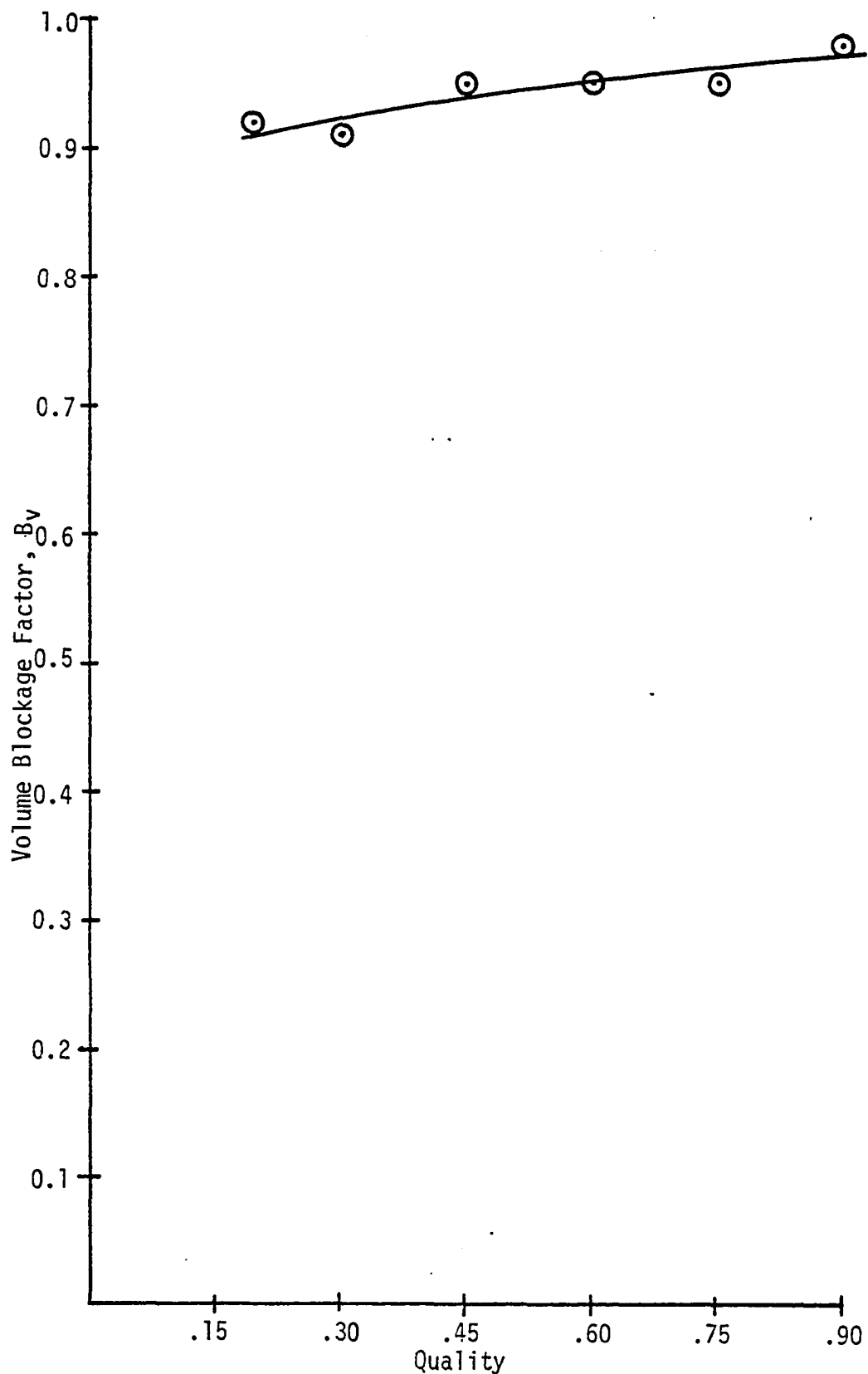
Figure 69. Average Value of the Volume Blockage Factor as a Function of Quality.
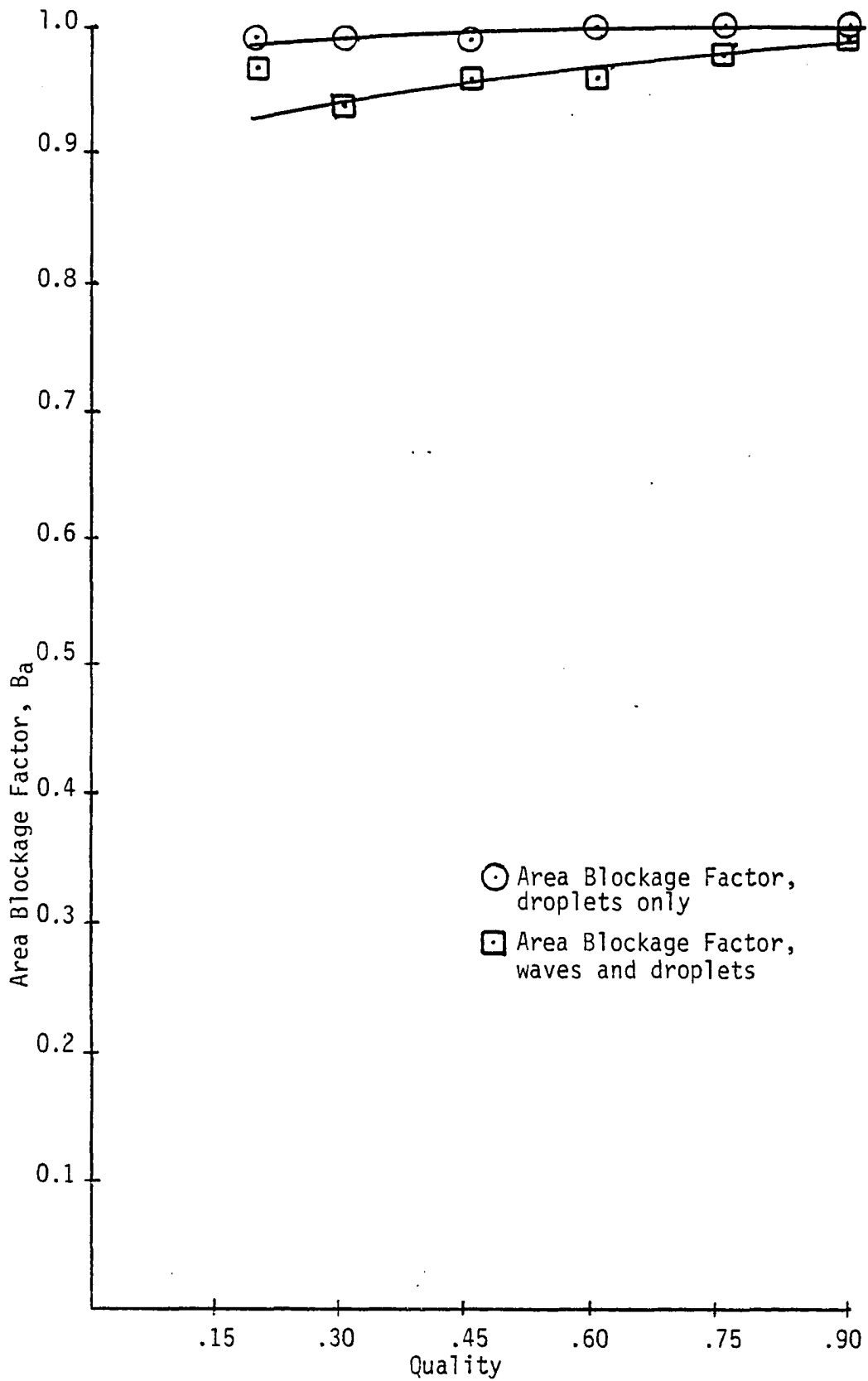
Figure 70. A Comparison of Area Blockage Factor With and Without Waves.
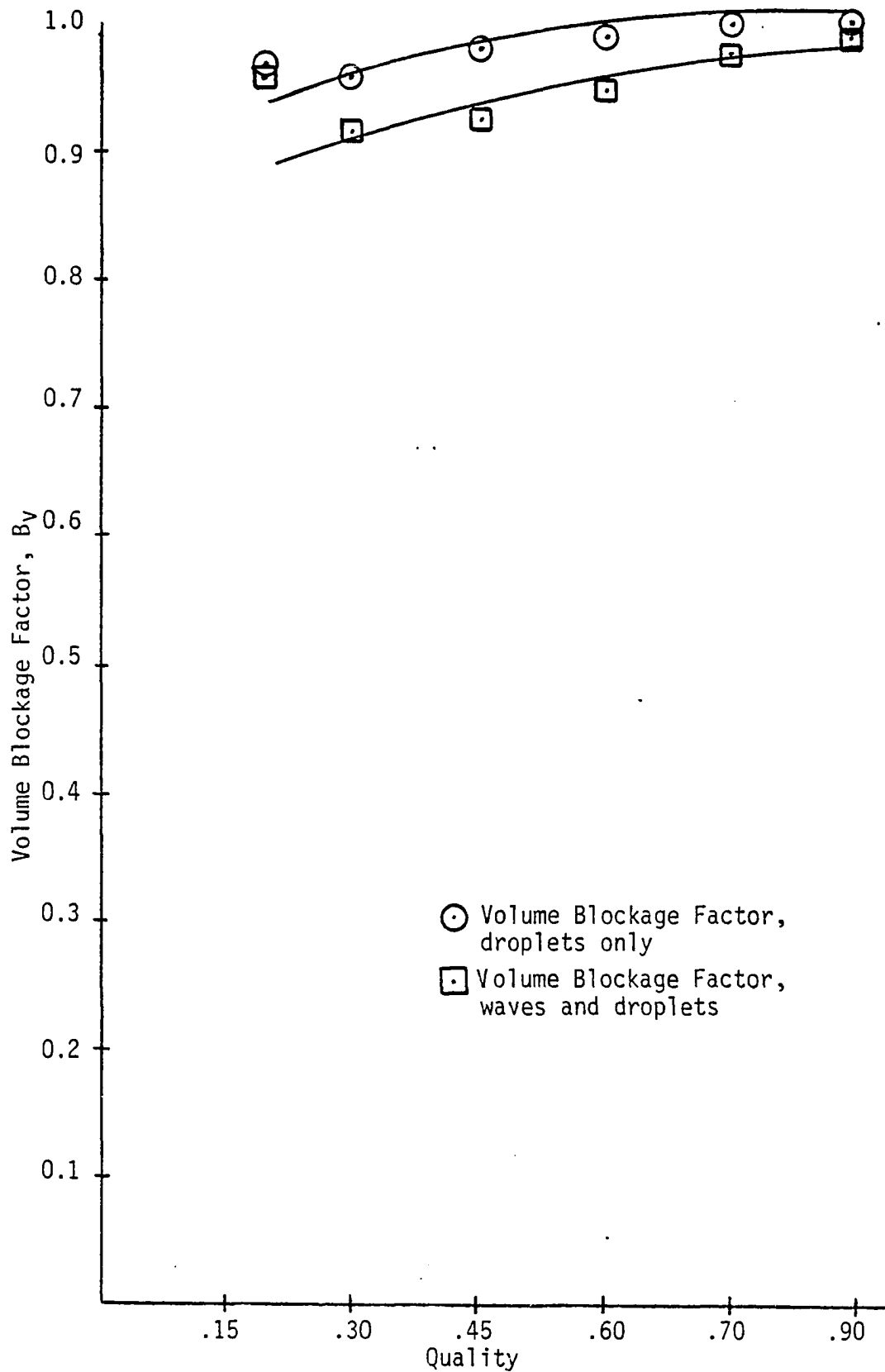
Figure 71. A Comparison of Volume Blockage Factor With and Without Waves.
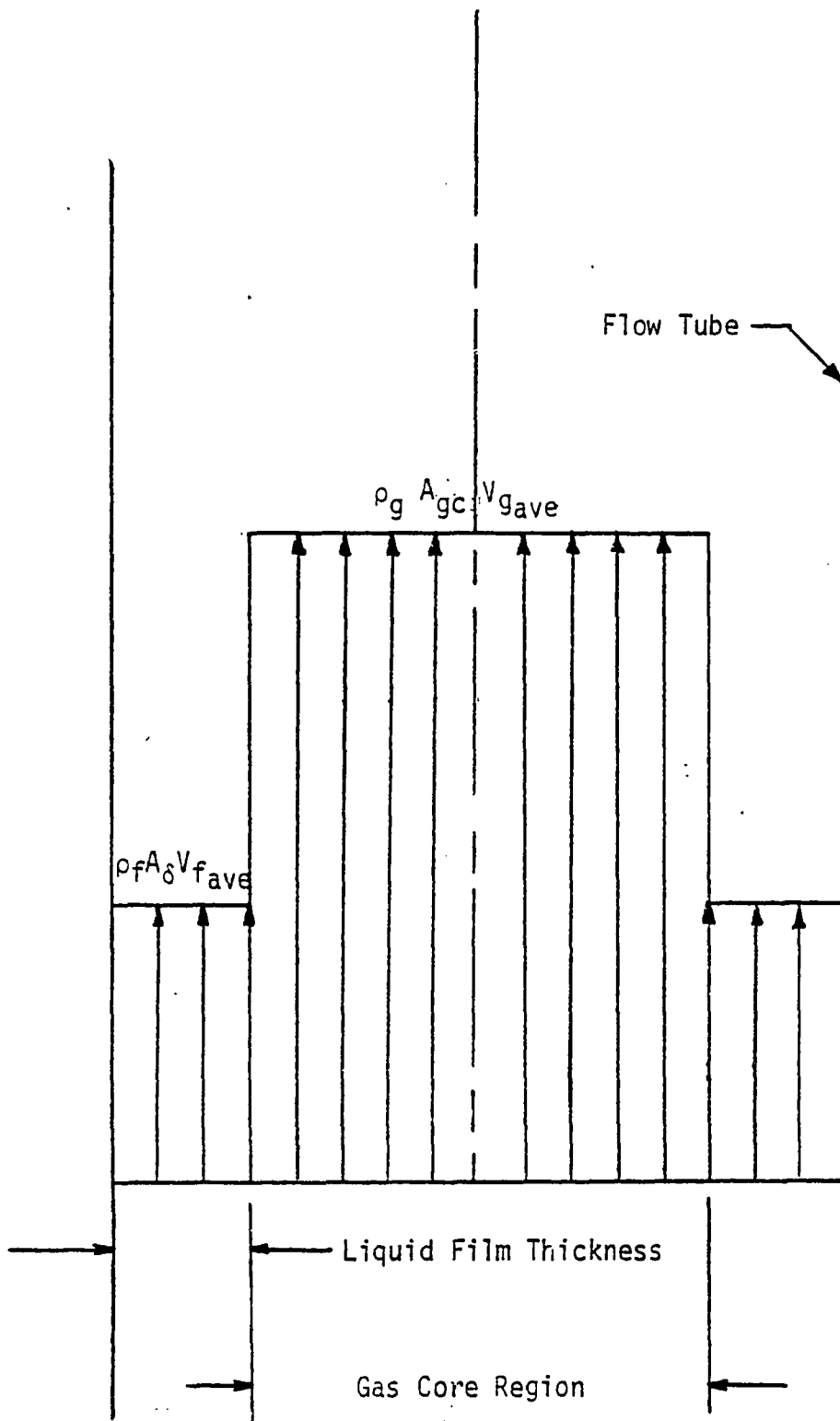
Figure 72. A Sketch of the Simplified Flow Pattern Assumed for Mass Blockage Factors B_1 and B_2.

From a mass balance of the liquid layer on the wall,

$$\dot{m}_r = \rho_f A_\delta V_{f_{ave}} \tag{50}$$

where $V_{f_{ave}}$ is the average liquid velocity in the liquid film. Now using a total mass balance for the liquid in the tube and assuming constant liquid velocity throughout the two-phase mixture yields:

$$\dot{m}_f = \rho_f V_{f_{ave}} (A_t - A_g + A_d) \tag{51}$$

where A_g is the cross sectional area of the gas flow. Therefore:

$$V_{f_{ave}} = \frac{\dot{m}_f}{\rho_f (A_t - A_g + A_d)} = \frac{(1 - x)\dot{m}_t}{\rho_f (A_t - A_g + A_d)} \tag{52}$$

Substituting equation (52) into equation (50) and substituting equation (50) into equation (49), the blockage factor may be expressed as:

$$B_1 = \frac{x\dot{m}_t}{\dot{m}_t - \rho_f A_\delta \left[\frac{(1-x)\dot{m}_t}{\rho_f (A_t - A_g + A_d)}\right]} \tag{53}$$

or:

$$B_1 = \frac{x}{1 - (1-x)\left(\frac{A_\delta}{A_\delta + A_d}\right)} . \tag{54}$$

Notice that the area of the waves influences this blockage factor only through A_δ, the cross sectional area of an equivalent liquid layer on the wall. Values of B_1 are plotted as functions of quality for all four gas flow rates in Figure 73. Again it was noticed that a best fit curve through an average value of B_1 at all the flow rates for a given quality was a reasonable representation of the data. These average points are represented in Figure 74.

Another form of the mass blockage factor can be determined if the mass flow in the core is described as:

$$\dot{m}_c = \dot{m}_{gas} + \dot{m}_{wave} + \dot{m}_{droplets}$$

or

$$\dot{m}_c = \rho_g A_g V_{g_{ave}} + \rho_f A_w V_{f_{ave}} + \rho_f A_d V_{f_{ave}} \qquad (55)$$

Again, using equation (52) as an expression of the average liquid velocity, and using

$$\dot{m}_g = x\dot{m}_t \; ,$$

the blockage factor can be written as:

$$B_2 = \frac{x\dot{m}_t}{x\dot{m}_t + \rho_f(A_w + A_d)\left[\dfrac{(1-x)\dot{m}_t}{\rho_f(A_t - A_g + A_d)}\right]} \; . \qquad (56)$$

Collecting terms and re-arranging,

$$B_2 = \frac{x}{x + (1-x)\left[\dfrac{A_w + A_d}{A_\delta + A_d}\right]} \; . \qquad (57)$$
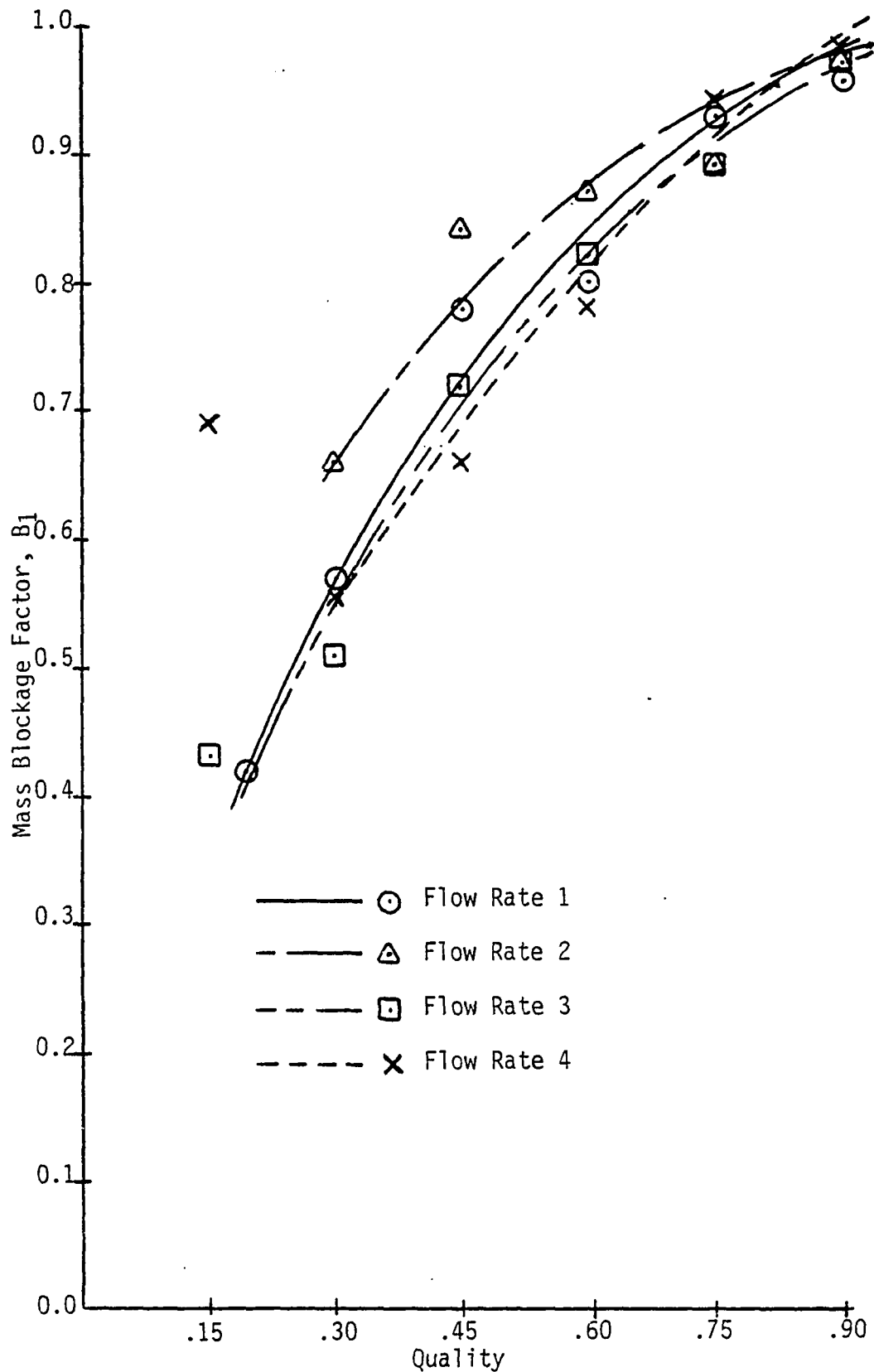
Figure 73. Mass Blockage Factor B_1 as a Function of Quality for Each Flow Rate.
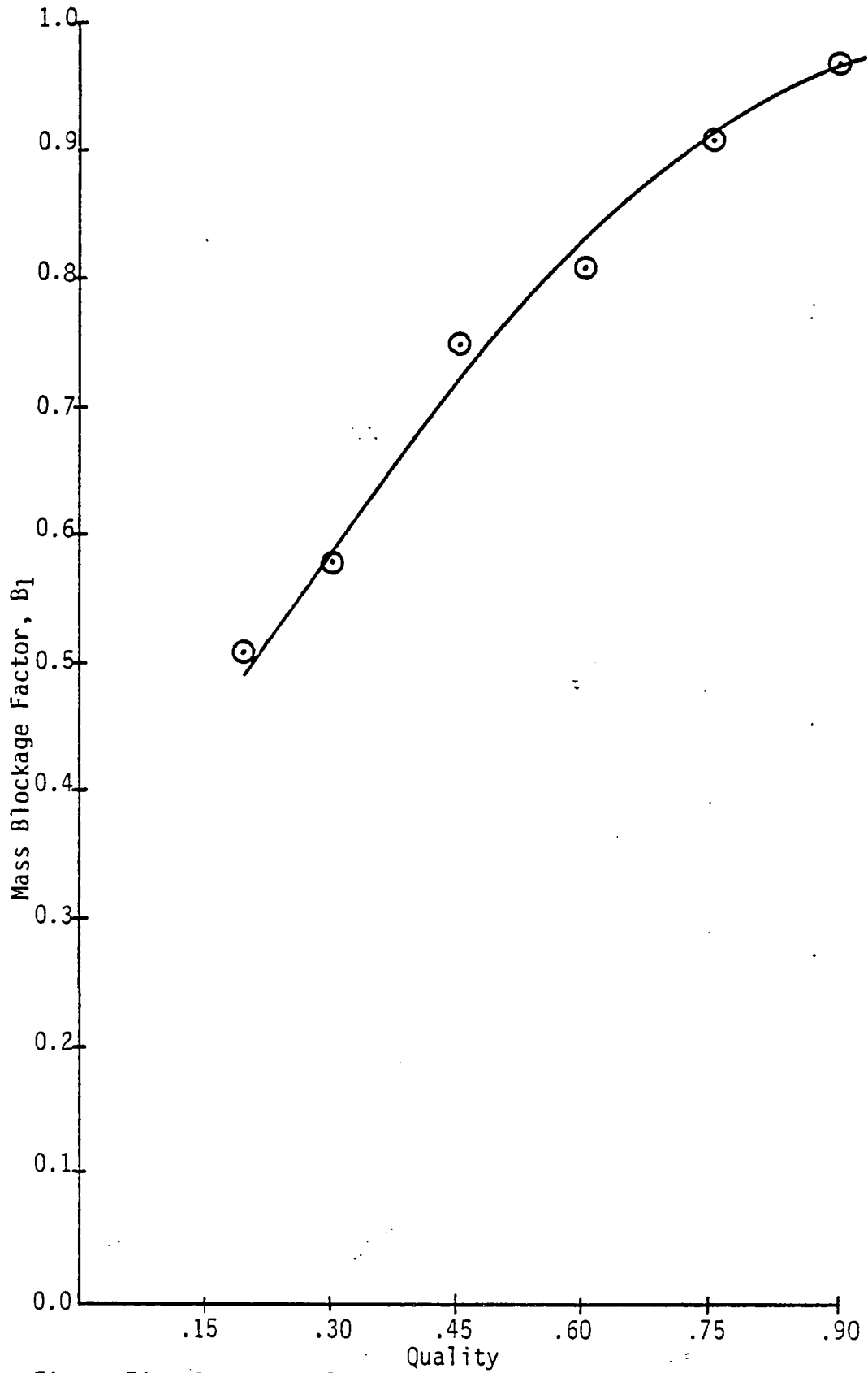
Figure 74. Average Value of the Mass Blockage Factor B_1 as a Function of Quality.

When the form of B_2 is compared to B_1 it is noticed that the combination of the wave and droplet blockage areas is used directly in equation (57). Figure 75 shows how B_2 varies with quality when an average value of B_2 from all flow rates is calculated.

Using the general definition of the mass blockage factor as expressed in equation (48) and recalling that only liquid flows in the δ film thickness on the wall of the tube, the blockage factor can be written as:

$$B = \frac{\dot{m}_g}{\dot{m}_t - 2\pi\rho_\ell \int_{R-\delta}^{R} v_\ell r dr} \qquad . \qquad (58)$$

Using this expression, mass blockage factors corresponding to some of the two-phase velocity profiles can be determined. For the ln-parabolic model and using V_ℓ given by equation (13), the blockage factor becomes:

$$B_3 = \frac{x}{1 + \dfrac{\pi \rho_\ell U_{max}-aR^2}{\dot{m}_t\left(\ln\sqrt{\alpha} - \dfrac{\mu r}{2}\right)} \left\{\alpha\ln\sqrt{\alpha} + \eta\left(1 - \dfrac{\eta}{2}\right)\right\}} \qquad . \qquad (59)$$

Figures 76 and 77 show the variation of B_3 with quality for all flow rates using δ_{ave} and δ_r respectively.

In a similar fashion the blockage factor for the ln-ln model can be expressed, using V_ℓ given by equation (21), as follows:
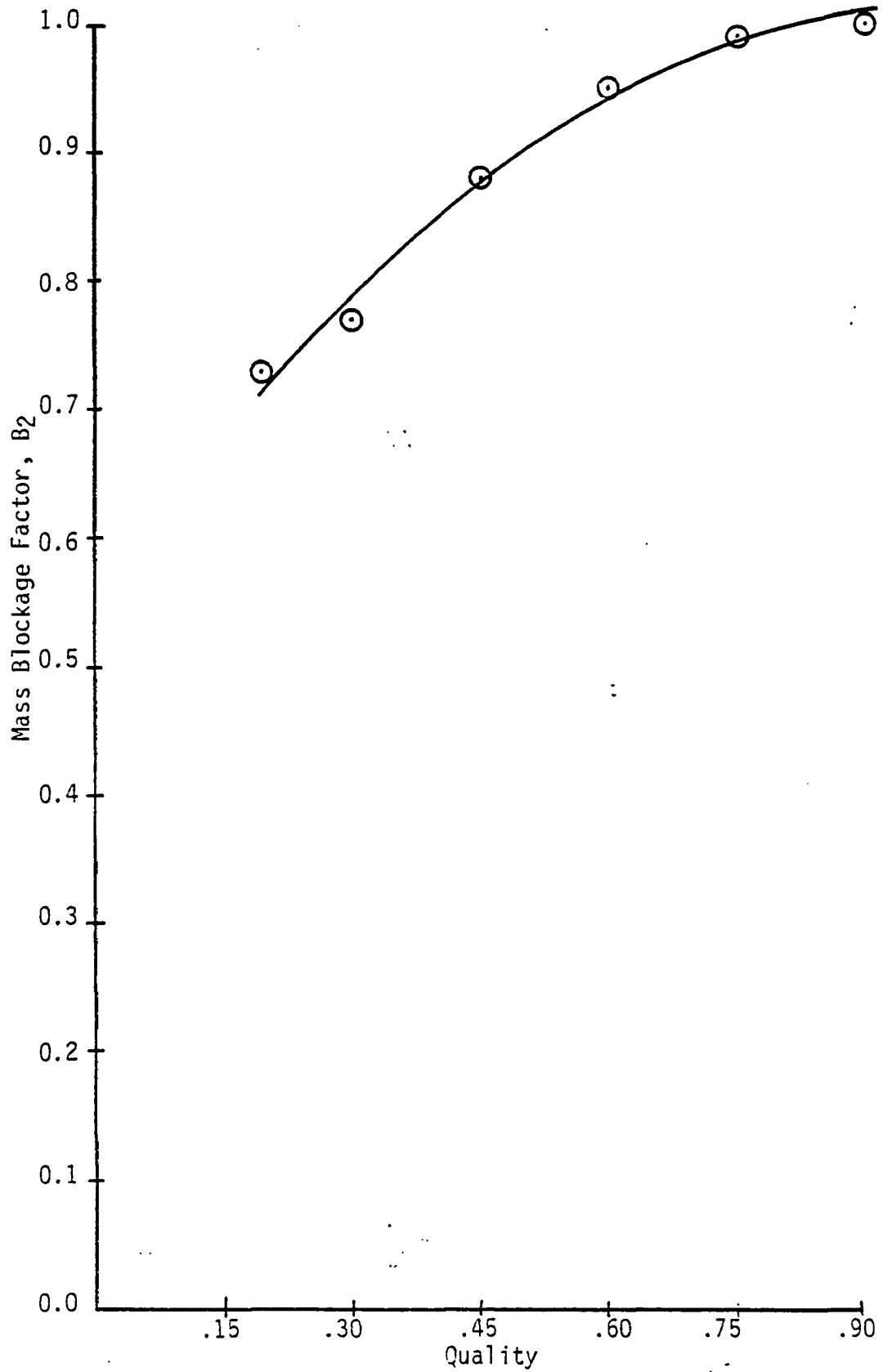
Figure 75. Average Value of the Mass Blockage Factor B_2 as a Function of Quality.
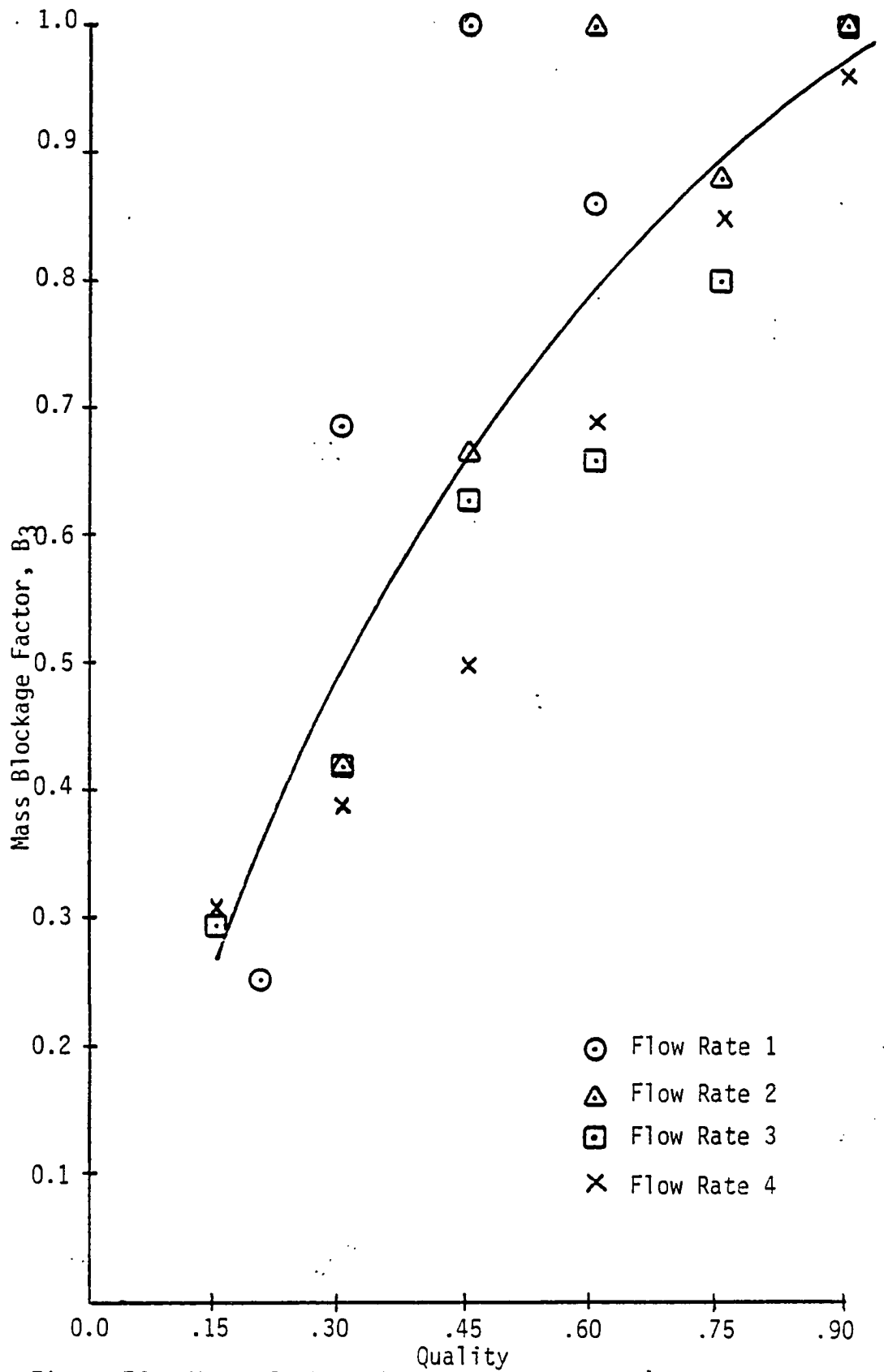
Figure 76. Mass Blockage Factor B_3 From the Ln-Parabolic Model as a Function of Quality Using δ_{ave}.
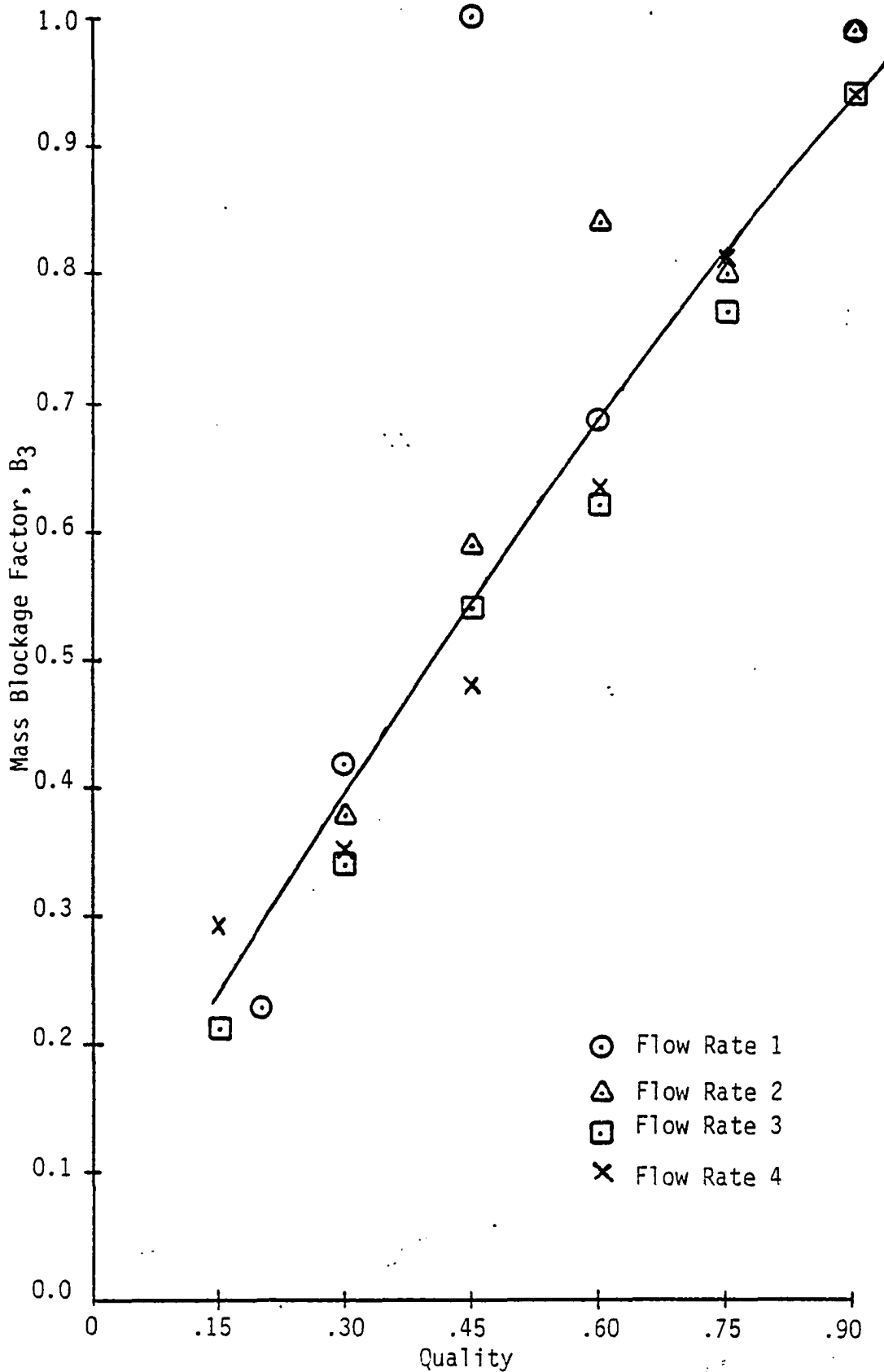
Figure 77. Mass Blockage Factor B_3 From the Ln-Parabolic Model as a Function of Quality Using δ_r.

$$B_4 = \frac{x}{1 - \left[\frac{2\pi\rho_\ell R^2 U_{max}-b\sqrt{\alpha}}{\dot{m}_t\mu_r n\Lambda_1}\right]\left[\frac{\alpha}{2}\ln\sqrt{\alpha} - \frac{\alpha}{4}\right]} \cdot \qquad (60)$$

Using a limiting value of one for the value of the blockage factor, an average value of B_4 from all flow rates are shown in Figure 78 for both δ_{ave} and δ_r.

For the linear-ln model, with V_ℓ given by equation (26), the blockage factor becomes:

$$B_5 = \frac{x}{1 - \frac{2\pi\rho_\ell R^2 U_{max}-c\Lambda_2}{\dot{m}_t\mu_r}\left(\frac{n}{2} - \frac{n^2}{3}\right)} \cdot \qquad (61)$$

Likewise for the ln-cos model, using V_ℓ given by equation (32), the blockage factor becomes:

$$B_6 = \frac{x}{1 - \left(\frac{\pi^2\rho_\ell R^2 U_{max}-d}{2\dot{m}_t\Lambda_3\mu_r}\right)\left[\alpha\ln\sqrt{\alpha} + n\left(1 - \frac{n}{2}\right)\right]} \cdot \qquad (62)$$

Figures 79 and 80 compare B_3, B_4, B_5 and B_6 using δ_{ave} and δ_r respectively. The values of blockage factor from the linear-ln and ln-ln models are approximately equal, as are the values of blockage factor from the ln-parabolic and ln-cos models. Figure 81 compares the values of B_1 and B_2, assuming average velocities in each phase, to B_3 and B_4, which use velocity profiles that vary with radial position through the tube. While the values of mass blockage factor
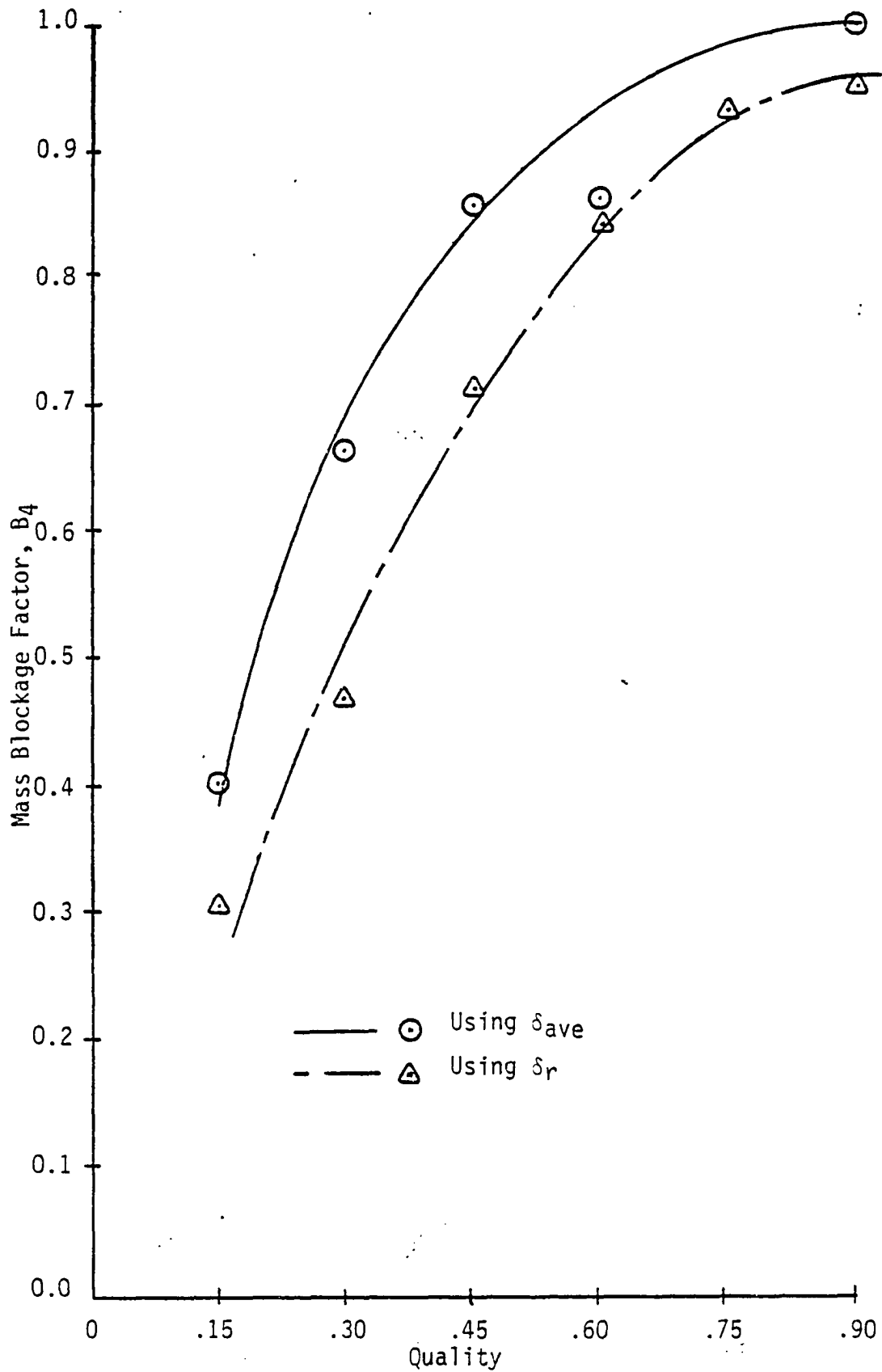
Figure 78. Mass Blockage Factor B_4 From the Ln-Ln Model as a Function of Quality
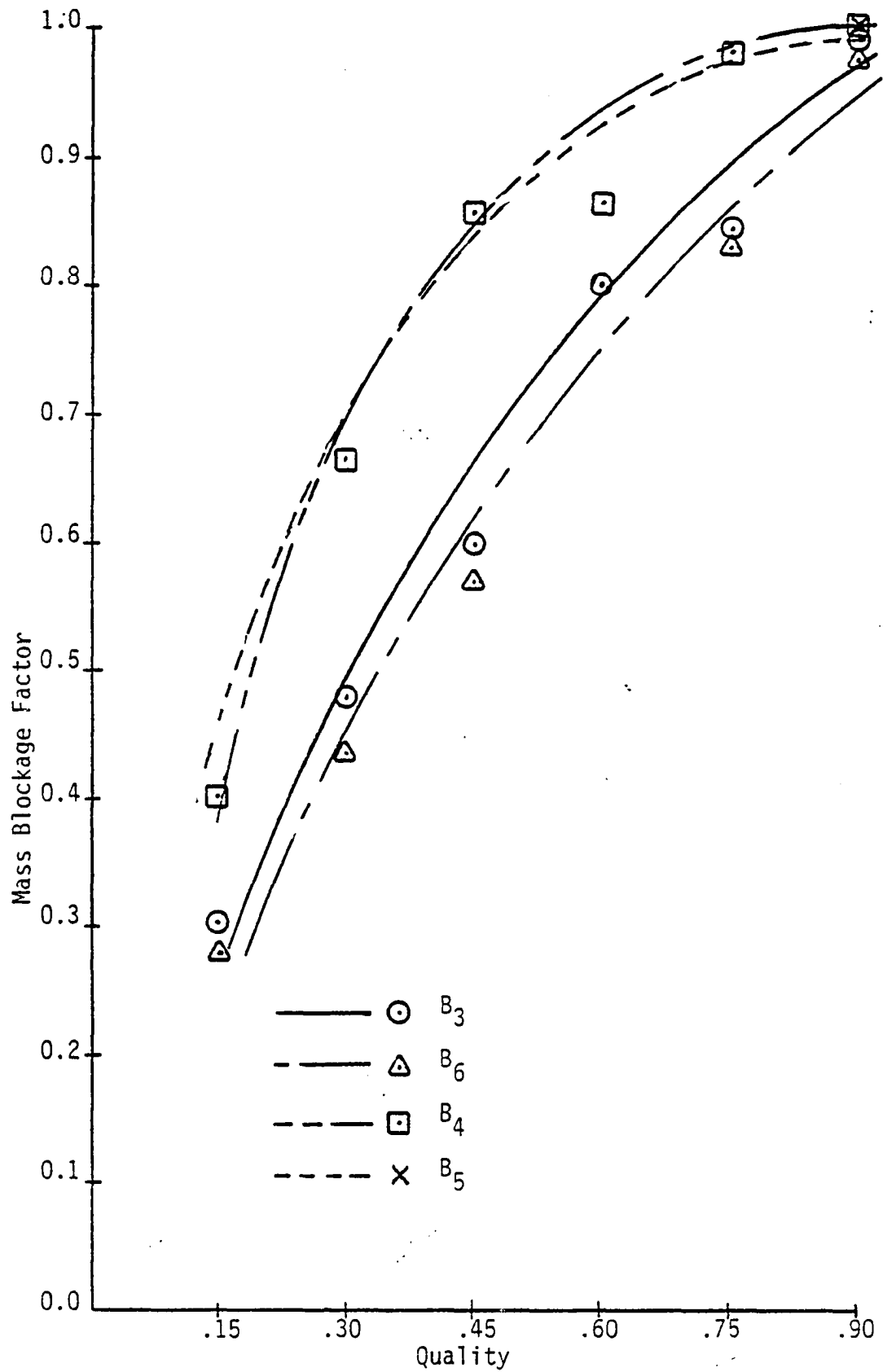
Figure 79. A Comparison of the Mass Blockage Factors from the Velocity Profile Models Using δ_{ave}.
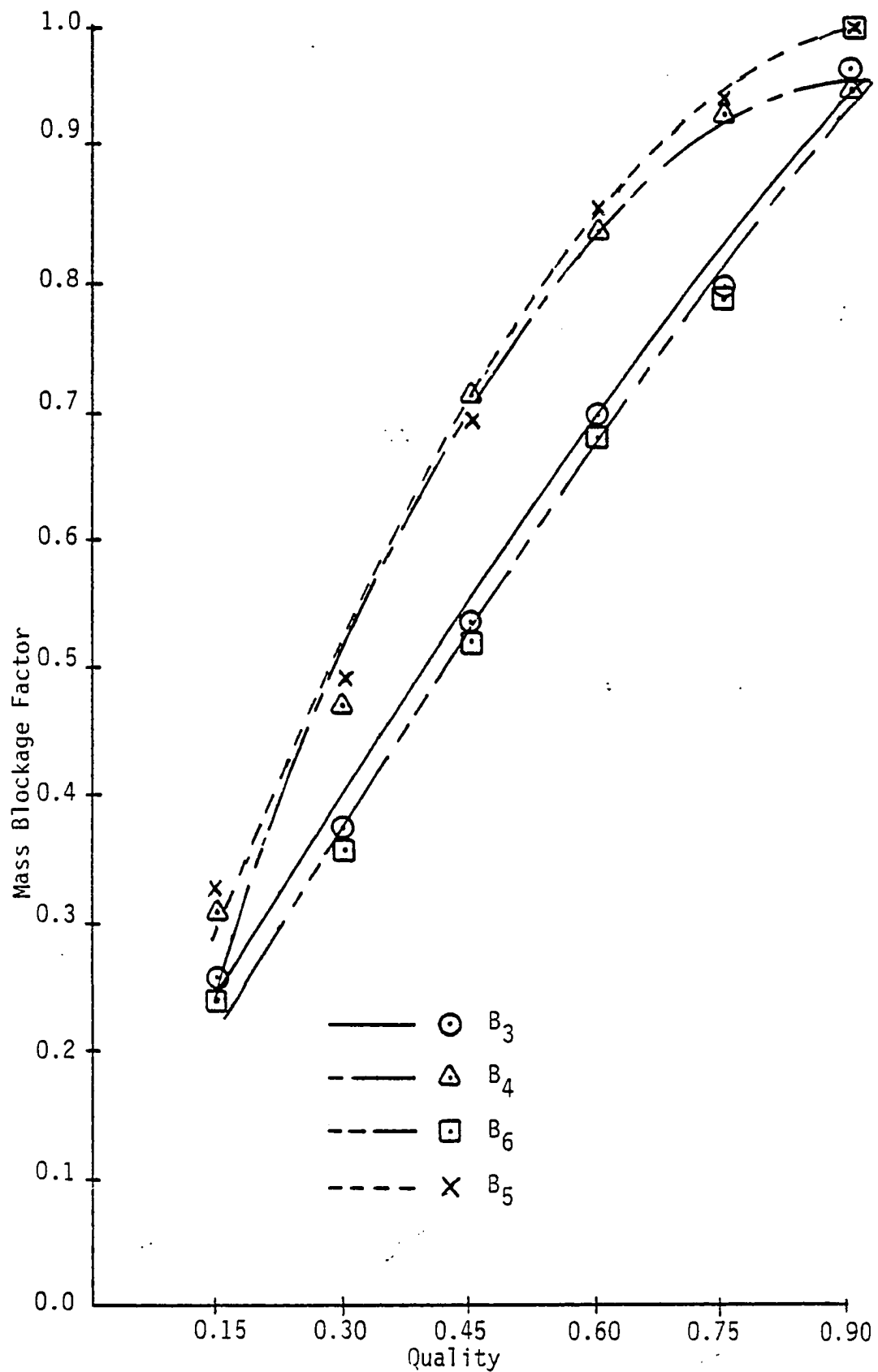
Figure 80. A Comparison of the Mass Blockage Factors From the Velocity Profile Models Using δ_r.
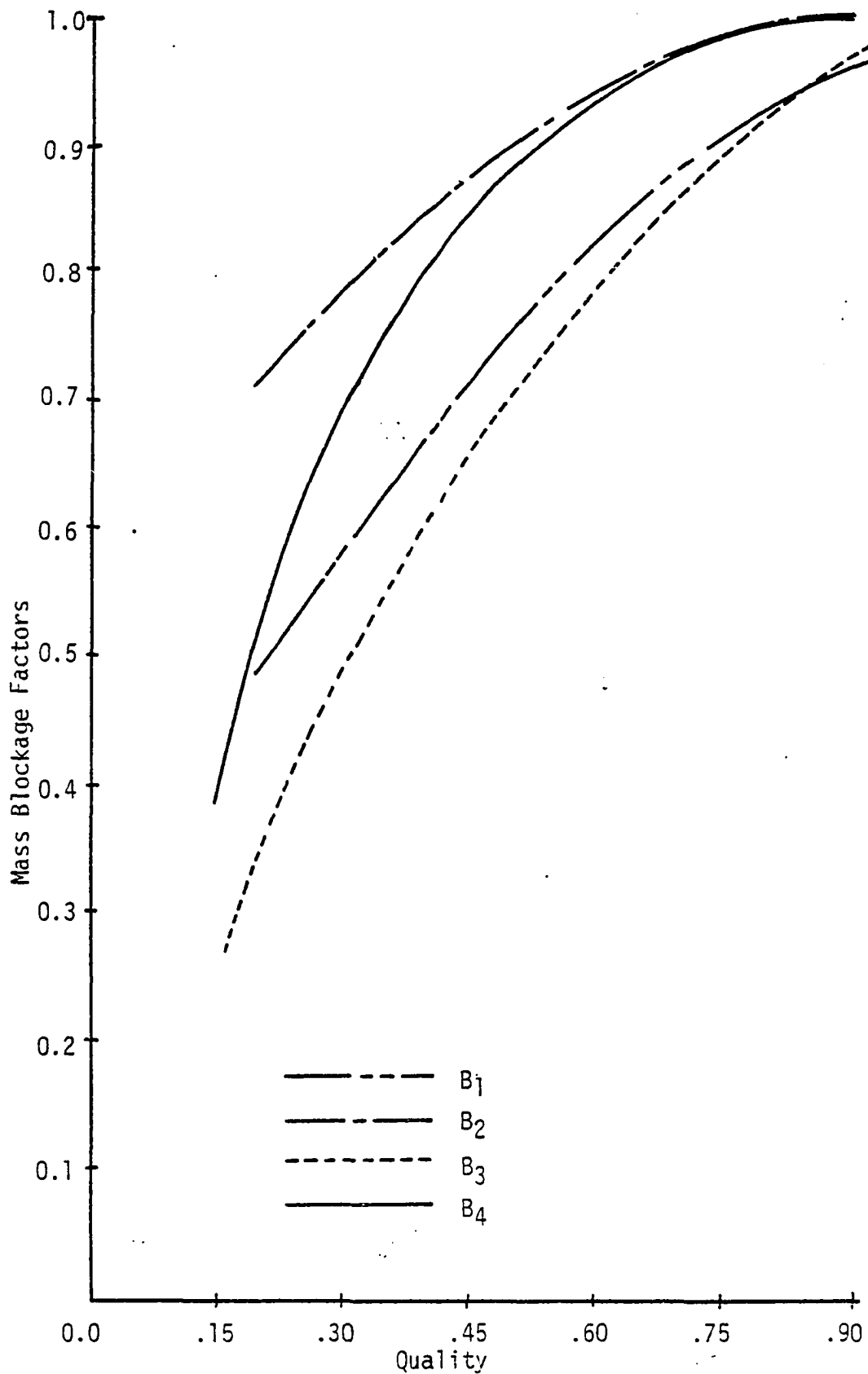
Figure 81. A Comparison of Mass Blockage Factors B_1 and B_2 to Mass Blockage Factors from the Ln-Parabolic and Ln-Ln Models Using δ_{ave}.

using the ln-parabolic model were lower than the other mass
blockage factor values, there was reasonable agreement be-
tween B_3 and B_2 above 45% quality. Likewise for the ln-ln
model blockage factor and mass blockage factor B_1; there
was excellent agreement at qualities greater than 45%.

An obvious application of the mass blockage factor
is to obtain a value of the core density, ρ_c, by modifying
the gas density as follows:

$$\rho_c = \frac{\rho_g}{B} .$$

A more important application of the mass blockage factor can
be made by modifying either the gas flow area or the gas ve-
locity as predicted by separated two-phase flow models.
Tables X and XI show the values of U_{max-a} and U_{max-b} modi-
fied by the mass blockage factors, thus accounting for the
liquid entrainment in the gas core region. The maximum ve-
locities from both models were scaled as follows:

$$U_a = \frac{U_{max-a}}{B_3} \quad \text{and} \quad U_b = \frac{U_{max-b}}{B_4}$$

for both δ_{ave} and δ_r. A comparison of the experimental
values of the maximum velocity for qualities of 75 to 90%
with U_a and U_b show that the difference between the modi-
fied values predicted by the ln-parabolic model actually
increased. However, the values predicted by the ln-ln model
and modified by the mass blockage factor were found to be in

Table X. Comparison of Modified Maximum Velocities from the Ln-Parabolic
and the Ln-Ln Models Using δ_{ave} with Experimental Data.

Flow Condition Number	$U_{max} - a$ (ft/sec)	B_3 δ_{ave}	U_a (ft/sec)	U_{max} Experimental (ft/sec)	U_b (ft/sec)	B_4 δ_{ave}	$U_{max} - b$ (ft/sec)
180	70.0*	.93	75.3	61.	60.9	.985	60.0*
190	66.9	.97	69.0	59.	57.3	.99	56.7
275	89.8	.90	99.8	81.	78.5	.98	76.9
290	89.1	.97	91.9	79.	76.2	.99	75.5
375	108.3	.90	120.3	100.	90.0	.98	88.2
390	112.7	.97	116.2	95.	95.8	.99	94.8
475	155.4	.90	172.7	136.	133.9	.98	131.2
490	151.1	.97	155.8	133.	123.6	.99	122.4

*Velocity values for flow condition 180 were interpolated from flow conditions 160 and 190.

Table XI.   Comparison of Modified Maximum Velocities from the Ln-Parabolic and the Ln-Ln Models Using δ_r with Experimental Data.

Flow Condition Number	$U_{max} - a$ (ft/sec)	B_3 δ_r	U_a (ft/sec)	U_{max} Experimental (ft/sec)	U_b (ft/sec)	B_4 δ_r	$U_{max} - b$ (ft/sec)
180	64.0*	.87	73.6	61.	56.4	.94	53.0*
190	65.2	.95	68.6	59.	55.7	.96	53.5
275	86.5	.82	105.5	81.	76.6	.92	70.5
290	86.7	.95	91.3	79.	74.0	.96	71.0
375	106.2	.82	129.5	100.	91.1	.92	83.8
390	110.3	.95	116.1	95.	93.8	.96	90.0
475	152.9	.82	186.5	136.	137.4	.92	126.4
490	149.5	.95	157.4	133.	124.1	.96	119.1

* Velocity values for flow condition 180 were interpolated from flow conditions 160 and 190.

excellent agreement with the experimental data. An additional application of the mass blockage factor will be discussed in the next section concerning interfacial shear stress values.

In general it is felt that the mass blockage factors offer an advantage over the blockage factors which just consider geometry for several reasons. Chiefly, the geometric blockage factors cannot reflect the interfacial property or the flow pattern as completely as the mass blockage factors can due to the dependence of the latter on the velocity profile. When using the geometric blockage factors, empirical factors were sometimes inserted just to insure good correlation of the data.[61] The insertion of these empirical factors indicates that geometry alone is not sufficient to describe the blockage of the flow pattern. It is felt that the mass blockage factors reflect those quantities, namely the flow pattern, velocity and interfacial processes, which more accurately describe two-phase flow.

Interfacial Shear Stress

One flow factor of considerable interest is the interfacial shear stress. Values of interfacial shear stress were calculated for this study as an application of the velocity profiles and the blockage factors in the following manner. Using the ln-parabolic model with the gas velocity profile given in equation (12), the interfacial shear stress can be expressed as:

$$\tau_{i-a} = -\mu_g \left. \frac{\partial U_g}{\partial r} \right|_{r=R-\delta} = \frac{-\mu_\ell U_{max-a}}{R\sqrt{\alpha}\left(\ln\sqrt{\alpha} - \frac{\mu_r}{2}\right)} . \tag{63}$$

Figures 82 and 83 show the interfacial shear stress as functions of quality using δ_{ave} and δ_r respectively. It is interesting to observe that τ_i decreases as the quality increases using this velocity model.

Using equation (20) for the gas velocity, the interfacial shear stress as predicted by the ln-ln model becomes:

$$\tau_{i-b} = \mu_g \left. \frac{\partial U_g}{\partial y} \right|_{y=\delta} = \frac{\mu_g U_{max-b}}{\eta R \Lambda_1} . \tag{64}$$

Figures 84 and 85 show interfacial shear stress as functions of quality for each flow rate using δ_{ave} and δ_r respectively.

Now using equations (27) and (33) for the gas velocity of the linear-ln model and the ln-cos model respectively, their predictions of interfacial shear stress are given as:

$$\tau_{i-c} = \mu_g \left. \frac{\partial U_g}{\partial y} \right|_{y=\delta} = \frac{\mu_g U_{max-c}\Lambda_2}{R\eta} \tag{65}$$

for the linear-ln velocity profile model, and

$$\tau_{i-d} = -\mu_g \left. \frac{\partial U_g}{\partial r} \right|_{r=R-\delta} = \frac{\pi\mu_g U_{max-d}}{2R\sqrt{\alpha}\Lambda_3} \tag{66}$$

for the ln-cos velocity profile models. Figures 86 and 87 show τ_i as a function of quality for the different flow
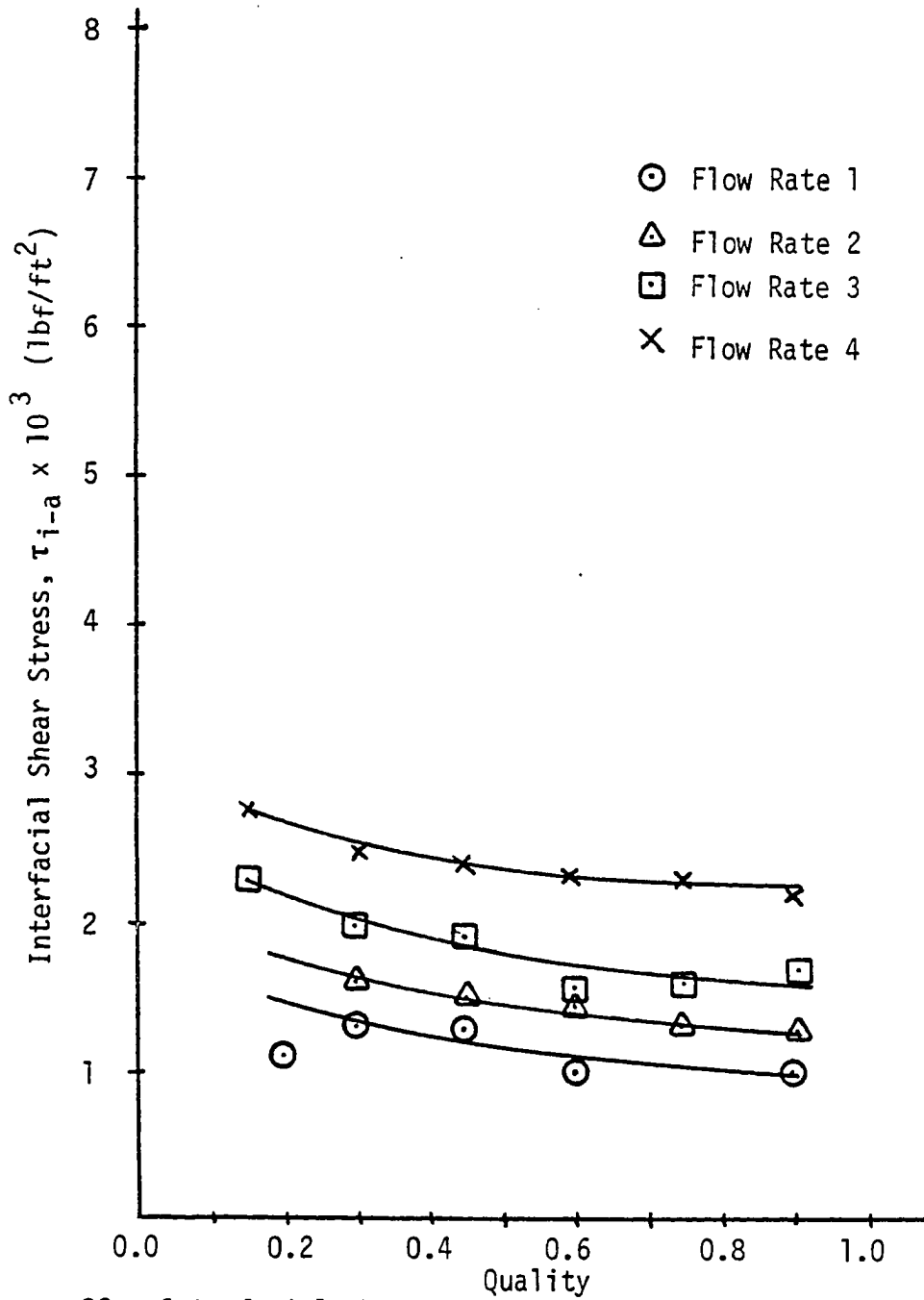
Figure 82. Interfacial Shear Stress vs. Quality for the Ln-Parabolic Model Using δ_{ave}.
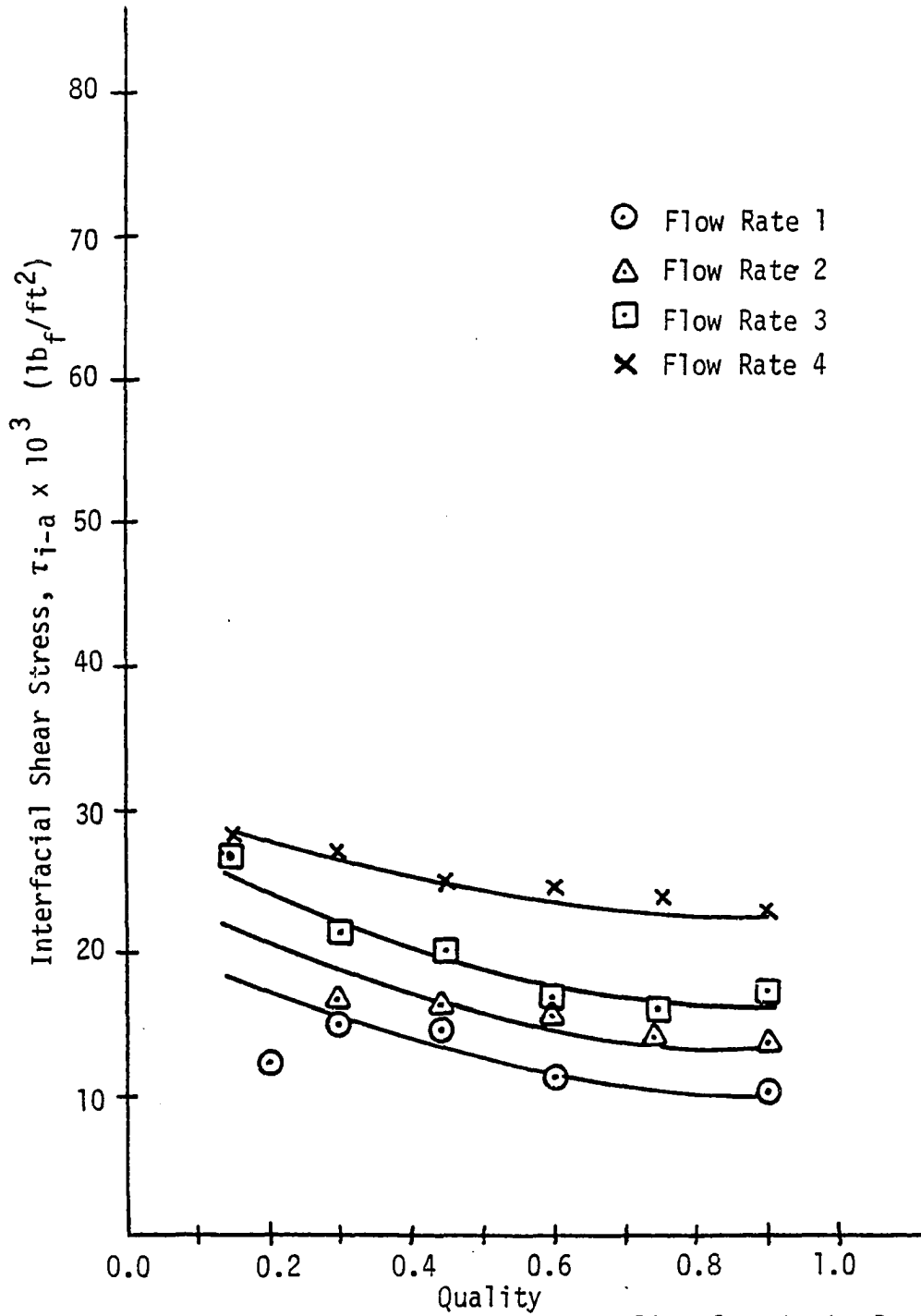
Figure 83. Interfacial Shear Stress vs. Quality for the Ln-Parabolic Model Using δ_r.
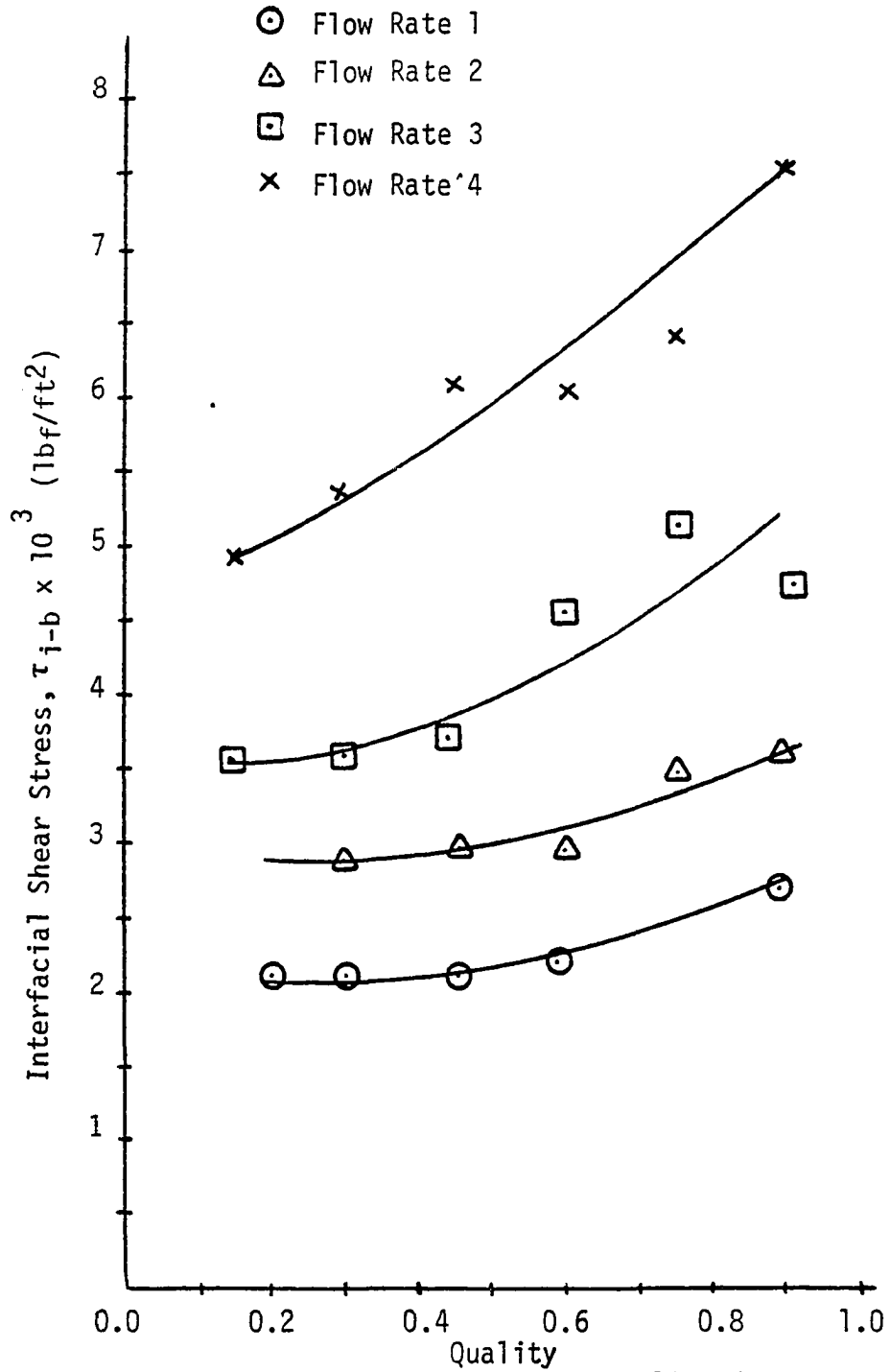
Figure 84. Interfacial Shear Stress vs. Quality for the Ln-Ln Model Using δ_{ave}.
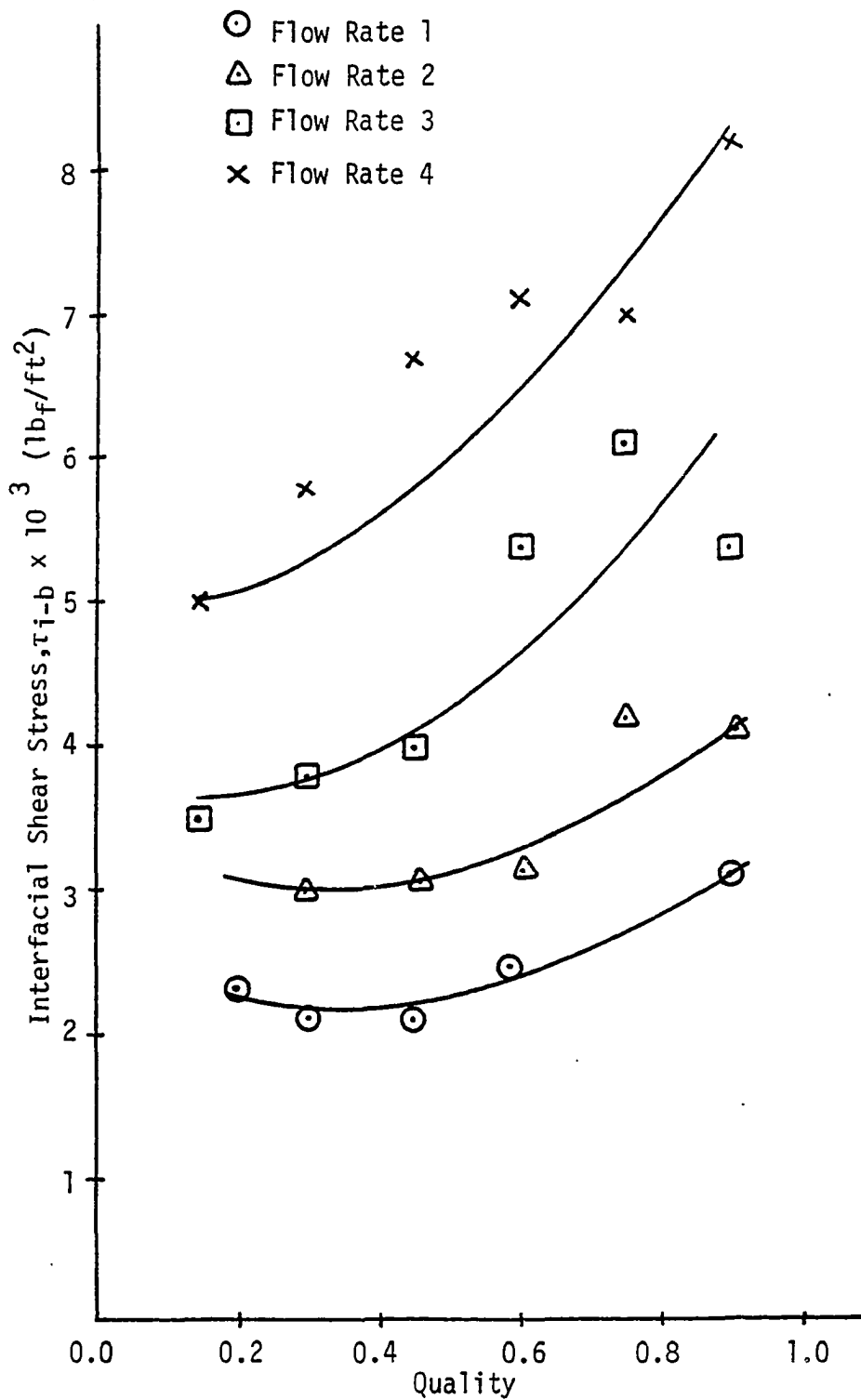
Figure 85. Interfacial Shear Stress vs. Quality for the Ln-Ln Model Using δ_r.
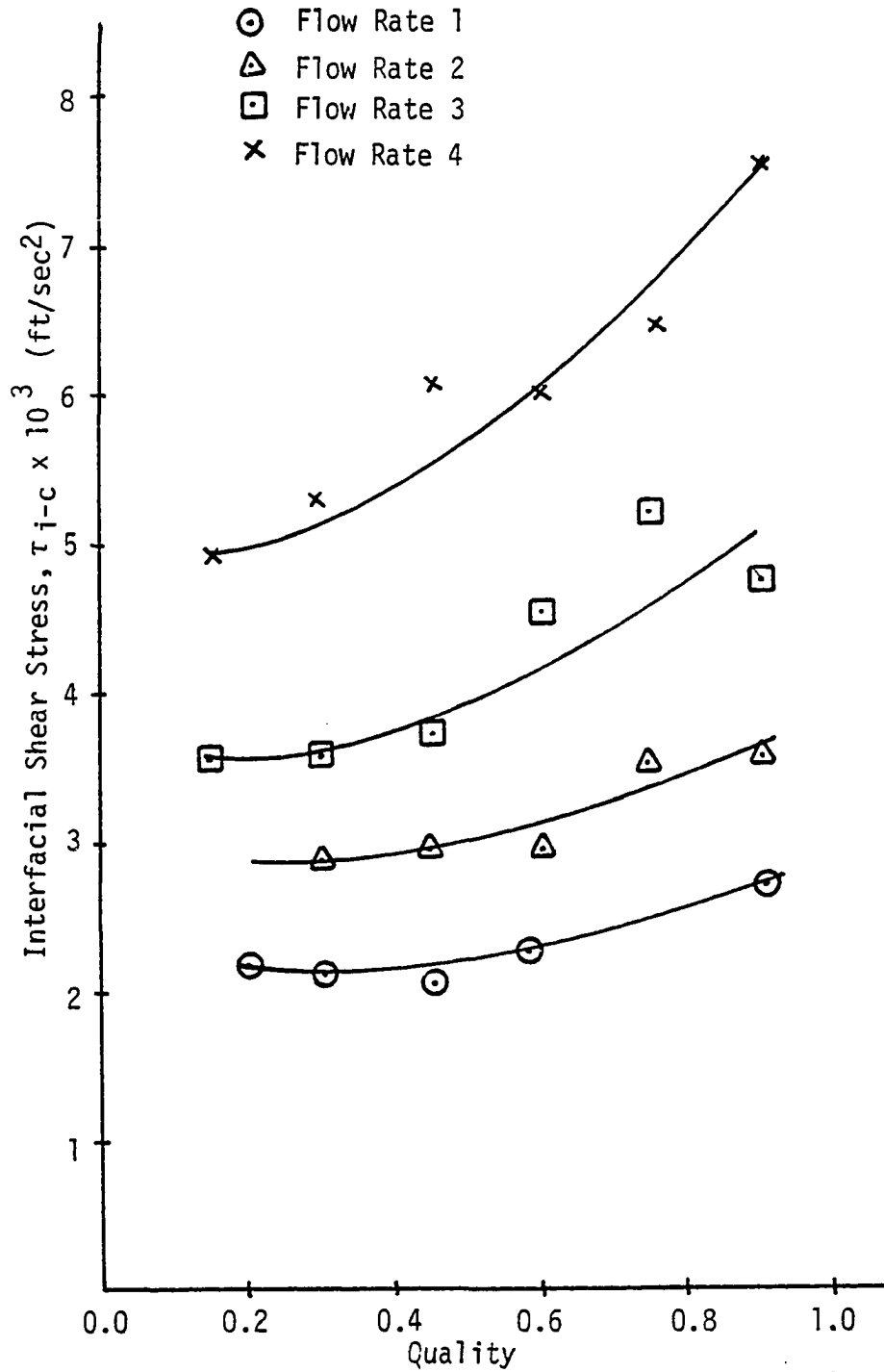
Figure 86.   Interfacial Shear Stress vs. Quality for the Linear-Ln
Model Using δ_{ave}.
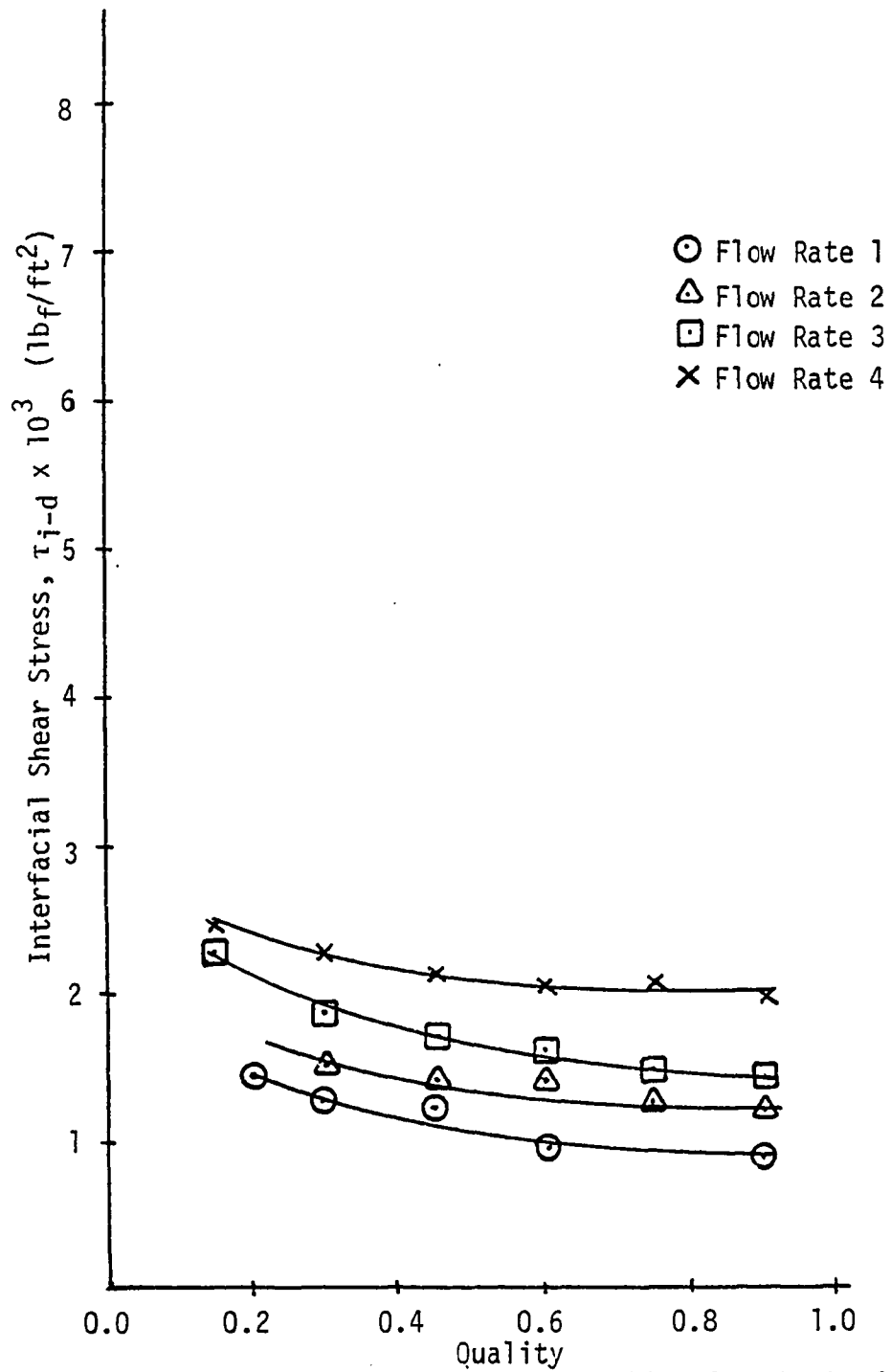
Figure 87. Interfacial Shear Stress vs. Quality for the Ln-Cosine
Model Using δ_{ave}.

rates using δ_{ave} for these two velocity models.

Table XII compares values of interfacial shear stress from Wallis[62] with values from this study. τ_1 was calculated using curves that relate gas and liquid flow rates to a non-dimensional pressure term. This non-dimensional pressure term is converted into an equivalent pressure and body force which is used to calculate an interfacial shear stress as follows:

$$\tau_1 = -\frac{D\sqrt{\alpha}\left(\frac{dP}{dz} + \rho_g g\right)}{4} ,\qquad (67)$$

where D is the diameter of the flow tube, dP/dz is the pressure gradient and $\rho_g g$ is the body force. τ_2 was calculated in a similar way except an equation relating non-dimension pressure as a function of the liquid flow rate was used. These values of interfacial shear stress are in reasonable agreement with values of other shear stress models, especially at high quality values.[63] Flow rates in the Wallis model can only be compared with the current study for flow rates 3 and 4.

Comparison of τ_{i-a} and τ_{i-b} with τ_1 and τ_2 show the values of shear stress from this study to be considerably lower. Even though the values of τ_{i-b} (from the ln-ln velocity model) are higher than τ_{i-a}, the values from the ln-parabolic model show the right trend by decreasing in magnitude as the amount of liquid increases.

Table XII. Comparison of Literature Values of Interfacial
Shear Stress to Values Calculated Using the
Ln - Parabolic Model and the Ln - Ln Model.

Note: All values given in lbf/ft^2.

Flow Condition Number	τ_1	τ_2	$\dfrac{\tau_{i-a}}{\delta_{ave}}$	$\dfrac{\tau_a}{\delta_{ave}}$	$\dfrac{\tau_{i-a}}{\delta_r}$	$\dfrac{\tau_a}{\delta_r}$	$\dfrac{\tau_{i-b}}{\delta_{ave}}$	$\dfrac{\tau_b}{\delta_{ave}}$	$\dfrac{\tau_{i-b}}{\delta_r}$	$\dfrac{\tau_b}{\delta_r}$
330	.400	.350	.0022	.0046	.0020	.0050	.0036	.0053	.0020	.0050
345	.090	.210	.0020	.0031	.0019	.0035	.0037	.0044	.0019	.0035
360	.058	.103	.0017	.0021	.0016	.0023	.0046	.0051	.0016	.0023
375	.058	.085	.0016	.0018	.0016	.0019	.0052	.0054	.0016	.0019
390	.030	.100	.0017	.0017	.0017	.0018	.0048	.0048	.0017	.0018
415	.213	.227	.0029	.0097	.0028	.0112	.0049	.0123	.0028	.0112
430	.163	.190	.0027	.0056	.0025	.0063	.0053	.0078	.0025	.0063
445	.120	.140	.0025	.0038	.0024	.0044	.0061	.0072	.0024	.0044
460	.090	.120	.0025	.0031	.0023	.0033	.0060	.0067	.0023	.0033
475	.060	.123	.0024	.0027	.0023	.0028	.0064	.0066	.0023	.0028
490	.023	.090	.0023	.0023	.0022	.0023	.0076	.0076	.0022	.0023

234

Wallis[64] has suggested that the effects of liquid entrainment can be taken into account by modifying the interfacial shear stress equation by the ratio of the mass of the gas to the total mass in the core region. This corresponds to the mass blockage factors of this current study. As a result, the values of interfacial shear stress can be modified as follows:

$$\tau_a = \frac{\tau_{i-a}}{B_3} \quad \text{and} \quad \tau_b = \frac{\tau_{i-b}}{B_4} \cdot \tag{68}$$

These results are also tabulated in Table XII. Again, they are less than τ_1 and τ_2 with values of τ_b being in closest agreement. It should be noted that not only does the blockage factor correction give results in closer agreement with the Wallis model but τ_b now shows the correct trend with higher values of interfacial shear stress at flow conditions having low quality, and decreasing as the amount of liquid decreases.

The reason for the differences in interfacial shear stress can be attributed to several factors. First, the boundary condition of equating interfacial shear stresses of the gas and the liquid has not been physically verified. Secondly, both the velocity profile and the blockage factors have been calculated using an integral, or averaging approach. Therefore, while these parameters may be reasonable in describing the flow pattern throughout the whole region,

they will not necessarily be accurate at any single point.

It should be remembered that velocity profiles and blockage factors can be obtained when either calculated or experimental values of interfacial shear stress are available by using a technique described earlier. In this approach, the equating of the interfacial shear stresses at the liquid-gas boundary is replaced by the constraint of a known shear stress at the boundary as shown by equation (35).

CHAPTER V

CONCLUSION

This study has dealt with both the experimental and
analytical aspects of axial photography as applied to two-
phase flow. The first stage of this study concentrated on
droplet and flow pattern data collection. The photographic
technique used is considered new and novel as applied to drop-
let measurement and no data of this exact nature is available
except for the work of Gass[65] which was restricted to a much
smaller range of flow rates and qualities. Hewitt and Hall-
Taylor[66] state that photography is the most advantageous
method of studying droplets, their distribution and their
flow. This technique eliminates the disturbance that comes
from inserting a probe into the flow stream. This is es-
pecially critical in two-phase flow since the presence of a
probe can cause coalescence of the liquid phase.

In this study photographic data was taken to record
droplet size, position and number over a wide range of quali-
ties, from approximately 15 to 90%, and at four different gas
flow rates. Using this data it is possible to realize more

237

completely the physical model of two-phase flow since each of the droplet variables were presented as a function of qualities for each of the flow rates. In addition to size, position and number of droplets, this study showed from a ratio of the major and minor axes that small droplets tend to be spherical while larger droplets are more elliptical in shape. Data also showed that the droplets were about evenly distributed across the gas core region based on constant area increments.

This study also yielded data on the thickness of the liquid film layer on the wall over a wide range of qualities at all four gas flow rates. Again, the photographic technique offers an advantage over many probe sampling techniques as film thickness measurements should be sensitive to any disturbance of the gas or liquid phase. The results of film thickness from this study are in reasonable agreement with film thicknesses reported in literature for similar conditions, especially at high quality flows.

Photographs and data from this study also confirmed the exchange of liquid between the film on the wall and the droplets in the core region. This resulted in considering single combined geometrical blockage factor for the tips of waves extending into the gas core region as well as the droplets in the gas core region. This geometrical blockage factor was found to be primarily a function of quality for the

range of gas flow rates studied. These geometrical blockage factors were calculated on both an area basis and on a volume basis, taking into account wakes behind both the droplets and the waves.

The concept of the blockage factor was then extended to a blockage factor based on the ratio of the mass flow of gas in the core to the total mass flow in core. The mass blockage factor takes into account the velocity and density as well as the area of each phase. As a result, this blockage factor is considered to be more indicative of the interfacial processes and the flow pattern of the two-phase mixture than the geometrical blockage factor. Assuming constant velocities in each phase while using droplet, film thickness and wave measurements, mass blockage factors based on experimental data were calculated and shown to be a strong function of quality, while approximately independent of the gas flow rate for the range of flow conditions in this study.

The second stage of this study was involved with analytical modeling of two-phase flow using the photographic data. First, several different velocity profile models based on separated flow were solved by using two different techniques. The first technique used four boundary conditions in addition to a mass balance on the gas phase to determine the velocity profiles and the maximum velocity. The second technique used only three boundary conditions but added an

additional constraint by specifying the shear stress at the interface of the gas and the liquid as well as the mass balance on the gas phase. This second technique allows a flow pattern to be established which would be in keeping with interfacial processes and the droplet, wave and film thickness data.

Experimental values of maximum velocity obtained for flow conditions at high qualities agreed reasonably well with the values predicted by the ln-parabolic velocity model but were in even closer agreement with the values predicted by the ln-ln velocity model.

The analysis section of this study also extended the velocity profile models for use in the mass blockage factor. Used with the velocity profiles, the blockage factor now reflects the flow pattern as well as the geometry. Values of mass blockage factor were calculated for each of the velocity profile models and presented as functions of quality for the range of gas flows used in this study. In using these values of mass blockage factors to modify the maximum velocity values obtained from separated flow equations for flow conditions with qualities of 75 to 90%, excellent agreement was found between the ln-ln model and the experimental data for all flow rates.

Application of both the velocity profile models and the mass blockage factors were used in the evaluation of the

interfacial shear stress expressions for each of the velocity models. Although the values of shear stress from this study were lower than the values obtained from other models in literature, modification of the predicted shear stresses by the blockage factors not only brought the magnitude of these shear stresses into closer agreement but also corrected the trend of the interfacial shear stresses so they were in keeping with other shear stress models. Thus, the mass blockage factor was established as an important parameter for extending the concept of separated two-phase flow models by taking into account the liquid entrainment in the core region and the variation in the velocities of both phases as well as other interfacial processes.

In view of the results of this study, and with further development, axial photography may become a predominant method for measuring and recording two-phase flow data.

<u>Recommendations For Future Research</u>

Research invariably raises more questions and introduces areas of interest that lead to further study. Such has been the case with this study as the following list of items will indicate.

1. A study should be made on how many slides at
    a given flow condition constitutes a valid
    data sample. Included in this work could
    be a study on the reproducibility of two-phase

data using the axial photographic technique,
comparing the results to similar tests using
some of the probe techniques.

2. A study on the size of the lighted opening
   should be undertaken, including changing the slit
   size as well as the lighting technique.

3. Expand the use of axial photography to include
   movies. Data taken from successive frames of a
   movie may be useful in establishing the number
   of photographs needed for a valid sample at a
   given flow rate.

4. Expand the range of gas flow rates.

5. Look for a quicker and less tedious method for
   determining droplet size, position and number.
   It is thought that a photograph could be digitized
   and displayed on a computer terminal screen. Be-
   cause of the judgment needed to select droplets
   and waves based on focus and color as well as
   brightness, all human participation may not be
   eliminated but the time for the calculation of
   wave and droplets areas, position and number as
   well as geometrical blockage factors could be
   greatly reduced.

6. Using other techniques, such as pressure measure-
   ments, obtain reliable values of interfacial shear

stresses and calculate velocity profile models and their corresponding blockage factors. Compare the shapes and values of these profile factors with the results from this study.

7. Continue to extend the use of the droplet, wave and film thickness data from this study to other existing two-phase flow models and then compare these new results to existing results.

8. Study the effect that disturbances due to geometric restrictions in the flow stream have on size, position, number and distribution of droplets and waves.

The author sees each of these items as challenging areas for additional study and plans to be involved with many of these in the immediate future.

LIST OF REFERENCES

[1] C.F. Tangren, C.H. Dodge, and H.S. Siefert, "Compressibility Effects in Two Phase Flow," *Journal of Applied Physics*, XX (1949).

[2] R.V. Smith, "Choking Two-Phase Flow Literature Summary and Idealized Design Solutions for Hydrogen, Nitrogen, Oxygen, and Refrigerants," Natl. Bur. of Standards Tech. Note 179 (1963).

[3] H. Fauske, "Critical Two-Phase Steam-Water Flows," Proceedings of 1961 Heat Transfer and Fluid Mechanics Institute, (Stanford: Stanford University Press, 1961) 79.

[4] F.J. Moody, "Maximum Flow Rate of a Single Component Two Phase Mixture," *Transactions of ASME*, Series C, No. 89, (1965), p. 134.

[5] J.E. Cruver and R.W. Moulton, "Critical Flow of Liquid Vapor Mixtures," *AIChE Journal*, No. 13 (1967), 52.

[6] R.E. Henry, "An Experimental Study of Low Quality Steam-Water Critical Flow at Moderate Pressure," ANL-7740, (1968).

[7] R.E. Henry and H.K. Fauske, "The Two-Phase Critical Flow of One Component Mixtures in Nozzles, Orifices, and Short Tubes," *ASME Journal of Heat Transfer*, (1971).

[8] J.A. Vogrin, Jr., "An Experimental Investigation of Two-Phase Two Component Flow in a Horizontal Converging-Diverging Nozzle," ANL 6754 (1963).

[9] W.J. Klingbiel, *Critical Flow Slip Ratios of Steam-Water Mixture* (Ph.D. Thesis, University of Washington, Seattle, 1964).

[10] Fauske, *op.cit.*, p. 79.

[11] R.V. Smith, "Critical Two-Phase Flow for Cryogenic Fluids," Natl. Bur. of Stands. Tech. Note 633 (1976), pp. 19-20.

[12]R.V. Smith, W.R. Martindale, and R.D. Lindsted, Two-Phase Sonic Velocity Measurements for Separated Flow (ASME paper no. 75-WA/HT-34).

[13]Smith, "Critical Two-Phase Flow for Cryogenic Fluids," op.cit., p. 11-21.

[14]G.B. Wallis, One-Dimensional Two-Phase Flow, (New York: McGraw-Hill, Inc., 1969), p. 394.

[15]G.F. Hewitt and W.S. Hall-Taylor, Annular Two-Phase Flow (Oxford, England, Pergamon Press, 1970).

[16]R.V. Smith, Two-Phase, Two Component Critical Flow in a Venturi, (Ph.D. Thesis, University of Oxford, England, 1968).

[17]R.V. Smith, "Two-Phase, Two-Component Critical Flow in a Venturi," Journal of Basic Engineering, (March, 1972), pp. 147-155.

[18]G.B. Wallis, "Annular Two-Phase Flow, Part I: A Simple Theory," Journal of Basic Engineering, (March, 1970).

[19]G.B. Wallis, "Annular Two-Phase Flow, Part II: Additional Effects," Journal of Basic Engineering, (March, 1970).

[20]D.A. Sullivan, "Two-Phase Annular Flow in Pipes: Analytical Models," (Report #27327-10, NSF Grant GK-1841, August 1970).

[21]W.R. Martindale, "Two-Phase Air-Water Upward Annular Flow in a Converging Nozzle," (unpubl. Ph.D. Thesis, Wichita State University, 1977).

[22]Sullivan, op.cit.

[23]D.G. Ryley and J.B. Fallon, Size Sampling of Steam-Borne Water Droplets, (Thermodynamics Fluid Mechanics Convention, Liverpool, paper #25, April 1966).

[24]R. Farmer, P. Griffith, and W.M. Rohsenow, "Liquid Droplet Deposition in Two-Phase Flow," Journal of Heat Transfer, LXXXXII, Series C (November, 1970), 587-594.

[25]S.S. MacLeod and G.B. Wallis, "Experience with the Wicks-Dukler Probe for Measuring Drop Size Distributions in Sprays," (unpubl. Dartmouth College Report, December, 1969).

[26]K.T. Cooper, J.F. Hewitt, and B. Pinchin, "Photography of Two-Phase Gas-Liquid Flow," Journal of Photographic Science, XII (1963), 269. (See also AERE-R 4301, 1963).

[27] C.R. Arnold and J.F. Hewitt, "Further Developments in the Photography of Two-Phase Gas-Liquid Flow," Journal of Photographic Science, XV (1967) 97-114. (See also AERE-R 5318, 1967).

[28] L.B. Cousins and J.F. Hewitt, "Liquid Mass-Transfer in Annular Two Phase Flow: Droplet Deposition and Liquid Entrainment," (AERE-R 5657, 1968).

[29] Hewitt and Hall-Taylor, op.cit.

[30] M. Cumo, G.E. Farello, G. Ferrari, and G. Pallazzi, "On Two-Phase Highly Dispersed Flows," (unpubl. paper presented at the ASME-AiChE Heat Transfer Conference, Atlanta, Georgia, 1973).

[31] Hewitt and Hall-Taylor, op.cit., p. 136a.

[32] J. Gass, "An Experimental Photographic Technique for the Study of the Liquid Droplets in Annular Two-Phase Flow," (unpubl. Master's Degree Thesis, Mechanical Engineering Department, Wichita State University, 1976).

[33] C.T. Crowe, M.P. Sharama, and D.E. Stock, The Particle-Source-in-Cell (PSI-Cell) Model for Gas-Droplet Flows, (ASME paper no. 75-WA/HT-25).

[34] A.E. Bergles, "Electrical Probes for Study of Two-Phase Flows," (Eleventh Natl. ASME-AIChE Heat Transfer Conf., Minneapolis, August, 1969) pp. 70-81.

[35] Electric Power Research Institute Report: Experimental Methods in Two-Phase Flow Studies (Harwell, England: Heat Transfer and Fluid Flow Service, Atomic Energy and Research Establishment, 1976), pp. 65-68, 115-120.

[36] Gass, op.cit.

[37] Wallis, One-Dimensional Two-Phase Flow, op.cit., p. 394.

[38] M. Wicks and A.E. Dukler, In Situ Measurements of Drop Size Distribution in Two-Phase Flow: A New Method for Electrically Conducting Liquids (Paper presetned at the International Heat Transfer Conference, Chicago, Illinois, 1966).

[39] L.E. Gill, G.F. Hewitt, J.W. Hitchon, and P.M.C. Lacey, Sampling Probe Studies of the Gas Core in Annular Two-Phase Flow, Parts I, II, and III (AERE-R 3954 (1962), AERE-R 3955 (1963), and AERE-M 1202 (1966) Harwell, Berkshire, U.K.).

[40]Smith, Martindale, and Lindsted, op.cit.

[41]Gass, op.cit., p. 19.

[42]R.D. Lindsted, D.L. Evans, J.C. Gass, and R.V. Smith, "Droplet Data from Vertical Two-Phase Flow Using Axial Photography," (unpubl. NU-REG report, 1977).

[43]D.L. Evans, "The Processing of Two-Phase Flow Droplet and Flow Pattern Data," (unpubl. Directed Studies Report, Mechanical Engineering Department, Wichita State University, June 1977), p. 9.

[44]Crowe, Sharama, and Stock, op.cit.

[45]S.F. Chien and W. Ibele, "Pressure Drop and Liq id Film Thickness of Two Phase Annular and Annular-Mist Flo ," Journal of Heat Transfer, (February, 1964), 89-96.

[46]L.E. Gill, G.F. Hewitt, and P.M.C. Lacey, "Part II: Studies of the Effect of Phase Flow Rates on Phase and Velocity Distribution," op.cit., p. 27.

[47]J.A. Hughmark, "Film Thickness, Entrainment and Pressure Drop in Upward Annular and Dispersed Flow," AIChE Journal, IXX (September, 1975), 1062-1065.

[48]Sullivan, op.cit., p. 44.

[49]Ibid., p. 44.

[50]R.B. Bird, W.E. Stuart, and E.N. Lightfoot, Transport Phenomena (New York: John Wiley and Sons, Inc., 1966) pp. 74-98.

[51]J.J. Lee, M.E. Fourney, and R.W. Moulton, "Determination of Slip Ratios in Air-Water Two-Phase Critical Flow at High Quality Levels Utilizing Holographic Techniques," AIChE Journal, XX (March, 1974).

[52]D. Chisholm, An Equation for Velocity Ratio in Two-Phase Flow (National Engineering Laboratory Report no. 535, December, 1972).

[53]Wallis, "Annular Two-Phase Flow, Part I," op.cit.

[54]L.B. Cousins and G.F. Hewitt, Liquid Phase Mass Transfer on Annular Two-Phase Flow Radial Liquid Mixing (AERE-R 5693, Harwell, Berkshire, U.K., 1968).

[55]R.V. Smith, L.B. Cousins, and G.F. Hewitt, _Two-Phase, Two-Component Critical Flow in a Venturi_, (UKAEA Report, AERE-R 536, 1968).

[56]Smith, "Two-Phase, Two-Component," _Journal of Basic Engineering_, op.cit., pp. 147-155.

[57]Smi.:h, "Cryogenic Fluids," _op.cit._, pp. 46-48.

[58]D.A. Sullivan, in a discussion of Smith, R.V., "Two-Phase, Two-Component Critical Flow in a Venturi," _Journal of Basic Engineering_, (March, 1972) pp. 152-154.

[59]G.B. Wallis and D.A. Sullivan, "Two-Phase Air-Water Nozzle Flow," _Journal of Basic Engineering_ (December 1972) 788-794.

[60]Wallis, "Annular Two-Phase Flow, Part II," _op.cit._, p. 76.

[61]Wallis and Sullivan, _op.cit._, p. 792.

[62]Wallis, "Annular Two-Phase Flow, Part I," _op.cit._, pp. 59-62.

[63]_Ibid._, pp. 64-65.

[64]Wallis, "Annular Two-Phase Flow, Part II," _op.cit._, p. 76.

[65]Gass, _op.cit._

[66]Hewitt and Hall-Taylor, _op.cit._, p. 272.

APPENDIX

249

APPENDIX A

The following page shows a sample of the computer output describing the droplet data profile as calculated for each slide. The information includes droplet size and position and the liquid film thickness corresponding to the tracings as well as the scaled-down sizes which refer to the actual dimensions of the flow tube. In addition, the droplet and wave areas and volumes are also shown along with values of the blockage factor for this particular slide. The dimensions are given in inches, the areas are given in square inches, the volumes are given in cubic inches and the blockage factors are dimensionless.

PICTURE NO.   475- 10

	REAL	PICTURE
INSIDE PIPE RAD (INCHES)	0.6290	2.6150
AVE. WATER LAYER THICK. (IN)	0.0342	0.1422
AVE. GAS CORE RAD. (INCHES)	0.5948	2.4728

DROPLET	POSITION		MAJOR AXIS		MINOR AXIS		CROSS AREA		VOLUME
NO.	REAL	PICTURE	REAL	PICTURE	REAL	PICTURE	REAL	PICTURE	H=5D REAL
1	0.3175	1.3200	0.0241	0.1000	0.0168	0.0700	0.0003	0.0055	0.000011
2	0.1563	0.6500	0.0649	0.2700	0.0216	0.0900	0.0011	0.0191	0.000069
3	0.1251	0.5200	0.0409	0.1700	0.0216	0.0900	0.0007	0.0120	0.000034
4	0.3079	1.2800	0.0192	0.0800	0.0120	0.0500	0.0002	0.0031	0.000005
5	0.5555	2.3100	0.0553	0.2300	0.0361	0.1500	0.0016	0.0271	0.000117
6	0.5196	2.1600	0.0457	0.1900	0.0313	0.1300	0.0011	0.0194	0.000071
7	0.1588	0.6600	0.0265	0.1100	0.0192	0.0800	0.0004	0.0069	0.000015
8	0.1443	0.6000	0.0289	0.1200	0.0192	0.0800	0.0004	0.0075	0.000017
9	0.3608	1.5000	0.0481	0.2000	0.0120	0.0500	0.0005	0.0079	0.000018
10	0.4185	1.7400	0.0216	0.0900	0.0144	0.0600	0.0002	0.0042	0.000007
11	0.4233	1.7600	0.0192	0.0800	0.0120	0.0500	0.0002	0.0031	0.000005

```
                        TOTAL REAL AREA      0.006707
                        TOTAL REAL VOLUME    0.000368
                        GAS CORE REAL VOL    0.333431


                        TOTAL REAL WAVE AREA  0.022564
                        TOTAL REAL WAVE VOL   0.006769
```

PICTURE NO.	NO. DROPLETS	BF1	BF2	BF4	BF4NW	BF5	BF5NW	BF6
10	11	0.93307	0.98383	0.97366	0.99397	0.97859	0.99889	0.19279

BIBLIOGRAPHY

Arnold, C.R. and Hewitt, G.F. "Further Developments in the Photography of Two-Phase Gas-Liquid Flow," Journal of Photographic Science, XV (1967), 97-114.

Bergles, A.E., "Electrical Probes for Study of Two-Phase Flows," Proceedings of Eleventh National ASME-AIChE Heat Transfer Conference, Minneapolis, August, 1969, pp. 70-81.

Bird, R.E., Stuart, W.E., and Lightfoot, E.N. Transport Phenomena. New York: John Wiley and Sons, Inc., 1966.

Butterworth, D. Air-Water, Annular Flow in a Horizontal Tube. AERE Report No. R 6687, Harwell, Berkshire, 1971.

Chien, S.F. and Ibele, W. "Pressure Drop and Liquid Film Thickness of Two-Phase Annular and Annular-Mist Flow," Journal of Heat Transfer, (February, 1964), 89-96.

Chisholm, D. An Equation for Velocity Ratio in Two-Phase Flow. National Engineering Laboratory Report No. 536, December, 1972.

_____. "Pressure Gradients During the Flow of Incompressible Two-Phase Mixtures through Pipes, Venturis, and Orifice Plates," British Chemical Engineering, XII (September, 1967), 454-457.

Cooper, K.D., Hewitt, G.F., and Pinchin, B. "Photography of Two-Phase Gas-Liquid Flow," Journal of Photographic Science, XII (1963).

Cousins, L.B. and Hewitt, G.F. Liquid Mass-Transfer to Annular Two-Phase Flow: Droplet Deposition and Liquid Entrainment. AERE-R 5657, Harwell, Berkshire, 1968.

_____. Liquid Phase Mass Transfer in Annular Two-Phase Flow: Radial Liquid Mixing. AERE Report R-5693, Harwell, Berkshire, 1968.

252

Crowe, C.T., Sharama, M.P., and Stock, D.E. The Particle-Source-in-Cell (PSI-Cell) Model for Gas-Droplet Flows. ASME paper no. 75-WA/HT-25.

Cruver, J.E. and Moulton, R.W. "Critical Flow of Liquid Vapor Mixtures," AIChE Journal, no. 13 (1967).

Cumo, M., Farello, G.E., Ferrari, J., and Pallozzi, G. "On Two-Phase Highly Dispersed Flows." Unpublished paper presented at ASME-AIChE Heat Transfer Conference, Atlanta, 1973.

Electric Power Research Institute Report: Experimental Methods in Two-Phase Flow Studies. Harwell, England: Heat Transfer and Fluid Flow Service, Atomic Energy and Research Establishment, 1976.

Evans, D.L. "The Processing of Two-Phase Flow Droplet and Flow Pattern Data," Unpublished Directed Studies Report, Mechanical Engineering Department, Wichita State University, June, 1977.

Farmer, R., Griffith, P., and Rohsenow, W.M. "Liquid Droplet Deposition in Two-Phase Flow," Journal of Heat Transfer, Series C (November, 1970), pp. 587-594.

Fauske, H. "Critical Two-Phase Steam-Water Flows," Proceedings of 1961 Heat Transfer and Fluid Mechanics Institute. Stanford: Stanford University Press, 1961.

Forslund, R.P., Rohsenow, W.M. Thermal Non-Equilibrium in Dispersed Flow Film Boiling in a Vertical Tube, NASA Report No. 75312-44, Contract No. NSF GK 39, November, 1966.

Gass, J. "An Experimental Photographic Technique for the Study of the Liquid Droplets in Annular Two-Phase Flow," Unpublished Master's Degree Thesis, Mechanical Engineering Department, Wichita State University, 1976.

Gill, L.E., Hewitt, G.F., Hitchon, J.W., and Lacey, P.M.C. Sampling Probe Studies of the Gas Core in Annular Two-Phase Flow, Parts I, II, and III. AERE Report No. R 3954 (1962), R 3955 (1963), M 1202 (1966), Harwell, Berkshire, United Kingdom.

Haberstroh, R.D., and Griffith, P. The Transition from the Annular to the Slug Flow Regime in Two-Phase Flow. Technical Report 5003-28, Mechanical Engineering Department, MIT, June, 1964.

Henry, R.E. An Experimental Study of Low Quality Steam-Water Critical Flow at Moderate Pressure. ANL-7740, 1968.

Henry, R.E. and Fauske, H.K. "The Two-Phase Critical Flow of One Component Mixtures in Nozzles, Orifices, and Short Tubes," ASME Journal of Heat Transfer, 1971.

Hewitt, G.F. and Hall-Taylor, W.S. Annular Two-Phase Flow. Oxford, England: Pergamon Press, 1970.

Hughmark, G.A. "Film Thickness, Entrainment, and Pressure Drop in Upward Annular and Dispersed Flow," AIChE Journal, IXX (September, 1975), 1062-1065.

Klingbiel, W.J. Critical Flow Slip Ratios of Steam-Water Mixture. PhD. Thesis, University of Washington, Seattle, 1964.

Lee, Y.J., Fourney, M.E., and Moulton, R.W. "Determination of Slip Ratios in Air-Water Two-Phase Critical Flows at High Quality Levels Utilizing Holographic Techniques," AIChE Journal, XX (March, 1974).

Lindsted, R.D., Evans, D.L., Gass, J.C., and Smith, R.V. "Droplet Data from Vertical Two-Phase Flow Using Axial Photography," Unpublished NU-REG report, 1977.

MacLeod, S.S. and Wallis, G.B. "Experience with the Wicks-Dukler Probe for Measuring Drop Size Distributions in Sprays," Unpublished Dartmouth College Report, Dec. 1969.

Martindale, W.R. "Two-Phase Air-Water Upward Annular Flow in a Converging Nozzle," Unpublished Ph.D. Thesis, Wichita State University, 1977.

Moody, F.J. "Maximum Flow Rate of a Single Component Two Phase Mixture," Transactions of ASME, Series C, No. 89, 1965.

Puskina, O.L. and Sorokin, Y.L. "Breakdown of Liquid Film Motion in Vertical Tubes," Heat Transfer-Soviet Research, I, No. 5, (September, 1969), pp. 56-64.

Ryley, D.J. "Two-Phase Critical Flow in Geothermal Steam Wells," International Journal of Mechanical Sciences, Vol. 6, 1964, pp. 273-285.

Ryley, D.J. and Fallon, J.B. Size Sampling of Steam-Borne Water Droplets, Paper # 25 presented at Thermodynamics Fluid Mechanics Convention, Liverpool, April, 1966.

Smith, R.V. "Choking Two-Phase Flow Literature Summary and Idealized Design Solutions for Hydrogen, Nitrogen, Oxygen, and Refrigerants," National Bureau of Standards Technical Note 179, (1963).

_____. "Critical Two-Phase Flow for Cryogenic Fluids," National Bureau of Standards Technical Note 633, (1976).

_____. Two-Phase, Two-Component Critical Flow in a Venturi. Ph.D. Thesis, University of Oxford, England, 1968.

_____. "Two-Phase, Two-Component Critical Flow in a Venturi," Journal of Basic Engineering, (March, 1972), pp. 147-155.

Smith, R.V., Cousins, L.B., and Hewitt, G.F. Two-Phase, Two Component Critical Flow in a Venturi, UKAEA Report, AERE-R 536, 1968.

Smith, R.V., Martindale, W.R., and Lindsted, R.D. Two-Phase Sonic Velocity Measurements for Separated Flow. ASME paper no. 75-WA/HT-34.

Sullivan, D.A. A discussion of Smith, R.V., "Two-Phase, Two-Component Critical Flow in a Venturi," Journal of Basic Engineering, (March, 1972), pp. 152-154.

_____. "Two-Phase Annular Flow in Pipes: Analytical Models," Report #27327-10, NSF Grant GK-1841, August, 1970.

Tangren, C.F., Dodge, C.H., and Siefert, H. "Compressibility Effects in Two-Phase Flow," Journal of Applied Physics, XX (1949).

Vogrin, J.A., Jr. "An Experimental Investigation of Two-Phase, Two Component Flow in a Horizontal Converging-Diverging Nozzle," ANL 6754 (1963).

Wallis, G.B. One-Dimensional Two-Phase Flow, New York: McGraw-Hill, Inc., 1969.

_____. "Annular Two-Phase Flow, Parts I and II," Journal of Basic Engineering, (March, 1970).

Wallis, G.B. and Sullivan, D.A. "Two-Phase Air-Water Nozzle
     Flow," Journal of Basic Engineering, (December, 1972),
     pp. 788-794.

Wallis, G.B. and Makkenchery, S. "The Hanging Film Phenome-
     non in Vertical Annular Two-Phase Flow," Journal of
     Fluids Engineering, (September, 1974), pp. 297-298.

Wicks, M. and Dukler, A.E. In Situ Measurements of Drop
     Size Distribution in Two-Phase Flow: A New Method
     for Electrically Conducting Liquids, presented at the
     International Heat Transfer Conference, Chicago,
     Illinois, 1966.